Université Côte d'Azur

Habilitation à Diriger des Recherches

présentée par

Giorgio Krstulovic

A theoretical description of vortex dynamics in superfluids.
Kelvin waves, reconnections and particle-vortex interaction

le 20 octobre 2020

Jury

Gabriele Ferrari	Rapporteur
Miguel Onorato	Rapporteur
Alain Pumir	Rapporteur
Bérengère Dubrulle	Examinatrice
Robin Kaiser	Examinateur
Victor L'Vov	Examinateur
John Christos Vassilicos	Examinateur
Thomas Frisch	Président

Remerciements

Contents

About this HDR manuscript

This *Habilitation à diriger des recherches* (HDR) manuscript presents a selection of my works realised after my PhD completion in 2010. It covers different aspects of superfluids on which I have contributed to the field. I have chosen to present only three topics: Kelvin waves, quantum vortex reconnections and particle-vortex interactions. Furthermore, I restricted the discussion to low-temperature superfluids, in particular to those described in the framework of the Gross-Pitaevskii model.

The first two chapters of the manuscript contain a general introduction to superfluid turbulence and its theoretical description. Chapter 3 presents the physics of Kelvin waves and explains the wave turbulence cascade associated with it. Two of my contributions to that topic ([Krs12; VPK16]) are integrally included in this chapter. Chapter 4 gives a brief introduction to vortex reconnections, providing the basic elements to understand three included publications ([VPK17; VPK20; GK20b]). Chapter 5 discusses the use of particles for studying superfluid turbulence and quantum vortex dynamics. After a discussion on the theoretical modelling, I present three of my recent contributions to the field ([GK19; GKN20; GK20a]).

The choice of topics and publications presented in this manuscript left aside many other of my works. I refer to some of them in the manuscript. For conciseness, I did not include some works concerning the dynamics of finite temperature superfluids, intermittency, large-scale co-flow and counterflow turbulence.

Since I joined CNRS in October 2013, my works have received the support of different funding agencies, such as the CNRS/Royal Society International Exchanges with Davide Proment (UEA, Norwich, UK), the PHC Ulysses with M. Bustamante (UCD, Dublin, Ireland), the Royal Society International Exchanges with Luca Galantucci (and the Newcastle University team) and the PHC ECOS Sud with Gustavo Düring (PUC, Chile). It was consolidated with the attribution in 2018 of an ANR Jeune Chercheur. Besides, I am currently a member of the SIMONS Collaboration on Wave Turbulence. Some of these grants and the local support of Université Côte d'Azur allowed me to advise the Ph.D students Umberto Giuriato and Nicolas P. Müller and the postdoctoral researcher Juan I. Polanco. Working with them has been crucial for my research achievements.

Finally, I would like to mention that my research is not only focused on superfluids. I have devoted a considerable part of my research to classical turbulence, Lagrangian dynamics and the study of wave turbulence on different physical systems. I give in the following, a list of publications (not related with my Ph.D. work) that were not selected for this manuscript. The full list of publications is available in my web page [1].

Quantum turbulence

1. N.P Müller, J.I. Polanco, G. Krstulovic. *Intermittency of velocity circulation in quantum turbulence.* arXiv:2010.07875 (2020).

2. U. Giuriato, G. Krstulovic. *Stochastic Motion of Finite-Size Immiscible Impurities in a Dilute Quantum Fluid at Finite Temperature.* arXiv:2009.10596 (2020).

3. N.P Müller, G. Krstulovic. *Kolmogorov and Kelvin wave cascades in a generalized model for quantum turbulence.* arXiv:2007.00540 (2020). Phys. Rev. B (2020, in press).

4. L.Galantucci, A.W. Baggaley, C.F. Barenghi, G. Krstulovic. *A new self-consistent approach of quantum turbulence in superfluid helium.* The European Physical Journal Plus 135, 7 (2020).

---

[1] https://gkrstulovic.gitlab.io

Wave turbulence

Langrangian dynamics in classical flows

Hydrodynamic and magnetohydrodynamic turbulence

Chapter 1

Superfluid turbulence. From nanometres to metres

This chapter presents a brief introduction to superfluids. We discuss some of the main theoretical and experimental achievements, from the discovery of superfluid helium to the first experimental realisation of a Bose-Einstein condensate. We provide a general description of superfluid turbulence and discuss the physical phenomena taking place at different length scales.

What are superfluids and where can we find them?

In very general terms, superfluids form a particular category among compressible fluids, distinguished essentially by the absence of molecular viscosity at very low temperatures. Perhaps, the most famous one is ^{4}He that becomes superfluid below 2.1768K. The superfluidity of helium was discovered almost simultaneously by J.F Allen and A.D Misener [AM38] and P. Kapitsa [Kap38] in 1938, and published in the same issue of *Nature*. Figure 1.1 (left) shows the phase diagram of ^{4}He. The line separating the
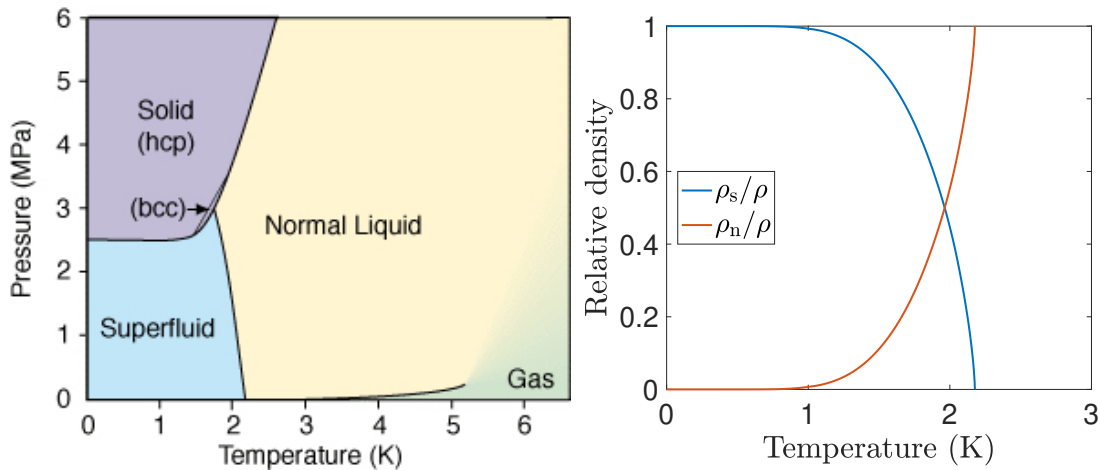
Figure 1.1: **Left:** Phase diagram of ^{4}He taken from Low Temperature Laboratory, Aalto University web page. **Right:** Normal and superfluid density ρ_s and ρ_n, normalised by the total helium density ρ. Data taken form [BD77].

superfluid and the normal fluid is called the λ-line. Its name comes from the specific heat of helium, because its curve, as a function of temperature, resembles the Greek letter λ, having a peak at the transition temperature. This critical temperature is often denoted by T_λ. Its name was suggested by

W.H. Keesom, who first observed that something was going on with helium at T_λ, well before 1938 (see [Bal04]). He also denoted the two phases of as helium as helium I and II, for temperatures above and below T_λ, respectively.

The same year that superfluid was discovered, and also in *Nature*, F. London [Lon38] made the connection between the λ-transition and Bose-Einstein condensation, a phenomenon well known at that time:

> *In his well-known papers, Einstein has already discussed a peculiar condensation phenomenon of the "Bose-Einstein" gas; but in the course of time the degeneracy of the Bose-Einstein gas has rather got the reputation of having a purely imaginary existence. Thus it is perhaps not generally known that this condensation phenomenon actually represents a discontinuity of the derivative of the specific heat ...*
>
> *Though actually the λ-point of helium resembles rather a phase transition of second order, it seems difficult not to imagine a connection with the condensation phenomenon of the Bose-Einstein statistics.*
>
> *...*
>
> *On the other hand, it is obvious that a model which is so far away from reality that it simplifies helium to an ideal gas, cannot ...*

<div align="right">F. London, Nature 1938.</div>

Amazingly, also the same year and again in the same journal, L. Tisza [Tis38] introduced the idea that two fluids are needed to explain some of the experimental observations made in superfluid helium. Some years later, L. Landau introduced his famous two-fluid model [Lan41]. In this description, a fraction of the fluid is superfluid while the remaining part is "normal". The total density ρ of helium thus decomposes as $\rho = \rho_\mathrm{n} + \rho_\mathrm{s}$, where ρ_n and ρ_s are the densities of the normal and superfluid components respectively. The temperature dependence of ρ_n and ρ_s is shown in figure 1.1 (right). The history of superfluid helium is fascinating, I refer to the excellent historical reviews by S. Balibar [Bal04; Bal07], from where the previous paragraphs were inspired.

Bose-Einstein condensation had to wait almost 60 years to completely clean its reputation "of having a purely imaginary existence". In 1995, the first experimental realisation of a Bose-Einstein condensation was achieved with rubidium atoms [And+95], and soon after their superfluid behaviour was observed. Since then, many experimental groups around the world perform experiments with Bose-Einstein condensates with different types of atoms and address questions of the most diverse kinds.

The formation of condensates has been observed in very different systems. Classical light propagating in a self-defocusing photorefractive crystal, that is roughly described by the same equations as Bose-Einstein condensates (BECs), was also observed to go through a (classical) wave condensation process [Sun+12]. Moreover, recent experiments with quantum fluids of light, a many-photon system with photon-photon interactions induced by the optical nonlinearity of the medium, have revealed interesting hydrodynamic superfluid properties [CC13]. Besides, there is another example of superfluids appearing in nature. It is believed that the core of neutron stars contains a superfluid part. Such an assumption is needed to explain some astronomical observations [AI75; Pag+11]. Finally, it is worth mentioning that superfluid helium is commonly used in industrial and technological applications for cooling superconducting materials and infrared detectors.

The most manifest quantum effect of a superfluid is the presence of quantum vortices, whose circulation (contour integral of the velocity) is quantised. This quanta is called the Onsager-Feynman quantum of circulation. Quantum vortices are extremely thin filaments with a core size as small as a couple of Angstroms (in ^{4}He). They are topological defects of the order parameter that describes the system, and for this reason, they are incredibly stable. Even though they are purely quantum objects, they advect each other as classical vortices described by the Euler equations. Such vortices can reconnect despite the lack of molecular dissipation, a phenomenon that is forbidden in classical ideal (inviscid) fluids because of

the Kelvin theorem. Reconnections between quantum vortices can lead to the formation of very complex tangles and turbulent states.

Typical length scales

Let's first discuss the case of superfluid helium at low temperatures. Current experiments have a typical size of $0.1 - 1m$, which is 10^{10} times larger than the vortex core size, the smallest intrinsic scale of the system. When looking at scales much larger than the typical inter-vortex distance ℓ, a classical hydrodynamic behaviour emerges. Based on the idea that turbulence is a universal phenomenon and that vortices interact at large scales in a similar manner than classical ones, it is natural to think that at length scales smaller than the injection scale L_I and much larger than ℓ, a classical-like turbulent cascade transfers the kinetic energy. Indeed, at such scales, the quantum nature of vortices can be neglected, and small-scale physical processes can be considered as an effective energy sink, ignoring the fine details of the mechanisms involved. In that vision, we imagine a coarse-grained description of a superfluid, more in the spirit of the Landau two-fluid model. Such a classical-like scenario was first confirmed by the experimental work of J. Maurer and P. Tabeling [MT98]. They measured the energy spectrum of superfluid helium and observed no change when helium is cooled down through the λ-point. The appearance of Kolmogorov turbulence at scales larger than ℓ is today a well-established fact [BSS14; VD07].

At scales of the order of the mean inter-vortex distance ℓ, this coarse-grained vision of superfluid helium breaks down. We can no longer ignore the fact that vortices have a quantised circulation. Energy arrives from the large scales via the Kolmogorov cascade to the scale ℓ. At low temperatures, dissipation through viscosity is absent, so that new physical mechanisms are need to take care of this energy input. There are two main mechanisms responsible for this transfer, the Kelvin wave cascade and vortex reconnections, both discussed in Chapters 3 and 4 respectively. During vortex reconnections, some energy of the vortex is dissipated by the emission of sound (phonons), while at the same time, they can also change their size, redistributing their energy at different scales and excite Kelvin waves [Kiv+01]. Kelvin waves are waves that propagate non-linearly along quantum vortices. If one considers scales much smaller than ℓ, but much larger than the vortex core size ξ, the theory of weak wave turbulence can predict that energy is transferred towards smaller scales through a direct energy cascade. While there are direct visualisations of quantum vortex reconnections [Bew+08] and Kelvin waves [Fon+14], no experimental confirmation of the aforementioned energy transfer mechanisms has been achieved.

At the crossover scales, where the Kolmogorov cascade reaches the mean inter-vortex distance, the situation is less clear. The natural scenario, proposed by L'Vov et al. [LNR07], is that as the Kolmogorov cascade is "strong" and the Kelvin wave cascade is "weak", a bottleneck will form, eventually leading to a thermalised zone joining the classical and quantum ranges. Such a scenario is far from being confirmed by experiments, and numerical simulations are challenging. In a recent numerical work [MK20], we observed a clear Kolmogorov and relatively well established Kelvin wave range. We indeed found a bottleneck but far from exhibiting a thermalised spectrum, although this could be explained by the limited inertial range of the Kelvin wave cascade. The phenomenology of low-temperature superfluid turbulence is summarised in figure 1.2.

If we now consider superfluid helium at finite temperatures, the description becomes more complex as new degrees of freedom are introduced. At finite temperatures, one needs to consider the interaction between the superfluid component and the normal fluid. The normal fluid dissipates energy through molecular dissipation, as any classical fluid. Depending on the temperature, both components are more or less coupled and can be locked to each other. Besides, a very different turbulent state, with no classical analogous, can emerge from this two-fluid description in the case that the two components have a non-zero mean relative velocity. Such state is known as counterflow turbulence [Don91]. Counterflow turbulence typically develops in channels where a heat source is placed in one of its ends. In this situation, the normal component carries the heat away from the source, while the superfluid flows in the opposite direction in
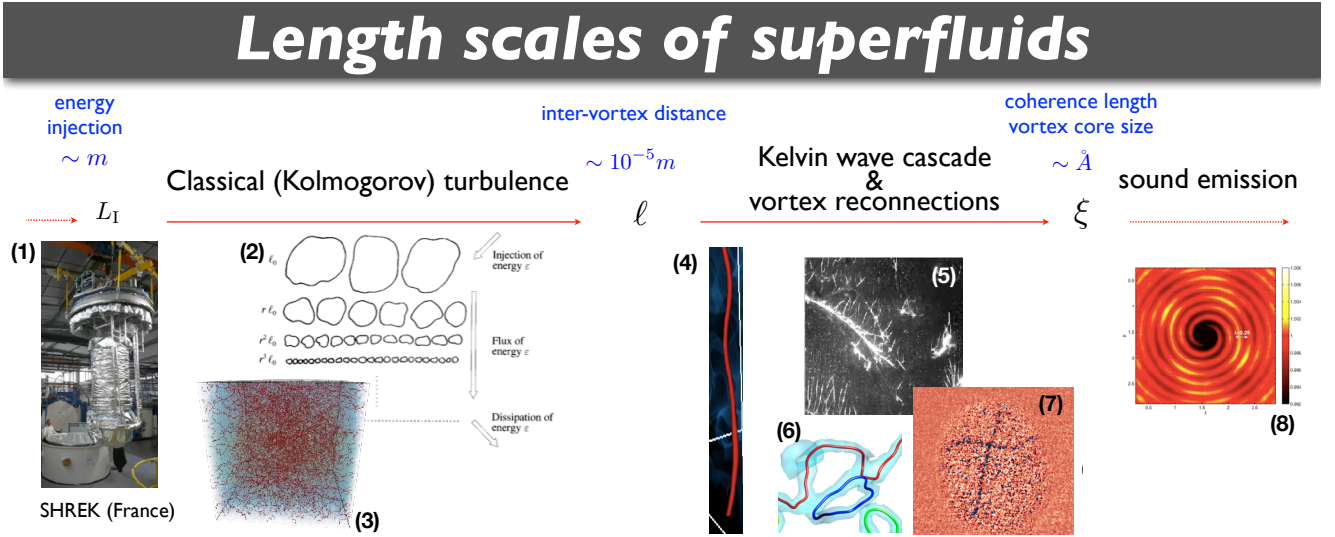
Figure 1.2: Length scales and physics of superfluid turbulence. Energy is injected at scales of the order of the metre. It is then transferred towards small scales through a Kolmogorov classical cascade. At the scale of the mean inter-vortex distance ℓ, new physical mechanisms are responsible for transferring energy further down to the scale of the vortex core size ξ. **(1)** A picture of the *Superfluide à Haut Reynolds en Ecoulement de von Karman* (SHREK) experiment in Grenoble, taken from the SHREK webpage. **(2)** The Richardson cascade, picture from [Fri95]. **(3)** Gross-Pitaevskii (GP) simulation of a turbulent vortex tangle (vortices in red). **(4)** A GP simulation of a Kelvin wave propagating along a quantum vortex (in red). **(5)** Visualisation of a quantum vortex, from [BLS06]. **(6)** GP simulation of quantum vortex reconnections, from [VPK17]. **(7)** Visualisation of quantum vortices in a BEC, from [Ser+15]. **(8)** GP simulation of phonon radiation produced by rotating quantum vortices, from [KBT08].

order to conserve the mass. Counterflow turbulence is not discussed much in this manuscript, but some interesting effects of counterflow can be found in the works [PK20b; PK20a].

In what concerns Bose-Einstein condensates (BEC), most of the previous phenomenology applies, at least from a theoretical point of view. In BECs experiments, the healing length ξ can be adjusted using Feshbach resonances [Chi+10], but roughly speaking, it is typically of the order of micrometres. The size of the experiments is also smaller than in superfluid helium, not more than some hundreds healing lengths, at best. Therefore, the scale separation occurring in superfluid helium experiments is never achieved in BECs. Also, the compressibility of the fluid is much more important than in helium. From the experimental side, the BECs community has achieved an incredible control of the experiments, and it is even possible the direct visualisation of quantum vortex filaments [Ser+15].

Although in principle very different, both systems, BEC and superfluid helium have some complementarity. Whereas in superfluid helium, new experimental techniques are pushed to sample smaller and smaller scales, hopefully soon smaller than ℓ, in BECs larger and large traps are produced, with shapes that allow for a better study of turbulence. From a theoretical point of view, experimental results coming from both communities are crucial to test and confront new theories and models.

In this manuscript, we will generically talk of superfluids or quantum turbulence without making a major distinction of the type of concerned superfluid. Depending on the scales at play, or on the physics discussed, a given result could find a better application in BECs or in helium. In this spirit, the next chapter discusses several models of superfluids, valid for different ranges of scales and temperatures.

Chapter 2

Models of superfluid turbulence

In this chapter, we give a (biased) overview of the different models used for studying quantum turbulence. We start by introducing the Gross-Pitaevskii equation and discussing its main properties and how it can be used to study quantum turbulence. We then briefly introduce and discuss some other models that are useful to describe quantum flows at different scales and temperatures.

As we discussed in the previous chapter, superfluid or quantum turbulence is characterised by a large scale separation, with the occurrence of a myriad of physical phenomena. In general terms, a turbulent quantum fluid can refer to an atomic BEC, where non-linear waves weakly interact, to a Bose-Einstein condensate (BEC) containing vortex tangles or to superfluid helium where quantum vortices interact with the normal fluid having or not a mean counterflow. It is kind of obvious that there is not a unique, first principle model that would be able to account for all those complex phenomena. Depending on the scale of interest, one is constrained to the use of one model or another.

In this chapter, we will introduce some of the models that are used today to model quantum turbulence. The presentation is of course biased, as the works that have been selected for this manuscript, they have been all performed in the framework of the Gross-Pitaevskii (GP) equation. However, my current research is not constrained only to GP.

2.1 The Gross-Pitaevskii model

We shall start by considering one of the simplest (but not less complex) cases of superfluid. We will consider a dilute weakly interacting BEC at zero temperature. In this limit, it is possible to derive from first principles (and a mean-field approximation) one of the most important models for superfluids: the Gross-Piteavskii equation. We will not give a derivation of the model here, as it can be found in many excellent books and reviews (see for instance [Dal+99]). In addition, this manuscript is mainly concerned with the hydrodynamical aspects of superfluids, hence this interpretation will be discussed in more detail.

The GP model is an equation for the macroscopic wave function ψ describing the condensate. It satisfies the partial differential equation

$$i\hbar \frac{\partial \psi}{\partial t} = -\frac{\hbar^2}{2m}\nabla^2 \psi + V(\mathbf{x})\psi + g|\psi|^2\psi, \tag{2.1}$$

where $\hbar$ is the reduced Planck constant, m is the mass of the condensed particles and $g = \frac{4\pi a\hbar^2}{m}$, with a the s-wave scattering length. The potential $V(\mathbf{x})$ typically describes an external trap that confines the condensate. This equation is also known as the (defocusing) non-linear Schrödinger (NLS) equation. When $g < 0$, it is known as the focusing NLS equation.

Equation (2.1) derives from a variational principle with the action

$$\mathcal{A} = \int \left[\frac{i\hbar}{2}\left(\bar{\psi}\frac{\partial \psi}{\partial t} - \psi\frac{\partial \bar{\psi}}{\partial t}\right)\right]\mathrm{d}^3\mathbf{x}\,\mathrm{d}t - \int H\mathrm{d}t, \tag{2.2}$$

where

$$H = \int \left(\frac{\hbar^2}{2m} |\nabla \psi|^2 + V(\mathbf{x}) |\psi|^2 + \frac{g}{2} |\psi|^4 \right) \mathrm{d}^3 \mathbf{x} \tag{2.3}$$

is the Gross-Pitaevskii Hamiltonian. For the sake of simplicity, we will consider in the following a free condensate, i.e. $V(\mathbf{x}) \equiv 0$.

2.1.1 Conserved quantities

Thanks to the Noether theorem, the variational formulation (2.2) is particularly useful to determine the conserved laws associated to the GP equation [SS04]. Equation (2.1) is invariant under the unitary group $U(1)$, i.e a phase rotation $\psi \to \psi e^{i\theta}$ with θ any real number, and to time and space translations. Using Noether theorem it is straightforward to show that the conservation laws are [NAB97]

$$\partial_t (\psi \overline{\psi}) + \partial_k \left\{ i \frac{\hbar}{2m} (\psi \partial_k \overline{\psi} - \overline{\psi} \partial_k \psi) \right\} = 0 \tag{2.4}$$

$$\partial_t \left(\frac{i\hbar}{2} (\psi \partial_j \overline{\psi} - \overline{\psi} \partial_j \psi) \right) + \partial_k \Pi_{kj} = 0 \tag{2.5}$$

$$\partial_t \left(\frac{\hbar^2}{2m} \partial_k \psi \partial_k \overline{\psi} + \frac{1}{2} g |\psi|^4 \right) + \partial_k Q_k = 0 \tag{2.6}$$

where the momentum and energy fluxes respectively are

$$\Pi_{kj} = \frac{\hbar^2}{2m} (\partial_k \overline{\psi} \partial_j \psi + \partial_k \psi \partial_j \overline{\psi}) + (\frac{g}{2} |\psi|^4 - \frac{\hbar^2}{4m} \partial_{ll} |\psi|^2) \delta_j^k \tag{2.7}$$

$$Q_k = \frac{i\hbar^3}{4m^2} \left(\partial_k \psi \partial_{jj} \overline{\psi} - \partial_k \overline{\psi} \partial_{jj} \psi \right) + g |\psi|^2 \left(\frac{i\hbar}{2m} (\psi \partial_k \overline{\psi} - \overline{\psi} \partial_k \psi) \right). \tag{2.8}$$

It follows directly from (2.4-2.6) that the Hamiltonian H, the total number of particles N and the momentum $\mathbf{P}$ defined by

$$H = \int_V \left(\frac{\hbar^2}{2m} |\nabla \psi|^2 + \frac{g}{2} |\psi|^4 \right) \mathrm{d}^3 \mathbf{x} \tag{2.9}$$

$$N = \int_V |\psi|^2 \, \mathrm{d}^3 \mathbf{x} \tag{2.10}$$

$$\mathbf{P} = \int_V \frac{i\hbar}{2} \left(\psi \nabla \overline{\psi} - \overline{\psi} \nabla \psi \right) \mathrm{d}^3 \mathbf{x}, \tag{2.11}$$

are conserved by the GP dynamics.

Finally remark that the GP equation (2.1) is invariant under the Galilean transformation

$$\psi'(\mathbf{x}, t) = \psi(\mathbf{x} - \mathbf{v}_\mathrm{s} t, t) \exp \left\{ \frac{im}{\hbar} \left[\mathbf{v}_\mathrm{s} \cdot \mathbf{x} - \frac{1}{2} v_\mathrm{s}^2 t \right] \right\}. \tag{2.12}$$

Associated with this last invariance, the conserved charge is the centre of mass of the system

2.1.2 Wave propagation

The simplest excitations of the GP equation are waves. Obviously, $\psi = 0$ is a solution of the GP equation. Assuming small perturbations, we observe that the non-linear term can be dropped and waves propagate with the dispersion relation

$$\omega_k = \frac{\hbar}{2m} k^2, \tag{2.13}$$
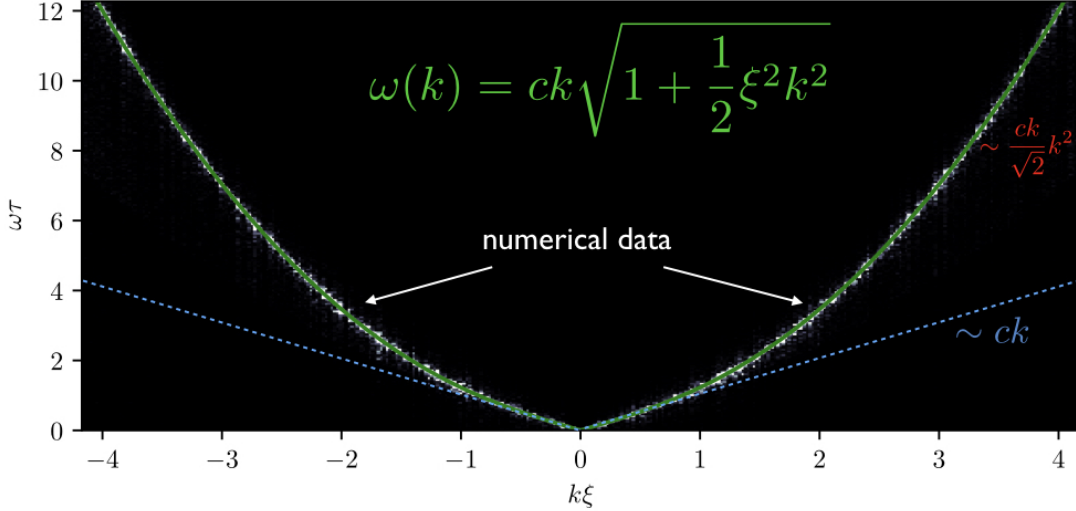
Figure 2.1: Dispersion relation of Bogoliubov waves obtained numerically by measuring the spatio-temporal spectrum of weak amplitude waves driven by the GP model.

where $k = |\mathbf{k}|$ is its wave vector. Such kind of waves, are dispersive waves and they are solutions of the Schrödinger equation. They are often called free particles.

Less trivial solutions are waves that propagate about a flat condensate $\psi = \sqrt{\rho_0/m}e^{i\mu t}$, where ρ_0 is the mean mass density and $\mu = g\rho_0/m$ is the chemical potential. Linearising about this flat state, we obtain the famous Bogoliubov dispersion relation

$$\omega_k^{\text{Bogo}} = \sqrt{\frac{g\rho_0}{m^2} + \frac{\hbar^2}{4m^2}k^4} = ck\sqrt{1 + \frac{1}{2}\xi^2 k^2}, \tag{2.14}$$

where we have defined the speed of sound c and the healing length ξ as

$$c = \sqrt{\frac{g\rho_0}{m^2}}, \quad \xi = \sqrt{\frac{\hbar^2}{2g\rho_0}}. \tag{2.15}$$

The healing length ξ thus defines the scale at which dispersive effects become important. Note that we can rewrite the ratio $\hbar/m = \sqrt{2}c\xi$. As a matter of illustration, figure 2.1 displays the dispersion relation of weak Bogoliubov waves obtained numerically from the GP model by performing a spatio-temporal spectrum. The different asymptotic limits are clearly visible.

In many applications, in particular to compare different physical systems or experiment and numerics, it is useful to rewrite the GP equation in terms of c, ξ and ρ_0/m:

$$i\frac{\partial\psi}{\partial t} = \frac{c}{\xi\sqrt{2}}\left(-\xi^2\nabla^2\psi + \frac{m}{\rho_0}|\psi|^2\psi - \psi\right), \tag{2.16}$$

where we have include the chemical potential term $\mu\psi$, and expressed μ in terms of c and ξ (last term inside the r.h.s).

2.1.3 Hydrodynamics: from a quantum vortex to Kolmogorov turbulence

The connection of the GP equation with hydrodynamics is given by the Madelung transformation defined by

$$\psi(\mathbf{x}, t) = \sqrt{\frac{\rho(\mathbf{x},t)}{m}}\exp\left[i\frac{m}{\hbar}\phi(\mathbf{x},t)\right] = \sqrt{\frac{\rho(\mathbf{x},t)}{m}}\exp\left[i\frac{\phi(\mathbf{x},t)}{\sqrt{2}c\xi}\right], \tag{2.17}$$

where $\rho(\mathbf{x}, t)$ is the density and $\phi(\mathbf{x}, t)$ is the potential velocity such that $\mathbf{v} = \nabla\phi$. Replacing the transformation in (2.16) one directly obtains

$$\frac{\partial \rho}{\partial t} + \nabla \cdot \rho\mathbf{v} = 0 \tag{2.18}$$

$$\frac{\partial \phi}{\partial t} + \frac{1}{2}(\nabla\phi)^2 = \frac{c^2}{\rho_0}(\rho_0 - \rho) + c^2\xi^2\frac{\nabla^2\sqrt{\rho}}{\sqrt{\rho}} \tag{2.19}$$

Equations (2.18) and (2.19) are the continuity and Bernoulli equations respectively. Compared to classical fluids, the Bernoulli equation contains an extra term that is called the quantum pressure. Such equations are the ones governing the dynamics of isentropic, compressible and irrotational fluids. Note that in the hydrodynamic variables, the Bogoliubov dispersion relation (2.1) is easily obtained by perturbing the solution $\phi = 0$ and $\rho = \rho_0$.

Quantum vortices

Although the fluid is potential, it admits vortices as topological defects of the wave function. Indeed, the Madelung transformation (2.17) is not defined if the wave function vanishes. If such is the case, the phase can have a jump over a branch of discontinuity. As a zero of the wave function implies two conditions ($Re[\psi] = Im[\psi] = 0$), quantum vortices are generically points in two dimensions and filaments in three. Figure 2.2 displays a numerical solution of the GP model containing one straight three-dimensional quantum vortex. Such a solution was first studied by Pitaevskii and Ginsburg [Pit61; GP58], and it is the most fundamental hydrodynamical excitation of a quantum fluid.

A topological defect arises as a discontinuity of the phase of the wave function; as such, its associated circulation might be not zero, even if the velocity fluid is potential. Indeed, we have that the velocity circulation over a closed contour surrounding the defect is given by

$$\Gamma = \oint_{\mathcal{C}} \nabla\phi \cdot \mathrm{d}\ell = \phi^+ - \phi^-, \tag{2.20}$$

where ϕ^+ and ϕ^- are the values of the phase in two sides of the branch of discontinuity, as displayed in the top right panel of figure 2.2. Because the wave function needs to have a single value while crossing this branch, it follows from the Madelung transformation (2.17) that $\phi^+ - \phi^- = n2\pi\hbar/m$, with $n \in \mathbb{Z}$. The circulation of a quantum vortex is thus quantised and takes the value

$$\Gamma = n\frac{h}{m} = n2\pi\sqrt{2}c\xi, \quad \text{with } n \in \mathbb{Z}. \tag{2.21}$$

The ratio h/m is called the Feynman-Onsager quantum of circulation [Fey55; Don91]. As a consequence of the quantisation of circulation, the velocity $\mathbf{v}_{\mathrm{v}}$ and vorticity ω_{v} fields are

$$\mathbf{v}_{\mathrm{v}}(\mathbf{x}) = \frac{\Gamma}{2\pi r}\hat{\theta}, \quad \omega_{\mathrm{v}}(\mathbf{x}) = \Gamma\hat{k}\delta(\mathbf{x}), \tag{2.22}$$

where we have used a system of coordinates as the one in figure 2.2. The velocity field is displayed in green dashed lines in the bottom right panel.

So far, we have only discussed the phase of a quantum vortex. The precedent discussion is valid for any topological defect described by a complex field, in particular for solutions of the Schrödinger equation. What makes a GP quantum vortex very important is that due to its non-linearity, such a solution is very stable and leads to a pressure term (see equation 2.19), so that quantum vortices behave as real hydrodynamic vortices. Besides, dispersion regularises the solution and give an effective core size to the vortex. Indeed, the vortex profile can be straightforwardly obtained from the GP equation.
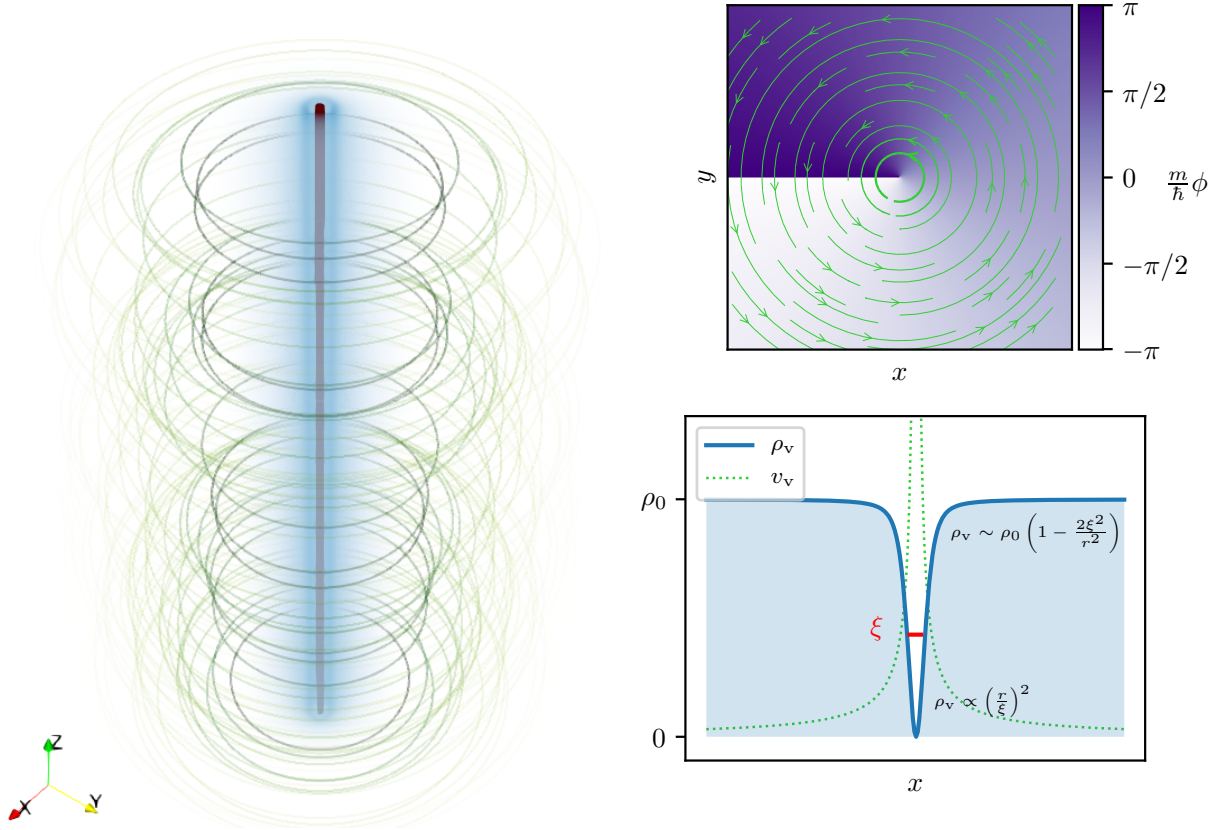
Figure 2.2: Quantum vortex in the Gross-Pitaevskii model. **Left:** 3D visualisation of a straight quantum vortex. The vortex is represented as a red isosurface of low values of the density field, whereas the variation of the density field around the bulk value ρ_0 are rendered in blue. Streamlines of the velocity field are displayed in green. **Top right:** Phase and velocity streamlines of a straight vortex solution in the plane orthogonal to the filament. **Bottom right:** Vortex density and velocity profiles. Figure courtesy of U. Giuriato taken from his Ph.D. manuscript [Giu20]

Expressing the (steady) GP equation in polar coordinates and looking for a solution of the type $\psi(r,\theta) = \sqrt{\rho_0}R(r)\exp(in\theta)$ yields an ordinary differential equation for the vortex profile

$$\frac{\xi^2}{r}\frac{\mathrm{d}}{\mathrm{d}r}\left(r\frac{\mathrm{d}R}{\mathrm{d}r}\right) + \left(1 - \frac{n^2\xi^2}{r^2} - R^2\right)R = 0, \tag{2.23}$$

where the boundary conditions are $R(0) = 0$ and $R(\infty) = 1$. This equation cannot be solved analytically. The vortex profile is sketched in the bottom right panel of figure 2.2. The asymptotic behaviour of the vortex profile is easily obtained from equation 2.23 and reads

$$\lim_{r\to 0} R(r) \approx c_1(r/\xi)^{|n|}, \quad \lim_{r\to\infty} R(r) \approx 1 - \frac{n^2\xi}{r^2} \tag{2.24}$$

where the pre-factor c_1 may be determined numerically. For practical purposes, a Padé approximation can be computed by imposing both asymptotic limits. A Padé approximation with $n = 1$ is

$$R(r) = \sqrt{\frac{\tilde{r}^2(a_2 + a_4\tilde{r}^2 + a_6\tilde{r}^4)}{1 + b_2\tilde{r}^2 + b_4\tilde{r}^4 + b_6\tilde{r}^6}}, \tag{2.25}$$

where $\tilde{r} = r/\xi$. The coefficients are $a_2 = 0.340038$, $a_4 = 0.0360207$, $a_6 = b_6 = 0.000985125$, $b_2 = 0.355931$ and $b_4 = 0.037502$. The vortex profile obtained numerically from equation (2.23), the Padé approximation
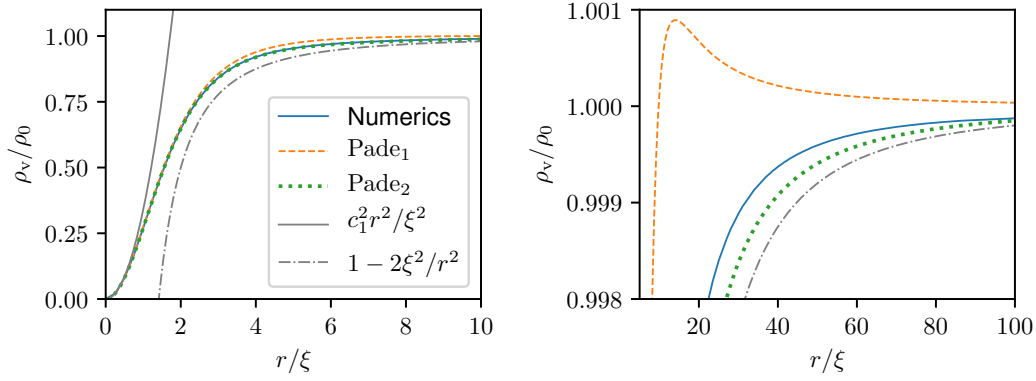
Figure 2.3: Density profile of a quantum vortex. The numerical solution is compared with two Padé approximations: $Pade_1$ N. Berloff [Ber04] and $Pade_2$ (2.25). The asymptotic limits (2.24) are also displayed. Figure courtesy of U. Giuriato taken from his Ph.D. manuscript [Giu20].

published in the book by L.M. Pismen [Pis99] and often associated to Berloff [Ber04] (denoted by $Pade_1$ in the legend) and the one in equation (2.25) (denoted by $Pade_2$) are compared in figure 2.3. The asymptotic limits (2.24) are also displayed for comparison. Although all approximations look similar, $Pade_1$, that is commonly used in the community, presents an unphysical maximum close to the vortex core and approaches 1 from above. The Padé approximation 2.25 was actually derived during my undergraduate studies [Krs05] and recently used with U. Giuriato [GK19] for studying the capture of a particle by a quantum vortex.

Finally, one is usually concerned with vortices having $n = \pm 1$, as quantum vortices with higher charges are typically unstable.

Now that quantum vortices have been introduced, we can come back to the hydrodynamic equations (2.18) and (2.18). The continuity equation involves of course the velocity field and, as we have seen, it diverges at the vortex position. Fortunately, the density vanishes there and regularises the problem ($\rho\nabla\phi$ is the momentum density and it is completely regular). Concerning the Bernouilli equation, its interpretation is more difficult but still possible. One needs to consider ϕ, and impose jumps on moving discontinuity branches. For instance, in my first contribution to the field [KBT08], I studied the sound emitted by quantum vortices dealing with these moving boundary conditions. Quite often in literature and seminars, the dispersive Euler equation obtained by taking the gradient of Bernouillui equation is presented to make the connection between GP and fluids. Such a presentation hides under the carpet the presence of quantum vortices, especially if it is not specified that such an equation needs to be interpreted in the sense of distributions.

Energy spectra

It is customary in classical turbulence to study the kinetic energy spectrum of the velocity flow. In Navier-Stokes flows, the definition passing by the Fourier transform of the velocity is straightforward [Fri95]. In GP quantum turbulence, the definition is slightly more complex as the fluid is compressible and the velocity field $\nabla\phi$ is singular on the vortex core. In the seminal paper by Nore et al. [NAB97], the authors introduced the energy spectra for a turbulent GP flow. Since then, those definitions are commonly used.

The definition of the energy spectra are motivated on hydrodynamical backgrounds. We start by writing the free energy per unit of total mass

$$\mathcal{F} = \frac{1}{\rho_0 V}[H - \mu N - \frac{\mu^2 V}{2g}], \tag{2.26}$$
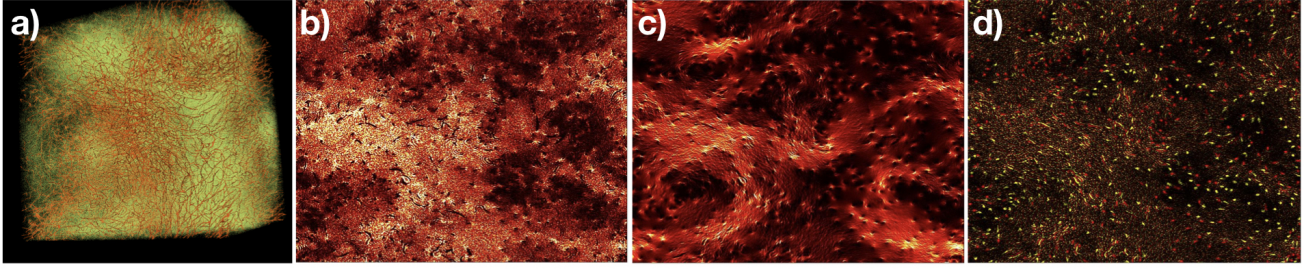
Figure 2.4: Visualisations of turbulent GP field. **a)** Three-dimensional visualisation of the density field. Vortices are displayed in red as low value iso-surfaces of the density. Fluctuations about the bulk value ρ_0 are rendered in yellowish colours. **b)** Slice of the total kinetic energy density. **c)** slice of the incompressible kinetic energy density.**d)** Slice of the filtered pseudo-vorticity (2.32). Data from numerical simulations of reference [MK20].

where we have subtracted the free energy of a flat condensate. Using the Madelung transformation (2.17), it explicitly reads

$$\mathcal{F} = \frac{1}{V\rho_0} \int \mathrm{d}^3\mathbf{x} \left[\frac{1}{2}(\sqrt{\rho}\mathbf{v})^2 + \frac{c^2}{2\rho_0}(\rho - \rho_0)^2 + c^2\xi^2 (\nabla\sqrt{\rho})^2 \right] \tag{2.27}$$

We recognise three terms, the total kinetic energy E_{kin}, the internal energy E_{int} and the quantum energy E_{q} defined by

$$E_{\mathrm{kin}} = \frac{1}{\rho_0 V} \int \mathrm{d}^3\mathbf{x}\frac{1}{2}(\sqrt{\rho}\mathbf{v})^2 \tag{2.28}$$

$$E_{\mathrm{int}} = \frac{1}{\rho_0 V} \int \mathrm{d}^3\mathbf{x}\frac{c^2}{2\rho_0}(\rho - \rho_0)^2 \tag{2.29}$$

$$E_{\mathrm{q}} = \frac{1}{\rho_0 V} \int \mathrm{d}^3\mathbf{x}c^2\xi^2 (\nabla\sqrt{\rho})^2 . \tag{2.30}$$

Apart from the quantum energy term, their interpretation is clear from a fluid mechanics point of view [LLL11].

To separate the energy coming from sound waves from the one of vortices, the total kinetic energy can be further decomposed into compressible $E_{\mathrm{kin}}^{\mathrm{c}}$ and incompressible $E_{\mathrm{kin}}^{\mathrm{i}}$ by computing the kinetic term as $\sqrt{\rho}\mathbf{v} = (\sqrt{\rho}\mathbf{v})^{\mathrm{c}} + (\sqrt{\rho}\mathbf{v})^{\mathrm{i}}$ where $\nabla \cdot (\sqrt{\rho}\mathbf{v})^{\mathrm{i}} = 0$. This decomposition is obtained by applying the projector $P_{\mu\nu} = \partial_\mu\partial_\nu - \frac{\delta_{\mu\nu}}{\nabla^2}$. The incompressible kinetic energy mainly contains the contribution of vortices. To illustrate this decomposition, figure 2.4 displays visualisations of a quantum turbulent flow from reference [MK20]. Quantum vortices creating large scale structures are apparent in figure 2.4.a. Figure 2.4.b-c show a slice of the total kinetic and incompressible energy densities, respectively. While the total energy density contains structures akin to quasi-shocks, the incompressible part displays large scale eddies. It is important to notice that the velocity field $\sqrt{\rho}\mathbf{v}$ is regular at the vortex core. Indeed, the asymptotic formulas 2.24 imply that $\sqrt{\rho}\mathbf{v} \sim r^0$ at the vortex core. For this reason, this field is called the regularised velocity.

As the quantities inside the integrals (2.28-2.30) are quadratic, the respective spectra $E_{\mathrm{kin}}^{\mathrm{c}}(k)$, $E_{\mathrm{kin}}^{\mathrm{i}}(k)$, $E_{\mathrm{int}}(k)$ and E_{q} can be easily defined by Parseval theorem summing over the angles [NAB97]. For instance the kinetic energy spectrum is defined as

$$E_{\mathrm{kin}}(k) = \frac{1}{2\rho_0} \int |\widehat{\sqrt{\rho}\mathbf{v}}(\mathbf{k})|^2 \mathrm{d}\Omega_k, \tag{2.31}$$

where $d\Omega_k$ is the surface measure of the sphere [1].

---

[1]Remark that by definition $E_{\mathrm{kin}} = \int_k E_{\mathrm{kin}}(k)\mathrm{d}k$

Finally, a useful quantity, in particular to track vortices, is the pseudo-vorticity. It is defined from the momentum density as

$$\mathbf{J} = \nabla \times \rho \mathbf{v} = 2\hbar \nabla Re[\psi] \times \nabla Im[\psi]. \tag{2.32}$$

From its definition, it follows that it is a regular field at the vortex core and oriented in the direction of the vortex. We have used these properties to develop a vortex tracking algorithm [Vil+16]. Figure 2.4.d shows the filtered pseudo-vorticity over a slice of the turbulent vortex tangle. The yellow and red dots correspond to vortices of opposite sign.

2.1.4   Beyond low-temperature weakly interacting Bose-Einstein condensates

Formally, the GP equation should be applied to describe only low-temperature weakly interacting BECs. This fact naturally excludes, a priori, superfluid helium. However, many aspects, especially those related to vortex dynamics, are well reproduced by GP, and the role of compressible waves is negligible. There are several approaches providing a better description of superfluid helium and different kinds of BECs, that remain within the framework of GP.

Finite temperature BECs

There are many models for describing finite temperature BECs, with different degrees of complexity and accuracy. We do not intend to provide here an overview of this challenging topic, but to explain how the standard GP model can be easily modified to include finite temperature effects. We refer to the excellent review article [PJ08] for a detailed discussion on other models.

The Gross-Pitaevskii model can be adapted to describe finite temperature superfluids by considering the discrete version of it and states close to thermal equilibrium. Such a model is called the projected (or truncated) Gross-Pitaevskii equation. The physical motivation of introducing an UV cut-off is, that because of quantum mechanics, excitations having very high wave vectors contribute very little to statistics and can thus be neglected in a semi-classical approximation. In principle, we can consider that excitations such that $\hbar\omega(k) \ll k_\text{B}T$, where k_B is the Boltzmann constant, can be treated classically. In practice, the projection is done by imposing a UV cut-off to the field by performing a Galerkin truncation at given wavenumber k_max. The resulting projected GP equation is

$$i\hbar\frac{\partial \psi}{\partial t} = \mathcal{P}_\text{G}[-\frac{\hbar^2}{2m}\nabla^2\psi + g\mathcal{P}_\text{G}[|\psi|^2]\psi], \tag{2.33}$$

where the Galerkin projector $\mathcal{P}_\text{G}$ truncates the system acting in Fourier space as: $\mathcal{P}_\text{G}[\hat{\psi}_\mathbf{k}] = \theta(k_\text{max}-|\mathbf{k}|)\hat{\psi}_\mathbf{k}$ with $\theta(\cdot)$ the Heaviside theta function, $\hat{\psi}_\mathbf{k}$ the Fourier transform of $\psi(\mathbf{x})$ and $\mathbf{k}$ the wave vector (see for instance [KB11b]). The extra projector acting on the $|\psi|^2$ term, ensures the exact conservation of momentum (see [KB11b]). See Appendix A.2 for details on the conservation of invariants and the correct de-aliasing of this model.

Note that, if the wave function is a regular (analytic) solution of the GP equation, in the limit of $k \to \infty$ we have that $|\hat{\psi}_\mathbf{k}|^2 \to 0$ fast enough, and the projected and standard GP model coincides, provided that k_max is large enough. On the other hand, for a thermal solution, $|\hat{\psi}|^2$ do not decrease fast, and the cut-off plays an important role. In this case, equation (2.33) is not defined mathematically as partial differential equation (because gradients do not exist) and needs to be considered as a (very large) set of ordinary differential equations. This discrete system, given by equation (2.33), conserves the truncated invariants of the original GP equation.

In two and three dimensions, if one starts from a random initial condition with energy H, momentum $\mathbf{P}$ and number of particles N, the system will generically equilibrate and reach thermal equilibrium after a very long evolution. Assuming equivalence of ensembles, such states will have a distribution

$$\{\psi_\mathbf{k}\}_{|\mathbf{k}|<k_\text{max}} \sim e^{-\beta(H-\mu N+\mathbf{W}\cdot\mathbf{P})}, \tag{2.34}$$

where β, μ and $\mathbf{W}$ are Lagrange multipliers. We immediately recognise, the inverse temperature β and the chemical potential μ, whereas $\mathbf{W}$ can be related to a counterflow velocity [KB11b]. If we consider the case with no mean momentum $\mathbf{W} = \mathbf{0}$, we remark that $H - \mu N$ exactly corresponds to the action of the famous two-components $\lambda - \phi^4$ theory describing second-order phase transitions [Le 91]. In 2001, Davis et al. [DMB01], performed a series of simulations varying the initial energy and showed that the condensation transition is observed in this system. Such thermal states are obtained after a very long temporal evolution of equation (2.33) and they are thus by definition micro-canonical states. Instead, one can generate such states in a grand canonical ensemble by performing simulations of the stochastic Ginsburg-Landau equation (or GP in imaginary time plus noise). This technique was introduced during my Ph.D and has the advantage of controlling temperature and chemical potential and to be much more efficient numerically.

Thermal solutions, generated by whatever mean, are useful to study the interaction of the thermal cloud and vortices. For instance, they can be used to analyse how a vortex ring decay [BY07], the effect of counterflow on vortices and to characterise mutual friction [KB11b], to study thermally excited Kelvin waves [KB11a] and finite temperature quantum turbulence and its effective viscosity [Shu+19].

Although the projected GP equation is a very natural model to qualitatively study finite temperature superfluids, it is numerically costly because of the small time steps required for simulations. Furthermore, it is not well suited for turbulent superfluids as extremely large resolutions are needed [Shu+19].

Superfluid helium

There is not a simple, first principle model to describe the dynamics of superfluid helium. In the GP description, even at zero temperature, there are two main missing properties. Firstly, it is known that the superfluid helium dispersion relation exhibits a minimum, called the roton minimum. The dispersion relation is not as simple as the one shown in figure 2.1. Secondly, it is known that the internal energy of helium does not have the same functional form like the one in equation (2.29). Such phenomenology can be easily included in the GP description, with some numerical cost, by replacing the contact particle-particle potential (not written in the previous equation as it takes the form of δ-function) by a non-local interaction potential and with the addition of high-order terms. Such ideas were first introduced by Pomeau and Rica [PR93], then further studied by Berloff and Robert [BR99]. More recently, the vortex profile and the dynamics of vortices were also investigated [VCC12; RSC18].

In a recent work [MK20], we used a generalised GP model to study the decay of quantum turbulence. This model reads

$$i\hbar\frac{\partial\psi}{\partial t} = -\frac{\hbar^2}{2m}\nabla^2\psi - \mu(1+\chi)\psi + g\left(\int V_{\mathrm{I}}(\mathbf{x}-\mathbf{y})|\psi(\mathbf{y})|^2\mathrm{d}^3y\right)\psi + g\chi\frac{|\psi|^{2(1+\gamma)}}{n_0^\gamma}\psi. \qquad (2.35)$$

where γ and χ are two dimensionless parameters that determine the order and amplitude of the high-order terms. The non-linear term with exponent $2(1+\gamma)$ can be considered as the next order expansion on the density to phenomenologically reproduce the ground state energy, density, and compressibility of homogeneous superfluid helium [BR99]. Also, it results from beyond mean-field corrections to account for the effect of quantum fluctuations. There χ and γ take explicit values in terms of physical constants [BBP14]. In [MK20], we showed that the inclusion of high order terms leads to a renormalisation of the speed of sound and the healing length. It has no major impact on the vortex profile.

The interaction potential V_{I} is normalised such that $\int V_{\mathrm{I}}(\mathbf{x})\mathrm{d}^3x = 1$. The chemical potential and the interaction coefficient of the high-order terms have been renormalised such $|\psi_0|^2 = n_0 = \mu/g$ is the density of particles of the ground state for all values of parameters. The GP equation is recovered by simply setting $V_{\mathrm{I}}(\mathbf{x}-\mathbf{y}) = \delta(\mathbf{x}-\mathbf{y})$ and $\chi = 0$. To model superfluid helium, we use an interaction potential that in Fourier space reads $\hat{V}_{\mathrm{I}}(\mathbf{k}) = \left[1 - V_1\left(\frac{k}{k_{\mathrm{rot}}}\right)^2 + V_2\left(\frac{k}{k_{\mathrm{rot}}}\right)^4\right]\exp\left(-\frac{k^2}{2k_{\mathrm{rot}}^2}\right)$, where k_{rot} is the wave number associated with the roton minimum and $V_1 \geq 0$ and $V_2 \geq 0$ are dimensionless parameters
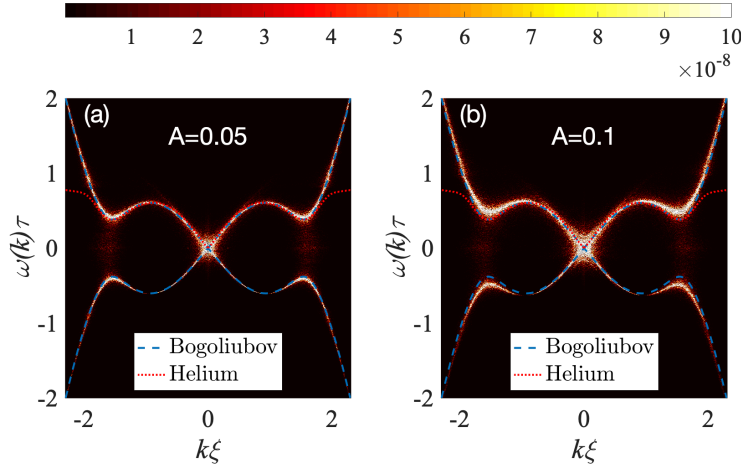
Figure 2.5: Spatiotemporal dispersion relations of weak density waves of amplitude A obtained with the model (2.35). Light zones correspond to excited frequencies. Figures (a) and (b) correspond to different amplitude of the perturbation A, both exhibiting a roton minimum. Experimental observations (red dotted line, see [BD77]) and theoretical dispersion relation for this model. See [MK20] for details and discussion.

to be adjusted to mimic the experimental dispersion relation of helium II. The spatio-temporal spectra of small amplitude waves, obtained with this model, is displayed in figure 2.5. When the parameters are adjusted to fit the helium dispersion relation, high order terms are necessary to avoid the crystallisation observed in [RSC18].

Note that the model (2.35) can be easily adapted to study dipolar BECs, in the supersolid phase [SSL03; Gri07; Lah+09]. They are today the subject of intense theoretical and experimental studies.

2.1.5   Vortex nucleation

If an object moves with a constant (low) velocity in a superfluid, it does not experience any drag. This fact is, of course, the most fundamental property of a superfluid. However, as L. Landau realised [LLL11], if the object moves fast enough, superfluidity can break accompanied with the emission of an excitation. The object thus losses some energy to "pay" the cost of that excitation. Landau predicted the critical velocity, based on very simple conservation arguments and it is given by the following expression

$$v_{\rm c} = \min_{p} \frac{\epsilon(p)}{p}, \tag{2.36}$$

where $\epsilon(p)$ is the energy of an excitation having momentum p.

We note that for a non-interacting BEC, its dispersion curves is $\epsilon(\mathbf{p}) \sim p^2$, and hence $v_{\rm c} = 0$. It follows that there is no superfluidity for non-interacting BECs. For a weakly interacting BEC, the Landau critical velocity is equal to the speed of sound (see equation 2.14), and for superfluid helium it has a smaller value due to the roton minimum (see figure 2.5).

The case of a weakly interacting BEC, that is in principle well described by the GP equation, it is very interesting and well studied. The critical velocity is actually much smaller than the speed of sound, as the excitation "emitted" by a moving object can be a quantum vortex. The boundaries of the moving object play an important role there. The first numerical observation of vortex nucleations in GP was performed by T. Frisch et al. [FPR92]. A visualisation of vortex nucleations, reproduced from [FPR92], is displayed
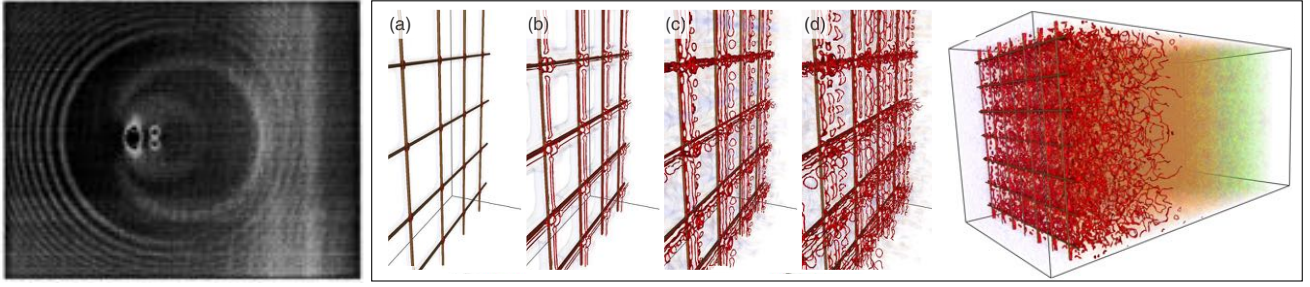
Figure 2.6: Vortex nucleation in the GP model. **Left:** Nucleation of a vortex dipole by a moving cylinder, reproduced from [FPR92]. **Right:** Quantum vortex rings (in red) nucleated by a moving grid (in brown). Sound waves are rendered in blueish colours. Figure reproduced from [Krs16].

in figure 2.6 (left). With a very simple argument, based on perfect fluids, they provided a good estimate of the critical velocity. Later, this instability was further studied by C. Huepe and M. Brachet [HB00], where they found a series of bifurcations as a function of the Mach number of the object. Vortex nucleation is a well study problem since the early experimental works with BECs [Ram+01; Hod+01] and today, many experiments use vortex nucleation as way of injecting vortices in superfluids (see for instance [Wal+14; Zme+15; vSL17]).

In the GP framework, vortex nucleations can also be used to inject vortices to the system. However, vortex nucleation is accompanied by the emission of sound waves what can easily kill the development of turbulence if they are not purged away by some external mechanism. In figure 2.6 (left), the sound emitted is clearly visible. The right panel of figure 2.6 shows the nucleation of quantum vortices behind a grid, reproduced from [Krs16]. The grid generates a superfluid vortex tangle, where Kolmogorov turbulence is observed.

Vortex nucleation is an important property of superfluids, and it has to be taken account in experiments. Particles moving can interact with the vortices they nucleate, leading to very complex dynamics [WA00; VS18]. Besides, vortices can be easily nucleated close to the walls of the containers and by thermal fluctuations [Don91]. The GP model naturally contains this physics, that is absent in the models described in the next sections.

2.2 The vortex filament model

A completely different approach that was pioneered by Schwartz [Sch85] is to consider only the dynamics of vortex filaments. We shall first consider the case of zero temperature. We denote by $\mathcal{L}$ the collection of all vortex filaments $\mathbf{s}$ present in the system. The vorticity field associated with the filaments is a straightforward three-dimensional generalisation of equation (2.22) and it reads

$$\omega_{\mathrm{s}}(\mathbf{x}, t) = \kappa \oint_{\mathcal{L}} \mathbf{s}'(\zeta, t)\delta(\mathbf{x} - \mathbf{s}(\xi, t))\mathrm{d}\zeta, \tag{2.37}$$

where $\mathbf{s}'$ is the tangent of the vortex line. By inverting the equation $\nabla \times \mathbf{v}_{\mathrm{s}} = \omega_{\mathrm{s}}$ using the Biot-Savart formula, we obtain the superfluid velocity flow

$$\mathbf{v}_s(\mathbf{x}, t) = \frac{\kappa}{4\pi} \oint_{\mathcal{L}} \frac{\mathbf{s}'(\zeta, t) \times (\mathbf{x} - \mathbf{s}(\zeta, t))}{|\mathbf{x} - \mathbf{s}(\zeta, t)|^3} d\zeta. \tag{2.38}$$

The vortex filament (VF) model is obtained by imposing that velocity of a vortex filament segment is given by (2.38). The vortex filament model then reads

$$\dot{\mathbf{s}}(\zeta, t) = \frac{\Gamma}{4\pi} \oint_{\mathcal{L}}' \frac{\mathrm{d}\mathbf{s}(\zeta', t) \times (\mathbf{s}(\zeta, t) - \mathbf{s}(\zeta', t))}{|\mathbf{s}(\zeta, t) - s(\zeta', t)|^3}, \tag{2.39}$$

15

where the prime over the integral means that the integral must be regularised introducing a vortex core cut-off. Indeed, the integral diverges logarithmically when $\zeta' \to \zeta$. Several methods are possible to avoid this problem. The most common one, introduced by Schwartz [Sch85], is to remove the divergent point of the integral and to add a local term arising from the local induced approximation (LIA). In Section 3.3.1, we provide a geometrical interpretation of this approximation. The vortex filament method thus consists of local and non-local contributions. Schwartz quickly realised that vortex reconnections are very important for quantum turbulence [Sch88]. Reconnections are of course not allowed in this model and need to be added by an ad-hoc "cut and connect" method. Vortex reconnections are discussed in Chapter 4.

Most of the current numerical simulations of the VF model use a discretisation of the Biot-Savart integral that is very coarse compared to the vortex core size in helium. This approximation is consistent with neglecting the density profile of the vortex core and allows to address the dynamics of superfluids at scales much larger than those typically achieved by the GP model.

The generalisation of the VF model to include finite temperature effects is straightforward. At finite temperatures, normal fluid excitations interact with vortices and exchange energy and momentum. This process results in mutual friction forces that couple both fluids [Don91]. Assuming an ambient normal fluid velocity $\mathbf{v}_n$, the VF model describing a finite temperature superfluid is given by

$$\mathbf{v}_L = \mathbf{v}_{sl} + \alpha \mathbf{s}' \times (\mathbf{v}_n - \mathbf{v}_{sl}) - \alpha' \mathbf{s}' \times [\mathbf{s}' \times (\mathbf{v}_n - \mathbf{v}_{sl})], \qquad (2.40)$$

where $\mathbf{v}_{sl}$ is the local superfluid velocity that is the sum of the ambient superfluid velocity $\mathbf{u}_s$ and the self-induced vortex velocity given by equation (2.39). The constants α, α' depend on the temperature and they are proportional to the normal density ρ_n [BD77]. Note that this model assumes that normal fluid velocity field is given, and ignores the action of the filaments on it.

2.3 FOUCAULT : A self-consistent model of quantum turbulence in superfluid Helium

As it was mentioned in the previous section, numerical simulations of the VF model neglect the action of the filaments on the normal fluid. Such approximation can be valid in the case where we consider a very viscous normal fluid, or in other words, the Kolmogorov scale associated with the normal fluid is much larger than the size of any of the vortices. If such is the case, any disturbance caused by the vortices is immediately damped by viscosity. In many situations, the Kolmogorov scale of the normal fluid can be smaller than the intervortex distance, and the action of the filaments on the normal fluid cannot be ignored. We can imagine that there exist situations where normal fluid turbulence is induced by superfluid vortex tangles and mutual friction. An example is counterflow induced turbulence [Don91], where for large values of counterflow, the normal fluid passes from a laminar to a turbulent steady state. This transition is known as the T1-T2 transition [MT83].

We have recently introduced *FOUCAULT: Fully cOUpled loCAl model of sUperfLuid Turbulence* that aims at providing a self-consistent description of superfluid helium [Gal+20]. The basic idea is to model the normal fluid with the Navier-Stokes equations, and to couple it with the VF model. In this new model, we generalised previous studies [KBS00; Ido+00] and provide a detailed study both, numerically and theoretically, to validate the method.

For the sake of completeness, we report the full model here

$$\frac{\partial \mathbf{v}_n}{\partial t} + (\mathbf{v}_n \cdot \nabla)\,\mathbf{v}_n = -\nabla\left(\frac{p}{\rho_n}\right) + \nu_n \nabla^2 \mathbf{v}_n + \frac{1}{\rho_n}\oint_{\mathcal{L}} \delta(\mathbf{x}-\mathbf{s})\mathbf{f}_{ns}(\mathbf{s})\mathrm{d}\xi + \frac{1}{\rho_n}\mathbf{F}_{\text{ext}} \tag{2.41}$$

$$\nabla \cdot \mathbf{v}_n = 0 \tag{2.42}$$

$$\frac{1}{\rho_n}\mathbf{f}_{ns}(\mathbf{s}) = -\frac{1}{\rho_n}\mathbf{f}_{sn}(\mathbf{s}) = -\Gamma\mathbf{s}' \times (\dot{\mathbf{s}} - \mathbf{v}_n)\; -D\mathbf{s}' \times \left[\mathbf{s}' \times (\dot{\mathbf{s}} - \mathbf{v}_n)\right] \tag{2.43}$$

$$\dot{\mathbf{s}} = \mathbf{v}_s(\mathbf{s}) + \beta\,\mathbf{s}' \times (\mathbf{v}_n(\mathbf{s}) - \mathbf{v}_s(\mathbf{s})) + \beta'\,\mathbf{s}' \times \left[\mathbf{s}' \times (\mathbf{v}_n(\mathbf{s}) - \mathbf{v}_s(\mathbf{s}))\right] \tag{2.44}$$

$$\mathbf{v}_s(\mathbf{x},t) = \frac{\Gamma}{4\pi}\oint_{\mathcal{L}} \frac{\mathbf{s}'(\xi,t) \times (\mathbf{x} - \mathbf{s}(\xi,t))}{|\mathbf{x} - \mathbf{s}(\xi,t)|^3}d\xi, \tag{2.45}$$

where ν_{n} and ρ_{n} are the kinematic viscosity and density of the normal fluid, respectively. The mutual friction coefficient β, β' and D are computed from a creeping flow analysis. We refer the reader to [Gal+20] for details. The FOUCAULT model is an important improvement of the VF model.

This new model opens the avenue for many new investigations. As an example, figure 2.7 displays a visualisation of a superfluid vortex ring that creates two other normal fluid rings next to it. Such a
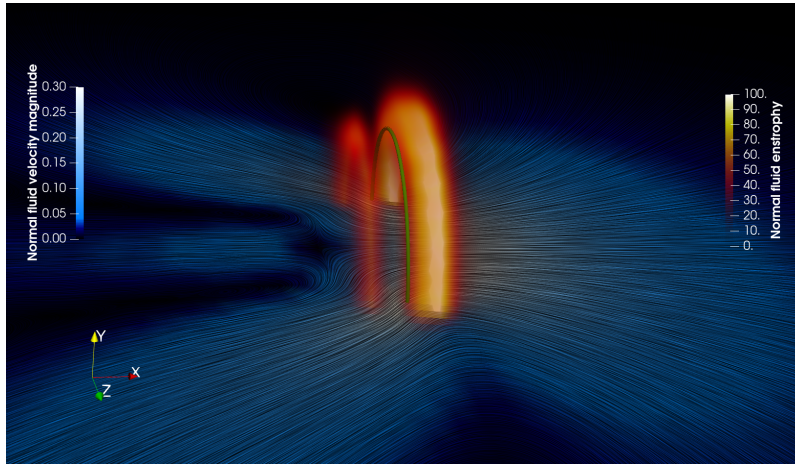
Figure 2.7: A superfluid vortex ring moving in the normal fluid initially at rest. Half of the superfluid vortex ring is visible as a green line intersecting the xy plane; the superfluid vortex ring moves to the right along the x direction. The normal fluid enstrophy is displayed by the orange-reddish-black rendering: two concentric normal fluid vortex rings are visible, slightly ahead and slightly behind the superfluid vortex ring, travelling in the same direction. The normal fluid velocity magnitude is also displayed using a black-blue-white rendering on the xy plane. Figure taken from [Gal+20].

phenomenon was first observed by Kivotides et al. [KBS00], and we are now investigating its consequences for quantum turbulence.

Because no model is perfect, FOUCAULT possesses several inconveniences. It is based on the VF model, so it lacks the physics of small scales (unlike the GP model). For instance, vortex reconnections need also to be added in an ad-hoc manner. From a numerical point of view, the number of vortex points N_{v} describing the filaments might become very large. Although FOUCAULT solves the Biot-Svart integrals by a tree-algorithm method that reduces the computational cost from N_{v}^2 to $N_{\mathrm{v}}\log N_{\mathrm{v}}$, the cost of the VF part of FOUCAULT might overwhelm the cost of the Navier–Stokes integration. This situation happens for instance with a turbulent normal fluid if we one is interested in the steady state, in which the total vortex length reaches equilibrium. This limitation imposes a drastic constraint on the size of the system and thus on the Reynolds numbers than can be in practice achieved.

2.4   Hall-Vinen-Bekarevich-Khalatnikov model

If one intends to model large scales of turbulent superfluids, a direct approach by the GP or VF-based models (including FOCAULT) can become easily unfeasible. In particular, if one is interested in scales that are much larger than the mean distance between quantum vortices, a coarse-grained approach might be more appropriate. In such approximation, we ignore the quantum nature of vortices, and the superfluid is described by continuous coarse-grained field.

For the sake of simplicity, we consider the dynamics of a constant temperature, incompressible superfluid helium flow at finite temperature. In the simplest case of the Hall-Vinen-Bekarevich-Khalatnikov (HVBK) model [Don91], the dynamics of the superfluid is described by the coarse-grained superfluid velocity field $\mathbf{v}_\mathrm{s}$, which interacts with the viscous normal component $\mathbf{v}_\mathrm{n}$ via two coupled Navier-Stokes equations,

$$\frac{\partial \mathbf{v}_\mathrm{n}}{\partial t} + \mathbf{v}_\mathrm{n} \cdot \nabla \mathbf{v}_\mathrm{n} = -\frac{1}{\rho_\mathrm{n}} \nabla p_\mathrm{n} + \nu_\mathrm{n} \nabla^2 \mathbf{v}_\mathrm{n} - \frac{\rho_\mathrm{s}}{\rho_\mathrm{n}} \mathbf{f}_\mathrm{ns} + \phi_\mathrm{n}, \tag{2.46}$$

$$\frac{\partial \mathbf{v}_\mathrm{s}}{\partial t} + \mathbf{v}_\mathrm{s} \cdot \nabla \mathbf{v}_\mathrm{s} = -\frac{1}{\rho_\mathrm{s}} \nabla p_\mathrm{s} + \nu_\mathrm{s} \nabla^2 \mathbf{v}_\mathrm{s} + \mathbf{f}_\mathrm{ns} + \phi_\mathrm{s}, \tag{2.47}$$

$$\nabla \cdot \mathbf{v}_\mathrm{n} = \nabla \cdot \mathbf{v}_\mathrm{s} = 0, \qquad \mathbf{f}_\mathrm{ns} = \alpha \Omega_0 (\mathbf{v}_\mathrm{n} - \mathbf{v}_\mathrm{s}). \tag{2.48}$$

The total density of the fluid is $\rho = \rho_\mathrm{n} + \rho_\mathrm{s}$. The normal fluid viscosity ν_n is related to the helium dynamic viscosity μ by $\nu_\mathrm{n} = \mu/\rho_\mathrm{n}$. The two fluids are coupled through the mutual friction force $\mathbf{f}_\mathrm{ns}$ that originates from the scattering of the excitations constituting the normal fluid component on quantum vortices. It is proportional to the relative velocity of the fluids and to a characteristic time scale. In general, this characteristic time scale is proportional to the temperature dependent mutual friction coefficients and to a characteristic superfluid vorticity Ω_0 [Bif+19]. The frequency Ω_0 is in principle proportional to the vortex line density and to the quantum of circulation. Both fluid can be stirred by independent forces ϕ_s and ϕ_n. In equation (2.47), the effective superfluid viscosity ν_s models the small-scale physics not resolved by the HVBK equations, including for instance the energy dissipation due to quantum vortex reconnections and Kelvin wave excitations. The values of the effective viscosity have been determined in references [VN02; Bou+15]. In the original model, the mutual friction force coupling the fluids has a more complex expression (see [Don91]), that simplifies to (2.46-2.48) under some assumptions.

This model has been largely used to study co-flow turbulence [RBL09; Bif+18], counterflow turbulence [Bif+19; PK20a] and particle concentrations in quantum turbulence [PK20b]. It has the advantage that standard numerical tools of computational fluid dynamics can be used to solve it, but requires, as in classical turbulence, the use of HPC clusters. From the physical point of view, the model fails at low temperatures, and it assumes that the Kolmogorov scales of the fluid components (the smallest active scales of the flow) are much larger than the mean inter-vortex distance.

2.5   Which model should we use for studying quantum turbulence and superfluid vortex dynamics?

There is not a single or straightforward question to this answer. Given the enormous scale separation involved in turbulent superfluids, and the myriad of physical phenomena present in the system, one needs to make a choice depending on the physical problem to be studied. For instance, if one is interested in quantum vortex reconnections, the HVBK model may not provide any valuable information. For such a study, one might want to use GP as a first principle model, but then tracking of vortex lines is required. If one chooses the vortex filament method instead, direct information on the reconnecting lines is provided by the model. However, the reconnection process needs to be added in an ad-hoc manner. To study vortex reconnections at finite temperatures or to investigate if the normal fluid may affect the process, FOCAULT should be the proper choice. Similarly, to study the T1-T2 counterflow induced
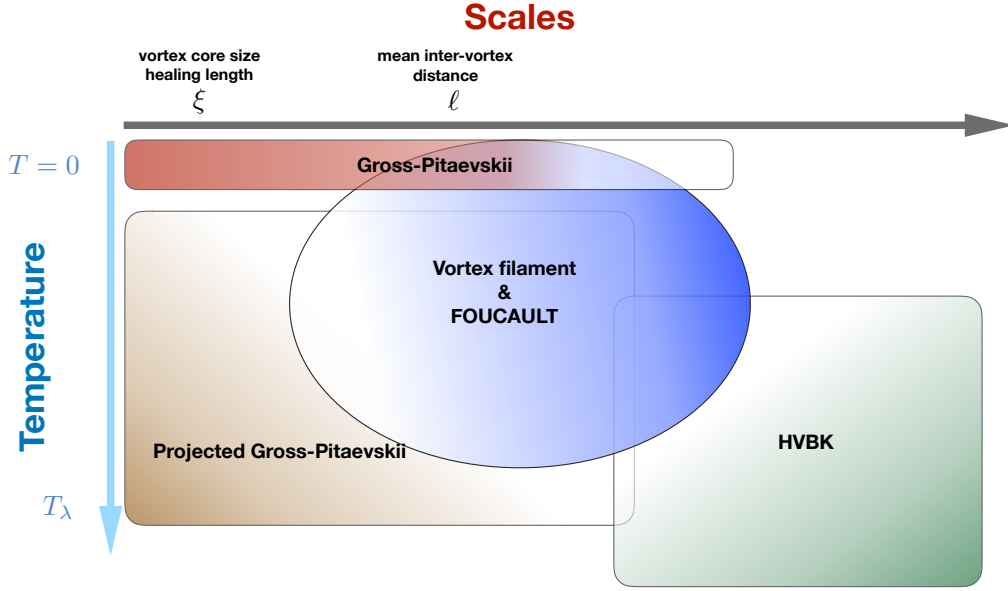
Figure 2.8: Different models of quantum turbulence and superfluid vortex dynamics. The axis represent temperatures and scale ranges where they could be, in practice, used.

transition [MT83], FOUCAULT is certainly the most realistic model. If one is interested in turbulence, for GP, one needs to resolve scales from the vortex core size to scales much larger than the inter-vortex distance. In the case of helium, that will imply to consider fields with at least $(10^9)^3$ degrees of freedom, what is not feasible, even in the most massive computers available today. So then, an HVBK approach might be better suited if one forgets about describing individual vortices. If ones need to study thermal fluctuations, among the models mentioned earlier, only the projected GP might provide an answer. If thermal fluctuations are not of interest, but finite temperature modelling is needed, then the VF method or HVBK might be better. The lack of a unique model is a consequence of the richness of superfluid turbulence. Figure 2.8 shows, in a very schematic manner, some of the most used models for studying quantum turbulence and superfluid vortex dynamics, and where they apply and how they intersect. Each model is coloured in a gradient scale, where the white zones denote the limits of the model, either by physical applicability or numerical feasibility.

Chapter 3

Kelvin waves

This chapter presents a review on Kelvin waves, starting from the derivation by Sir William Thomson of his famous dispersion relation for vortex waves, to a discussion on the wave turbulence Kelvin wave cascade. Two works are included at the end of the chapter.

Vortices are one of the most important structures in fluid dynamics. Roughly speaking, they are highly rotating zones of a fluid that can be strongly confined in space. Typical examples are smoke rings, the fluid structures appearing in the wake of an airfoil and tornadoes. Such structures are never rigid, they can deform and vibrate. Sir William Thomson, also known as Lord Kelvin, pioneered the study of vortex filament vibrations or waves propagating along vortices [Tho80b]. Quoting his 1880's paper, Kelvin introduced the problem of *Vibrations of Columnar Vortex* as.

This is a case of fluid-motion, in which the stream-lines are approximately circles, with their centres in one line (the axis of the vortex) and the velocities approximately constant and approximately equal at equal distances from the axis. As a preliminary to treating it, it is convenient to express the equations of motion of a homogeneous incompressible inviscid fluid (the description of fluid to which the present investigation is confined) in terms of "columnar coordinates," r, θ, z–that is, coordinates such that $r\cos\theta = x$, $r\sin\theta = y$.
. . .
Now let the motion be approximately in circles round Oz, with velocity everywhere approximately equal to T, a function of r . . .

Sir William Thomson, 1880.

The main result of the work of Kelvin was the derivation of the formula today known as the Kelvin wave dispersion relation

$$\omega(k) = -\frac{\Gamma}{8\pi}k^2 \left(\log\left(1/a_0 k\right) - b\right), \text{ for } ka_0 \ll 1, \tag{3.1}$$

where $\omega(k)$ is the frequency of a Kelvin wave of wave vector k. Here, Γ is the circulation of the vortex (assumed to be constant), a_0 is the vortex core size and b is a constant that depends on the model used for the vortex core.

Although Kelvin waves can be observed in vortex filaments in classical fluids, it is the quantum turbulence community who has devoted a big effort to their study. As we have seen in Chapter 2, quantum vortices are topological defects and they are topological protected objects. In superfluid helium, Kelvin waves were visualised in 2013 by using micrometer sized hydrogen particles [Fon+14]. They are very important in quantum turbulence as they appear to be of one the main mechanisms to carry energy towards the smallest scales of a superfluid. They are easily excited by vortex reconnections [Kiv+01]. Energy of Kelvin waves is transferred along scales thanks to non-linear . When the amplitude of waves is small, the theory of weak wave turbulence can be used to predict the scaling of the energy spectrum. There was an agitated controversy on the theoretical derivation of this prediction that has to wait for

accurate numerical simulations. We will discuss the Kelvin wave turbulent cascade, later in this chapter. At the beginning of this chapter, we will focus on the description of linear Kelvin waves.

Before we proceed, one remark is in order to avoid confusions. In the geophysics or atmospheric communities, it is often talked about Kelvin waves or modes [Tho80a]. Such waves are not at all related with the one discussed in this chapter. Kelvin modes in that context arise as balance between Coriolis force and some kind of waveguide. In particular, unlike Kelvin (vortex filament) waves, they are not dispersive.

3.1   Derivation of the Kelvin wave dispersion relation

In this section we reproduce the original work of Kelvin [Tho80b], using a modern notation. We shall then express the velocity field using cylindrical coordinates $\mathbf{v}(r,\theta,z) = v_r \hat{r} + v_\theta \hat{\theta} + v_z \hat{z}$. We consider an ideal incompressible fluid of constant density ρ_0 satisfying the Euler equations:

$$\frac{\partial u_r}{\partial t} + u_r \frac{\partial u_r}{\partial r} + \frac{u_\theta}{r} \frac{\partial u_r}{\partial \theta} + u_z \frac{\partial u_r}{\partial z} - \frac{u_\theta^2}{r} = -\frac{1}{\rho_0} \frac{\partial p}{\partial r} \tag{3.2}$$

$$\frac{\partial u_\theta}{\partial t} + u_r \frac{\partial u_\theta}{\partial r} + \frac{u_\theta}{r} \frac{\partial u_\theta}{\partial \theta} + u_z \frac{\partial u_\theta}{\partial z} + \frac{u_\theta u_r}{r} = -\frac{1}{\rho_0 r} \frac{\partial p}{\partial \theta} \tag{3.3}$$

$$\frac{\partial u_z}{\partial t} + u_r \frac{\partial u_z}{\partial r} + \frac{u_\theta}{r} \frac{\partial u_z}{\partial \theta} + u_z \frac{\partial u_z}{\partial z} = -\frac{1}{\rho_0} \frac{\partial p}{\partial z} \tag{3.4}$$

$$\frac{1}{r} \frac{\partial (r u_r)}{\partial r} + \frac{1}{r} \frac{\partial u_\theta}{\partial \theta} + \frac{\partial u_z}{\partial z} = 0. \tag{3.5}$$

We look for a steady solution containing a straight vortex aligned with the z-axis. Such a vortex can be simply defined as

$$\mathbf{v}(r,\theta,z) = \frac{\alpha(r)}{r} \hat{\theta}, \quad \text{and} \quad p(r,\theta,z) = p_0(r) = \rho_0 \int_{a_0}^{r} \frac{\alpha(s)^2}{s^3} \mathrm{d}s. \tag{3.6}$$

The profile of the vortex core is implicitly defined by $\alpha(r)$ and we denote by a_0 it core size, that is implicitly defined by $\alpha(r)$. Note that

$$\Gamma(r) = \oint_{\mathcal{C}} \mathbf{v}(r,\theta,z) \cdot \mathrm{d}\ell = 2\pi\alpha(r), \tag{3.7}$$

with $\mathcal{C}$ a close path surrounding the vortex, is the circulation around the vortex [1].

A Kelvin wave of frequency ω, wave vector k and azimuthal wave number n, is a perturbation of the previous solution that can be written as

$$u_r(r,\theta,z,t) = \epsilon v_r(r) \cos kz \sin(\omega t - n\theta) \tag{3.8}$$

$$u_\theta(r,\theta,z,t) = \frac{\alpha(r)}{r} + \epsilon v_\theta(r) \cos kz \cos(\omega t - n\theta) \tag{3.9}$$

$$u_z(r,\theta,z,t) = \epsilon v_z(r) \sin kz \sin(\omega t - n\theta) \tag{3.10}$$

$$p(r,\theta,z,t) = p_0(r) + \epsilon\rho_0\, p_1(r) \cos kz \cos(\omega t - n\theta), \tag{3.11}$$

where ϵ is assumed to be small. Linearising for $\epsilon \ll 1$ leads to the following equation for the perturbations

$$v_r(r) + n v_\theta(r) = -rk v_z - r v_r'(r) \tag{3.12}$$

---

[1]For the sake of simplicity we assume that $\mathcal{C}$ is a circular circuit, centred in the vortex.

The velocity fields v_r, v_θ and the pressure $p_1(r)$ can be expressed as a function of v_z:

$$p_1(r) = v_z(r)\frac{\omega}{k}\left(1 - \frac{n\alpha}{\omega r^2}\right) \tag{3.13}$$

$$v_r(r) = \frac{\left(1 - \frac{n\alpha}{\omega r^2}\right)}{\Lambda(r)k}\left[-\left(1 - \frac{n\alpha}{\omega r^2}\right)v_z' + \frac{n}{\omega r^2}\alpha' v_z\right] \tag{3.14}$$

$$v_\theta(r) = \frac{1}{\Lambda(r)k}\left[-\left(1 - \frac{n\alpha}{\omega r^2}\right)\frac{\alpha'}{\omega r}v_z' + \left(\Lambda(r) + \frac{\alpha'^2}{\omega^2 r^2}\right)\frac{n}{r}v_z\right], \tag{3.15}$$

where $\Lambda(r) = \left(1 - \frac{n\alpha(r)}{\omega r^2}\right)^2 - \frac{1}{\omega^2 r^3}2\alpha\alpha'$. Replacing (3.14-3.15) in (3.12) leads to a linear equation for v_z only. Equations (3.12)-(3.15) supplied with some suitable boundary condition leads the Kelvin wave dispersion relation $\omega(k)$.

We will consider now two particular cases of the vortex profile.

3.1.1 Case of a core with solid rotation

We consider here a vortex with a core of size a_0, with the fluid performing a solid rotation inside and being irrotational outside. In this case the vortex profile is given by

$$\alpha(r) = \frac{\Gamma}{2\pi}\begin{cases}\frac{r^2}{a_0^2} & \text{if } r \leq a_0 \\ 1 & \text{if } r \geq a_0.\end{cases} \tag{3.16}$$

With this profile, the velocity v_z satisfies the equations

$$v_z'' + \frac{1}{r}v_z' - \left(k^2\left[(1 - \frac{4}{(n-\tilde{\omega})^2)})\right] + \frac{n^2}{r^2}\right) = 0 \quad \text{if} \quad r \leq a_0 \tag{3.17}$$

$$v_z'' + \frac{1}{r}v_z' - \left(k^2 + \frac{n^2}{r^2}\right) = 0 \quad \text{if} \quad r \geq a_0. \tag{3.18}$$

where $\tilde{\omega} = \omega/(\Gamma/2\pi a_0^2)$. The solution of the previous equation is simply given as a linear combination of the modified Bessel functions I_n and K_n. Imposing that v_z is finite at $r = 0$ and $r = \infty$, together with the continuity of v_r and v_z at $r = a_0$, leads to a transcendental equation relating ω and k. It reads

$$\begin{cases}\frac{2n}{2+n-\tilde{\omega}} + \frac{|k|K_{n-1}(|k|a_0)}{K_n(|k|a_0)} + \frac{2n\,_0F_1\left[n;\frac{1}{4}a_0^2k^2\left(1-\frac{4}{(n-\tilde{\omega})^2}\right)\right]}{\left(1-\frac{4}{(n-\tilde{\omega})^2}\right)\,_0F_1\left[n+1;\frac{1}{4}a_0^2k^2\left(1-\frac{4}{(n-\tilde{\omega})^2}\right)\right]} = 0 & \text{if } n \neq 0 \\ \\ \frac{|k|K_1(|k|a_0)}{K_0(|k|a_0)} + \frac{a_0^2k^2\,_0F_1\left[2;\frac{1}{4}a_0^2k^2\left(1-\frac{4}{\tilde{\omega}^2}\right)\right]}{2I_0\left(a_0k\sqrt{1-\frac{4}{\tilde{\omega}^2}}\right)} = 0 & \text{if } n = 0,\end{cases} \tag{3.19}$$

where $_0F_1[\nu; z]$ is the confluent hypergeometric function. The dispersion relation for different values of n is plotted in figure 3.1.a and it will be commented later. For $n = 1$, in the limit of $a_0 k \ll 1$, the dispersion relation simplifies to

$$\omega(k) = -\frac{\Gamma}{8\pi}k^2\left(\log\frac{1}{a_0|k|} + b\right), \text{ with } b = -\gamma_E + \log 2 + \frac{1}{4} = 0.366\ldots \tag{3.20}$$

and $\gamma_E = 0.577216\ldots$ the Euler constant. Note that a Kelvin wave oscillates in the opposite direction with respect to the flow around the vortex.

3.1.2   Case of a hollow vortex core

In this case, the flow is irrotational outside the vortex core , i.e. $\alpha(r) = \frac{\Gamma}{2\pi}$, but "hollow" inside. The vortex core is a free boundary initially a cylinder of radius a_0.

The velocity v_z satisfies the equation (3.18) everywhere. By imposing that there is no radial velocity at infinite, the solution simply reads

$$v_z(r) = CK_n(|k|r). \tag{3.21}$$

The boundary condition determining the dispersion relation is that the total pressure (3.11) must vanish at the boundary of the disturbed cylinder. In the present case, the total pressure simply reads

$$p(r,\theta,z,t) = \rho_0 \left(\frac{\Gamma}{2\pi}\right)^2 \frac{r^2 - a_0^2}{2a_0^2 r^2} + \epsilon \rho_0\, u_z(r)\frac{\omega}{k}\left(1 - \frac{n\Gamma}{2\pi\omega r^2}\right)\cos kz \cos(\omega t - n\theta), \tag{3.22}$$

where we have used (3.6) and (3.13).

The disturbed surface is defined by following fluid particles initially located at the cylinder boundary. Such trajectories satisfy $\dot{r}_\mathrm{p} = u_r$ and $\dot{\theta}_\mathrm{p} = u_\theta/r_\mathrm{p}$, where the fluid velocities are defined in (3.8) and (3.9) respectively. At the leading order, they are given by

$$\theta_\mathrm{p} = \int \frac{\alpha(r_\mathrm{p})}{r_\mathrm{p}^2}\,\mathrm{d}t = \theta_\mathrm{p}^0 + \frac{\Gamma}{2\pi a_0^2}t, \tag{3.23}$$

$$r_p = \int \epsilon v_r(a_0)\cos kz \sin(\omega t - n\theta_\mathrm{p})\mathrm{d}t = a_0 - \frac{\epsilon v_r(a_0)\cos kz \cos(\omega t - n\theta_\mathrm{p})}{\omega - n\frac{\Gamma}{2\pi a_0^2}}. \tag{3.24}$$

Notting that $r^2 - a_0^2 \approx 2a_0(r - a_0)$ close to the cylinder, using (3.22) and (3.24) the condition $p(r_\mathrm{p}, \theta_\mathrm{p}, z, t) = 0$ implies

$$-\left(\frac{\Gamma}{2\pi}\right)^2 \frac{v_r(a_0)}{a_0^3(\omega - n\frac{\Gamma}{2\pi a_0^2})} + u_z(a_0)\frac{\omega}{k}\left(1 - \frac{n\Gamma}{2\pi\omega a_0^2}\right) = 0 \tag{3.25}$$

or simply,

$$u_z(a_0)(\tilde{\omega} - n)^2 - ka_0 u_r(a_0) = 0, \tag{3.26}$$

where $\tilde{\omega}$ was defined above for the previous case. By noting from equation (3.14) that $u_r(r) = -u_z'(r)/k$ and replacing (3.21), we obtain an equation defining the dispersion relation. Solving for ω gives the hollow vortex Kelvin wave dispersion relation [2]

$$\omega_n^\pm(k) = \frac{\Gamma}{2\pi a_0^2}\left(n \pm \sqrt{n + \frac{a_0|k|K_{n-1}(a_0|k|)}{K_n(a_0|k|)}}\right) \tag{3.27}$$

The dispersion relation (3.27) is much simpler than the one of the previous case and it is the one often found in the literature. The case $n = 0$, is given by

$$\omega_0^\pm(k) = \pm\frac{\Gamma}{2\pi a_0^2}\sqrt{\frac{a_0|k|K_1(a_0|k|)}{K_0(a_0|k|)}}. \tag{3.28}$$

For $n = 1$, in the limit of small wave numbers it reduces to

$$\omega^-(k) = -\frac{\Gamma}{8\pi}k^2\left(\log\frac{1}{a_0|k|} + b\right), \text{ with } b = \log 2 - \gamma_\mathrm{E} \tag{3.29}$$

$$\omega^+(k) = \frac{\Gamma}{8\pi a_0^2}. \tag{3.30}$$

---

[2]We have use the identity $nK_n(z) + zK_{n-1}(z) = -zK_n'(z)$.

We observe that the only difference between (3.20) and (3.29) is the core constant b. We also note that the positive branch takes values much larger than the negative one for $k \to 0$. As we will see in Chapter 5, this frequency is related to the Magnus force and the mass inside the core.

The previous results were derived by Kelvin in [Tho80b] in 1880. Much later, in 2003 P.H. Roberts generalised Kelvin results to the case of a compressible classical fluid [Rob03a].

3.1.3 Discussion on vortex wave excitations

We start this discussion by plotting the dispersion relation of vortex excitation for both core models. The dispersion relations are displayed in figure 3.1. We clearly note from the figure that there are several
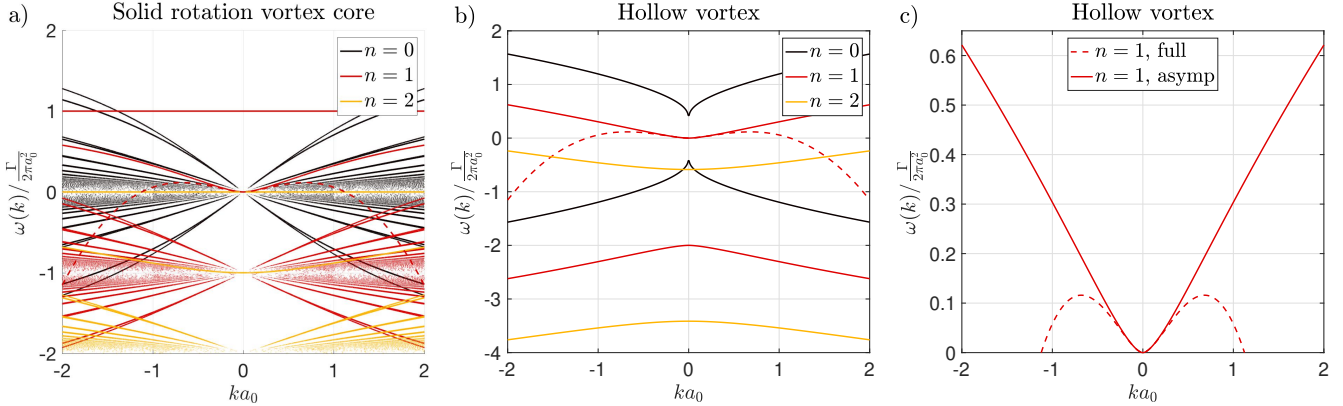
Figure 3.1: Wave excitations of a vortex filament in an incompressible fluid. **a)** A vortex with solid rotating fluid in its core (3.19). **b)** The hollow core vortex dispersion relation (3.27). **c)** A zoom of **b)**. The asymptotic predictions for $n = 1$ are displayed in dashed lines. We use the convention that $\Gamma < 0$, so the the Kelvin wave dispersion curve lays on the upper plane.

branches of vortex excitations. The waves having $n = 0$ are known as *varicose* waves as they do not have any angular dependence. Most interesting, it is the branch with $n = 1$. In particular the branch having values of opposite sign respect to Γ. The literature usually refers as Kelvin waves to this particular branch. We will refer to in the following as Kelvin waves to the negative mode with $n = 1$ and it will be simply denoted by ω.

3.2 Vortex excitations in the Gross-Pitaevskii model

Vortices in superfluids are in some sense ideal vortices, they are topological defects and their circulation around them is quantised so it is constant over time. They are actually nodal lines of the complex order parameter describing the system. In Bose-Einstein condensates, their core has a finite and well determined size that is of the order of the healing length. Kelvin waves in the context of superfluids were first studied by L.P. Pitaevskii by using the Gross-Piteavskii (GP) equation [Pit61].

Vortex waves in GP were later studied in much detail by P.H. Roberts [Rob03b], generalising L.P Pitaevskii work. In his work, P.H. Roberts perturbs a straight quantum vortex in order to determine the vortex excitations of a quantum vortex. He was able to find analytically the Kelvin dispersion in the limit $k \to 0$. As in the case of an incompressible fluid, it can be expressed as

$$\omega(k) = -\frac{\Gamma}{8\pi}k^2\left(\log\frac{1}{\xi|k|} + b\right), \text{ with } b = \log 2 - \gamma_{\mathrm{E}} + C_{\mathrm{R}} \tag{3.31}$$

$$C_{\mathrm{R}} = \lim_{L\to\infty}\int_0^L\left\{\left(\frac{\mathrm{d}R}{\mathrm{d}r}\right)^2 + \left(\frac{R}{r}\right)^2\right\}r\mathrm{d}r - \log L = -0.119118\ldots \tag{3.32}$$

where ξ is the healing length and $R(r)$ is the density profile of a quantum vortex (see Section 2.1.3, equation (2.23)). The constant C_{R} was evaluated numerically in his work.

Like in the case of compressible fluids [Rob03a], probably inspired by quantum mechanics, Roberts used the concept of bound and free (Kelvin wave) states. In his notation, the perturbation of the straight vortex wave function has a dependence given by $e^{-i\omega t \pm \mu r}$, where ω and μ are in general complex numbers and r is the radial distance to the straight vortex. For a *bound* state the amplitude of the wavefunction perturbation decreases with r. In this case, the vortex wave travels along the vortex axis without loss of energy. On the contrary, for a *free* state, there are density waves escaping to infinity. Such waves are waves radiated by the vortices. Roberts found that in general vortex excitations are *free* for all k, except for the cases $n = 1$ and $n = 2$ that are a bit special.

The case $n = 1$ is the most interesting one. It was found that this mode is *bounded* for all k, with ω always being a real number. As a consequence, the $n = 1$ mode does not radiate energy and it is thus the most likely to be observed. The numerical solution found by Roberts is displayed in figure 3.2.a. The
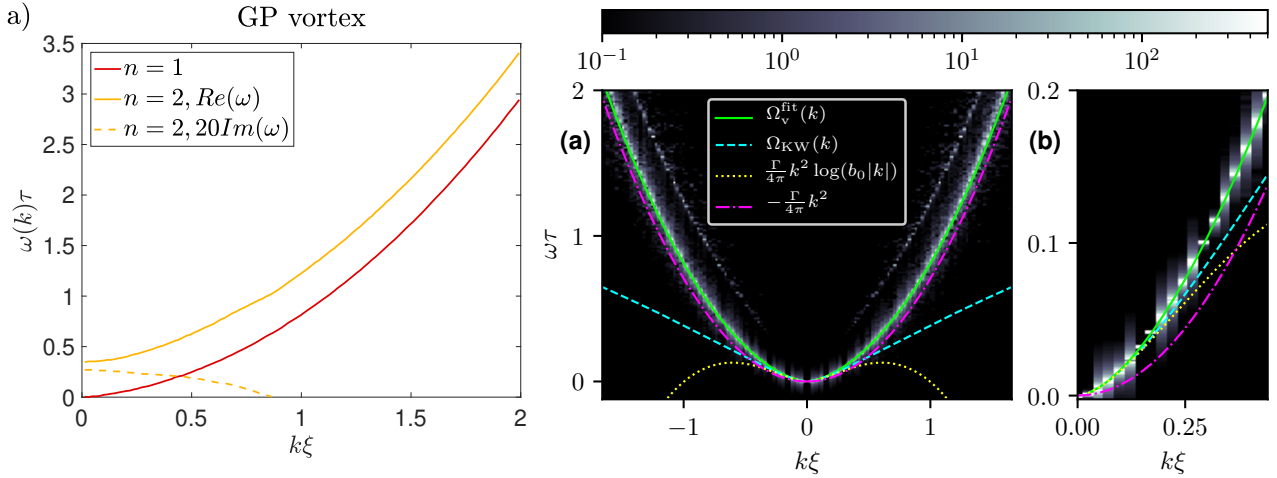
Figure 3.2: Wave excitations of a vortex filament in a Gross-Pitaevskii quantum vortex. **a)** Dispersion relation of GP vortex waves for the $n = 1$ and $n = 2$ modes. The imaginary part of the $n = 2$ has been amplified by a factor 20. Data extracted form figure 1 of reference [Rob03a]. **b)** Dispersion relation computed numerically with the vortex filament tracking method used in [Krs12]. We clearly observe the effect of discreetness. The figure also displays a fit that reproduces well both, small and large k asymptotics. In this figure ξ is the healing length and $\tau = \xi/c$ a characteristic time scale. Figure reproduced from [GKN20].

case $n = 2$ was found to be *bounded* only for $k\xi > 0.87 \ldots$. For $k\xi < 0.87$, the $n = 2$ mode frequency has a small imaginary part, but the vortex solution remains stable. The real and imaginary part of the $n = 2$ frequency are also displayed in figure 3.2.a. Roberts did not find any indication that a vortex solution could be unstable for any mode or wave vector.

Finally, also mentioned by Roberts, in the large k limit, the vortex wave dispersion relation tends to the free particle one $-\Gamma k^2/4\pi$. In reference [GKN20], we introduced a fit based on the two known asymptotic behaviours that turned out be useful for simulation and theory. This fit reads

$$\Omega_{\mathrm{v}}^{\mathrm{fit}}(k) \;=\; \Omega_{\mathrm{KW}}(k)\left(1 + \epsilon_{\frac{1}{2}}(a_0|k|)^{\frac{1}{2}} + \epsilon_1(a_0|k|) + \frac{1}{2}(a_0|k|)^{\frac{3}{2}}\right), \tag{3.33}$$

where $\Omega_{\mathrm{KW}}(k)$ is the hollow vortex core dispersion relation 3.27 with $a_0 = 1.1265\xi$ determined in order to match Roberts result (3.31). The dimensionless parameters $\epsilon_{\frac{1}{2}} = -0.20$ and $\epsilon_1 = 0.64$ were obtained by measuring dispersion relation in GP numerical simulations and a vortex tracking algorithm (see Appendix A.1). $\Omega_{\mathrm{v}}^{\mathrm{fit}}(k)$ is also displayed in 3.2.b.

3.3 Non-linear Kelvin wave dynamics

The aim of this section is to provide an introduction to the dynamics of vortex waves, including a short description on the wave turbulence Kelvin wave cascade. We start by describing the basic non-linear models of vortex dynamics.

3.3.1 Local Induced Approximation

The so-called Local Induced Approximation (LIA) is perhaps the simplest description of the dynamics of a vortex line. As its names suggest, it is based on a local approximation that was introduced by Da Rios in 1906 [Da 06].

Let us start by recalling that the translational velocity of a vortex ring of radius R and circulation Γ is simply [Don91]

$$v_{\text{ring}} = \frac{\Gamma}{2\pi R}(\log(R/a_0) - d), \tag{3.34}$$

where d is some core dependent constant. We parametrise the vortex line as $\mathbf{s}(\zeta)$, where ζ is the natural parametrisation.
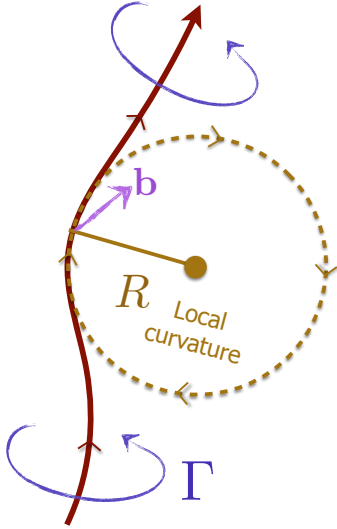
Figure 3.3: Sketch of the local induced approximation model LIA. The vortex is displayed in red. The blue arrows indicate orientation of the velocity of the flow. The red and brown arrow denote the vorticity of the filament and the the vortex ring respectively. Figure courtesy of U. Giuriato, adapted from his Ph.D. thesis [Giu20].

The LIA model assumes that each point of the vortex line moves with the velocity of a vortex ring tangent to that point (respecting its vorticity orientation) and of radius equal to the radius of curvature of that point. This is clearly sketched in figure 3.3. The unit binormal vector $\widehat{\mathbf{b}}$ indicates the direction in which a vortex point will move. Note that it is in the opposite direction respect to the flow around the vortex. The LIA model, is then simply given by

$$\dot{\mathbf{s}} = \frac{\Gamma\Lambda}{4\pi R}\widehat{\mathbf{b}} = \frac{\Gamma\Lambda}{4\pi}\mathbf{s}' \times \mathbf{s}'', \tag{3.35}$$

where the dot and primes denote derivatives respect to time and ζ respectively. The pre-factor is $\Lambda = \log R_0/a_0$ where R_0 is the characteristic or mean radius, that is usually assumed to be constant. Note that the LIA model conserves the total vortex length

$$\mathcal{L} = \int \left|\frac{\partial \mathbf{s}}{\partial \zeta}\right| d\zeta. \tag{3.36}$$

In the case of an almost straight vortex aligned along the z axis, the filament can be parametrised using cartesian coordinates $\mathbf{s} = (X(z), Y(z), z)$. Denoting by $s(z) = X(z) + iY(z)$, and assuming small deformations ($|s'| \ll 1$), the LIA equation becomes

$$i\Gamma\dot{s} = \frac{\delta H_{\text{LIA}}}{\delta s^*} = -\frac{\Gamma^2\Lambda}{4\pi}\frac{\partial^2 s}{\partial z^2}, \quad \text{with} \quad H_{\text{LIA}} = \frac{\Gamma^2\Lambda}{4\pi}\int |\frac{\partial s}{\partial z}|^2 dz. \tag{3.37}$$

The Hamiltonian structure of the LIA model is apparent. Its Hamiltonian is actually an energy per unit of density. The energy of Kelvin waves is given by $E_{\text{KW}} = \rho_0 H_{\text{LIA}}$. The term $\rho_0\Gamma^2\Lambda/4\pi$ is called the vortex line tension as it relates the energy and the total length of the vortex.

Note that the LIA model trivially leads to the LIA Kelvin wave dispersion relation

$$\omega_{\text{LIA}}(k) = -\frac{\Gamma\Lambda}{4\pi}k^2, \tag{3.38}$$

that misses the logarithmic correction in the dispersion relations discussed in the previous sections.

3.3.2 Non-local model for an almost straight vortex

As it was discussed in Chapter 2.2, the full description of the vortex filament dynamics is given by replacing the LIA vortex velocity by the full Biot-Savart integral. We recall the model here

$$\dot{\mathbf{s}}(\zeta) = \frac{\Gamma}{4\pi} \oint' \frac{d\mathbf{s}(\zeta') \times (\mathbf{s}(\zeta) - \mathbf{s}(\zeta'))}{|\mathbf{s}(\zeta) - s(\zeta')|^3}, \tag{3.39}$$

where the integral extends over all the vortices and the prime means that the integral must to be regularised introducing a vortex core cut-off.

As one could expect, there is a much simpler form in the case of an almost straight vortex. Using a cartesian parametrisation, as in the previous section, it was shown by Sonin [Son87] and Svistunov [Svi95] that the vortex filament method can be reduced to the following non-local Hamiltonian equation

$$i\Gamma\dot{s}(z) = \frac{\delta H_{\mathrm{NL}}}{\delta s^*(z)}, \qquad H_{\mathrm{NL}} = \frac{\Gamma^2}{4\pi} \int \frac{1 + \mathcal{R}e[s'^*(z_1)s'(z_2)]}{\sqrt{(z_1 - z_2)^2 + |s(z_1) - s(z_2)|^2}} dz_1 dz_2. \tag{3.40}$$

Assuming that waves have a period L, the vortex disturbances can be written as $s(z) = \Gamma^{-1/2} \sum_k a_k(t)e^{ikz}$. In these new variables, the equations for the vortex displacement becomes

$$i\frac{da_k}{dt} = \frac{\partial \mathcal{H}}{\partial a_k^*}, \quad \text{with} \quad \mathcal{H}[a, a^*] = \frac{1}{L} H[z, z^*]. \tag{3.41}$$

Note that a_k does not have units of length. Furthermore, if the amplitudes of waves are small, the new Hamiltonian can be expressed perturbatively as

$$\mathcal{H} = \sum_k \omega_k |a_k|^2 + \mathcal{H}_4 + \mathcal{H}_6 + \dots, \tag{3.42}$$

where $\mathcal{H}_n$ is of order n on the wave amplitude and it contains the interaction of n waves. An expression for those high order terms can be found for instance in [LN10; Bou+11; Lau+10]. The dispersion relation is thus given by ω_k and it is found to be

$$\omega_{\mathrm{NL}}(k) = \omega_k = -\frac{\Gamma}{4\pi} k^2 (\log (k\ell) - \Lambda), \tag{3.43}$$

where here $\Lambda = \log (\ell/a_0)$. The length ℓ is an IR cut-off that here represents the mean inter-vortex distance at which the description of Kelvin wave propagating in isolated vortices breaks down. Note that, if the logarithmic correction is neglected, $\mathcal{H}_2$ reduces to the LIA Hamiltonian (3.37). As $\mathcal{H}_2$ is quadratic, waves with different k do not interact, therefore energy can not be redistributed among different modes. High order terms are necessary to transfer energy along scales. Such energy exchange is described by the theory of wave turbulence.

3.3.3 Theoretical description of the Kelvin wave cascade

A very brief description of the weak wave turbulence theory

In this section we intend to provide a quick overview of the wave turbulence theory. Only the final results of the theory will be presented in order to give some elements to understand the Kelvin wave cascade. The interested reader is directed for instance to the books [ZLF12; Naz11], to see the derivation and applications of the theory.

As in classical turbulence, where energy is transferred along scales in a cascade process thanks to the non-linear interaction of "eddies" [Fri95], non-linear waves interact and can transfer energy or other invariants with a constant flux. When the scales of energy injection and dissipation are well separated, an out-of-equilibrium state, known as wave turbulence emerges. Such cascade process is depicted in
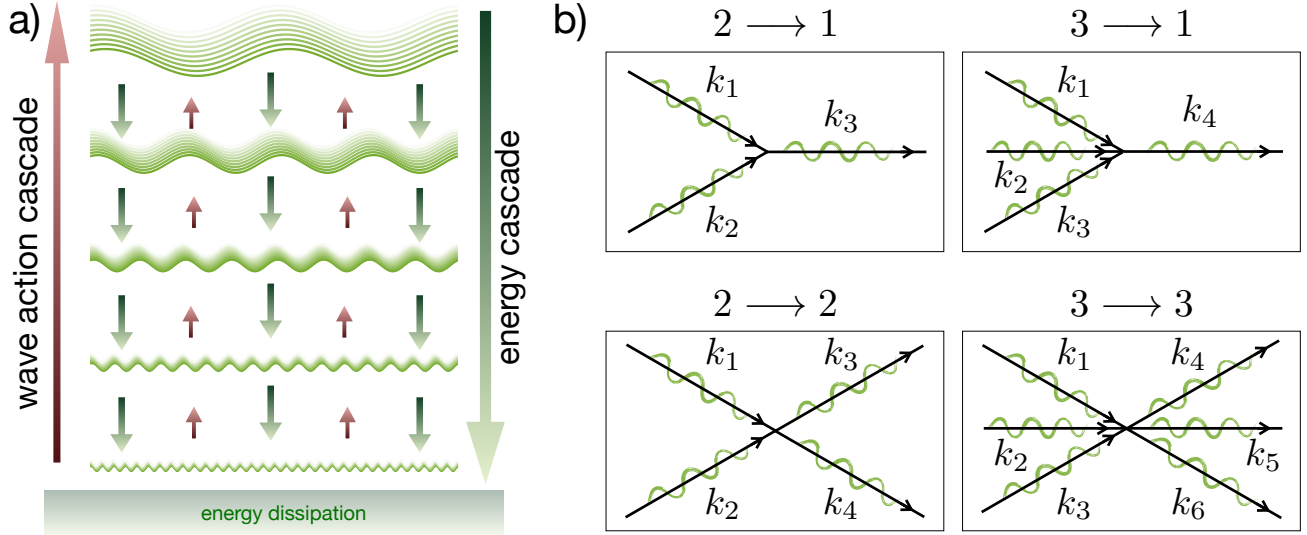
Figure 3.4: Sketch of wave turbulence cascades. **a)** Waves of large wavelengths interact and excite waves at smaller wavelengths and those repeat the process until energy is dissipated. The inverse cascade process can take place for wave action. **b)** Different kinds of wave are depicted by arrows with obvious notation : $2 \to 1$, $3 \to 1$, $2 \to 2$ and $3 \to 3$.

figure 3.4.a, where a direct energy cascade and/or an inverse wave-action cascade takes place. The wave-action is an extra invariant of some non-linear wave systems, such as the free particle excitations of the Gross-Piteavskii equation (see Section 2.1.2).

For sake of simplicity, we will consider here a non-linear wave system with a cubic non-linearity. In general, after performing a Fourier transform, and eventually of some change of variables, such system can be rewritten as

$$\frac{\mathrm{d}a_{\mathbf{k}}^s}{\mathrm{dt}} = -is\omega_k a_{\mathbf{k}}^s + \epsilon^2 \sum_{s_1,s_2,s_3} \int L_{\mathbf{k},\mathbf{k}_1,\mathbf{k}_2,\mathbf{k}_3}^{s,s_1,s_2,s_3} \delta(\mathbf{k} + s_1\mathbf{k}_1 + s_2\mathbf{k}_2 + s_3\mathbf{k}_3) a_{\mathbf{k}_1}^{s_1} a_{\mathbf{k}_2}^{s_2} a_{\mathbf{k}_3}^{s_3} \mathrm{d}\mathbf{k}_1 \mathrm{d}\mathbf{k}_2 \mathrm{d}\mathbf{k}_3, \qquad (3.44)$$

where $s, s_1, s_2, s_3 = \pm 1$ and we use the notation $a_{\mathbf{k}}^+ = a_{\mathbf{k}}$ and $a_{\mathbf{k}}^- = a_{\mathbf{k}}^*$. The term $L_{\mathbf{k},\mathbf{k}_1,\mathbf{k}_2,\mathbf{k}_3}^{s,s_1,s_2,s_3}$ is the interaction coefficient and is usually assumed to have some scaling properties with $\mathbf{k}$. We have also implicitly assumed that waves amplitudes have been rescaled so $a_{\mathbf{k}}$ is of order one and ϵ is a small parameter.

The theory of weak wave turbulence takes advantage of the small parameter ϵ to develop a closed model that can be treated analytically. Thanks to this small parameter, a large time scale separation between the time associated to waves and the one related to the non-linear terms is ensured. This allow for a controlled multi-time expansion [NR11]. The main object of study in the theory is the particle number spectrum defined as

$$n_{\mathbf{k}} = \frac{1}{V} \langle |a_{\mathbf{k}}|^2 \rangle, \qquad (3.45)$$

where V is the volume of the system and average is performed over different kinds of fluctuations (e.g. realisations of the initial conditions, forcing, etc.).

Summarised in one sentence, the theory of weak wave turbulence starts from $n_{\mathbf{k}}$, takes its time derivative, use equation (3.44) several times, then take some very delicate limits and finally succeed to obtain a closed equation for $n_{\mathbf{k}}$. This equation is called the kinetic wave equation and can be generically

written as

$$\frac{dn_{\mathbf{k}}}{dt} = \epsilon^4 \sum_{s_1 s_2 s_3 = \pm 1} \int |J^{1,s_1,s_2,s_3}_{\mathbf{k}\mathbf{k}_1\mathbf{k}_2\mathbf{k}_3}|^2 n_{\mathbf{k}_1} n_{\mathbf{k}_2} n_{\mathbf{k}_3} n_{\mathbf{k}} \times \left(\frac{1}{n_{\mathbf{k}}} - \frac{s_1}{n_{\mathbf{k}_1}} - \frac{s_2}{n_{\mathbf{k}_2}} - \frac{s_3}{n_{\mathbf{k}_3}} \right) \delta(\mathbf{k}_1 + \mathbf{k}_2 + \mathbf{k}_3 - \mathbf{k})$$

$$\times \delta(s_1 \omega_{\mathbf{k}_1} + s_2 \omega_{\mathbf{k}_2} + s_3 \omega_{\mathbf{k}_3} - \omega_{\mathbf{k}}) \mathrm{d}\mathbf{k}_1 \mathrm{d}\mathbf{k}_2 \mathrm{d}\mathbf{k}_3. \quad (3.46)$$

The term $|J^{1,s_1,s_2,s_3}_{\mathbf{k}\mathbf{k}_1\mathbf{k}_2\mathbf{k}_3}|^2$ can be seen as a collisional kernel and expressed in terms of the functions $L^{s,s_1,s_2,s_3}_{\mathbf{k},\mathbf{k}_1,\mathbf{k}_2,\mathbf{k}_3}$ defined in (3.44). Depending on the problem, it can vanish for different combinations of s_1, s_2 and s_3. Although the kinetic equation (3.46) seems to be very complex, it has the advantage to posses some simple analytical solutions.

The simplest steady solution is the Raleigh-Jeans spectrum that corresponds to a thermal solution where, by definition, there is no flux. It simply reads

$$n^{\mathrm{RJ}}_{\mathbf{k}} = \frac{T}{\omega_{\mathbf{k}}}. \quad (3.47)$$

Replacing $n^{\mathrm{RJ}}_{\mathbf{k}}$ in (3.46) and using the δ-function on frequencies, one notes that the integrand vanishes exactly.

A less trivial steady solution corresponds to the one having a constant energy flux P. It is called the Kolmogorov-Zakharov spectrum and is found to be of the form

$$n^{\mathrm{KZ}}_k = C_{\mathrm{KZ}} P^{1/3} k^{-x}. \quad (3.48)$$

The theory predicts the exponent $1/3$ on the energy flux and the value of the exponent x that depends on the scaling of the dispersion relation, the collisional kernel and the dimension of the space. Furthermore, the theory also predicts the numerical value of the Kolmogorov-Zakharov constant C_{KZ}, although it is usually difficult to compute it.

In the context of wave turbulence, the kind of non-linear interaction we just described is said to be 4-waves, as 4 wave vectors are involved. In a wave system with a quadratic non-linearity, like acoustic waves in fluids or large scale Bogoliubov waves, the wave interaction is called 3-waves and so on for a general non-linearity of order $\mathcal{N} - 1$. For $\mathcal{N}$-wave , the Kolmogorov-Zakharov spectrum scales with the flux as $P^{1/(\mathcal{N}-1)}$. Figure 3.4.b depicts different types of 3-, 4- and 6-wave . Furthermore, a $\mathcal{N}$-wave interaction process is classified depending on its particular type of interaction determined by the coefficients $s_i = \pm$ in the kinetic equation. For instance, in the case of 4-wave , when $s_1 = s_2 = s_3 = 1$ the interaction is called $3 \to 1$. The case when $s_1 = -1$ and $s_2 = s_3 = 1$, it is called $2 \to 2$ and it is particularly interesting. In this case, a new invariant appears [3]:

$$N = \int n_{\mathbf{k}} \mathrm{d}\mathbf{k}. \quad (3.49)$$

This new invariant it is called the wave wave-action or, in analogy with quantum mechanics, the total number of particles. It is not necessarily a conserved quantity of the initial partial differential equation. Associated to this invariant there is a new cascade with a constant wave-action/particle flux Q

$$n^Q_{\mathbf{k}} = C_Q Q^{1/3} k^{-y}. \quad (3.50)$$

In general, for $\mathcal{N}$-wave process, of the kind $X \to X$ conserve wave-action. Note that a chemical potential can be included in the Raleigh-Jeans spectrum $n^{\mathrm{RJ}}_{\mathbf{k}} = T/(\omega_{\mathbf{k}} - \mu)$.

Finally, the energy spectrum is simply obtained multiplying by ω_k and summing over the angles

$$E_k = \int \omega_k n_{\mathbf{k}} \delta(|\mathbf{k}| - k) \mathrm{d}\mathbf{k}, \quad (3.51)$$

such that the total energy at the leading order is simply given by $\int_0^\infty E_k \mathrm{d}k$.

---

[3] This can be directly checked by permuting wave-vectors.

Kozik-Svistunov and L'Vov-Nazarenko predictions

When looking at the KW problem, one is naturally tempted to apply the theory of wave turbulence to the equation (3.40). Before we proceed, some remarks are in order concerning the dimensions of energy, wave action and fluxes. Note that starting point to apply the weak wave turbulence to Kelvin waves, is the Hamiltonian written in its canonical form 3.41. The amplitude A_k of a Kelvin wave with given wave number k relates to the particle number spectrum as

$$n_k = \frac{L}{2\pi}\langle|a_k|^2\rangle = \frac{\Gamma L}{2\pi}\langle|A_k|^2\rangle, \tag{3.52}$$

where we recall that L is the periodicity of the straight vortex. Its dimensions is $[n_k] = Length^5/Time$. In addition, the Hamiltonian $\mathcal{H}$ is an energy per unit of density ρ_0 and length L. It follows that the total energy of the Kelvin waves is given by

$$E_{\mathrm{KW}} = \rho_0 L \int_{k_0}^{\infty} \omega_k n_k \mathrm{d}k = \rho_0 L \int_{k_0}^{\infty} E_{\mathrm{KW}}(k)\mathrm{d}k, \tag{3.53}$$

where $k_0 = 2\pi/L$. Note that $[E_{\mathrm{KW}}] = Mass \times Length^2/Time^2$ and $[E_{\mathrm{KW}}(k)] = Length^5/Time^2$. Finally, as in the theory of wave turbulence the energy is expressed as $\int \omega_k n_k \mathrm{d}k$, the energy flux has dimensions $[P] = Length^4/Time^3$. The previous dimensional considerations are not important in the following and we will refer indistinguishably to n_k as the amplitude or the number KW spectrum.

The application of the theory of weak wave turbulence to describe Kelvin wave interations was in fact the origin of an agitated debate concerning the prediction of the energy spectrum. Two independent groups leaded by Kozik & Svitsunov [KS04] and L'vov & Nazarenko [LN10] respectively, starting from the same equations (3.41), and applying the same theory, derived different predictions. Although the equations describing the dynamics of KWs are one dimensional, the wave turbulence calculations are far from simple. First of all, it was quickly noticed that the quartic term in the expansion (3.42) leads to non-resonant terms, that means that they can removed with a suitable canonical transformation. From the point of view of wave turbulence, the resulting Hamiltonian contains thus 6-wave .

The Kozik & Svitsunov [KS04] prediction for the energy cascade was derived from this 6-wave Hamiltonian and reads

$$n_{\mathrm{E}}^{\mathrm{KS}}(k) = C_{\mathrm{KS}}^{\mathrm{E}} \frac{\Gamma^{2/5}P^{1/5}}{k^{17/5}}. \tag{3.54}$$

It was also predicted that associated to wave action, an inverse cascade should also take place and obey the following prediction

$$n_{\mathrm{N}}^{\mathrm{KS}}(k) = C_{\mathrm{KS}}^{N} \left(\frac{Q\Gamma}{\Lambda}\right)^{1/5} k^{-3}. \tag{3.55}$$

These predictions were soon criticised by L'vov & Nazarenko [LN10], as they turned out to be non-local, meaning that once replaced into the kinetic equations, the integrals are not convergent. To deal with this divergence, L'vov & Nazarenko derived an effective theory, showing that the dominant sextets contributing to 6-wave processes are those in which two wave vectors are much smaller than the other ones [Lau+10]. In this theory, the effective Hamiltonian becomes 4-waves and contains only $3 \to 1$. L'vov & Nazarenko prediction for the direct energy cascade is

$$n_{\mathrm{E}}^{\mathrm{LN}}(k) = C_{\mathrm{LN}} \frac{P^{1/3}}{\Psi^{2/3}k^{11/3}}, \tag{3.56}$$

where the dimensionless number ψ depends itself on the spectrum as

$$\Psi = \frac{8\pi E}{\Lambda\Gamma^2}, \quad E = \frac{\Gamma\Lambda}{4\pi}\int_{1/\ell}^{\infty} k^2 n_{\mathrm{E}}^{\mathrm{LN}}(k)\mathrm{d}k \tag{3.57}$$

and the Kolmogorov-Zakharov constant was found numerically to be $C_{\mathrm{LN}} = 0.304$ [Bou+11]. Laurie et al. [Lau+10] noticed that wave-action inverse energy cascade prediction 3.55 was marginally non-convergent. In such cases, a logarithmic correction can be introduced and the proposed spectrum for the inverse wave-action cascade by Laurie et al. is

$$n_{\mathrm{N}}^{\mathrm{KS}}(k) = C_{\mathrm{LLNR}}^{N} \frac{(Q\Gamma)^{1/5}}{k^3 \log^{1/5}(\ell k)} \tag{3.58}$$

It is worth mentioning that a third possibility was considered by Vinen [VTM03; Vin05] in which it was argued that weak-wave turbulence prediction might not apply and critical balance should be considered. This prediction is based on the assumption that linear and non-linear terms are comparable and thus no time scale separation exists to apply the weak wave turbulence theory. The critical balance spectrum is given by

$$n_{\mathrm{E}}^{\mathrm{KS}}(k) = C_{\mathrm{CB}}^{E} \ell^{-1} k^{-3}. \tag{3.59}$$

Finally, note that E. Sonin [Son12] claimed that universally should not be expected in the energy spectrum.

The following table summarise the predictions for the KW cascades.

Theory	Direct energy cascade	Inverse wave-action cascade
Kozik-Svistunov	$n_{\mathrm{E}}^{\mathrm{KS}}(k) = C_{\mathrm{KS}}^{E} \Gamma^{2/5} P^{1/5} k^{-17/5}$	$n_{\mathrm{N}}^{\mathrm{KS}}(k) = C_{\mathrm{KS}}^{N} \left(\frac{Q\Gamma}{\Lambda}\right)^{1/5} k^{-3}$
L'vov & Nazarenko (and collaborators)	$n_{\mathrm{E}}^{\mathrm{LN}}(k) = C_{\mathrm{LN}} \frac{P^{1/3}}{\Psi^{2/3} k^{11/3}}$ $\Psi = \frac{2}{\Gamma} \int_{1/\ell}^{\infty} k^2 n_{\mathrm{E}}^{\mathrm{LN}}(k)\mathrm{d}k, \quad C_{\mathrm{LN}} = 0.304$	$n_{\mathrm{N}}^{\mathrm{KS}}(k) = C_{\mathrm{LLNR}}^{N} \frac{(Q\Gamma)^{1/5}}{k^3 \log^{1/5}(\ell k)}$
Vinen	$n_{\mathrm{CB}}(k) = C_{\mathrm{CB}}^{E} \ell^{-1} k^{-3}$	

Table 3.1: Wave turbulence predictions for Kelvin wave cascades. To obtain the corresponding energy spectrum one should multiply by the Kelvin wave dispersion relation $\omega(k) = \frac{\Gamma}{4\pi} \Lambda k^2$.

3.3.4 Numerical simulations of the Kelvin wave cascade

The controversy on the prediction of the Kelvin wave cascade was accompanied by several numerical simulations of models where different approximations were made [KS05; VTM03; BB11; Bou+11]. The main problem is that Biot-Savart simulations are costly, require a delicate regularisation and dissipation is not very well controlled.

Instead of dealing with Biot-Savart, a different approach based on the GP model was used in [Krs12]. There, an almost straight vortex was studied. The novelty of that study is that the vortex line was tracked with a highly accurate method taking advantage of the spectral convergence of pseudo-spectral codes (see Appendix A.1). From the physical point of view, the Gross-Pitaevskii model has the advantage of naturally dissipate energy of vortex waves by emission of sound waves (phonons). Furthermore, vortices are regular structures and there is no need of any cut-off. Although the range of scales was rather limited in [Krs12], a Kelvin wave cascade was indeed observed and the scaling of the wave amplitude spectrum was found in agreement with L'vov & Nazarenko predictions. This work is integrally included at the end of the chapter so it will not be discussed here in detail. It is fair mentioning, that an independent similar work was conducted by another group [PBO13]. This nice coincidence led later to a fruitful collaboration between D. Proment (UEA, Norwich) and myself.

In posterior work, A. Baggaley and J. Laurie [BL14] performed equivalent numerical simulations using the Biot-Savart model where they were able to control and measure accurately the energy dissipation. They found a good agreement with the L'vov & Nazarenko prediction, including the scaling with the energy flux.

3.4 Kelvin wave cascade in quantum turbulence

The theory of the Kelvin wave cascade, discussed in section 3.3.3, is formally derived for an incompressible model in an extremely simplified theoretical setting. One can naturally wonder, why such a theory should be relevant in quantum turbulence, where very complex vortex tangles coexist and interact with phonon waves and other vortices. It is always possible to argue, that at scales smaller than the inter-vortex distance ℓ, quantum vortices can be considered somehow as isolated objects, and thus the theory of weak wave turbulence should apply. Although intuitive, this assumption is far from obvious. At such scales, vortices can also interact with each other through vortex reconnections, changing abruptly their topology. Still, we can always claim that for scales even smaller, vortex reconnections could also be neglected for the Kelvin wave cascade. It was then important, to investigate if the Kelvin wave cascade can be observed in quantum turbulent flows.

Quoting Clark di Leoni et al. [CMB15], studying Kelvin waves in a turbulent vortex tangle is like "looking for a needle in a haystack". In that reference, the authors made use of the spatio-temporal spectra to observe that, despite the fact the flow is turbulent, Kelvin waves propagate along vortices and the Kelvin wave dispersion relation can be glimpsed (among many other things). Then, by performing a space-time filtering of the fields to keep only excitations close to the Kelvin wave branch, a scaling in the energy spectrum compatible with the Kelvin wave cascade prediction was observed.

A different approach was taken by us in Villois et al. [VPK16]. Taking advantage of the powerful vortex tracking algorithm we developed in [Vil+16], we studied the evolution of a vortex tangle by tracking all the vortex lines present in the field. Such study unveiled several interesting physical properties of vortex lines. Here, we only describe the results concerning the Kelvin wave cascade. This work is also integrally included at the end of the chapter. The algorithm developed in [Vil+16], was inspired from the one used in [Krs12] but is able to track with high accuracy any vortex configuration without any prior knowledge of the vortex line geometry. Figure 3.5 sketches the procedure employed in [Vil+16]. The algorithm receives as an input, the complex wave field ψ, then it identifies all nodal lines of the field, and generate a list of three-dimensional filaments $\{\mathbf{s}_1(\zeta), \mathbf{s}_2(\zeta), \ldots\}$. Finally, the longest vortex lines were analysed individually to determine the KW amplitude spectrum (see technical details in the attached publication).

In Villois et al. [VPK16], a Taylor-Green initial condition was generated and evolved under GP dynamics. The initial condition consists on a collection of large scale (almost perfect) vortex rings [NAB97]. The Kelvin wave spectrum of the initial condition is displayed in figure 3.6.a, only the largest scale of the rings are excited. As the system evolves, more and more modes are populated, eventually developing a clear scaling with wave numbers. Figure 3.6.b displays the Kelvin wave amplitude spectra for an equivalent run at larger resolution. The range of scaling extends for almost two decades and it is clearly in favour of the $-11/3$-LN prediction. For completeness, the inset displays the spectrum compensated by the KS and LN predictions.

What is remarkable in 3.6.b is that the range of scales where the KW cascade spectrum is observed extends at scales larger than the inter-vortex distance where Kolmogorov turbulence is known to emerge, here roughly in the range $10^{-2}k\xi - 10^{-1}k\xi$ (energy spectra not shown in this work). The main message of this work, can be thus summarised as follows. In quantum turbulence, we observe at large scales Kolmogorov turbulence. Such classical behaviour with a strong energy cascade, is the result of the collective effect of many vortex lines each of them obeying the physics of a weak wave turbulent cascade. The coexisting of weak and strong cascades, with a myriad of different physical processes, is one of the main characteristics of quantum turbulence.
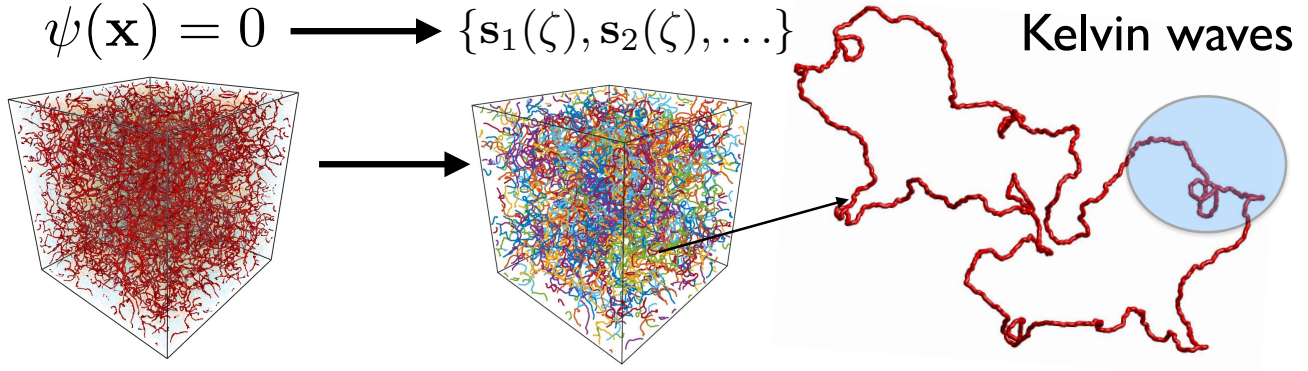
Figure 3.5:   Studying Kelvin waves in turbulent vortex tangle [VPK16]. The vortex tracking algorithm [Vil+16] takes the wave function ψ as an input and output a collection of vortex line $\mathbf{s}_1(\zeta), \mathbf{s}_2(\zeta), \ldots\}$. The figure at the left displays low density iso-surfaces of ψ (in red) and density fluctuations about the bulk values in blueish colours. The middle figure, displays all the lines outputted by the algorithm. The panel at the right, shows one particular vortex ring with Kelvin waves at all scales.
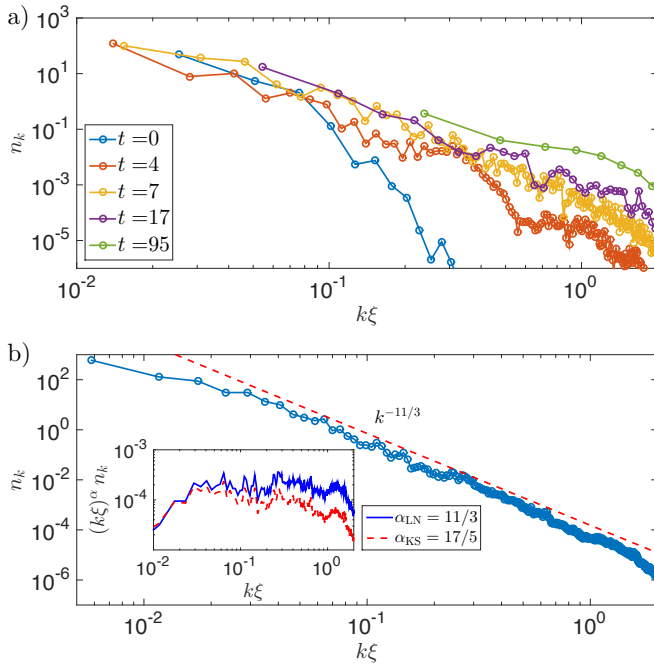

Figure 3.6: Kelvin wave amplitude spectrum of large ring during the decay of quantum turbulence. Figure reproduced from [VPK16] **a)** Temporal evolution of the spectra. **b)** Larger resolution run taken at the time where turbulence is the most active. The inset shows compensated spectra by KS and LN theoretical predictions. ξ is the healing length. Details on the numerics can be found in [VPK16] attached at the end of this chapter.

Tracking the vortex lines of a quantum turbulent tangle is extremely expensive numerically. For this reason, the largest resolution used in [VPK16] was of 512^3 grid points. Whiles it guaranties some scaling in the Kolmogorov rage, it is relatively modest for today's computational capabilities. A different approach could be to apply some "brute-force" and go to much higher resolution numerical simulations. Such an approach was taken in [CMB16; Shu+19], a secondary scaling range somehow compatible with Kelvin wave cascade predictions was observed directly in the incompressible energy spectrum from GP simulations. However, it is not possible to directly apply the wave-turbulence predictions to the case of a three-dimensional turbulent tangle as the predictions for the spectra do not even match dimensionally. In a recent JETP Letters, Eltsov and L'Vov [EL20] discussed the dimensional factors in the wave turbulent cascade and explained how the prediction could be used for experiments. In Müller and Krstulovic [MK20], such considerations were adapted to the case of turbulent vortex tangles. We partially reproduce below the results of [MK20].

We shall consider a three-dimensional vortex tangle, where Kolmogorov energy spectrum takes place between the wave number k_0 (associated to the integral scale of the flux) and the wave number $k_\ell = 2\pi/\ell$. As customary in turbulence, we consider energy per unit of mass. We thus have that the energy flux ϵ that is expressed in units of

$Length^2/Time^3$. We recall here the Kolmogorov prediction

$$E_{K41}(k) = C_K \epsilon^{2/3} k^{-5/3}. \tag{3.60}$$

where C_K is a constant of order one. Note that the energy spectrum has units of $Length^3/Time^2$ that are not the same as in wave turbulence predictions (see discussion at the beginning of section 3.3.3).

In order to compare wave turbulence predictions with measurements of the three-dimensional energy spectrum, one needs to necessarily make some phenomenological considerations. We start by noticing that the total energetic contribution of Kelvin waves can be estimated as $\rho_0 \mathcal{L} \int_{k_{\min}}^{\infty} E_{KW}(k) dk$. Here we replaced the IR cut-off by the largest scale of excited Kelvin waves. We assume that $k_{\min} \sim k_\ell$. In addition, the KW periodicity length of the filament is replaced by the total vortex length of the system as we assume that there are many individual vortex lines ($\sim k_{\min} \mathcal{L}$), and each of them contributes additively to the energy at a given scale. between filaments are neglected. In a turbulent tangle, the total vortex length is related to the mean inter-vortex distance and the volume V of the system by $\mathcal{L} = V\ell^{-2}$. It follows that the mean kinetic energy spectrum per unit of mass is given by $E_{KW}^{\text{tangle}}(k) = E_{KW}(k)\ell^{-2}$. The same reasoning, relates the energy flux P of the Kelvin wave cascade to the global energy flux ϵ of a tangle by $P = \epsilon \ell^2$ [EL20]. In the previous phenomenological considerations, we have made the assumption that the energy flux is the same in the Kolmogorov range than in the Kelvin wave cascade. This strong assumption might be questioned as energy could be already dissipated into sound by vortex reconnections at different scales diminishing this value [VPK20; PK20c]. Such extra sinks of energy are difficult to quantify and will not be taken into account.

Taking into account the previous considerations, the LN energy spectrum becomes

$$E_{KW}(k) = C_{LN}^{3/5} \frac{\Gamma \Lambda \epsilon^{1/3} \ell^{-4/3}}{\tilde{\Psi}^{2/3} k^{5/3}}, \quad \tilde{\Psi} = \frac{(12\pi)^{3/5} (\epsilon \ell^2)^{1/5}}{\Gamma^{3/5} k_\ell^{2/5}} \tag{3.61}$$

Note that the value of the constant $C_{LN} = 0.304$ can not be expected to still be exact after all the previous phenomenological assumptions.

In the work [MK20], we performed high-resolution numerical simulations of a generalised GP equation, intended to be a better model of superfluid helium, and observed a very clear Kolmogorov range followed by a secondary $k^{-5/3}$ scaling. It is reproduced in figure 3.7.a. Figure 3.7.b displays the incompressible
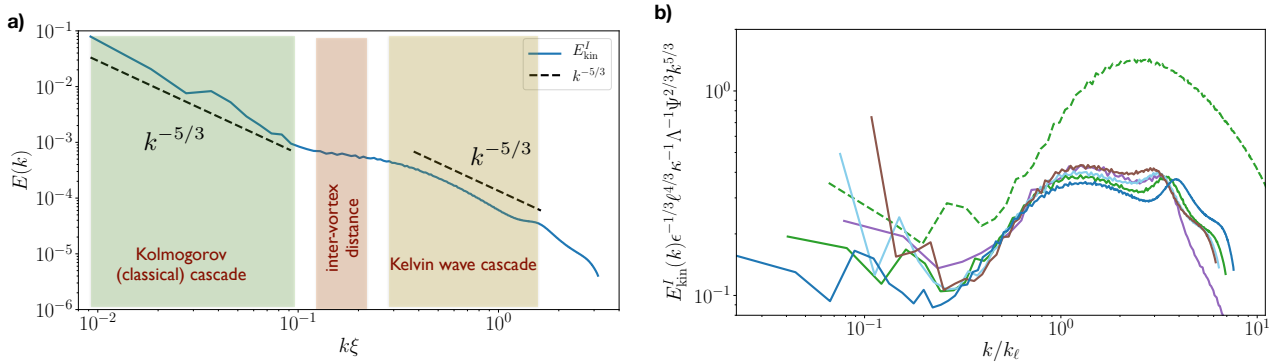
Figure 3.7: **a)** Incompressible kinetic energy spectrum of decaying quantum turbulence from a GP simulation [MK20]. The different scaling ranges and the $k^{-5/3}$ scaling are displayed in the figure. **b)** Compensated energy spectrum by prediction (3.61). Different curves correspond to runs performed with different values of the flux, inter-vortex distance and integral scale.

kinetic energy spectrum compensated by the LN Kelvin wave cascade prediction (without considering the constant C_{LN}). Several runs having different values of the flux, inter-vortex distance and healing length are plotted together presenting a relatively good collapse. For more details, the interested reader is referenced to [MK20].

3.5   Selected publications

In this chapter we integrally include two selected publications where I have contributed to the problem of Kelvin waves. Both publications have already been mentioned in this chapter.

- Giorgio Krstulovic. "Kelvin-Wave Cascade and Dissipation in Low-Temperature Superfluid Vortices". In: *Physical Review E* 86.5 (Nov. 9, 2012), p. 055301. ISSN: 1539-3755, 1550-2376. DOI: 10.1103/PhysRevE.86.055301

- Alberto Villois, Davide Proment, and Giorgio Krstulovic. "Evolution of a Superfluid Vortex Filament Tangle Driven by the Gross-Pitaevskii Equation". In: *Physical Review E* 93.6 (June 30, 2016), p. 061103. ISSN: 2470-0045, 2470-0053. DOI: 10.1103/PhysRevE.93.061103

The first publication considers Kelvin waves in an almost straight vortex. This work corresponds to the first direct measurement of the Kelvin wave cascade in the the framework of the Gross-Pitaevskii model. The second publication discusses the evolution of a vortex tangle driven by the GP model. In particular, in addition to the Kelvin wave cascade of large rings extracted from the tangle, the Vinen decay law [Don91] was also clearly observed.

Kelvin-wave cascade and dissipation in low-temperature superfluid vortices

Giorgio Krstulovic

*Laboratoire Lagrange, UMR7293, Université de Nice Sophia-Antipolis, CNRS, Observatoire de la Côte d'Azur,
B.P. 4229, 06304 Nice Cedex 4, France*

We study the statistical properties of the Kelvin waves propagating along quantized superfluid vortices driven by the Gross-Pitaevskii equation. No artificial forcing or dissipation is added. Vortex positions are accurately tracked. This procedure directly allows us to obtain the Kevin-wave occupation-number spectrum. Numerical data obtained from long time integration and ensemble average over initial conditions support the spectrum proposed in L'vov and Nazarenko [JETP Lett. **91**, 428 (2010)]. Kelvin-wave modes in the inertial range are found to be Gaussian as expected by weak-turbulence predictions. Finally the dissipative range of the Kelvin-wave spectrum is studied. Strong non-Gaussian fluctuations are observed in this range.

Superfluid turbulence has been the subject of many experimental and theoretical works for the last decades. It is now possible to realize turbulent Bose-Einstein condensates (BECs) [1], turbulent flows with ^{3}He [2,3], and visualize vortices in ^{4}He [4]. As in classical turbulence [5], a Kolmogorov energy cascade has been observed experimentally and numerically. In superfluids, this takes place at scales larger than the mean intervortex distance ℓ [6–8]. At low temperature, when damping due to mutual friction is negligible, it is believed that dissipation at small scales is carried by phonon radiation which dissipates energy into heat [9]. At scales smaller than ℓ the energy is transferred down by a series of reconnection processes of quantized vortices that excite waves on the filaments. These perturbations, called Kelvin waves (KWs), are known for more than one century [10] in fluid dynamics. These waves obey a set of nonlinear equations where the energy is transferred towards small scales by a wave-turbulence cascade. The energy distribution along different scales is crucial for the understanding of the dissipative processes in superfluids. The energy spectrum of such a cascade is not yet fully determined, except in the limit of small-amplitude KWs, where the theory of weak turbulence is applicable [11]. However, a heated debate on the locality of KW energy transfer has taken place in the last years [12–17]. Two different groups, Kozik and Svistunov [18] and L'vov and Nazarenko [19], starting from the very same equations and by using the same theory, have derived two different spectra (hereafter KS and LN spectra, respectively). The origin of this controversy is mainly due to a symmetry argument by KS (tilt of a vortex line) that eventually leads to a vanishing vertex in the perturbative expansion. This leads to locality in the energy transfer and makes the six-wave interaction theory realizable. The energy spectrum found by KS is

$$E_{KS}(k) \sim \epsilon^{1/5}\kappa^{7/5}k^{-7/5}, \tag{1}$$

where ϵ is the energy flux, κ is the circulation quantum, and k is the wave vector. This symmetry argument was questioned by LN and they claimed that the energy transfer is nonlocal. They derived an effective four-wave interaction theory that leads to the energy spectrum

$$E_{LN}(k) \sim \kappa\epsilon^{1/3}\Psi^{-2/3}k^{-5/3}, \tag{2}$$

where $\Psi \sim (1/\kappa)\int E_{LN}(k)dk$ is the mean-square angular deviation of the vortex. For more technical details on the controversy see [13–17]. The exponent $7/5 = 1.4$ and $5/3 \approx 1.67$ of (1) and (2) are supposed to be universal, but their relatively close values makes it difficult to numerically elucidate which theory is correct. A number of numerical works supporting both theories have been published but none presenting strong arguments to settle this controversy [17,20,21]. These works are all done in the framework of the vortex filament with an *ad hoc* dissipative mechanism. In the case of strong wave turbulence, when the local slope of KW is order 1, weak turbulence breaks down and Vinen *et al.* [22] propose a spectrum scaling as k^{-1}. Finally, It was suggested by Sonin [16] that no universality can be expected.

In this Rapid Communication, we address the small-amplitude KW cascade problem by performing direct numerical simulations of the Gross-Pitaevskii equation (GPE). The GPE describes a weakly interacting BEC at low temperature. It is also expected to at least qualitatively reproduce the dynamics of superfluid helium. As the Gross-Pitaevskii (GP) vortices can naturally radiate and excite phonons no artificial dissipation is needed. The (1D) KW occupation-number spectrum is precisely obtained and data are found to support the wave-turbulence prediction (LN) [19]. The KW spectrum is analyzed within the dissipative range and an exponential decay is found. Finally, the probability distribution function (PDF) of KW amplitudes is observed to be Gaussian in the inertial range in contrast with the power-law tails observed for modes in the dissipative range.

The GPE describing a homogeneous BEC of volume V with wave function ψ is given by

$$i\hbar\frac{\partial\psi}{\partial t} = -\frac{\hbar^2}{2m}\nabla^2\psi + g|\psi|^2\psi, \tag{3}$$

where m is the mass of the condensed particles and $g = 4\pi a\hbar^2/m$, with a the s-wave scattering length. Equation (3) conserves the energy $H = \int(\frac{\hbar^2}{2m}|\nabla\psi|^2 + \frac{g}{2}|\psi|^4)d\mathbf{x}$ and the number of particles $N = \int|\psi|^2 d\mathbf{x}$. Madelung's transformation $\psi(\mathbf{x},t) = \sqrt{\frac{\rho(\mathbf{x},t)}{m}}\exp[i\frac{m}{\hbar}\phi(\mathbf{x},t)]$ relates the wave function ψ to a superfluid of density $\rho(\mathbf{x},t)$ and velocity $\mathbf{v} = \nabla\phi$, where $\kappa = h/m$ is the Onsager-Feynman quantum of velocity circulation around the $\psi = 0$ vortex lines. When Eq. (3) is

TABLE I. List of runs. $N_\perp$ and N_z are the resolutions in the perpendicular and parallel directions with respect to the vortex. $N_{\rm rea}$ is the number of realizations. n is the number of initial KW modes and m is the exponent k^{-m} of the KW spectrum.

Run	$N_\perp$	N_z	$N_{\rm rea}$	n	ξ	A	m
I	256	128	31	3	0.025	2ξ	3.85 ± 0.24
II	256	128	31	2	0.025	4ξ	3.682 ± 0.13
III	256	256	11	2	0.025	4ξ	3.753 ± 0.17
IV	512	256	1	2	0.0125	4ξ	4.116 ± 0.56
V	128	512	11	2	0.1	4ξ	

linearized around a constant $\psi = \hat{\psi}_0$, the sound velocity is given by $c = (g|\hat{\psi}_0|^2/m)^{1/2}$ with dispersive effects taking

place at length scales smaller than the coherence length $\xi = (\hbar^2/2m|\hat{\psi}_0|^2 g)^{1/2}$ that also corresponds to the vortex core size. In this Rapid Communication the density $\rho \equiv mN/V = 1$ and the physical constants are determined by the values of ξ and $c = 2$. Numerical integration of Eq. (3) is performed in a cubic box of length $V^{1/3} = 2\pi$ by using a standard pseudospectral code with an exponential time-splitting temporal scheme (see Table I). Ensemble averaging is done over 30 initial conditions.

To address the KW problem, an array of four alternate-sign vortices is used. To obtain a clean initial condition and reduce initial phonon emission, in a first step, an exact stationary solution of the GPE with straight vortices is numerically obtained by a Newton method [23]. Vortices are separated by a distance π and can be considered isolated when $\xi \to 0$, as the
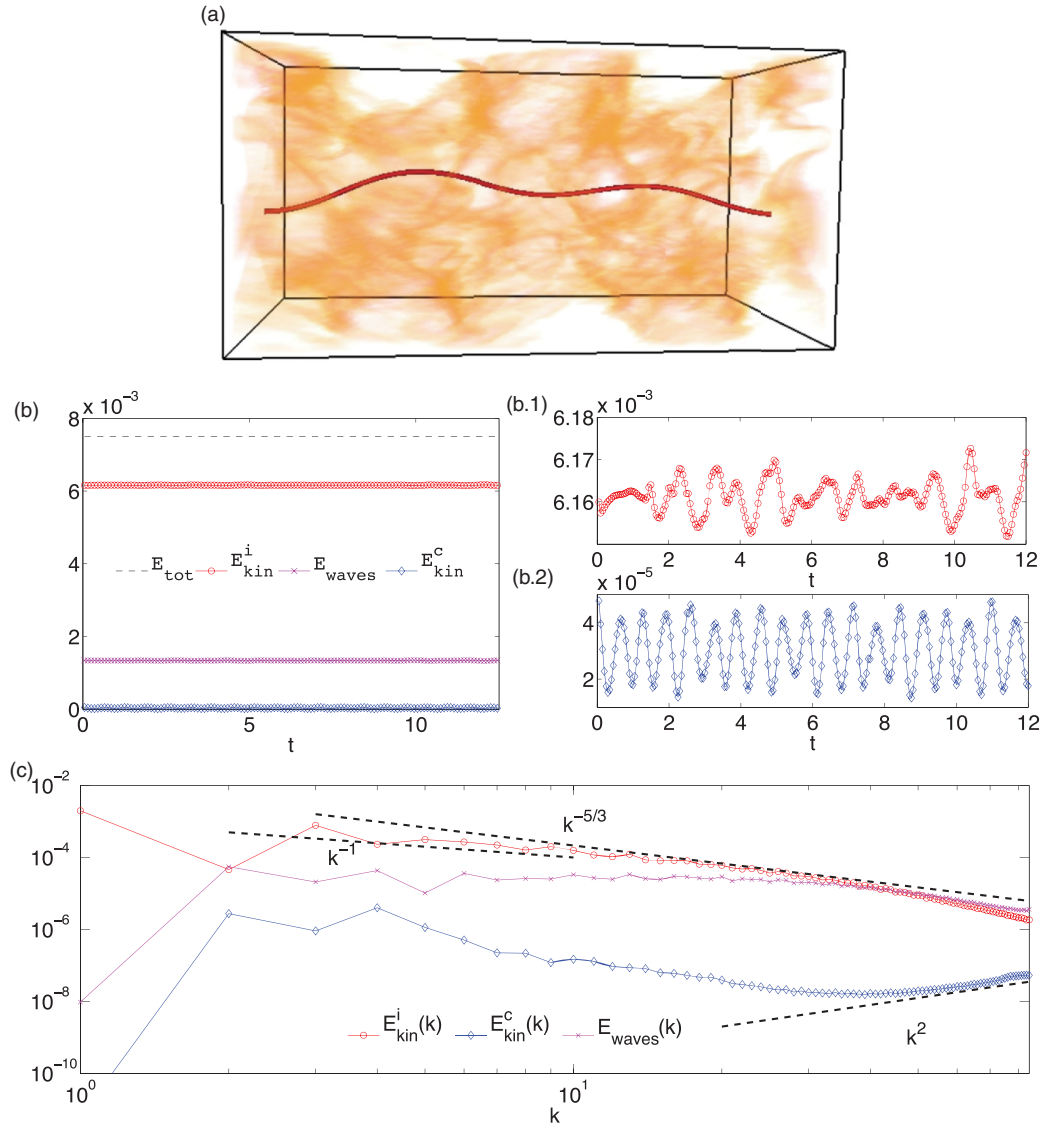
FIG. 1. (Color online) (a) 3D visualization of the density $|\psi|^2$ in the sub-box $[0,\pi]^2 \times [0,2\pi]$. In red an isosurface of the vortex and a (orange) density plot shows sound waves. (b) Temporal evolution of energies. (b.1), (b.2) Zoom of $E_{\rm kin}^i$ and $E_{\rm kin}^c$, respectively. (c) Incompressible-kinetic, compressible-kinetic, and wave energy spectra. Dashed lines display k^2, k^{-1}, and $k^{-5/3}$ power-law scalings.

resolution is increased. Then, a KW is introduced perturbing the vortex. It reads

$$x(z) = A \sum_{i=1}^{n} \cos\left(i\,z + \phi_i^x\right), \quad y(z) = A \sum_{i=1}^{n} \cos\left(i\,z + \phi_i^y\right),$$

(4)

where $\phi_i^{\{x,y\}}$ are random phases. A visualization of the the density $\rho(\mathbf{x})$ is displayed in Fig. 1(a) at $t = 10$. The KW is observed with the (red) isosurface. Phonon waves correspond to the (orange) cloud that is a density plot of $\rho(x)$ in a narrow threshold centered around the mean-density value $\rho = 1$. In superfluid turbulence, interaction and reconnection between vortices can influence KW propagation. Here such effects are neglected. To quantify the vortical and wave energy of the configuration, we use the standard hydrodynamic energy decomposition, obtained by using the Madelung transformation (see [24] for details). The total energy is thus decomposed in two terms: the incompressible-kinetic energy E_{kin}^i containing the contribution of vortical structures and the energy of phonon waves $E_{\text{wav}} = E_{\text{kin}}^c + E_{\text{int}} + E_q$, where E_q, E_{int}, E_{kin}^c, are the quantum, internal, and compressible-kinetic energy, respectively. Figure 1(b) displays the temporal evolution of E_{kin}^i, E_{kin}^c, E_{wav}, and $E_{\text{tot}} = E_{\text{kin}}^i + E_{\text{wav}}$. Observe in Fig. 1(b) that their temporal evolution rapidly reaches a (quasi)statistical stationary regime. The same energy decomposition can be applied to the energy spectra that are displayed on Fig. 1(c) at $t = 10$. The energy spectrum of the compressible-kinetic energy presents at large wave numbers a k^2-equipartition regime. This range is also present in the initial condition albeit with smaller values. It rapidly reaches the stationary state observed in Fig. 1(c) showing that thermalized waves coexist with vortices. As $E_{\text{wav}} \ll E_{\text{kin}}^i$, the large-scale GPE dynamics is mainly driven by vortices setting a clean configuration.

The energy spectra displayed in Fig. 1(c) present a k^{-1} scaling at small k; this can be associated with decaying of the velocity field of an isolated vortex at long distances [24,25]. At an intermediate range a scaling compatible with $k^{-5/3}$, however, it cannot be associated with Kolmogorov turbulence as the scale separation $V^{1/3} \gg \ell$ is not realized (here $V^{1/3} \sim \ell$). Note that a $k^{-5/3}$ has been also observed in a situation where the Kolmogorov regime is not clear to be applicable [25]. The scaling could be explained by the presence of a KW cascade and predictions (1) or (2), as the principal contribution to energy of the fluid (see Fig. 1) is coming from vortices. However, the relationship between the KW spectrum and 3D (hydrodynamical) energy spectra is not clearly established. To explicitly study the KW cascade, we numerically track the coordinates $(x(z), y(z))$ of the vortex. For each value of z the equation $\psi(x(z), y(z)) = 0$ is solved by using a Newton method. Derivatives of the fields at intermesh points are obtained by Fourier interpolation. This allows us to accurately obtain the vortex coordinates with a precision much larger than the one given by the mesh size. Once the coordinates are obtained, it is possible to compute (1D) KW occupation-number spectrum defined by

$$n(k) = |\hat{w}(k)|^2 + |\hat{w}(-k)|^2,$$

(5)

where $\hat{w}(k)$ is the Fourier transform of $w(z) = x(z) + iy(z)$. The KW spectrum allows us to construct the KW energy $E_{\text{KW}} = \sum_k \omega(k)n_k$ and the dissipation $\epsilon = -dE_{\text{KW}}/dt$, where $\omega(k)$ is the KW dispersion relation. It can be approximated by $\omega(k) = C(\kappa/4\pi)k^2$, where C is a numerical constant which eventually depends logarithmically on ξ/ℓ. Figures 2(a) and 2(b) show the temporal evolution of the total vortex length $L = \int \sqrt{1 + |\partial_z w(z)|^2}dz$ and the mean curvature $K = \int |\partial_z w(z) \times \partial_{zz} w(z)|/|\partial_z w(z)|^3 dz$, normalized by their initial values. Note that their temporal fluctuations are small. Finally, in Fig. 2(b) the temporal evolution of the KW
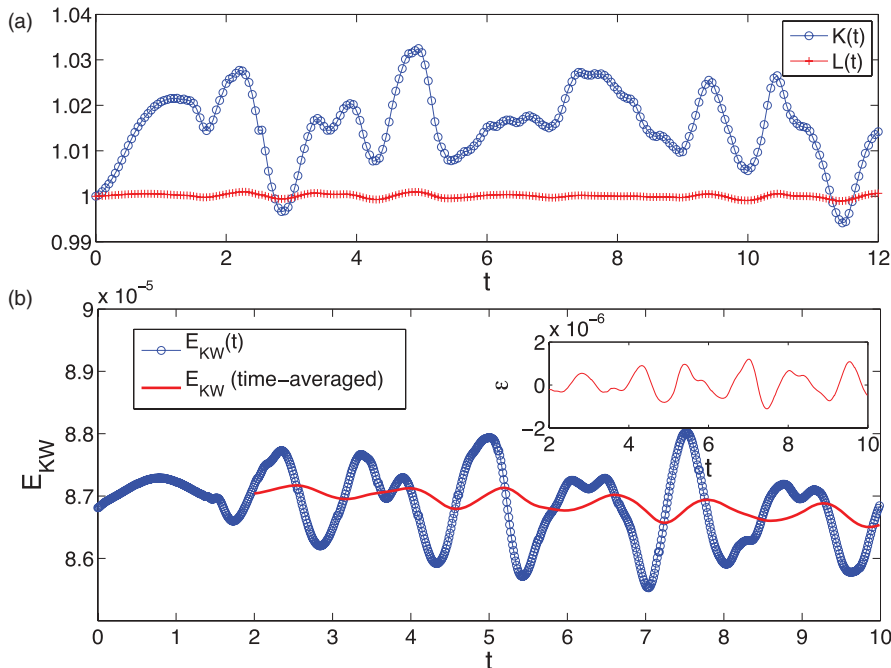

FIG. 2. (Color online) (a) Vortex length $L(t)$ (blue circles) and curvature $K(t)$ (red crosses) normalized by $L(0) = 6.51$ and $K(0) = 0.44$. (b) KW energy $E_{\text{KW}}(t)$ (circles). The (red) solid line displays $E_{\text{KW}}(t)$ averaged over temporal windows of width $\Delta t = 2$. Inset: energy dissipation ϵ.

energy is displayed. Note that the energy fluctuates, especially after the arrival of phonon waves coming from neighboring cells at $t \sim \pi/c \approx 1.5$. The solid (red) line presents the energy averaged over temporal windows of width $\Delta t = 2$; the decrease in energy is apparent. The inset of Fig. 2(b) displays temporal evolution of the energy dissipation showing also some negative values. This can be related to the presence of phonon waves that excite KW at small scales. Its temporal average is positive as more energy is radiated than absorbed by the vortex.

We now turn to the KW spectrum. Two kinds of simulations are presented: the first trying to enhance the scale separation between $V^{1/3}$ and ξ and thus obtaining a larger inertial range; the second concerns the dissipative range of the KW spectrum and then presents a large number of modes between ξ and smallest resolved scale $V^{1/3}/N_z$. Details of runs are listed in Table I.

Let us focus now on the inertial range of the KW cascade. The two KS and LN predictions for $n(k)$ read

$$n_{KS}(k) = \frac{4\pi C_{KS}\kappa^{2/5}\epsilon^{1/5}}{k^{17/5}}, \quad n_{LN}(k) = \frac{4\pi C_{LN}\epsilon^{1/3}}{\Psi^{2/3}k^{11/3}}, \quad (6)$$

where C_{KS} and C_{LN} are numerical constants. The temporal evolution of the KW spectrum is displayed in Fig. 3(a) for run III. KW are rapidly exited, and populate all wave numbers. At low wave numbers an excess of energy is observed. For Bose gases, a wave-turbulence energy transport to large scales was reported in [26]; here for KW, data do not allow to clearly observe such a behavior. When energy arrives to scales small enough to be efficiently dissipated, a steep decay zone called dissipative range in hydrodynamic turbulence [5] is observed. As dissipation by phonon emission is very weak [27], the spectrum stabilizes and a clear inertial range is observed. For all modes the amplitude of KW remains small; it is thus expected that weak-turbulence theory applies for wave numbers such that $V^{-1/3} \ll k \ll 2\pi/\xi$. Temporal-averaged KW spectrum of runs I–IV are displayed in Fig. 3(b). A power-law scaling is clearly appreciated for almost one decade.

The exponent m, obtained from a fit k^{-m}, is shown on Table I with their respective errors.

For all runs the exponent is slightly larger than the one predicted by the two weak-turbulence results (6) and presents a variation of 5%. However, for all runs data support the exponent $-5/3 - 2$ predicted by LN, that it is within errors, and excludes the $-7/5 - 2$ KS prediction. Note that although the power-law range extends until near $1/\xi$, where dissipation can start to play a role, the exponent m is stable for the different runs. Experimentally, one usually has access only to the (3D) kinetic energy, that for small amplitude KW is dominated by the singularity of the velocity at the vortex core. However, a singularity cannot transfer energy and the KW cascade is thus crucial for understanding low-temperature dissipative mechanisms of superfluids.

We now turn to the dissipative range of the KW spectrum, that takes place at wave numbers larger than $k_\xi = 2\pi/\xi$. For such small scales it is known that dispersive effects of phonon waves slow down the dynamics producing a bottleneck and quasithermalization [28]. This effect was observed for large values of ξk_{max}, where k_{max} is the largest wave number. A natural question is can this slowdown affect the dissipative mechanism of the KW cascade? If excitations of high-wave-number phonons are difficult, one could expect that dissipation of KW by sound emission should be reduced at such scales. To investigate such a configuration we have performed simulations with a large value of $\xi k_{max} = 17$ (run V). For such a configuration, the inertial range of the KW cascade is not clearly identified in Fig. 4(a). At very early times, KWs stop to be populated at wave numbers larger than $k_\xi \sim 60$ displaying an equipartition of KW spectrum followed by a faster than exponential decay for $k > k_\xi$. Unlike, the 3D dispersive bottleneck, this behavior does not last long and the statistics of KW modes in this range is not Gaussian. At later times, the equipartition range is destroyed and a large-k exponential decay of rate $2\delta(t)$ [see Fig. 4(a)] is observed.

Finally we study the statistics of KW amplitudes in the inertial and dissipative range. The PDF of KW amplitudes
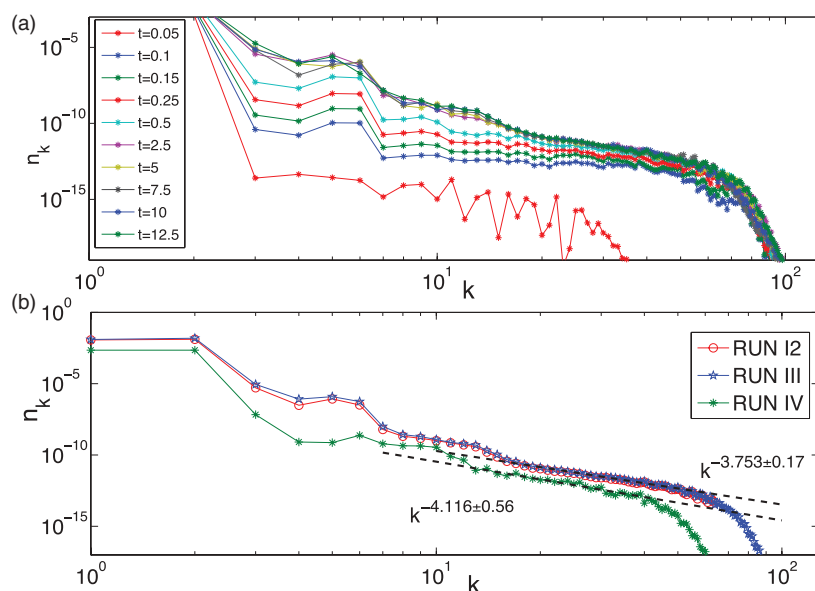

FIG. 3. (Color online) (a) Temporal evolution of KW spectrum, run III. (b) Time-averaged KW spectra, runs I–V. Dashed line displays the power-law fits.
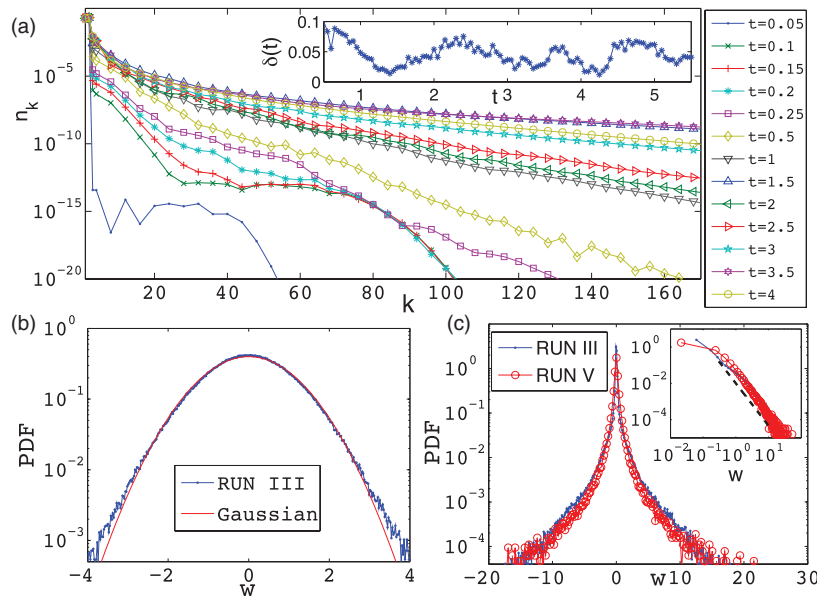
FIG. 4. (Color online) (a) Temporal evolution of KW spectrum for run V. Inset: temporal evolution of the exponential decay rate $\delta(t)$. (b) PDF of KW amplitudes in the inertial range $20 < k < 40$ (run III). (c) PDF of KW amplitudes in the dissipative range $80 < k < 100$ (run III) and $30 < k < 170$ (run V). Inset: same PDF in log-log, the power law $w^{-7/3}$ is drawn for reference.

varying at scales inside the inertial range for run III is obtained by filtering in Fourier space and keeping modes in the range $20 < k < 40$. The normalized PDF is displayed in Fig. 4(b). The quasi-Gaussian behavior is manifest as expected from weak turbulence predictions. $|w(z)|^2$ consequently presents exponential tails. In the dissipative range (for $80 < k < 100$) the PDF shows a strong non-Gaussian character as apparent in Fig. 4(c). Better statistics are obtained for run V. The PDF has power-law tails as shown in the inset of Fig. 4(b) and present, as in turbulent flows, an asymmetry of skewness $\langle w^3 \rangle / \langle w^2 \rangle^{2/3} = -0.15$. Recently, in Biot-Savart simulations [29], a crossover between Gaussian and non-Gaussian statistics was found in the velocity field at the mean intervortex scale ℓ. Here, for KWs, the crossover takes place at the scale $\xi \ll \ell$. At scales smaller than ξ, KWs are somehow decoupled of the large-scale dynamics prescribed by wave turbulence and are in direct interaction with a strongly fluctuating superfluid velocity field, as the one found in the GP simulations of Ref. [30], and hence inherit some properties of the surrounding fluid.

The behavior of KWs at very small scales is important at low temperature where mutual friction is absent. In all vortex-filament models, some small-scale artificial dissipation is needed to avoid energy pileup. Although vortex-filament models are not concerned with such small scales, how the energy is dissipated in those models can affect the vortex dynamics. It would be important to check if the dissipative mechanisms used are consistent with dissipation produced by phonon radiation. A natural extension of this work is to include thermal waves and vortex interaction by using the projected GPE, where mutual friction effects are present [31].

[1] E. A. L. Henn J. A. Seman, G. Roati, K. M. F. Magalhaes, and V. S. Bagnato, Phys. Rev. Lett. **103**, 045301 (2009).

[2] D. I. Bradley, S. N. Fisher, A. M. Guénault, R. P. Haley, G. R. Pickett, D. Potts, and V. Tsepelin, Nat. Phys. **7**, 473 (2011).

[3] V. Eltsov *et al.*, Phys. Rev. Lett. **99**, 265301 (2007).

[4] G. P. Bewley, D. P. Lathrop, and K. R. Sreenivasan, Nature (London) **441**, 588 (2006).

[5] U. Frisch, *Turbulence: The Legacy of A. N. Kolmogorov* (Cambridge University Press, Cambridge, 1995).

[6] J. Maurer and P. Tabeling, Europhys. Lett. **43**, 1 (1998).

[7] C. Nore, M. Abid, and M. E. Brachet, Phys. Rev. Lett. **78**, 3896 (1997).

[8] J. Yepez, G. Vahala, L. Vahala, and M. Soe, Phys. Rev. Lett. **103**, 084501 (2009).

[9] W. F. Vinen and J. J. Niemela, J. Low Temp. Phys. **128**, 167 (2002).

[10] W. Thompson (Lord Kelvin), Philos. Mag. **10**, 155 (1880).

[11] V. Zakharov, V. Lvov, and G. Falkovich, *Kolmogorov Spectra of Turbulence I—Wave Turbulence* (Springer-Verlag, Berlin, 1992).

[12] J. Laurie, V. S. Lvov, S. Nazarenko, and O. Rudenko, Phys. Rev. B **81**, 104526 (2010).

[13] V. V. Lebedev and V. S. L'vov, J. Low Temp. Phys. **161**, 548 (2010).

[14] E. V. Kozik and B. V. Svistunov, J. Low Temp. Phys. **161**, 603 (2010).

[15] V. V. Lebedev, V. S. L'vov, and S.V. Nazarenko, J. Low Temp. Phys. **161**, 606 (2010).

[16] E. B. Sonin, Phys. Rev. B **85**, 104516 (2012).

[17] L. Boué, R. Dasgupta, J. Laurie, V. L'vov, S. Nazarenko, and I. Procaccia, Phys. Rev. B **84**, 064516 (2011).

[18] E. V. Kozik and B. V. Svistunov, Phys. Rev. Lett. **92**, 035301 (2004).

[19] V. S. L'vov and S.V. Nazarenko, J. Low Temp. Phys. **36**, 785 (2010).

[20] E. V. Kozik and B. V. Svistunov, Phys. Rev. Lett. **94**, 025301 (2005).

[21] A. W. Baggaley and C. F. Barenghi, Phys. Rev. B **83**, 134509 (2011).

[22] W. F. Vinen, M. Tsubota, and A. Mitani, Phys. Rev. Lett. **91**, 135301 (2003).

[23] C. Huepe and M. Brachet, Physica D **140**, 126 (2000).

[24] C. Nore, M. Abid, and M. Brachet, Phys. Fluids **9**, 2644 (1997).

[25] B. Nowak, J. Schole, D. Sexty, and T. Gasenzer, Phys. Rev. A **85**, 043627 (2012).

[26] J. Schole, B. Nowak, and T. Gasenzer, Phys. Rev. A **86**, 013624 (2012).

[27] G. Krstulovic, M. Brachet, and E. Tirapegui, Phys. Rev. E **78**, 026601 (2008).

[28] G. Krstulovic and M. Brachet, Phys. Rev. Lett. **106**, 115303 (2011).

[29] A. W. Baggaley and C. F. Barenghi, Phys. Rev. E **84**, 067301 (2011).

[30] A. C. White, C. F. Barenghi, N. P. Proukakis, A. J. Youd, and D. H. Wacks, Phys. Rev. Lett. **104**, 075301 (2010).

[31] G. Krstulovic and M. Brachet, Phys. Rev. E **83**, 066311 (2011).

Evolution of a superfluid vortex filament tangle driven by the Gross-Pitaevskii equation

Alberto Villois and Davide Proment

School of Mathematics, University of East Anglia, Norwich Research Park, Norwich NR4 7TJ, United Kingdom

Giorgio Krstulovic

Laboratoire J.L. Lagrange, UMR7293, Université de la Côte d'Azur, CNRS, Observatoire de la Côte d'Azur,
Boîte Postale 4229, 06304 Nice Cedex 4, France

The development and decay of a turbulent vortex tangle driven by the Gross-Pitaevskii equation is studied. Using a recently developed accurate and robust tracking algorithm, all quantized vortices are extracted from the fields. The Vinen's decay law for the total vortex length with a coefficient that is in quantitative agreement with the values measured in helium II is observed. The topology of the tangle is then investigated showing that linked rings may appear during the evolution. The tracking also allows for determining the statistics of small-scale quantities of vortex lines, exhibiting large fluctuations of curvature and torsion. Finally, the temporal evolution of the Kelvin wave spectrum is obtained providing evidence of the development of a weak-wave turbulence cascade.

The full understanding of turbulence in a fluid is one of the oldest yet still unsolved problems in physics. A fluid is said to be turbulent when it manifests excitations occurring at several length scales. Due to the large number of degrees of freedom and the nonlinearity of the governing equations of motion, the problem is usually tackled statistically by introducing assumptions and closures in terms of correlators. This is the case in the seminal work of Kolmogorov in 1941 based on the idea of Richardson's energy cascade, where energy in classical fluids is transferred from large to small scales [1].

Superfluids form a particular class among fluids characterized essentially by two main ingredients: the lack of dissipation and the evidence that vortex circulation takes only discrete values that are multiples of the quantum of circulation [2]. Superfluid examples are superfluid liquid helium (He II) and Bose-Einstein condensates (BECs) made of dilute alkali-metal gases. Here the superfluid phase is usually modeled via a complex field describing the order parameter of the system and vortices appear as topological defects where the superfluid density vanishes.

In three spatial dimensions those defects organize themselves into closed lines (or even open lines at the boundaries if confining sides are considered) of different configurations. Any vortex line point induces a velocity field which affects the motion of any object in the system including the vortex line itself. In general, even for a single closed vortex line, the dynamics are chaotic and the problem does not have analytical solutions. Superfluid turbulence regards the study of the evolution of many vortex lines, a tangle, which induce velocity field gradients in the fluid at several length scales.

Different mathematical models have been devised to mimic the dynamics of a superfluid. An example is the vortex filament (VF) model based on the Biot-Savart law that relates vorticity and velocity [3]. This model is able to mimic the dynamics of dense vortex tangles due to a relatively fast numerical integration technique [4]. The VF model implicitly assumes that the superfluid density is constant everywhere and the vortex structure is a line with vanishing core. This assumption is generally satisfied in He II where the characteristic experimental setup sizes, and consequently the largest scales

of the motion, are order of 10^{-1} m and the vortex core is of the order of 1 Å $= 10^{-10}$ m. Moreover, since He II is in its liquid phase, the compressibility effects can be usually neglected. However, the VF model fails to describe vortex reconnections. These are rapid changes in the topology of the vortex configuration which occur naturally in a superfluid [5] and are one of the main mechanisms responsible for the energy transfer. Reconnections are thus introduced by some *ad hoc* mechanism.

Another superfluid model that admits quantized vortices and inherently possesses vortex reconnections is the Gross-Pitaevskii (GP) equation that describes the evolution of the superfluid order parameter ψ. In contrast to the VF model, the GP equation allows density fluctuations in terms of phonons and density depletion at the vortex cores. Although it has been formally derived as a mean-field theory for a dilute boson gas in the limit of zero temperature [6], it also qualitatively reproduces He II dynamics. The vortex core size here is of the order of the healing length ξ, the only intrinsic characteristic length scale of the model; nowadays experimental techniques are able to create BEC setups that are 10^1–10^2 healing lengths where superfluid turbulence can develop [7]. In turbulent superfluids, vortices constantly rearrange themselves following reconnections into complex tangles with nontrivial geometrical, algebraic, and topological properties [8]. At small scales, helical excitations of vortex lines known as Kelvin waves (KWs) are believed to be the ultimate mechanism of energy dissipation via phonon emission [9]. To study such dynamics, the GP equation has the advantage that no extra modeling is needed (unlike the VF model). However, GP does not provide direct information on vortices.

In this work we apply a numerical algorithm [10] to accurately track the configuration of a turbulent vortex tangle evolving according to the GP model. First, we show that after the onset of turbulence, the vortex line density satisfies the Vinen's decay law [11] with a coefficient that is in agreement with the values measured in He II. Different algebraic and topological quantities of the tangle are then measured. The tracking allows for obtaining curvature and torsion distributions of the vortex tangle. Finally, we perform a direct measurement of

KWs during the dynamics and compute a KW spectrum that appears to be consistent with L'vov-Nazarenko's weak-wave turbulence theoretical prediction [12].

The GP model for the condensate wave function ψ is

$$i\hbar\frac{\partial\psi}{\partial t} = -\frac{\hbar^2}{2m}\nabla^2\psi + g|\psi|^2\psi, \tag{1}$$

where m is the mass of the bosons and $g = 4\pi a\hbar^2/m$, with a the s-wave scattering length. Madelung's transformation $\psi(\mathbf{x},t) = \sqrt{\rho(\mathbf{x},t)/m}\exp[i\frac{m}{\hbar}\phi(\mathbf{x},t)]$ relates the wave function ψ to a superfluid of density $\rho(\mathbf{x},t)$ and velocity $\mathbf{v} = \nabla\phi$. The quantum of circulation about the $\psi = 0$ vortex lines is $\Gamma = h/m$. When Eq. (1) is linearized about a constant value $\psi = \hat{\psi}_0$, the sound velocity is given by $c = (g|\hat{\psi}_0|^2/m)^{1/2}$, with dispersive effects taking place at length scales smaller than the healing length $\xi = (\hbar^2/2m|\hat{\psi}_0|^2 g)^{1/2}$.

In the simulations presented here, the mean density is fixed to the unity and the physical constants in Eq. (1) are determined by the values of ξ and $c = 1$. The quantum of circulation results in $\Gamma = 4\pi c \xi/\sqrt{2}$. Numerical integration of Eq. (1) is performed using a standard pseudospectral code. We integrate an initial condition characterized by the so-called Taylor-Green flow [13], a well-studied flow in superfluid turbulence. Symmetries are not enforced during the evolution and we use resolutions of 256^3 and 512^3 uniformly distributed collocation points with $\xi = 2\pi/256$ and $\xi = 2\pi/512$, respectively. Mirror symmetries are broken during the evolution although traces of such symmetries will be present even at very large times. With units used in this work, the large eddy turnover time is of the order of the unity.

The Taylor-Green flow initially contains a configuration of unstable large-scale rings that develop to create a turbulent tangle. Vortices can be spotted by plotting the low-value isosurfaces of the density field as displayed in Fig. 1. Low-density regions corresponding to vortex lines are plotted in red, while density fluctuations (sound) are rendered in light blue. The initial condition is visualized in Fig. 1(a), the complex turbulent tangle at $t = 12$ in Fig. 1(c), and the final state at $t = 105$, where few vortices are present with a lot of sound in the background, in Fig. 1(e). We track the vortex lines with a recently developed algorithm [10] that allows for identifying separately each single line forming the tangle. Vortex lines are followed using the pseudo-vorticity field as in [14] and the exact vortex positions are obtained by applying a Newton-Raphson method. The algorithm is robust and accurate as it takes full advantage of the spectral resolution. The intermesh values of the field ψ and its derivatives needed for the Newton-Raphson method are directly evaluated by Fourier transforms; the locations of vortices are thus found with precision given the *machine-ϵ* (double in the present simulations). See [10] for all technical details and a complete validation of the algorithm. Figures 1(b), 1(d), and 1(f) show the corresponding tracked vortices displayed in different colors (see Supplemental Material [15]).

We focus first on the later evolution times. During the decay, vortices radiate phonons at small scales creating a thermal bath that exchanges energy and momentum with the vortices. This process mimics mutual friction and leads eventually to the total annihilation of vortex rings [16]. In superfluids such a
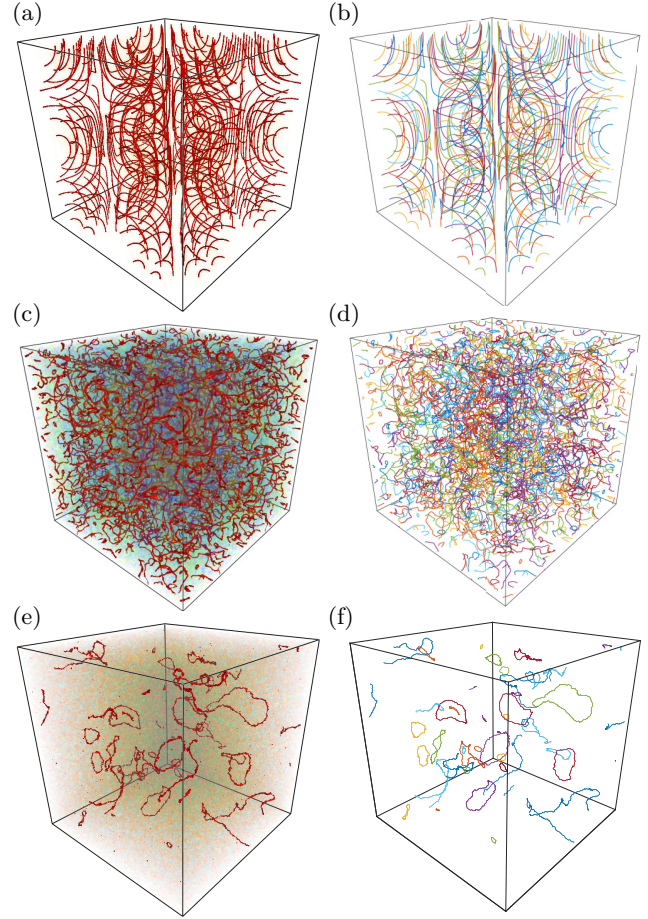

FIG. 1. Left: Isosurfaces of density field at different times. Low-density regions that correspond to vortex lines are plotted in red, while density fluctuations (sound) are rendered in light blue. Right: Corresponding tracked vortices. Different colors correspond to different vortices. Snapshots taken at $t = 0$ [(a) and (b)], $t = 12$ [(c) and (d)], and $t = 105$ [(e) and (f)]. Resolution 256^3.

decay is modeled by the Vinen equation [11] for vortex line density $\mathcal{L}$:

$$\frac{d\mathcal{L}}{dt} = -\chi_2\frac{\Gamma}{2\pi}\mathcal{L}^2, \tag{2}$$

where χ_2 is a constant of the order of unity. Its solutions manifest a $\mathcal{L} \sim t^{-1}$ behavior at long times: this power-law decay has been named quantum turbulent decay and measured in He II experiments [17] and VF numerical simulations [18]. In Fig. 2(a) we show the temporal evolution of $\mathcal{L}$. It is worth noticing that it grows at the initial stages: this is caused by the instability of the initial Taylor-Green configuration and the subsequent vortex stretching due to numerous vortex reconnections. The data is compared with an estimation of $\mathcal{L}$ obtained by computing the ratio between the volume of points such that $\rho(\mathbf{x}) < 0.2$ and the corresponding surface of a perfect two-dimensional vortex profile. This latter method has become a standard technique within GP numerical simulations to compute the vortex line density [19]. Even if this technique is able to capture the qualitative behavior of $\mathcal{L}$, it fails to grasp at long times the power law predicted by Vinen's
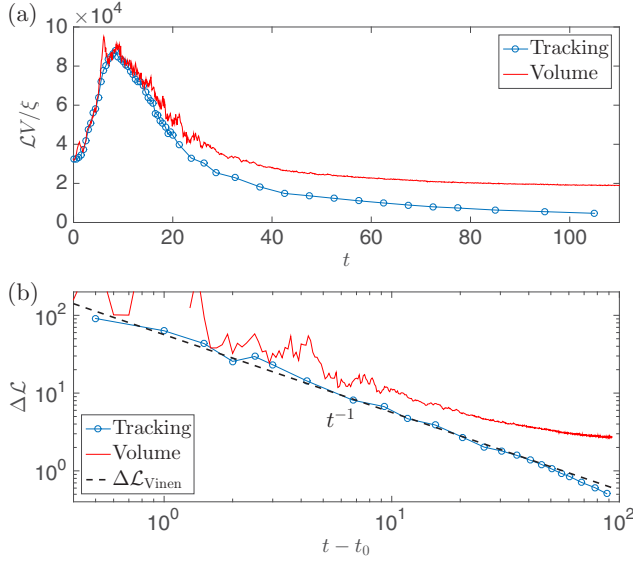
FIG. 2. (a) Temporal evolution of the vortex line density: tracked data are plotted using blue circles, and volume estimation in a solid red line. (b) Long time decay of $\Delta \mathcal{L}$ (see text), together with Vinen's prediction $\Delta \mathcal{L}_{\text{Vinen}} = [\chi_2 \frac{\Gamma}{2\pi}(t - t_0)]^{-1}$, setting $\chi = 0.65$ (solid black line). Resolution 256^3.

equation. This is shown in Fig. 2(b) where the measured $\Delta \mathcal{L}(t) = [\mathcal{L}(t)^{-1} - \mathcal{L}(t_0)^{-1}]^{-1}$, setting $t_0 = 17$, is compared to Vinen's prediction. We can explain this discrepancy by reasoning that the vortex core size (proportional to the uniform condensate state) varies in time because more and more sound excitations are created by the superfluid decay, altering the estimation of $\mathcal{L}$ by fixing the (non-time-dependant) density threshold. The tracked data also allow for determining the numerical constant $\chi_2 = 0.65$. This value is in remarkable agreement with experimental values measured in He II in the low temperature limit [11]. Between the time of maximal vortex length ($t \approx 8.5$) and t_0 there is a faster decay that could be explained by the quasiclassical turbulent decay law [20], although the data (not shown here) do not allow for a precise corroboration and further studies are needed.

From Fig. 1 and the movie provided in the Supplemental Material, it is clear that the complexity of tangle first increases and then decreases. The complexity of tangle can be measured by computing the changes in some of its algebraic and topological quantities [8]. We compute the total average crossing $\bar{C} = \sum_{i \neq j} C_{i,j}$, the total linking $\text{Lk} = \sum_{i \neq j} \text{Lk}_{ij}$, and the writhe $\text{Wr} = \sum_i \text{Wr}_i$, by directly performing the line integrals over the vortex ring(s) [8] as

$$\bar{C}_{i,j} = \frac{1}{4\pi} \oint_{\mathcal{C}_i} \oint_{\mathcal{C}_j} \left| \frac{(\mathbf{R}_i - \mathbf{R}_j) \cdot d\mathbf{R}_i \times d\mathbf{R}_j}{|\mathbf{R}_i - \mathbf{R}_j|^3} \right|, \quad (3)$$

$$\text{Lk}_{ij} = \frac{1}{4\pi} \oint_{\mathcal{C}_i} \oint_{\mathcal{C}_j} \frac{(\mathbf{R}_i - \mathbf{R}_j) \cdot d\mathbf{R}_i \times d\mathbf{R}_j}{|\mathbf{R}_i - \mathbf{R}_j|^3}, \quad (4)$$

$$\text{Wr}_i = \frac{1}{4\pi} \oint_{\mathcal{C}_i} \oint_{\mathcal{C}_i} \frac{(\mathbf{R}_i - \mathbf{R}_i') \cdot d\mathbf{R}_i \times d\mathbf{R}_i'}{|\mathbf{R}_i - \mathbf{R}_j|^3}. \quad (5)$$
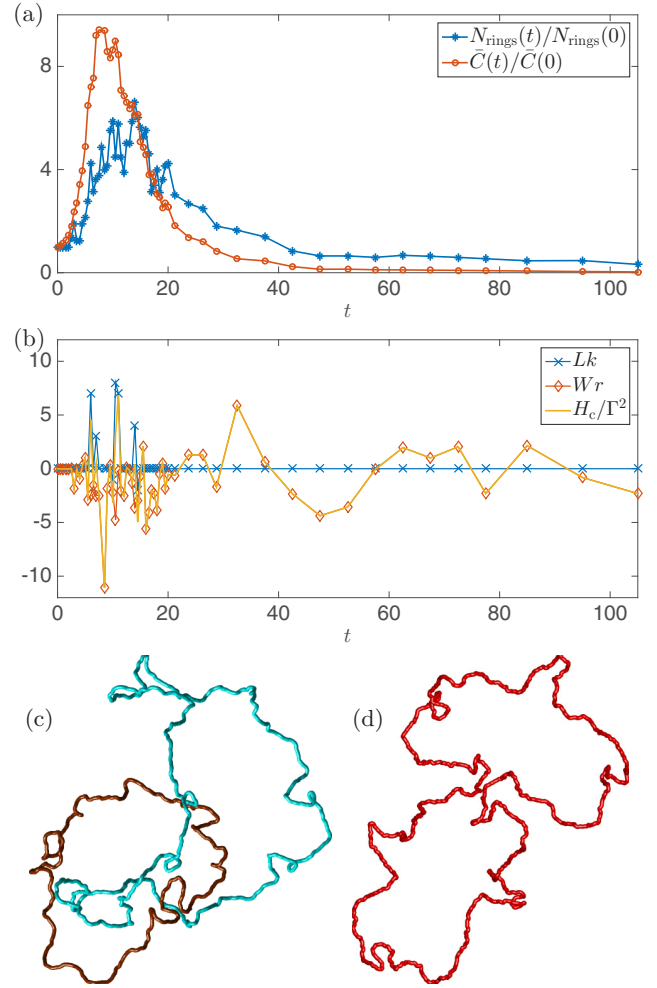

FIG. 3. (a) Temporal evolution of the (normalized) total number of rings and crossing number. At $t = 0$, $N_{\text{rings}}(0) = 128$ and $\bar{C}(0) = 758$. (b) Temporal evolution of the total linking Lk, writhe Wr and center-line helicity H_c / Γ^2. (c) Visualization of two linked rings at $t = 21$. (d) Visualization of a ring with high Wr at $t = 24.5$. Resolution 256^3.

Here $\mathbf{R}_i$ corresponds to the points identifying the ith ring $\mathcal{C}_i$; for the writhe number, $\mathbf{R}_i$ and $\mathbf{R}_i'$ correspond to two different points of the same ring. In Fig. 3(a) we plot the total number of rings N_{rings} and $\bar{C}$ normalized by their initial values versus time. It is worth noticing that the average crossing number reaches qualitatively a maximum at the same stage of the vortex line $\mathcal{L}$ maximum, while the ring number maximum is slightly shifted forward in time. The former observation follows the idea that vortex lines simultaneously stretch, bend, and coil during reconnection events. The latter is due to the fact that longer vortex rings continue to break into pieces during the evolution until the tangle density becomes low enough and the main vortex length dissipation mechanism is given by sound interaction. We then focus on the center-line helicity $H_c / \Gamma^2 = \text{Lk} + \text{Wr}$ [21] related to the helicity in classical fluid dynamics, an important inviscid invariant. The linking number Lk takes integer values and gives information about the number of linked rings present in the system, whereas the writhe takes real values and its contribution

VILLOIS, PROMENT, AND KRSTULOVIC

comes from self-linked (knots), an integer contribution, and KWs [22]. Figure 3(b) shows the temporal evolution of these three quantities. Initially, Lk = Wr = 0, as expected for the Taylor-Green flow. Surprisingly, during the evolution Lk becomes nonzero, indicating the presence of linked rings, such as the ones displayed in Fig. 3(c) [23]. This is remarkable as in the GP model sufficiently simple vortex configurations usually decay by reducing their complexity [24]. Once the decay is established, no linked rings are present and only writhe contributes to H_c. Note that the writhe number is not enough to determine whether a ring is self-linked (knotted) or not. The center-line helicity, however, fluctuates about a zero mean, an indication of the presence of KWs. KWs are indeed apparent in Fig. 3(d) where an unknotted ring with high Wr is displayed. KWs have already been indirectly observed in the Taylor-Green flow during the turbulent stage [25], in agreement with the large values of writhe observed around $t \sim 10$.

We now study statistical properties of some geometrical quantities of the vortex filaments by exploring the time behavior of the probability density functions (PDFs) of the curvature κ and torsion τ of the entire set of vortices in the system. In Fig. 4(a) we present the PDF of curvature, normalized by its mean value, at different stages. The temporal evolution of the mean curvature $\langle \kappa \rangle$ and its *rms* value κ_{rms} are also displayed in the inset. We can observe that $\langle \kappa \rangle$ increases rapidly at early stages and then almost saturates, an indication that the average vortex size (inversely proportional to the curvature) slowly decreases at later times. The rms value of the curvature presents the same tendency with the exception of peaks. These are evidence of reconnection events where high values of curvature are found in localized regions. It is worth noticing that the PDFs, rescaled by their mean curvature, exhibit a relatively good collapse to a self-similar form. This
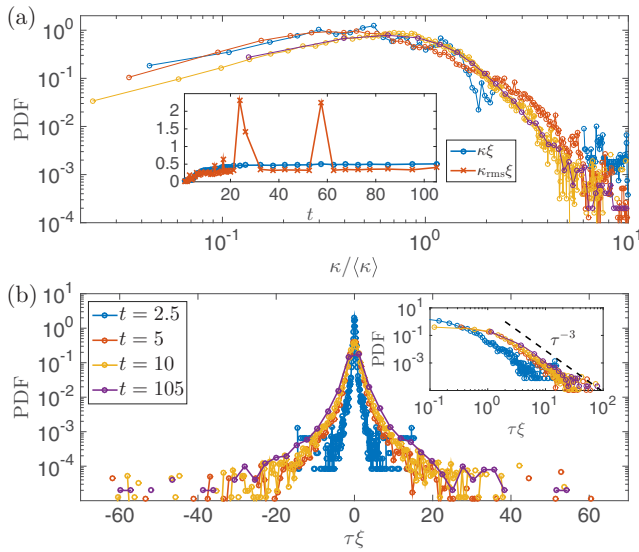

FIG. 4. (a) PDFs of curvature κ normalized by their respective mean values $\langle \kappa \rangle$ at different times [same legend as (b)]. The inset displays the temporal evolution of the mean and rms values of κ. (b) PDFs of torsion τ at different times. The inset emphasizes their τ^{-3} power-law tail. Resolution 256^3.

latter observation indicates a power-law behavior $\sim \kappa^1$ at small curvature values, while an exponentially decaying tail is present at large curvature values. A similar behavior has also been observed within the VF model [26]. In Fig. 4(b) we plot the torsion PDFs at the same stages. The mean torsion is always about zero and there is no evidence of any skewness in the PDFs. The distributions' tails show a universal power-law behavior of τ^{-3} at all times, meaning that the second and higher moments of the torsion diverge during the decay. The same scaling appears in vortex tangles of random wave fields that are solutions of the Helmholtz equation [27]. This may be an indication that for one-time small-scale quantities, quantum turbulent tangles can be interpreted simply as random vortices.

The large curvature fluctuations and the torsion fluctuation about a zero mean are evidence of KWs at all scales propagating on quasiplanar vortex rings. By exploiting the accuracy of the tracking algorithm we are able to directly detect KWs on those rings. Competing theories have been put forward to statistically predict a power-law KW spectrum in the form of $n_k \sim k^{-\alpha}$ (here k is the Kelvin wave number) and explain the energy transfer through KW scales. Vinen *et al.* considered strong nonlinear interactions and derived by a scaling argument the exponent $\alpha_V = 3$ [28]. On the other hand, assuming weak nonlinearity (small amplitude KWs compared to their respective wavelengths), Kozik and Svistunov [29] and L'vov and Nazarenko [12] obtained the exponents $\alpha_{KS} = 17/5$ and $\alpha_{LN} = 11/3$, respectively, considering two different orders of interaction. We can compute the KW spectrum of a ring R by applying a Gaussian kernel of width αL in order to establish the configuration of the unperturbed ring R_{ump}. This can be used to define the KWs on it as $R_{KW}(s) = R(s) - R_{ump}(s)$, where $s \in [0,L]$ is the arc-length parametrization of the ring. Being R_{KW} a periodic set of three signals (one for each spatial dimension), the KW spectrum is then defined as $n_k = |\widehat{R_{KW}}(k)|^2 + |\widehat{R_{KW}}(-k)|^2$, where $\widehat{R_{KW}}(k)$ is the Fourier transform of $R_{KW}(s)$. In [10] we checked that this procedure is able to capture well the KWs superimposed on a ring. Here we compute the KW spectrum averaging over the spectra of the 50 largest rings such that it has small fluctuations and it always spans over two Kelvin wavelength decades. For the Gaussian filter, we use the value $\alpha = 0.1$; varying this fraction weakly modifies the large-scale values of the spectrum, but the data in the inertial range remain unchanged. The KW spectra are shown for different times in Fig. 5(a). It is evident that all accessible KW modes get populated at early times due to reconnection events that trigger the cascade [30]. We observe KW spectra exhibiting power laws with an exponent independent of time where the best scaling is appreciated at the time where the rings are the longest ($4 \leqslant t \leqslant 7$). To get the best estimation of the power-law exponent, we repeated the Taylor-Green decay in a simulation box twice larger; in this new configuration the scaling range spans almost two wave-number decades. In Fig. 5(b) we show the spectrum at $t \sim 5$: the observed power-law exponent is close to the weak-wave turbulence predictions and seems to agree with the L'vov and Nazarenko $\alpha_{LN} = 11/3$ one. This can be better appreciated by looking at the compensated spectra with respect to α_{LN} and α_{KS} shown in the inset. This finding supports the result in favor of L'vov and Nazarenko's prediction previously obtained while studying the KW oscillations about a perfect
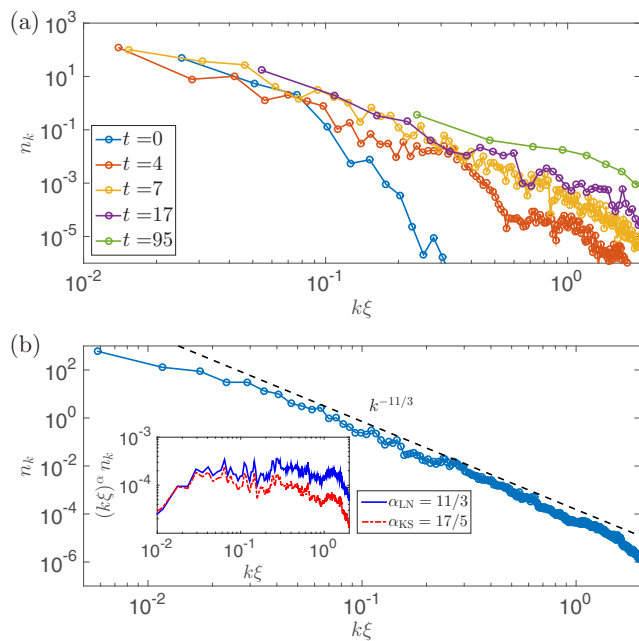
FIG. 5. (a) Temporal evolution of KW spectra (averaged over the 50 longest rings). Resolution 256^3. (b) KW spectrum at $t \sim 5$ (averaged over the 50 longest rings) for run at resolution 512^3. The dashed line displays the $k^{-11/3}$ scaling. The inset displays the respective $k^{11/3}$ (solid blue) and $k^{17/5}$ (dashed red) compensated spectra.

straight line in the GP model [31]. We highlight that although the weak-wave turbulence prediction for the KW spectrum is formally derived for KWs on an isolated straight vortex line using the VF model, it remarkably turns out to be valid in a dense turbulent tangle also driven by the GP model. This

is certainly due to the fact that the predicted KW spectrum was found for the longest rings. Small rings quickly lose their energy by phonon radiation and exchange momentum with sound waves. Both contributions are important to understand dissipation of superfluids at very low temperature and further studies are still needed to fully comprehend the relevance of such mechanisms.

Tracking vortices in GP turbulence opens up a new way for studying and understanding the topological configuration and properties of quantum vortex tangles. Although unlikely, we show that rings can link creating a local (in time and space) fluctuation of the center-line helicity. It will be of great interest to repeat a similar analysis setting where the mean helicity of the flow is not zero, like the ABC flow introduced in [22] where linking and self-linking processes could be substantially enhanced. Overall, the results presented in this work confirm that some predictions traditionally associated to superfluid liquid helium become important in weakly interacting BECs at low temperature described by the GP model. Nowadays BEC experimentalists are able to create and track few vortices in harmonic traps [32,33]. A controlled experimental setting with a turbulent BEC, such as the one presented in this work, has yet to be achieved but it should be realizable in the near future.

[1] U. Frisch, *Turbulence: The Legacy of AN Kolmogorov* (Cambridge University Press, Cambridge, UK, 1995).

[2] R. Donnelly, *Quantized Vortices in Helium II* (Cambridge University Press, Cambridge, UK, 1991), Vol. 3.

[3] K. W. Schwarz, Phys. Rev. B **38**, 2398 (1988).

[4] A. W. Baggaley and C. F. Barenghi, J. Low Temp. Phys. **166**, 3 (2011).

[5] G. P. Bewley, M. S. Paoletti, K. R. Sreenivasan, and D. P. Lathrop, Proc. Natl. Acad. Sci. USA **105**, 13707 (2008).

[6] L. Pitaevskii and S. Stringari, *Bose-Einstein Condensation* (Oxford University Press, New York, 2003), Vol. 116.

[7] E. Henn, J. Seman, G. Roati, K. Magalhaes, and V. Bagnato, Phys. Rev. Lett. **103**, 045301 (2009).

[8] C. F. Barenghi, R. L. Ricca, and D. C. Samuels, Phys. D (Amsterdam, Neth.) **157**, 197 (2001).

[9] W. F. Vinen, Phys. Rev. B **64**, 134520 (2001).

[10] A. Villois, D. Proment, H. Salman, and G. Krstulovic, arXiv:1604.03595.

[11] W. F. Vinen, Proc. R. Soc. London, Ser. A **242**, 493 (1957).

[12] V. L'vov and S. Nazarenko, JETP Lett. **91**, 428 (2010).

[13] C. Nore, M. Abid, and M. Brachet, Phys. Fluids **9**, 2644 (1997).

[14] C. Rorai, J. Skipper, R. M. Kerr, and K. R. Sreenivasan, arXiv:1410.1259.

[15] See Supplemental Material at http://link.aps.org/supplemental/10.1103/PhysRevE.93.061103 for a movie of full time evolution.

[16] G. Krstulovic and M. Brachet, Phys. Rev. E **83**, 066311 (2011).

[17] P. M. Walmsley and A. I. Golov, Phys. Rev. Lett. **100**, 245301 (2008).

[18] A. W. Baggaley, C. F. Barenghi, and Y. A. Sergeev, Phys. Rev. B **85**, 060501 (2012).

[19] A. C. White, C. F. Barenghi, N. P. Proukakis, A. J. Youd, and D. H. Wacks, Phys. Rev. Lett. **104**, 075301 (2010).

[20] S. R. Stalp, L. Skrbek, and R. J. Donnelly, Phys. Rev. Lett. **82**, 4831 (1999).

[21] M. W. Scheeler, D. Kleckner, D. Proment, G. L. Kindlmann, and W. T. M. Irvine, Proc. Natl. Acad. Sci. USA **111**, 15350 (2014).

[22] P. Clark di Leoni, P. D. Mininni, and M. E. Brachet, arXiv:1602.06880.

[23] Although linked rings are present in the flow, the probability of finding them is very small. It can be estimated counting all the linked rings and it is at most of the order 10^{-4} for the Taylor-Green flow.

[24] D. Kleckner, L. H. Kauffman, and W. T. M. Irvine, Nat. Phys. (2016), doi:10.1038/nphys3679.

[25] P. Clark di Leoni, P. D. Mininni, and M. E. Brachet, Phys. Rev. A **92**, 063632 (2015).

[26] L. Kondaurova, V. L'vov, A. Pomyalov, and I. Procaccia, Phys. Rev. B **89**, 014502 (2014).

[27] A. J. Taylor and M. R. Dennis, J. Phys. A: Math. Theor. **47**, 465101 (2014).

[28] W. F. Vinen, M. Tsubota, and A. Mitani, Phys. Rev. Lett. **91**, 135301 (2003).

[29] E. Kozik and B. Svistunov, Phys. Rev. Lett. **92**, 035301 (2004).

[30] D. Kivotides, J. C. Vassilicos, D. C. Samuels, and C. F. Barenghi, Phys. Rev. Lett. **86**, 3080 (2001).

[31] G. Krstulovic, Phys. Rev. E **86**, 055301 (2012).

[32] G. Lamporesi, S. Donadello, S. Serafini, F. Dalfovo, and G. Ferrari, Nat. Phys. **9**, 656 (2013).

[33] S. Serafini, M. Barbiero, M. Debortoli, S. Donadello, F. Larcher, F. Dalfovo, G. Lamporesi, and G. Ferrari, Phys. Rev. Lett. **115**, 170402 (2015).

[34] See https://www.vapor.ucar.edu.

Chapter 4

Quantum vortex reconnections

This chapter presents a brief introduction to vortex reconnections in quantum fluids. We start by discussing the general properties of the process of vortex reconnections. We then state the differences between reconnections in classical and quantum fluids. Finally, we summarise the main properties of vortex reconnection in quantum fluid and discuss in which sense vortex reconnections can be seen as an irreversible process in superfluids. Three works are included at the end of the chapter.

In a classical fluid, vorticity is a continuous three-dimensional vector field. It occurs often in nature that vorticity takes very high values in narrow fluid structures supported in vortex patches like tubes, sheets or filaments [Saf93]. The latter is the case for instance of tornadoes in classical fluids and quantum vortices in superfluids. As we have seen in previous chapters, such fluid structures have a complex dynamics. A vortex filament can interact with itself, generating the self-propulsion of vortex rings, and with other surrounding filaments leading to the formation of vortex tangles. When two filaments approach each other, they can recombine through a process known as vortex reconnections. Vortex reconnection is one of the most fundamental processes in fluid dynamics. Such process plays a fundamental role in several physical phenomena like eruptive solar events [Xue+16], energy transfer and fine-scale mixing [HD11] and turbulent states in superfluids [Bew+08]. Vortex reconnections are also a stand-alone mathematical problem, related for instance, to the presence of singularities in the Euler and Navier-Stokes equations [Sig85; PS87; SMO93; KT94; FM96; Mof00].

A vortex reconnection is necessarily accompanied by a change in the topology of vortex lines. For this reason, only some configurations are generically possible. Figure 4.1 shows a sketch of the approach of two vortices. The black arrow indicates the alignment of vorticity (the flow is turning accordingly to the right-hand rule). In the case of an anti-parallel approach, we notice that a reconnection is possible by a

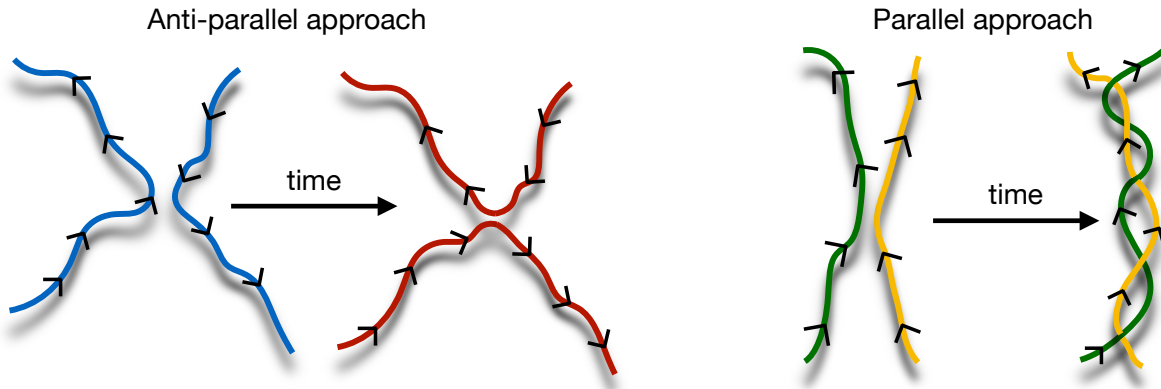Anti-parallel approach   Parallel approach

time   time

Figure 4.1: Sketch of vortex approach. The black arrows indicate the orientation of the vortex.

"cut and connect" process. Indeed, each one of the blue vortices could be "cut" in two pieces and the
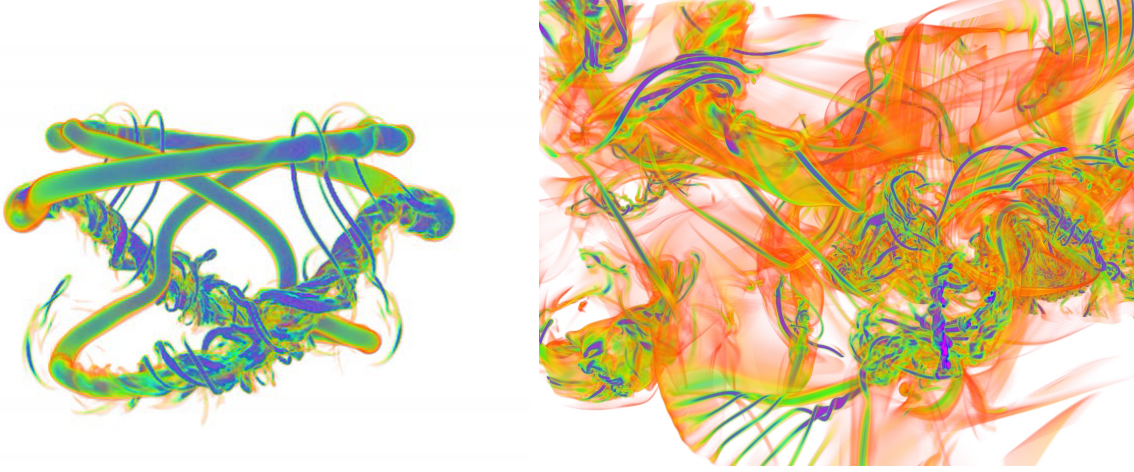
Figure 4.2: Enstrophy visualisation. Left: Reconnection of trefoil know under Navier-Stokes equations. Right: Snapshot of a turbulent decay in hyper-viscous Navier-Stokes equation (in collaboration with S. Nazarenko).

"glued" to create the red vortices respecting the direction of the arrows. On the contrary, in the parallel approach, vortices will tend to roll each other creating a thread. Of course, in the last case viscosity could become quickly important.

The image sketched in figure 4.1 is extremely simplified. First of all, in classical fluids, a filament always has a finite core size, so during the approach, the vortex core might substantially deform [Saf90; BHP16]. The description above only makes sense if we look at distances between the vortices where the vortex core size is negligible. Furthermore, the reconnection is not so simple, many secondary structures appear during the process. As a matter of illustration, we show in figure 4.2 three-dimensional visualisations of the enstrophy field from (classical) Navier-Stokes simulations. Inspired by the experiments in water carried on in Ref. [KI13], we simulate the evolution of a tree foil knot. At the left, we observe the reconnection of the knot where many bridges (thin filaments connecting the main ones) develop. On the panel at the right, we observe a turbulent decay in hyper-viscous Navier-Stokes. Vortices of the same sign start rolling each other creating threads and more dissipative structures.

A full mathematical understanding of vortex reconnections is certainly a very difficult or almost impossible task. We shall start by recalling the most fundamental constraint of perfect fluids. The Kelvin circulation theorem states that in barotropic ideal fluids, the circulation

$$\Gamma = \oint_{\mathcal{C}} \mathbf{v} \cdot d\ell \tag{4.1}$$

around a material (moving with the fluid) closed curve $\mathcal{C}$ is conserved [Tho68]. As a consequence, we deduce that in perfect fluids, i.e. fluids driven by the Euler equations, vortex reconnections are not allowed. On the contrary, in Navier-Stokes dynamics, the circulation is not conserved and it is dissipated by the viscous term

$$\frac{d\Gamma}{dt} = \nu \oint_{\mathcal{C}} \nabla^2 \mathbf{v} \cdot d\ell, \tag{4.2}$$

where ν is the kinematic viscosity of the flow. In particular, during a reconnection event in classical fluids, a fraction of the circulations is dissipated [KT94; MBG01; HD11; HD11; YH20a].

From the point of view of a theoretician, one would like to isolate the universal features (if any), from some model-dependent physical behaviour (finite core size a_0 and typical vortex size R, finite Reynolds number $Re_{\mathrm{v}} = \Gamma/\nu$, etc.). In that sense, we are interested in the limit

$$a_0 \ll R, \quad Re_{\mathrm{v}} \to \infty, \text{ keeping } \Gamma \text{ fixed.} \tag{4.3}$$
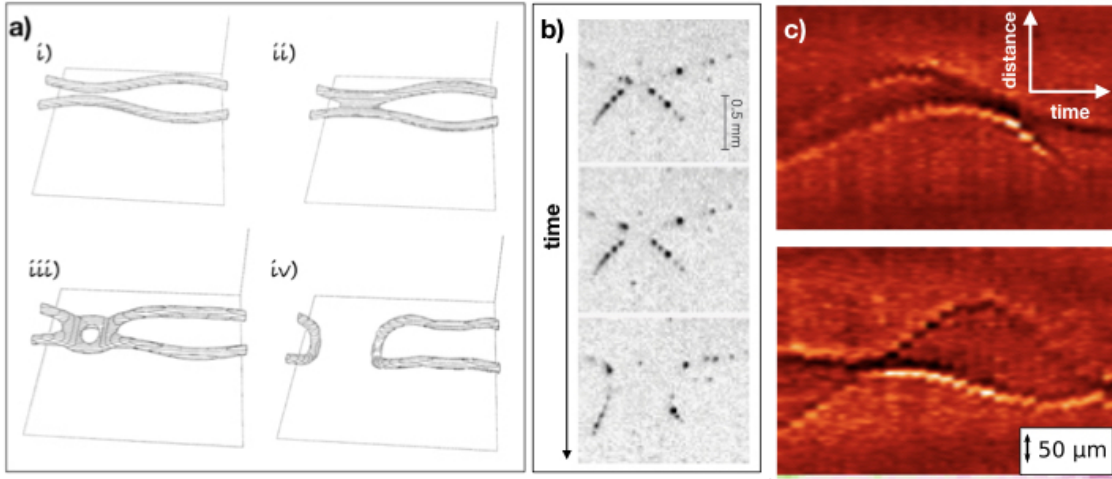
Figure 4.3: **a)** Vortex reconnection in the GP model from the work of Koplik and Levine [KL93]. **b)** Vortex reconnection in superfluid helium from the work of Bewley et al. [Bew+08]. The Black dots correspond to trapped particles of a (frozen) dilute mixture of atmospheric air in helium gas. **c)** Dynamics of vortices in sodium Bose-Einstein condensate form Serafini et al. [Ser+17]. The figure shows a vortex rebound.

Such limit is extremely complex form the mathematical point of view. For instance, we know that because the dissipative anomaly of turbulence [Fri95; Eyi08], in the limit of vanishing viscosity there is remanent dissipation [Sre84; Vas15; Dub19]. Similar ideas have been for instance applied to the Kelvin theorem [Che+06], showing that although it is violated in that limit, in some statistical sense the Kelvin theorem should be recovered for infinite Reynolds numbers.

Leaving aside all those interesting mathematical issues, the limit (4.3) becomes physically relevant for superfluids. Indeed, as discussed in Section 2.1.3, quantum vortices are topological defects of the wave function. The vorticity field resulting form a quantum vortex needs thus to be interpreted as a distribution

$$\omega(\mathbf{x}) = \Gamma \oint \delta(\mathbf{x} - \mathbf{s})\mathrm{d}\mathbf{s}, \tag{4.4}$$

where $\mathbf{s}$ is the filament parametrisation and the integral extends over the whole filament(s). The circulation Γ is now quantised and a multiple of the Onsager-Feynman quantum of circulation (see Section 2.1.3). Naively, as a superfluid is characterised by the absence of viscosity and driven by hydrodynamic equations, one could argue that because of Kelvin theorem, in superfluids vortex reconnections should not be possible. This claim is of course invalid. It was already suggested by Feynman in the 50's [Fey55] that quantum vortices should indeed reconnect. This idea was taken by Schwarz [Sch88], where he assumed that if vortex lines driven by hydrodynamic interactions (LIA) get close enough they will reconnect. He implemented this idea numerically and noticed that vortex reconnections are a very important mechanism for the generation of turbulent quantum vortex tangles. A couple of years later, Koplik and Levine [KL93] showed for the first time, by direct numerical simulations of the Gross-Pitaevskii model, that quantum vortices indeed reconnect. A figure taken from the original paper by Koplik and Levine is displayed in Fig.4.3.a. There is no conflict between quantum vortex reconnections and the Kelvin theorem. Indeed, the fluid density vanishes on the vortex filament and thus the theorem can not be applied there. Although in terms of velocity or vorticity (Eq.4.4) there is no notion of a vortex core, due to the dispersive term in the GP model, the density field vanishes at the filament giving an effective core size of the order of the healing length (see Section 2.1.3). It follows, as noticed by P.H Robert and C.A Jones [JR82], that during quantum vortex reconnections, at very small scales, the circulation simply disappears and the remanent of the vortex becomes a solitary wave of compression. Note however, that there is no net loss of circulation during the process as vortex circulation is quantised, after the reconnection, each vortex will have its own

quantum of circulation.

The direct observation of quantum vortex reconnection took many years. In superfluid helium, the vortex core is of the order of the angstrom, which makes very difficult their direct visualisation. Concerning atomic BECs, the vortex core is much larger (typically of the order of micrometers) but measurements are commonly destructive (*time of flight*). Despite this fact, both superfluid helium and atomic BECs had been visualised in the past by different techniques, particularly in the case of rotation, where Abrikosov lattices have been observed [WP74; YGP79; Abo+01]. The difficulty in the case of vortex reconnections is that measurements of the full dynamics of vortices are needed. This experimental breakthrough took place in 2006, where micrometer size hydrogen particles were used to visualise quantum vortices [BLS06]. Despite their large size, particles have been extensively used over the last 15 years to study different aspects of quantum vortex dynamics. In particular, quantum vortex reconnections were observed with this technique [BLS06; FSL19]. Figure 4.3.b shows a vortex reconnection taken form [FSL19] where quantum vortex reconnections are observed. At the end of this chapter, I include a work with U. Giuriato where reconnections of quantum vortices having trapped particles are studied.

Concerning BECs, the recent development of new experimental techniques have allowed for the visualisation of real-time vortex dynamics [Ser+15; Ser+17], opening the way for many interesting research avenues. A visualisation of the temporal evolution of quantum vortices in a trap, taken from reference [Ser+17], is shown in figure 4.3.c.

4.1   Rates of approach and separation

The simplest question that one can try to answer is how fast vortices approach and separate during a reconnection event. We consider a situation as the one depicted in figure 4.1 (left). Let's denote by $\delta^-(t)$ and $\delta^+(t)$ the distance between the closest points of the filaments before and after reconnection, respectively. We shall focus now, only on the case of quantum vortices (although the reasoning should be also valid for classical vortex reconnection in the limit 4.3). The first answer to this problem can be given by dimensional analysis. If we assume that the reconnection is local, in the sense that we can neglect the interaction with other vortices, the only relevant dimensional parameters are, the quantum of circulation Γ (with units of $Length^2/Time$) and the healing length ξ (proportional to the vortex core size). From dimensional analysis, if we denote by t_r the reconnection time, the distance should obey a relationship of the type

$$\Phi\left(\frac{\delta^\pm(t)}{\sqrt{\Gamma|t - t_r|}}, \frac{\delta^\pm(t)}{\xi}\right) = 0, \tag{4.5}$$

where $\Phi(\cdot, \cdot)$ is an unknown function.

In the Biot-Savart limit, i.e. when $\delta^\pm \gg \xi$, the second argument of the function Φ, can be replaced by ∞, where we of course assume that this limit exists. As a consequence, the Biot-Savart scaling for vortex reconnections is $\delta(t) \sim t^{1/2}$. On the opposite limit, when vortices are almost reconnecting, as the filament are nodal lines of the wave function, we can formally take the limit $\xi \to \infty$ (with Γ and $t - t_r$ fixed). As the reconnection process in superfluid is a regular process, we can replace the second argument of Φ equal to zero and recover again the same $t^{1/2}$ scaling. This last limit was derived analytically by Nazarenko and West [NW03]. We refer to this asymptotic as the linear regime because here, non-linear terms in GP can be neglected. We will discuss further this limit later.

To summarise, assuming that the only relevant physical parameters are Γ and ξ and based on two (opposite) asymptotic limits, we should have that during quantum vortex reconnections the distances between vortices obey the law

$$\delta^\pm(t) = A^\pm\sqrt{\Gamma|t - t_r|}, \tag{4.6}$$

where $A^\pm$ are two order one constants. Note that any scaling different from $1/2$ in superfluid vortex reconnections, needs necessarily the introduction of a different physical length or time scale. Indeed, for

instance, in [Gal+19], it was observed a crossover between a ballistic t^1 at long times and a reconnection $t^{1/2}$ scaling. The ballistic scaling simply corresponds to the one of two self-propagating vortices that approach at a constant speed (a new dimensional parameter is thus present).

In classical fluids, the scaling (4.6) does not necessarily need to hold, as the dynamics of the vortex core might be highly non-trivial [PK87]. Indeed, different scaling exponents have been found over the last decades [HD11; Ker18; YH20a]. However, in a recent paper, Yao and Hussain [YH20b] have found the $t^{1/2}$ scaling in Navier-Stokes simulations for rings having a very small vortex core (compared to their radius). For vortices in superfluid helium, the scaling (4.6) has been indeed observed in experiments [Bew+08; FSL19] and in Biot-Savart numerical simulations [Bag+12; TA11]. In what concerns numerical simulations of the Gross-Pitaevskii model, many studies reported disparate exponents, even having different values before and after the reconnection event. None of those exponents, violating the mathematical results of Nazarenko and West [NW03], have been explained. One possible reason is that the GP model does not provide direct information of the vortex filament and in order to study the reconnection processes, an accurate vortex tracking algorithm is needed. Thanks to the accurate vortex tracking method that we developed in [Vil+16], we were able for the first time to obtain a clear verification of the scaling 4.6 both, before and after reconnections, for very different vortex configurations [VPK17]. The scaling was also verified later by other groups [Ser+17; Gal+19], in two recent papers where about 40 reconnection events were studied [VPK20] and with vortices with trapped particles inside [GK20b]. The works [VPK17; VPK20; GK20b] are included at the end of this chapter.

4.1.1   The linear regime of vortex reconnections

In this section, we reproduce and adapt part of the results of [NW03] as they allow to understand the very process of reconnection. We have generalised such results in [VPK17; PK20c] in order to explained some of our numerical observations, we redirect the reader to those references for a detailed analysis.

For the sake of simplicity, as in [NW03], we shall only discuss here the case when reconnection process takes place fully in a plane. We recall we are in the limit in which $\delta^{\pm} \ll \xi$. As a consequence, the wave function takes here very small values and the GP model simply reduces to the Schrödinger equation

$$\frac{\partial \psi}{\partial t} = i \frac{\Gamma}{4\pi} \nabla^2 \psi, \tag{4.7}$$

where the quantum of circulation is $\Gamma = h/m$ with h the Plank constant and m the mass of the atoms. The solution of (4.7) is simply given by

$$\psi(x, y, z, t) = e^{i\frac{\Gamma(t-t_{\mathrm{r}})}{4\pi}\nabla^2} \psi_{\mathrm{r}}(x, y, z), \tag{4.8}$$

where $\psi_{\mathrm{r}}(x, y, z)$ is the wave function describing the reconnection event. It was known that vortices approach following asymptotically a pyramid [dWA94]. In particular, in the plane, vortices are hyperbolae approaching each other by following their asymptotes. A suitable choice for the reconnection wave function is

$$\psi_{\mathrm{r}}(x, y, z) = z + i(az + \tan^2\left(\frac{\phi^+}{2}\right)x^2 - y^2) \tag{4.9}$$

where the parameters have been written in such a way to facilitate the discussion later [1]. Equation 4.9 can be seen as particular choice of a second (leading) order polynomial development of ψ_{r} around zero. The choice in (4.9) is certainly not the most general one, and indeed misses several important physical phenomena (see [VPK17; PK20c]), but it is good enough to illustrate the main properties. Replacing (4.9) in (4.8) and setting $\psi(x, y, z, t) = 0$, yields and equation for the temporal evolution of the x and y

---

[1]Even in this planar case, the parameters have to obey some constraints. For the sake of simplicity we omit this discussion here.
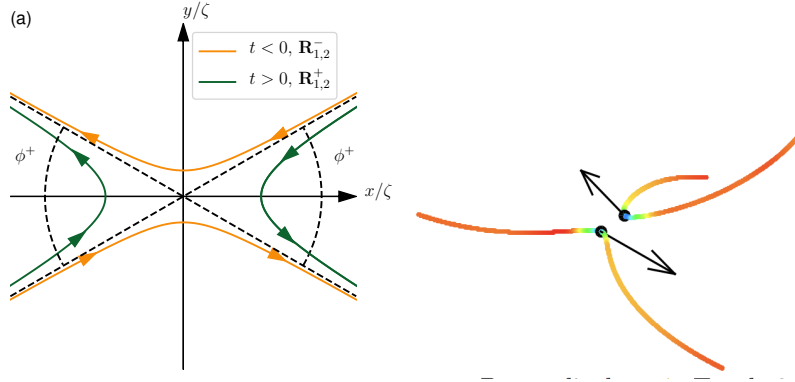
Figure 4.4: **a)** Sketch of vortex reconnection in the linear regime. The two asymptotes are displays by straight dashed lines. The the angle ϕ^+ is also indicated in the figure. **b)** Close up of a GP reconnection taken form [VPK17]. The arrows are the tangents to the filaments at the reconnection points. The colormap indicates the local curvature of the filaments, from low (red) to high (green).

component of the vortex filaments. It reads

$$\tan^2\left(\frac{\phi^+}{2}\right)x^2 - y^2 = \frac{\Gamma}{2\pi}(t - t_{\rm r})a\left(1 - \tan^2\left(\frac{\phi^+}{2}.\right)\right) \tag{4.10}$$

We can reinterpret now ϕ^+ as the angle between the two asymptotes of the vortices after reconnection, as sketched in Fig.4.4.a. Vortex reconnection literature usually refers to this angle as the reconnection angle. Note that, this angle is related to an asymptotic approach and it is different from the one between the tangents at the reconnection point that is always π (reconnections are always anti-parallel, see [VPK17]), as shown in 4.4.b.

Solving Eq.(4.10) for $t < t_{\rm r}$ and $t > t_{\rm r}$ directly leads to the reconnection distances

$$\delta^-(t) = \sqrt{\frac{2}{\pi}a\left[1 - \tan^2\left(\frac{\phi^+}{2}\right)\right]}\sqrt{\Gamma(t_{\rm r} - t)}, \quad \delta^+(t) = \sqrt{\frac{2}{\pi}\frac{a\left[1 - \tan^2\left(\frac{\phi^+}{2}\right)\right]}{\tan^2\left(\frac{\phi^+}{2}\right)}}\sqrt{\Gamma(t - t_{\rm r})}. \tag{4.11}$$

The first observation is that the $t^{1/2}$ scaling is recovered (as a consequence of dimensional analysis and the fact that the process is regular). Nothing can be said respect to the individual values of the pre-factors $A^\pm$ defined in equation (4.6), as the constant a is arbitrary. However, we notice that

$$\frac{A^+}{A^-} = \cot^2\left(\frac{\phi^+}{2}\right) = \tan^2\left(\frac{\phi^-}{2}\right). \tag{4.12}$$

i.e. the ratio of the pre-factors is related to the value of the reconnection angles ϕ^+ (or $\phi^- = \pi - \phi^+$). A very important remark: $A^+ > A^-$ if $\phi^- \leq \pi/2$, and $A^+ = A^-$ if the angle is exactly $\pi/2$. Note as well, that in principle all possible values of ϕ^+ are admissible in the linear regime.

Finally, as you can notice in 4.4.b, during reconnection a cusp is generated. Actually, we can show that the curvature diverges as $t^{-1/2}$ and the pre-factors are related to the value of $(A^+/A^-)^3$. Curvature, torsion and self-similarity are studied in the selected publication [VPK17].

At this point, we could state that the mechanism of vortex reconnections is a purely linear process in the GP framework, however, some caution is needed. The previous derivations are valid only very close to the reconnection point ($\delta \ll \xi$ and $|t - t_{\rm r}| \ll \xi/c$), and assume that vortices are already very close. Indeed, we could take two vortices that are already about to reconnect, switch the non-linearity off, and the process will not be very different from the one driven by the full GP model if the temporal evolution
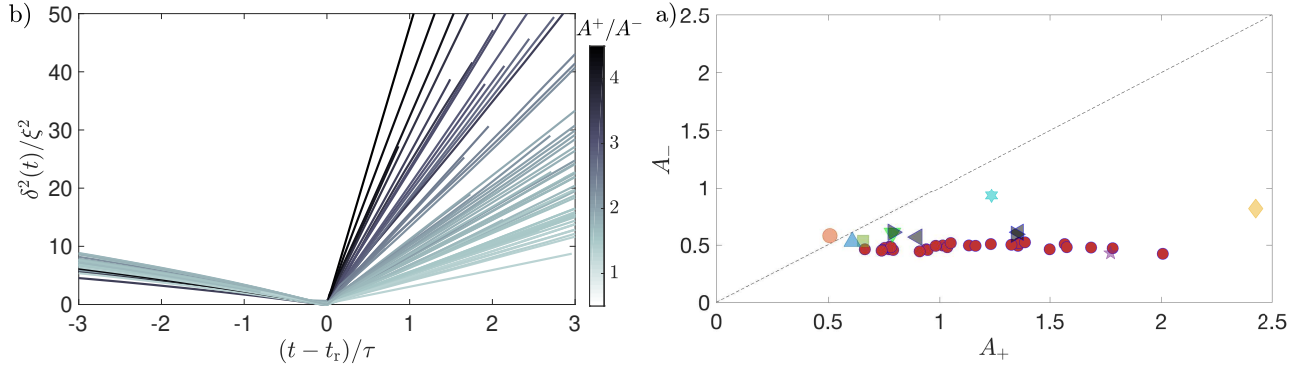
Figure 4.5: **a)** Squared distances δ^2 versus time of the reconnecting filaments. Time is expressed in units of $\tau = \xi/c$, with c the speed of sound. The grey-scale colour indicate the measured value of A^+/A^- in each case. **b)** Values of approach and separation pre-factors A^+ and A^-. Red points correspond to data of [VPK20]. Grey left and right triangles correspond to reconnections of free and trapped vortices respectively, from Galantucci et al.[Gal+19]; other symbols from Villois et al. [VPK17].

is short enough. However, one needs to keep in mind that vortices get close to each other because of their mutual hydrodynamic interaction, which is a fully non-linear process. Without non-linear interactions, the fluid has no pressure (other than the quantum part) and vortices do not present hydrodynamic behaviour.

4.2   Irreversibility of vortex reconnections

As we discussed in the previous section, the linear regime is a powerful mathematical tool to study reconnections and to link the filaments before and after that event. The most important parameter that fixes the reconnection is the approaching angle, that is simply related to the ratio of the pre-factors A^+/A^- of formula (4.6). At this point, we do not have any knowledge of their values or even of their ratio. In Villois et al. [VPK17] we have studied several configurations having very different geometries and we always observed that $A^+ > A^-$, in other words, vortices separate faster than they approach. This finding motivated a recent work [VPK20], where we study systematically more than 40 reconnections.

In reference [VPK20] we considered a Hopf link (two linked rings) and we varied their offset. We evolved the Hopf link under GP evolution and carefully tracked the vortices to compute their reconnecting distance. The rate of approach and separation are displayed in Fig.4.5.a. The very first remark is the good agreement with the $t^{1/2}$ law. As manifest in the colormap, we always observe that $A^+ > A^-$. This finding is put in evidence in Fig.4.5.b, where all the values of A^- are plotted against A^+ for all the reconnections, including data from other works. For almost all reconnections we observe $A^- \approx 0.5$, that is in agreement with theoretical prediction of $A^- \in (0.45, 4.8)$ by Boué et al. [Bou+13a]. A natural question arises, if the GP evolution is time reversible, why do we observe this time asymmetry? In other words, if an educated observer is provided with data from reconnections, he or she should be able to tell if the provided data is stored forward or backward in time.

In Villois et al. [VPK20], we provide an explanation to the observation in Fig.4.5. In a nutshell, the explanation is that in order to observe a reconnection with $A^+ < A^-$, we have to provide energy to the vortices, so this process should be generically excluded. We demonstrated that there is a loss of energy and momentum from the vortices during the reconnection process. As the dynamics is conservative, the energy and momentum need to be converted into compressible degrees of freedom. We observed a pulse that is emitted during the reconnection and we were able to find analytically its direction.

We have shown that there is an intrinsic irreversibility in the process of superfluid vortex reconnections. Reconnections generically imply a loss (or irreversible transfer) of momentum and energy. We can thus understand this process as a route to reach thermal equilibrium. What does it happen in classical fluids?

Remarkably, Yao and Hussain [YH20b] observed in Navier-Stokes simulations the $t^{1/2}$ scaling with a pre-factor of $A^- \sim 0.4$. More impressive, is that they also observed $A^+ > A^-$, although the value of A^+ is difficult to interpret, as in classical vortex reconnections, some circulation is lost. An emerging obvious question is, what is the limit of infinite Reynolds number? Figure 4.5.a remind us the idea of spontaneous stochasticity, a fundamental issue of turbulence (and other systems) [FGV01; ED15; TBM20]. Is something similar going on in this system?

To conclude this chapter and before going to the publications referenced previously, we present in Fig. 4.6, visualisations of the reconnection process of a Hopf link in quantum and classical fluids (Navier-Stokes and hyper-viscous Navier-Stokes). The emitted pulse in the quantum case, and the fluid structures dissipated by viscosity and hyper-viscosity are clearly visible. We leave the reader to enjoy the beauty of fluids and draw conclusions.
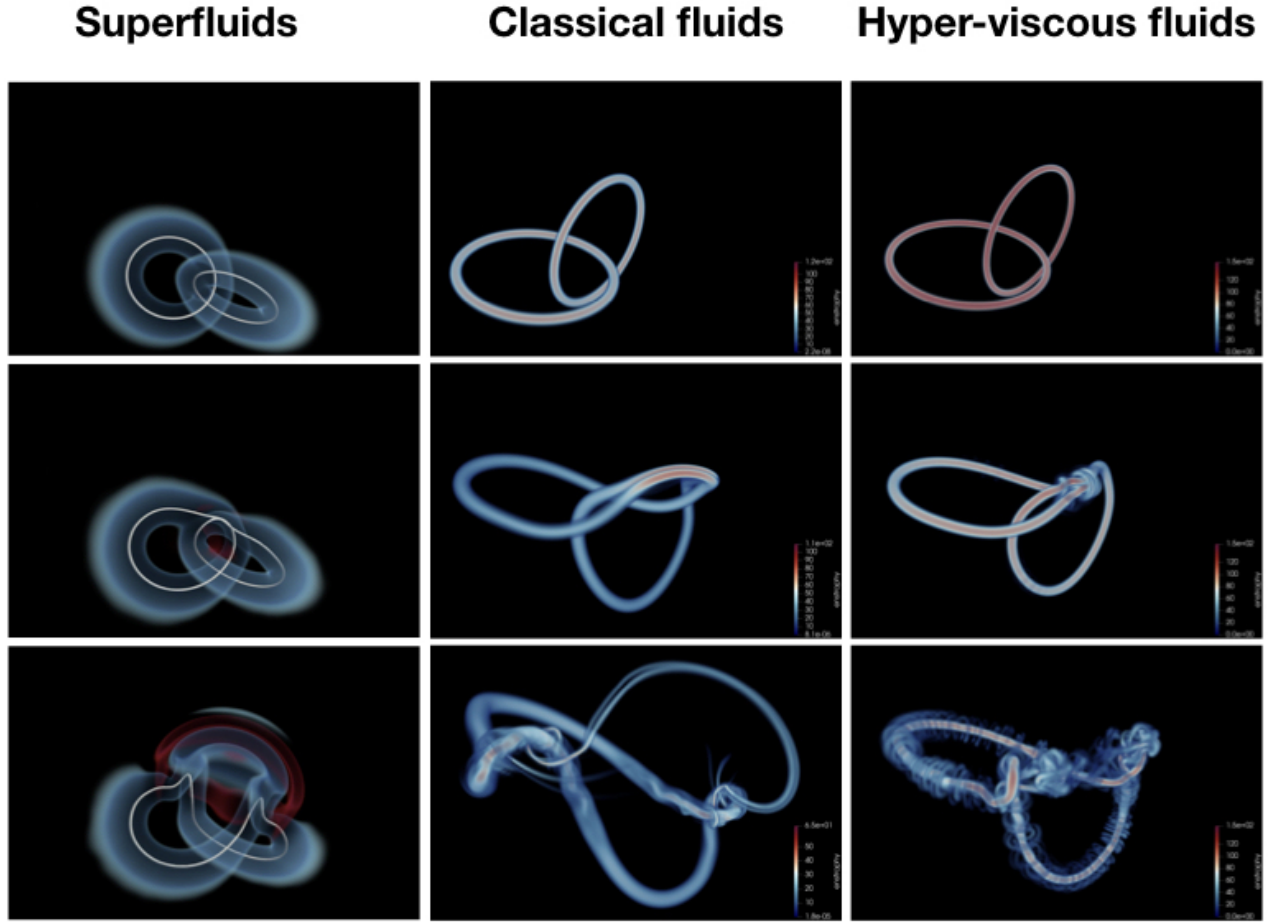
Figure 4.6: **Left panel:** vortex reconnections in superfluids. Visualisation of the density field produced by numerical simulations of the GP model. Vortices are displayed in white as iso-contours of low density values. Density waves are rendered in blue/red colours. **Middle panel:** vortex reconnections in classical fluids. Visualisation of the enstrophy field produced by numerical simulations of the Navier-Stokes equation with $Re_{\mathrm{v}} = \Gamma/\nu = 2500$. **Right panel:** Hyper-viscous simulation (with dissipation $(-\nabla^2)^3$) to mimic high Reynolds numbers. Helical secondary structures develop after reconnection, probably to compensate a loss of global helicity due to the unknotting of the link.

4.3   Selected publications

In this chapter we integrally include three selected publications where I have contributed to the problem of vortex reconnections.

- Alberto Villois, Davide Proment, and Giorgio Krstulovic. "Universal and Nonuniversal Aspects of Vortex Reconnections in Superfluids". In: *Physical Review Fluids* 2.4 (Apr. 4, 2017), p. 044701. ISSN: 2469-990X. DOI: 10.1103/PhysRevFluids.2.044701

- Alberto Villois, Davide Proment, and Giorgio Krstulovic. "Irreversible Dynamics of Vortex Reconnections in Quantum Fluids". In: *Physical Review Letters* 125 (16 Oct. 2020), p. 164501. DOI: 10.1103/PhysRevLett.125.164501

- Umberto Giuriato and Giorgio Krstulovic. "Quantum vortex reconnections mediated by trapped particles". In: *Physical Review B* 102 (9 Sept. 2020), p. 094508. DOI: 10.1103/PhysRevB.102.094508

The first paper contains my first contribution to vortex reconnections. There, we observe the $t^{1/2}$ temporal scaling within the framework of GP for a variety of configurations. We also highlight the importance of the ratio A^+/A^- and relate it to curvature, torsion and the breakdown of self-similarity. This work obtained an international recognition thanks to the *2018 François Naftali Frenkiel Award for Fluid Mechanics* of the APS Division of Fluid Dynamics in Atlanta. https://journals.aps.org/prfluids/pdf/10.1103/PhysRevFluids.4.010002

The second work, appearing in the cover of Physical Review Letter, explains the irreversibility of vortex reconnections. The main results are presented focusing on the physical implications are explained without going in to the mathematical details. All the technical aspects have been published in a joint publication in Physical Review Fluids [PK20c].

Finally, in the third work published in Physical Review B, we studied how quantum vortex reconnections are affected by the presence of particles. In this setting, relevant for experiments in superfluid helium, vortices exchange energy and momentum also with particles. We use a simple model of particle dynamics in the Gross-Pitaevskii equation that will be discussed in detail in the next chapter.

Universal and nonuniversal aspects of vortex reconnections in superfluids

Alberto Villois and Davide Proment

School of Mathematics, University of East Anglia, Norwich Research Park,
Norwich NR4 7TJ, United Kingdom

Giorgio Krstulovic

Université de la Côte d'Azur, OCA, CNRS, Lagrange, Boîte Postale 4229, 06304 Nice Cedex 4, France

Insight into vortex reconnections in superfluids is presented, making use of analytical results and numerical simulations of the Gross-Pitaevskii model. Universal aspects of the reconnection process are investigated by considering different initial vortex configurations and making use of a recently developed tracking algorithm to reconstruct the vortex filaments. We show that during a reconnection event the vortex lines approach and separate always according to the time scaling $\delta \sim t^{1/2}$ with prefactors that depend on the vortex configuration. We also investigate the behavior of curvature and torsion close to the reconnection point, demonstrating analytically that the curvature can exhibit a self-similar behavior that might be broken by the development of shocklike structures in the torsion.

I. INTRODUCTION

Reconnections in fluids have been a subject of study for a long time in the context of plasma physics [1] and both classical [2] and superfluid dynamics [3]. Depending on the physical system considered, such reconnections are events characterized by a rearrangement in the topology of either a magnetic field (magnetic reconnections) or vorticity field (vortex reconnections). Such topological modifications are believed to play a fundamental role in several physical phenomena such as eruptive solar events [4], energy transfer and fine-scale mixing [5], and turbulent states in superfluids [6]. Despite their physical relevance, reconnections represent also a stand-alone mathematical problem, related, for instance, to the presence of singularities in the Euler equation [2,7,8].

In classical fluids described by the Navier–Stokes-type equations, reconnecting vortex tubes stretch and deform, leading to complicated dynamics and the formation of structures like vortex bridges [5]. In order to understand fundamental aspects of vortex reconnections it is often desirable to work with a vortex configuration where the vorticity is confined along lines of zero core size. Such idealization is called a vortex filament. This limit naturally arises in superfluids such as superfluid liquid helium (He II) and Bose-Einstein condensates (BECs). Superfluids are in fact examples of ideal flows of quantum mechanical nature characterized by the lack of viscous dissipation and by a Dirac δ vorticity distribution supported on the vortex filaments. For such fluids, the velocity circulation is equal to a multiple of the Feynman-Onsager quantum of circulation $\Gamma = h/m$, with h the Planck constant and m the mass of the superfluid's bosonic constituents.

Due to Kelvin's circulation theorem (or Alfvèn's theorem in magnetohydrodynamics), in a barotropic ideal flow reconnections should be forbidden since the circulation of vortex lines transported by the flow is conserved and so their topology is frozen. However, as already suggested by pioneering works of Feynman [9] and Schwarz [10], vortex reconnections in superfluids do exist and play a fundamental role in superfluid turbulence. This was indeed confirmed by Koplik and Levine [3], who performed numerical simulations of reconnecting vortex lines within the Gross-Pitaevskii (GP) model. They showed that Kelvin's circulation theorem does not hold in this context because the superfluid density identically vanishes at the vortex filament. With the progress of experimental techniques in the past decade, reconnecting superfluid vortices have been visualized

in He II [6,11] and in BECs [12,13]. From the theoretical side, many works have been devoted to study the reconnecting vortex filaments in superfluids, by using either the so-called vortex filament (VF) model introduced by Schwarz [10] or the GP model.

The simplest question to ask, although contradictory answers appear in the literature, is related to the rates of approach and separation of two reconnecting vortices. Assuming that a reconnection event is a local process in space and the circulation Γ is the only relevant dimensional quantity involved, by simple dimensional analysis it follows that the distance $\delta(t)$ between two reconnecting filaments should scale as

$$\delta(t) \sim (\Gamma t)^{1/2}, \tag{1}$$

independently if it is measured before or after the reconnection. Such a prediction has been confirmed by numerical simulations of the VF model [14] and in He II experiments [11]. In the framework of the GP model, the same scaling was asymptotically derived in Ref. [15], but a number of numerical studies report disparate scaling exponents that may differ between the before and after reconnection stages [16–18]. Another fundamental question regards the universality of the geometrical shape of the vortex filaments at the reconnection. It is expected that vortices become locally antiparallel during the reconnection process [15]. However, using the VF model, it has been reported that the reconnection angle may follow a broad distribution that depends on the turbulent regime that is considered [14]. It has also been observed that during a reconnection event cusps are generated on the filaments and argument has been given either in favor of those cusps being universal [19] or not [20]. Finally, a great deal of interest has arisen recently in the generation of Kelvin waves (helical waves propagating along vortex filaments) [6,21–23] and the evolution of hydrodynamical helicity [24–28] during reconnection events.

The VF model is based on Biot-Savart equations that describe a regularized Dirac δ vorticity distribution field in the incompressible Euler equation; it provides direct information on the vortex filaments and is widely used to mimic superfluid vortex dynamics and turbulence in He II. However, due to Kelvin's circulation theorem in the Euler equation, reconnections here need to be added by some *ad hoc* cut-and-connect mechanisms. In addition, the VF model introduces a small-scale cutoff to regularize Biot-Savart integral divergence and thus cannot explore the vortex dynamics at the smallest scales where the reconnection events take place. The GP model represents an alternative in the study of vortex dynamics and reconnections, the main advantages being that it naturally contains vortex reconnections in its dynamics and that the entire reconnection process is regular due to the identically zero superfluid density field at the vortex core. Studying such small-scale dynamics is crucial for understanding how energy is transferred through scales and eventually dissipated. Unfortunately, no information can be directly inferred from the GP model on the vortex dynamics because this model described the evolution of an *order parameter* complex field, which contains simultaneously sound excitations and vortex lines in the form of topological defects. We will present here a detailed study of vortex reconnections by exploiting a recently developed tracking algorithm [29] that is able to track vortex filaments in numerical simulations of the GP model with a machine epsilon level of accuracy.

In order to understand what is universal in vortex filament reconnection mechanisms, we study the dynamics of four different initial configurations: (a) perpendicular and (b) almost antiparallel lines, (c) a trefoil knot, and (d) reconnections occurring in a fully turbulent tangle dynamics. We will show that reconnecting vortex lines always obey the dimensional analysis scaling (1) (both before and after reconnection) and they generally separate faster than they approach. In addition, we report that, regardless of the initial configuration, vortices become antiparallel at the reconnection. We also report a self-similar behavior of the curvature close to the reconnection point when torsion does not play an important role and shocklike structures appear in the torsion evolution for some configurations. Those findings are explained by some asymptotic calculations.

II. THE GP MODEL AND RECONNECTION CASE STUDIES

The GP model is a dispersive nonlinear wave equation describing the dynamics of the order parameter ψ of a BEC arising in dilute Bose gases; for the sake of completeness and clarity we introduce it in Appendix A. When ψ is linearized about a constant value $\psi_0 = \sqrt{\rho_0/m}$, the sound velocity results in $c = \sqrt{g\rho_0}/m$ and dispersive effects take place at length scales smaller than the healing length $\xi = \hbar/\sqrt{2\rho_0 g}$. This can be easily understood by rewriting the GP model using those physical parameters

$$i\frac{\partial\psi}{\partial t} = \frac{c}{\sqrt{2}\xi}\left(-\xi^2\nabla^2\psi + \frac{m}{\rho_0}|\psi|^2\psi\right) \tag{2}$$

and comparing the magnitude of the first and second terms on the right-hand side. Note also that by a suitable time and space rescaling, the parameters c and ξ can be reabsorbed; in this work length and time scales are expressed in units of the healing length ξ and its characteristic time $\tau = \xi/c$.

The relationship between the GP equation and a hydrodynamical model is immediately illustrated by introducing the Madelung transformation

$$\psi(\mathbf{x},t) = \sqrt{\frac{\rho(\mathbf{x},t)}{m}}e^{i[\varphi(\mathbf{x},t)/\sqrt{2}c\xi]}, \tag{3}$$

which relates ψ to an inviscid, compressible, irrotational, and barotropic superfluid of density $\rho(\mathbf{x},t)$ and velocity $\mathbf{v} = \nabla\varphi$. In the domain where the Madelung transformation is well defined ($\psi \neq 0$), the velocity field is potential. However, vortices may exist as topological defects of the order parameter. In places where the density vanishes (nodal lines) arg ψ is not defined. The field ψ still remains a single-value function if the circulation $\oint \mathbf{v} \cdot d\ell$ along a nodal line is a multiple of the quantum of circulation $\Gamma = h/m = 2\sqrt{2}\pi c\xi$. For this reason nodal lines of ψ are called quantum (or quantized) vortices. Their corresponding velocity field $\mathbf{v}$ thus decays as the inverse of the distance to the vortex and their vorticity is therefore a Dirac-supported distribution. Their typical vortex core size is order of ξ.

The GP equation (2) is numerically integrated with a pseudospectral code. The resolution is chosen carefully to sufficiently resolve the vortex core in space and the reconnections in time. We consider four different initial configurations in a cubic box of size L with N collocation points in each dimension.

(a) Perpendicular lines. The order parameter field is characterized by straight vortex filaments perpendicular to each other and having an initial distance of 6ξ. This initial configuration is shown in Fig. 1(a1) for $L/\xi = 128$ and $N = 256$.

(b) Antiparallel lines. Vortex filaments with opposite circulation are set at an average distance of 6ξ. In order to trigger a Crow instability [30], a small perturbation is introduced by adding a Kelvin wave of amplitude ξ and wavelength equal to the system size. The initial configuration is shown in Fig. 1(b1) for $L/\xi = 128$ and $N = 256$.

(c) Trefoil knot. A vortex filament reproducing a torus $\mathcal{T}_{2,3}$ knot (a trefoil) is produced following [31]; the torus on which the knot is built has toroidal and poloidal radii of $R_0 = 16\xi$ and $R_1 = 4\xi$, respectively. The initial configuration is shown in Fig. 1(c1) for $L/\xi = 128$ and $N = 256$.

(d) Turbulent tangle. We prepare an initial condition consisting of several large-scale vortex rings that replicates a Taylor-Green flow as in Ref. [32]. The initial condition then evolves in time: The rings reconnect, breaking the initial symmetry and creating a dense turbulent tangle displayed in Fig. 1(d1) (see [33] for a complete description of the field evolution). We study four successive vortex reconnection events occurring in a small volume [Fig. 1(d2)] at stages when the tangle density is higher for $L/\xi = 256$ and $N = 256$.

The time stepping scheme for cases (a) and (b) is a Strang-splitting method, whereas for cases (c) and (d) it is a second-order Runge-Kutta method. In each case, the time step is chosen to be smaller than the fastest linear time scale of the system. Conservation of the invariants has been carefully checked.
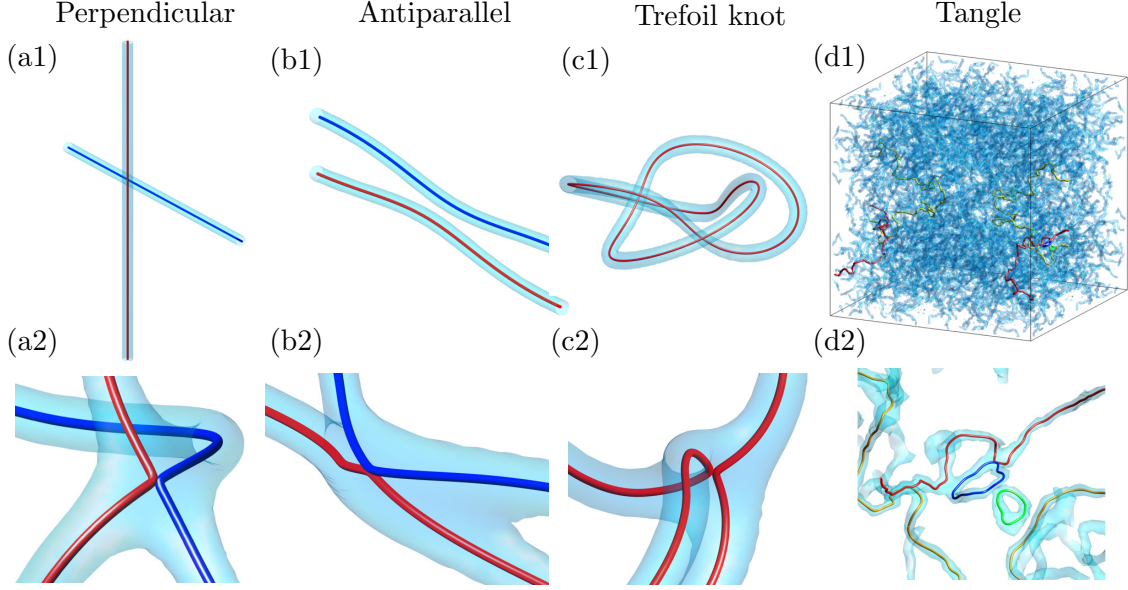
FIG. 1. Three-dimensional plot showing the reconnection events explored numerically. The initial configuration is displayed for (a1) the perpendicular vortex lines, (b1) the antiparallel lines, and (c1) the trefoil knot. (a2)–(c2) show a corresponding zoom at the moment of reconnection. Also shown are (d1) the turbulent tangle and (d2) a zoom in of where a reconnection takes place. Red and blue correspond to the reconnecting vortex filaments; the light blue isosurfaces render the density field at low values.

III. APPROACH AND SEPARATION RATES

Apart from the characteristic length scale ξ inherently present in the GP model, when quantized vortices are considered, the quantum of circulation Γ can be used to formulate an extra length scale. Hence, by dimensional analysis, the distance between two reconnecting lines is expected to be

$$\delta^{\pm}(t) = A^{\pm}\xi^{1-2\alpha^{\pm}}|\Gamma(t - t_r)|^{\alpha^{\pm}}, \tag{4}$$

where $\alpha^{\pm}$ and $A^{\pm}$ are dimensionless parameters and the superscript $\pm$ stands for before ($-$) and after ($+$) the reconnection event. The temporal evolution of the minimal distances between reconnecting filaments for the different case studies is displayed in Figs. 2(a)–2(d). An explanatory movie of the knot reconnection is also provided as Supplemental Material [34]. Remarkably, in all cases the approach and separation rates follow the same dimensional $t^{1/2}$ scaling. For each event we estimate the reconnection time t_r by doing a linear fit on $\delta^{\pm}(t)^2$ and compute t_r as the arithmetic mean between $t_r^{\pm}$ that satisfies $\delta^{\pm}(t_r^{\pm})^2 = 0$. The $t^{1/2}$ scaling extends beyond ξ and only slight deviations are observed in some cases. Perhaps this fact could explain the different results for the scaling obtained in Refs. [16–18], where it was concluded that the exponents before and after the reconnection are different. For instance, in Ref. [16] it was found that $\alpha^- \in (0.3, 0.44)$ and $\alpha^+ \in (0.6, 0.73)$ and in Ref. [18] that either $\alpha^{\pm} = 1/2$ or $\alpha^- = 1/3$ and $\alpha^+ = 2/3$, depending on the initial vortex filament configuration. In these works the time asymmetry was interpreted as a manifestation of the irreversible dynamics due to sound emission; we will return to this interesting point in Sec. VI. Let us stress that the tracking algorithm we used is able to measure the intervortex distances even in the presence of sound waves (the Taylor-Green tangle analyzed contains moderate sound at all scales) and no asymmetry concerning the exponent is observed.

Although the measured exponent is always $\alpha^{\pm} = 1/2$, the full dynamics is not symmetrical with respect to the reconnection time as it can be immediately deduced by observing Fig. 2. By estimating the prefactors $A^{\pm}$ with a fit, shown in Fig. 3(a), we conclude that these are always order of the unity but are not universal. Moreover, we observe that the vortex filaments usually separate faster than they approach ($A^- \lesssim A^+$).
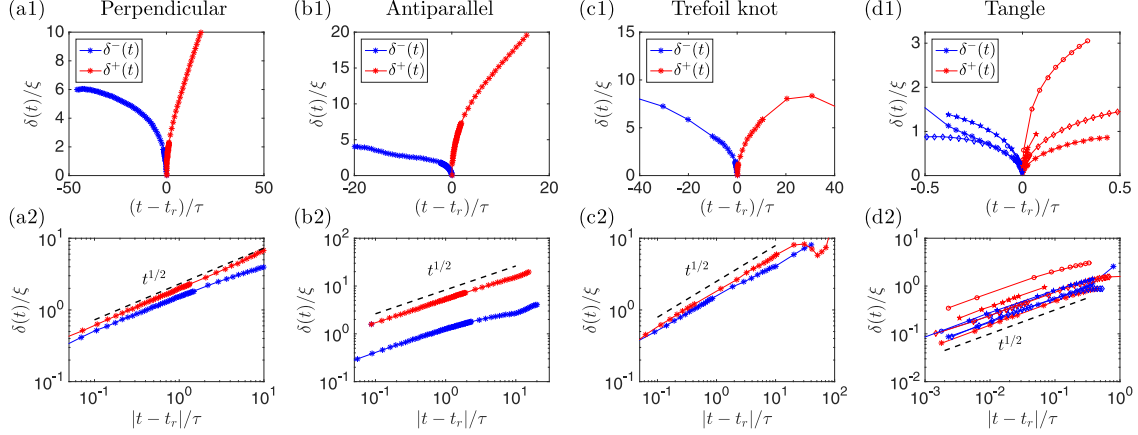
FIG. 2. Temporal evolution of the distance between the reconnecting vortex filaments before (blue) and after (red) the estimated reconnection time t_r for the (a) perpendicular, (b) antiparallel, (c) trefoil knot, and (d) turbulent tangle configurations. For the turbulent tangle four different reconnection events have been tracked. (a2)–(d2) Same plots as in (a1)–(d1) but on a log-log scale.

The tracking algorithm we use follows the pseudovorticity and naturally provides the orientation of the filament with respect to the circulation. It thus allows us to compute the tangent vectors to the lines and infer the orientation of the filaments by evaluating the cosine of the angle θ between the vectors at the two closest points as illustrated in Fig. 3(b) and in Ref. [34]. By approaching
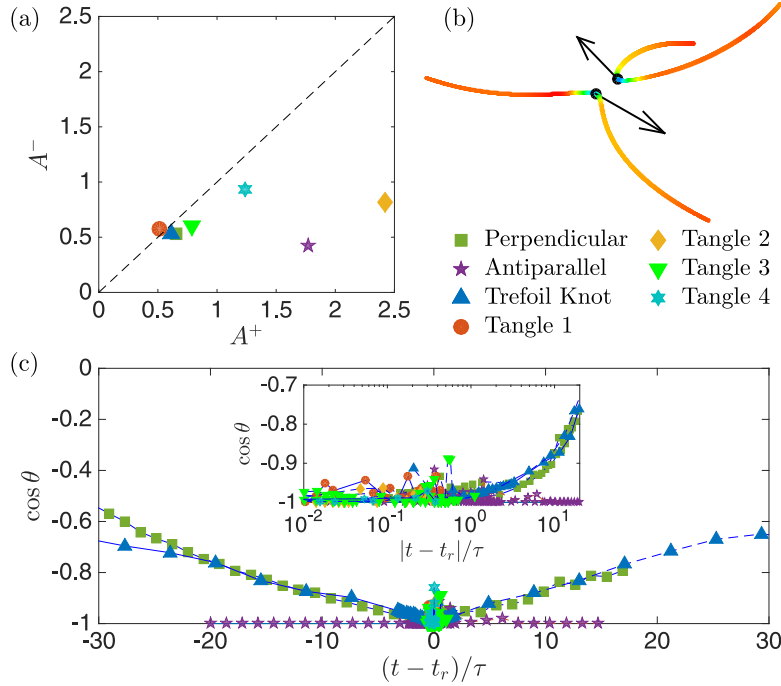
FIG. 3. (a) Fitted values of the prefactors $A^{\pm}$ corresponding to (4). (b) Example of reconnecting filaments (trefoil knot case). The black dots represent the points of minimal distances and are used to compute $\delta(t)$, the arrows are the tangents of the filaments at those points, and the reconnection angle θ is defined by using the scalar product of the tangents. The coloring is proportional to the filament curvature (low in red and high in green and blue). (c) Temporal evolution of the cosine of the reconnecting angle. The inset displays the same plot on a log-log scale.

the reconnection point each vortex filament develops a cusplike structure characterized by high and localized values of the curvature (displayed in green and blue). The temporal evolution of $\cos\theta$ for all the case studies is presented in Fig. 3(c). It is apparent that, independently of the initial configurations, vortices are always antiparallel at the reconnection point. This behavior appears to be time symmetric about the reconnection time and is smooth, as highlighted in the inset of Fig. 3(c), where we show $\cos\theta$ in log-lin coordinates for a better view of the short times before and after reconnection.

IV. ANALYTICAL PREDICTIONS USING A LINEAR APPROXIMATION

The results presented in Figs. 2 and 3 support the analytical predictions obtained by Nazarenko and West in Ref. [15]. Their seminal calculations consider a planar reconnection of two vortex filaments having a hyperbolic configuration at times close to t_r. As we will observe in the following, vortex reconnections do not always fully lie in a plane and the local torsion of the filament can play an important role. We generalize here the calculations performed in Ref. [15], including torsion of the vortex lines to understand its effect during the reconnection. Let us assume that at the reconnection time t_r and close to the reconnection point the order parameter of two reconnecting nonplanar vortex lines is given by

$$\psi_r(x,y,z) = z + \frac{\gamma}{a}(x^2+y^2) + i(az + \beta x^2 - y^2), \tag{5}$$

with $a \neq 0$ and $\frac{\beta-\gamma}{\gamma+1} > 0$ (the Nazarenko-West reconnecting vortex profile is recovered by setting $\gamma = 0$). In the vicinity of the vortex filaments, ψ is small and the nonlinear term in Eq. (2) can be neglected. Within this approximation the pre- and postreconnection solution is given by $\psi(x,y,z,t) = e^{[i(t-t_r)\Gamma/4\pi]\nabla^2}\psi_r(x,y,z)$. By solving $\psi(x,y,z,t) = 0$ we can explicitly obtain the temporal evolution of the vortex lines. Equation (4) is obtained with

$$\alpha^+ = \alpha^- = \frac{1}{2}, \quad \frac{A^+}{A^-} = \sqrt{\frac{1+\gamma}{\beta-\gamma}} \tag{6}$$

for $a > 0$ and $\beta < 1 - 2\gamma/a^2$ (refer to Appendix C for a figure of the vortex profiles, details on the above calculations, and different choices of a and β). Interestingly, the angle between the asymptotes of the hyperbolic vortex configuration close to reconnection is found to be $\phi = 2\tan^{-1}(A^-/A^+)$.

The linear approximation also allows for computing the curvature and torsion of the vortex lines. As pointed out by Schwarz in Ref. [10], the curvature $\kappa^\pm(s,t)$ should present a self-similar behavior close to the reconnection point of the form $\kappa^\pm(s,t) = \kappa_{max}^\pm(t)\Phi^\pm(\zeta^\pm)$, where $\zeta^\pm = (s-s_r)\kappa_{max}^\pm(t)$, s_r is the coordinate of the reconnecting point, and κ_{max} is the maximum value of curvature. The present calculations predict

$$\kappa_{max}^\pm(t) \propto |t-t_r|^{-1/2}, \quad \frac{\kappa_{max}^+(t)}{\kappa_{max}^-(t)} = \left(\frac{A^+}{A^-}\right)^3. \tag{7}$$

Note that the $t^{-1/2}$ scaling could be directly inferred by dimensional analysis arguments but not the scaling of the dimensionless prefactors. Moreover, these self-similar functions $\Phi^\pm(\zeta^\pm)$ can be expressed in compact forms for small values of γ and $t - t_r$ as

$$\Phi^\pm(\zeta) = \frac{1}{\{1 + [(\frac{A^\mp}{A^\pm})^2+1]\zeta^2\}^{3/2}} + O\left(\eta^\pm\gamma^2\frac{(t-t_r)}{\tau}\right), \tag{8}$$

with $\eta^\pm = (A^\mp/A^\pm)^2 - 1$. This function corresponds to a cusp in the vortex filament at $t = t_r$ and $s = s_r$. The dependence on the coefficient $(A^\mp/A^\pm)^2 + 1$ multiplying the self-similar variable $\zeta^\pm$ is unexpected and could not also be guessed by dimensional arguments. We also remark that the self-similarity is only exact when $\gamma = 0$ or $\eta^\pm = 0$.
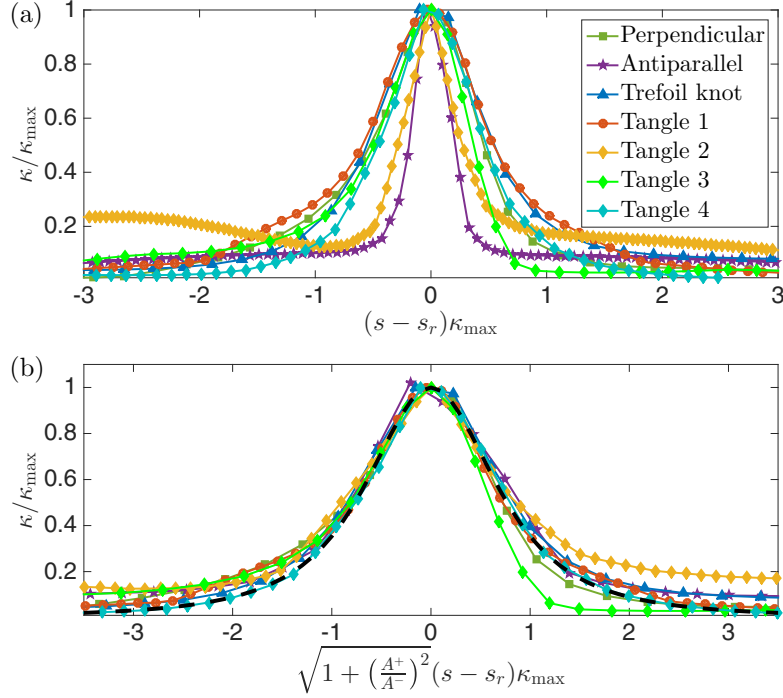
FIG. 4. (a) Curvature normalized by $\kappa_{\max}$ close to (just before) the reconnection time for all reconnection events explored as a function of $(s - s_r)\kappa_{\max}$. (b) Same data represented using the scaling suggested by the self-similar form (8). The black dashed line displays the theoretical prediction.

Finally, the torsion $\mathcal{T}^{\pm}(s,t)$ of the vortex line can also be computed within this approximation. When $\gamma \neq 0$ torsion is not identically null but it vanishes at s_r, thus confirming that reconnections occur locally on a plane. Also, it can be proved that it changes sign linearly at s_r with a slope that diverges as $\gamma |t - t_r|^{-1/2}$, creating shocklike structures. The slope ratio before and after the reconnection satisfies the relation $\frac{d\mathcal{T}^+}{ds}/\frac{d\mathcal{T}^-}{ds}|_{s=s_r} = A^+/A^-$.

We observe that in the context of Euler and Navier-Stokes flows, dynamical equations for torsion and curvature have been derived in Ref. [35]. These nonlinear equations do not allow for predicting the generation of curvature cusps and shocklike torsion structures. It would be interesting to investigate if the scaling laws reported above also remain valid in classical fluids and MHD flows.

V. NUMERICAL MEASUREMENTS OF THE CURVATURE AND TORSION

Motivated by the previous asymptotic results, we analyze the data coming from simulations. We start by looking at the curvature at a fixed time very close to the reconnection. In Fig. 4(a) the curvature just before t_r normalized using $\kappa_{\max}$ is shown for all configurations. We indeed observe the formation of a cusp at the reconnection point s_r in all cases. Note that, strictly speaking, no universal function of the curvature is observed. This is actually expected from the calculations of the curvature (8), which shows a dependence on the values A^+/A^- that differ from case to case. However, (8) suggests that if the variable $\sqrt{1 + (A^+/A^-)^2}(s - s_r)\kappa_{\max}$ is used instead, a universal form should be recovered. As shown in Fig. 4(b), the data indeed collapse into one universal function when using this new variable. The theoretical prediction (8) is also plotted with a dashed black line to appreciate the remarkable agreement.

We now study the temporal evolution of the curvature to determine if a self-similar evolution is observed. Figure 5(a) shows how the trefoil knot curvature curves, rescaled by their maximum values, almost perfectly collapse into a single plot, demonstrating the self-similar behavior for this
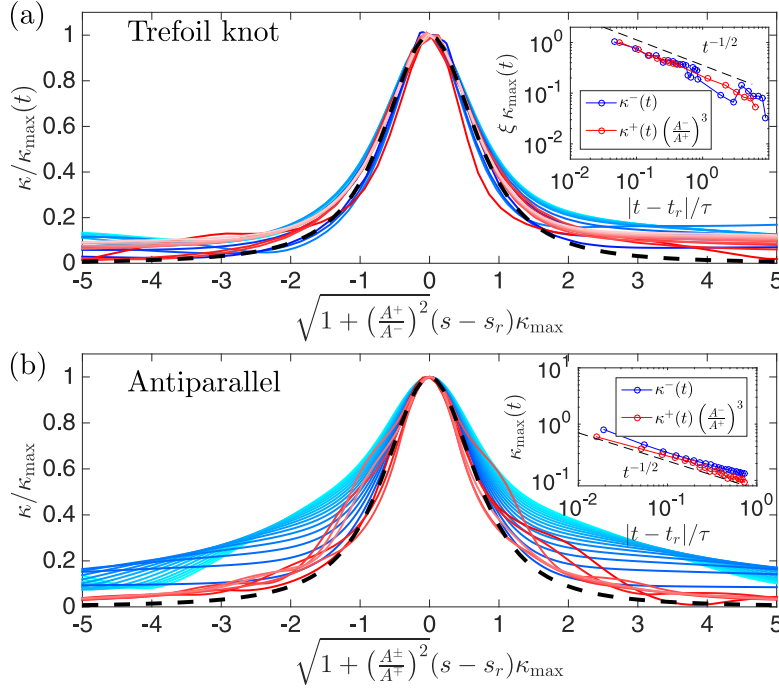
FIG. 5. (a) Self-similar evolution of the curvature close to the reconnection point for the trefoil vortex. Blue lines (from light to dark) correspond to times before reconnection and red lines (from dark to light) to times after reconnection. The inset displays the temporal evolution of the maximum value of the curvature on a log-log scale before and after, normalized as suggested in Eq. (7). (b) Same plot as in (a) but for the reconnection occurring in the antiparallel case. In both figures we consider times such that $|t - t_r| < 0.5\tau$ and the dashed line shows the $t^{-1/2}$ scaling. In both figures the black dashed line displays the theoretical prediction (8).

configuration. In the inset we plot the maximum value of the curvature as a function of time on a log-log scale. The predicted $t^{-1/2}$ scaling of (7) is clearly observed. In Fig. 5(b) we present the same analysis done for the antiparallel case where a clear breakdown of the self-similar behavior is observed. This can be explained by assuming a non-negligible value of γ, hence a strong torsion, that breaks the validity of the expansion done to obtain (8), only recovered when times are very close to t_r, as evident when comparing with the theoretical prediction displayed as a dashed black line. The temporal evolution of the maximum of curvature, shown in the inset of Fig. 4(b), still confirms the relations presented in Eq. (7), namely, the scaling $t^{-1/2}$ scaling normalized by the ratio of the prefactors is confirmed. Note that the agreement is very good given the large value $(A^+/A^-)^3 = 4.15^3$. For all other cases except tangle 2, self-similarity is observed (data not shown).

The breakdown of self-similarity is predicted by (8) when $A^+/A^- \neq 1$ and $\gamma \neq 0$. A nonzero value of γ is related, as we have seen, to torsion close to the reconnection point and a shocklike structure formation (see Appendix C). In Fig. 6(a) we show the temporal evolution of the torsion $\mathcal{T}$ for the antiparallel case. The shocklike structure formation, as well as the linear behavior close to the reconnection point, is clearly visible, thus explaining the breakdown of the self-similarity in Fig. 5(b). The inset shows that the temporal evolution of the slope of the torsion at s_r obeys the scaling $|t - t_r|^{-1/2}$ with the correct normalization A^+/A^- suggested by the analytical calculations. For completeness, in Fig. 6(b) we show the torsion normalized by the maximum value of the curvature for all the configurations close to the reconnection time. In all the other cases except for tangle 2, the slope of torsion is almost zero at the reconnection point. Remarkably, tangle 2 and antiparallel configurations correspond to the cases where vortices separate much faster than they approach [see Fig. 3(a)]. We remark finally that measuring quantities such as curvature and torsion is numerically very challenging as they involve high-order derivatives.
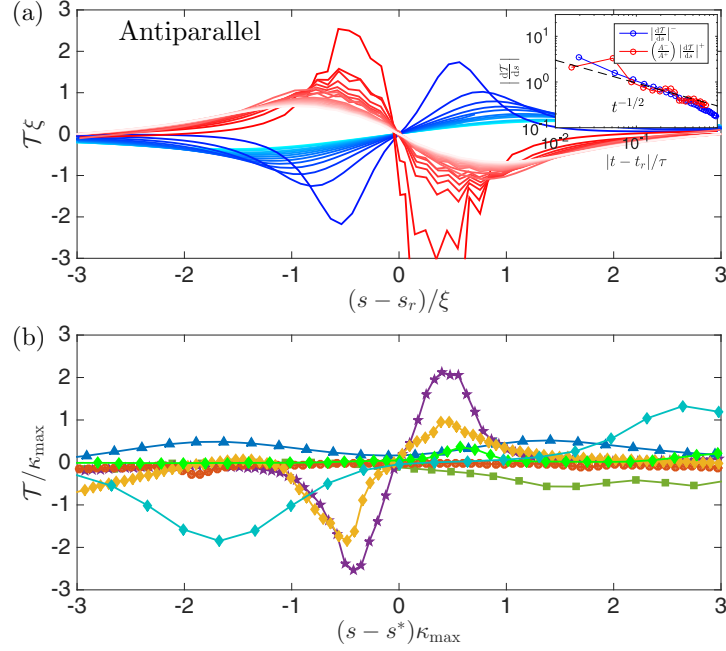
FIG. 6. (a) Temporal evolution of the torsion $\mathcal{T}$ as a function of the arc length in the antiparallel case. Blue lines (from light to dark) correspond to times before reconnection and red lines (from dark to light) to times after reconnection. The inset displays the temporal evolution of the slope of torsion computed at the reconnection point s_r on a log-log scale before and after, normalized as A^+/A^-. (b) Torsion $\mathcal{T}$ as a function of the arc length close to (just before) the reconnection for all configurations (same legend as in Fig. 4).

VI. DISCUSSION

The reconnection of quantized vortex filaments within the Gross-Pitaevskii model displays both universal and nonuniversal phenomena. We found that close to the reconnection the approach and separation rates follow the same scaling $\delta \sim (\Gamma t)^{1/2}$ and the vortex filaments always become locally antiparallel. Previous numerical studies reported scaling rates in the form of a power law with exponents depending on the configuration. By dimensional analysis, any scaling different from $\alpha = 1/2$ would introduce necessarily a new time or length scale to the problem that needs to be made explicit. The discrepancies in previous studies might be due to the fact that (i) the computational domain is not big enough, hence introducing a non-negligible system size length scale, (ii) the initial condition contains a considerable amount of sound waves such that the rms value of the compressible kinetic energy can be used to construct an extra time scale, or (iii) the observed scaling corresponds to dynamical regimes occurring much farther or later than the reconnection event and is thus driven by the specific vortex configuration and therefore is nonuniversal. In that spirit, reconnections within Navier-Stokes flows, a modified version of the model GP with nonlocal potential and/or high-order nonlinearities to better replicate superfluid liquid helium, or coupled GP equations modeling multicomponent or spinorial BECs could indeed lead to different scalings.

Our findings demonstrate that the prefactors $A^\pm$ are not universal in the GP method. However, once measured case by case, their ratio determines many properties of the reconnection dynamics. Note that the easiest way to determine this ratio is to look at the medium- to large-scale reconnection angle ϕ between the hyperbola asymptotes, which should be an accessible quantity in superfluid experiments [11,13,36]. Let us also remark that the $t^{1/2}$ scaling we observed extends beyond the distance ξ. This suggests that the linear approximation might be used as a matching theory in order to relate measurements done well before and far from the reconnection events. Bose-Einstein

condensate experimentalists are able today to study vortex dynamics and reconnections [13,36]. Our predictions should directly apply to those systems.

Finally, let us underline that understanding the dynamics of the reconnection events is crucial to provide a full comprehension of the dissipative processes occurring in superfluids in the low-temperature limit. It is largely believed that Kelvin waves play a fundamental role carrying the energy to the smallest scales where it finally gets dissipated by sound radiation. The cusps arising in the vortex filaments due to reconnection events are responsible for a rapid and efficient excitation of Kelvin waves at all scales. Here we provided an analytical formula for the dynamical formation of the cusps and we aim to use this result in further theoretical studies to estimate the rate of radiation during reconnection. Also, we have shown that non-negligible torsion of the reconnecting filaments implies the breakdown of self-similarity, resulting in the formation of shocklike structures of the torsion. This phenomenon seems to be linked to the large difference observed in the $A^{\pm}$ prefactors, hence to extreme events where vortices separate much faster than they approach, and to the irreversibility of the reconnection events. We do not have yet a theoretical understanding of this fact and more data would be desirable to perform a detailed statistical analysis.

APPENDIX A: THE GROSS-PITAEVSKII EQUATION

In the limit of very low temperature a weakly interacting Bose gas can be described using a mean field approximation in terms of a complex order parameter (or condensate wave function) ψ. Such a system is governed by a dispersive nonlinear wave equation called the Gross-Pitaevskii equation

$$i\hbar \frac{\partial \psi}{\partial t} = -\frac{\hbar^2}{2m} \nabla^2 \psi + g|\psi|^2 \psi - \mu \psi, \tag{A1}$$

where m is the mass of the bosons and $g = 4\pi a\hbar^2/m$, with a the boson s-wave scattering length. The chemical μ can in principle be absorbed by a global phase shift. Although formally derived for BECs, the GP model qualitatively reproduces many aspects of superfluid liquid helium too. It can be used to model classical vortex dynamics in situations where a large-scale separation between the vortex core and the size of such a vortex is present.

The GP equation possesses a Hamiltonian structure and conserves the total number of particles

$$N = \int |\psi|^2 d^3\mathbf{x}, \tag{A2}$$

the total energy

$$H = \int \left(\frac{\hbar^2}{2m} |\nabla\psi|^2 + \frac{g}{2}|\psi|^4 \right) d^3\mathbf{x}, \tag{A3}$$

and the total momentum

$$\mathbf{P} = \frac{\hbar}{2i} \int [\psi^* \nabla\psi - \psi \nabla\psi^*] d^3\mathbf{x}. \tag{A4}$$

The speed of sound for such a model is given by $c = \sqrt{g\rho_0}/m$. This value can be derived by linearizing (A1) about a constant value $\psi = \sqrt{\rho_0/m} = \sqrt{\mu/g}$. It is also possible to identify a characteristic length $\xi = \hbar/\sqrt{2\rho_0 g}$, called healing length, representing the scale where the linear contribution in Eq. (A1) equals the nonlinear one. Dispersive effects will then take place for length scales smaller than ξ. Equation (A1) can be rewritten in term of the two physical quantities c and ξ as

$$i\frac{\partial\psi}{\partial t} = \frac{c}{\sqrt{2}\xi}\left(-\xi^2\nabla^2\psi - \psi + \frac{m}{\rho_0}|\psi|^2\psi\right).\tag{A5}$$

By using the Madelung transformation

$$\psi(\mathbf{x},t) = \sqrt{\frac{\rho(\mathbf{x},t)}{m}}e^{i[\varphi(\mathbf{x},t)/\sqrt{2}c\xi]},\tag{A6}$$

it possible to relate the order parameter ψ to a compressible, irrotational, and barotropic superfluid having density $\rho(\mathbf{x},t)$ and velocity $\mathbf{v} = \nabla\varphi$. Indeed, plugging the transformation (A6) into (2), we directly obtain

$$\frac{\partial\rho}{\partial t} + \nabla \cdot (\rho\mathbf{v}) = 0,\tag{A7}$$

$$\frac{\partial\phi}{\partial t} + \frac{1}{2}\mathbf{v}^2 = c^2\frac{\rho_0 - \rho}{\rho_0} + c^2\xi^2\frac{\nabla^2\sqrt{\rho}}{\sqrt{\rho}}.\tag{A8}$$

Equations (A7) and (A8) are the continuity equation and the Bernoulli equation, respectively, except for the last term in Eq. (A8), which is called quantum pressure and has no analog in classical fluid mechanics.

Although the velocity field defined by the Madelung transformation (A6) is potential, solutions with nonzero circulation can exist in the form of topological defects of the order parameter ψ. For such vortex solutions the vorticity is supported on the curves (nodal lines) where the density field vanishes and the phase is not defined. In order to ensure that the order parameter stays single valued, the circulation around such nodal lines must be constant and equal to a multiple of the Onsager-Feynman quantum of circulation $\Gamma = h/m = 2\sqrt{2}\pi c\xi$. For this reason, nodal lines of the order parameter are called quantum (or quantized) vortices. The region around the topological defect where the density drops to zero is called the vortex core and its size is of the order of the healing length ξ. The hydrodynamical interpretation of superfluids is thus the one of a compressible (dispersive) flow where vorticity is a distribution (a superposition of Dirac δ's) supported on the vortex filament.

We would like to remark that often quantum vortices are misleadingly referred to as the singularities of the system, as the velocity field diverges as $1/r$, where r is the distance to the filament. This divergence is just a consequence of the change of coordinates given by the Madelung transformation. At the vortex position, the order parameter solution of the GP equation is a smooth field. We can thus precisely track vortices finding the zeros of ψ as described in Appendix B.

APPENDIX B: VORTEX TRACKING ALGORITHM

We have recently developed a robust and accurate algorithm to track vortex lines of the order parameter ψ in arbitrary geometries. The details of the algorithm and accuracy of the method can be found in Ref. [29]. We recall here the basic ideas. A quantized vortex line in three dimensions corresponds to a nodal line defined by

$$\text{Re}[\psi(x,y,z)] = \text{Im}[\psi(x,y,z)] = 0.\tag{B1}$$

The algorithm is based on a Newton-Raphson method to find zeros of ψ and on the knowledge of the *pseudovorticity* field $\mathbf{W} = \nabla\,\text{Re}[\psi] \times \nabla\,\text{Im}[\psi]$, always tangent to the filaments, to follow vortex lines [18]. Starting from a point $\mathbf{x}_0$ where the density $|\psi|^2$ is below a given small threshold (therefore
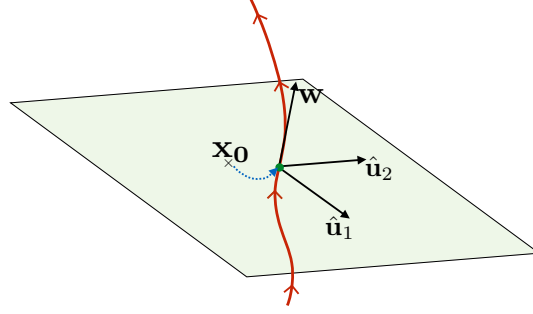
FIG. 7. Sketch of the plane on which the Newton-Raphson method is implemented.

very close to a vortex), we define the orthogonal plane to the vortex line using $\mathbf{W}(\mathbf{x}_0)$. The plane is then spanned by the two directors $\hat{\mathbf{u}}_1$ and $\hat{\mathbf{u}}_2$, as illustrated in Fig. 7. A better approximation for the vortex position $\mathbf{x}_v$ on the plane is then given by $\mathbf{x}_1 = \mathbf{x}_0 + \delta\mathbf{x}$. Here the increment $\delta\mathbf{x}$ is obtained using the Newton-Raphson formula (the linear approximation)

$$0 = \psi(\mathbf{x}_0 + \delta\mathbf{x}) \approx \psi(\mathbf{x}_0) + J(\mathbf{x}_0)\delta\mathbf{x}, \tag{B2}$$

where $J(\mathbf{x}_0)$ is the Jacobian matrix expressed as

$$J = \begin{pmatrix} \nabla \operatorname{Re}[\psi] \cdot \hat{\mathbf{u}}_1 & \nabla \operatorname{Re}[\psi] \cdot \hat{\mathbf{u}}_2 \\ \nabla \operatorname{Im}[\psi] \cdot \hat{\mathbf{u}}_1 & \nabla \operatorname{Im}[\psi] \cdot \hat{\mathbf{u}}_2 \end{pmatrix}. \tag{B3}$$

The increment can be therefore calculated using $\delta\mathbf{x} = -J^{-1}(\mathbf{x}_0) \cdot \{\operatorname{Re}[\psi(\mathbf{x}_0)], \operatorname{Im}[\psi(\mathbf{x}_0)]\}^T$. Sufficiently close to the line, the Jacobian matrix is always a nonsingular 2×2 matrix, so its inverse can be computed. We underline that the method requires the evaluation of the Jacobian (B3) at intermesh points. Making use of the spectral representation of ψ, we can precisely compute those values using Fourier transforms. This process can be iterated until the exact location $\mathbf{x}_v$ is determined upon a selected convergence precision.

To track the following vortex point of the same line we use as a next initial guess $\mathbf{x}_0 = \mathbf{x}_v + \zeta\mathbf{W}$, which is obtained evolving along $\mathbf{W}$ by a small step ζ. The process is reiterated until the entire line is tracked and closed and then repeated with another line until the whole computation domain has been fully explored.

APPENDIX C: DETAILED CALCULATIONS OF THE LINEAR APPROXIMATION

An analytical study of a reconnection event in the GP model was provided by Nazarenko and West [15], where it is shown that two vortices are antiparallel during a reconnection and their distance scales as $\delta(t) \sim t^{1/2}$. In the same spirit as [15], we assume that inside the vortex core the nonlinear term of the GP equation can be neglected and so a reconnection event should be governed by the (linear) Schrödinger equation. For the sake of simplicity, in dimensionless units this equations reads

$$i\partial_t\psi + \tfrac{1}{2}\nabla^2\psi = 0. \tag{C1}$$

Note that we absorbed the parameters c and ξ in Eq. (2) by a suitable time and space rescaling. We remark that in Ref. [15] reconnections are studied just on a plane, whereas here we consider vortex filaments with nonzero torsion. At the reconnection time t_r we use as the initial condition the ansatz

$$\psi_r(x,y,z) = z + \frac{\gamma}{a}(x^2 + y^2) + i(az + \beta x^2 - y^2). \tag{C2}$$

Looking for $\psi_r = 0$, one can recover the vortex profile, given by the curves

$$\mathbf{R}(s) = \left(s, \pm s\sqrt{\frac{\beta - \gamma}{\gamma + 1}}, -s^2\frac{\gamma(\beta + 1)}{a(\gamma + 1)}\right), \tag{C3}$$
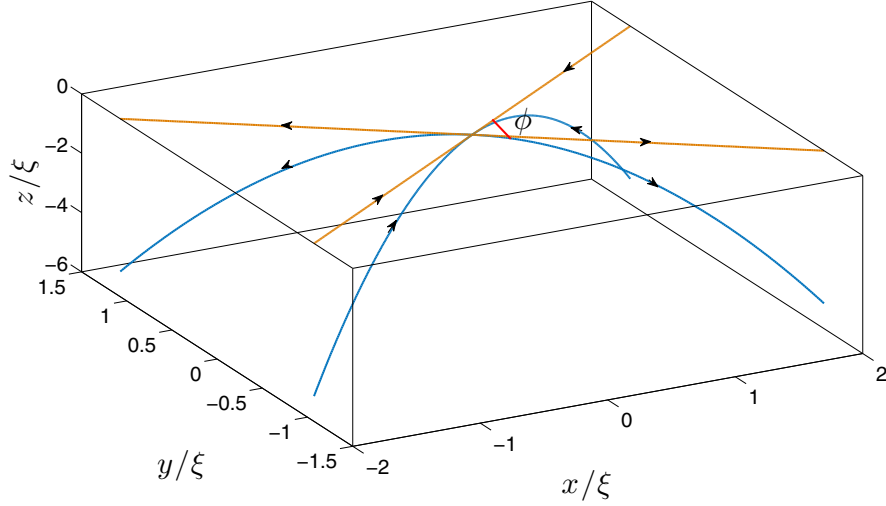
FIG. 8. Plot of the initial condition using $\gamma = 0.01$, $\beta = 1/2$, and $a = 1$. The vortex filaments are shown in blue while their projection on the x-y is shown in orange. The arrows identify the circulation around each vortex.

where s is the parametrization of the curve. We note that (C3) requires that

$$\frac{\beta - \gamma}{\gamma + 1} > 0. \tag{C4}$$

In Fig. 8 we plot the vortex filaments $\mathbf{R}(s)$ (blue lines) for our initial condition.

The vortices projected on the x-y planes form two hyperbola (orange lines) crossing at the reconnection point. We note that the values β and γ fix the angle

$$\phi = 2\tan^{-1}\left(\sqrt{\frac{1 + \gamma}{\beta - \gamma}}\right) \tag{C5}$$

between the two hyperbola. The arrows identify the circulation around each vortex.

The formal solution of Eq. (C1) is given by

$$\psi(t) = e^{i[(t-t_r)\nabla^2/2]}\psi_r, \tag{C6}$$

where t_r is the time when the reconnection occurs. The choice of a second-order polynomial for ψ_r allows us to find the exact solution of (C1):

$$\psi(t) = z + \frac{\gamma}{a}(x^2 + y^2) - 2t(\beta - 1) + i\left(az + \beta x^2 - y^2 + 4(t - t_r)\frac{\gamma}{a}\right). \tag{C7}$$

Assuming $a > 0$ and $\gamma < \beta < \frac{a^2 - 2\gamma}{a^2}$, the vortex lines before the reconnection ($t < t_r$) are given by

$$\mathbf{R}_{1,2}^-(s,t) = \left(s, \pm\sqrt{\frac{(t_r - t)(a^2(1 - \beta) - 2\gamma) + as^2(\beta - \gamma)}{a(\gamma + 1)}}, \right.$$

$$\left. \frac{(t - t_r)(a^2(\beta - 1) - 2\gamma^2) - a\gamma(\beta + 1)s^2}{(\gamma + 1)a^2}\right), \tag{C8}$$

FIG. 9. Dependence of the ratio $\frac{A^+}{A^-}$ and the angles ϕ^- and ϕ^+ on different values of β.

while after the reconnection $(t > t_r)$

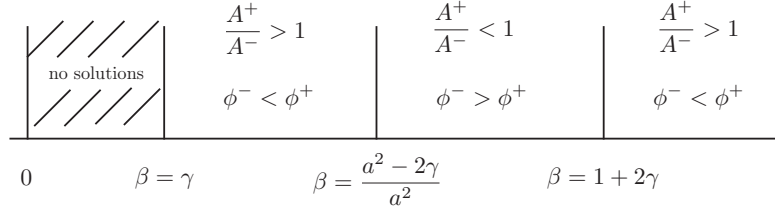$$\mathbf{R}_{1,2}^+(s,t) = \left(\pm \sqrt{\frac{(t - t_r)(a^2(1 - \beta) - 2\gamma) + as^2(1 + \gamma)}{a(\beta - \gamma)}}, s, \right.$$

$$\left. \frac{(t - t_r)(a^2(\beta - 1) + 2\gamma^2) - a\gamma(\beta + 1)s^2}{(\beta - \gamma)a^2} \right). \tag{C9}$$

From the above curves we observe that the two vortices approach along the y direction and separate along the x direction. It follows that

$$\delta^\pm(t) = |\mathbf{R}_1^\pm(0,t) - \mathbf{R}_2^\pm(0,t)| = \sqrt{2\pi}A^\pm|t - t_r|^{1/2}, \tag{C10}$$

where the ratio of prefactors satisfies

$$\frac{A^+}{A^-} = \sqrt{\frac{1 + \gamma}{\beta - \gamma}} > 1. \tag{C11}$$

From Eq. (C5) we can see how the quantity $\frac{A^+}{A^-}$ is related to the angle ϕ. Calling ϕ^- the angle of the approaching vortices and ϕ^+ the angle of the separating vortices, we can conclude that for $\beta < \frac{a^2 - 2\gamma}{a^2}$, $\phi^- > \phi^+$. On the other hand, when $\beta > \frac{a^2 - 2\gamma}{a^2}$ the two vortices approach along the x direction and separate along the y direction with $\frac{A^+}{A^-} = \sqrt{\frac{\beta - \gamma}{1 + \gamma}}$. For the sake of completeness, in Fig. 9 we show the values of the ratio $\frac{A^+}{A^-}$ and the angles ϕ^- and ϕ^+ for different values of β. We note that $\frac{A^+}{A^-} < 1$ for $\frac{a^2 - 2\gamma}{a^2} < \beta < 1 + 2\gamma$, while $\frac{A^+}{A^-} > 1$ for $\beta > 1 + 2\gamma$.

As a final remark, we note that changing the sign of a corresponds to looking at the reconnection back in time, hence each value of $\frac{A^+}{A^-}$ in Fig. 9 will then be reversed. The linear approximation also allows for computing the curvature

$$\kappa(s,t) = \frac{|\mathbf{R}'(s,t) \times \mathbf{R}''(s,t)|}{|\mathbf{R}'(s,t)|^3} \tag{C12}$$

and torsion

$$\mathcal{T}(s,t) = \frac{[\mathbf{R}'(s,t) \times \mathbf{R}''(s,t)] \cdot \mathbf{R}'''(s,t)}{|\mathbf{R}'(s,t) \times \mathbf{R}''(s,t)|^2} \tag{C13}$$

of the vortex lines.

The curvature can be directly evaluated. Its maxima as a function of time before and after reconnection are given by

$$\kappa_{\max}^-(t)\sqrt{\frac{4\gamma^2(1 + \beta)^2[a^2(\beta - 1) + 2\gamma](t - t_r) + a^3(\beta - \gamma)^2(1 + \gamma)}{a^2(1 + \gamma)^2[a^2(\beta - 1) + 2\gamma](t - t_r)}} \tag{C14}$$
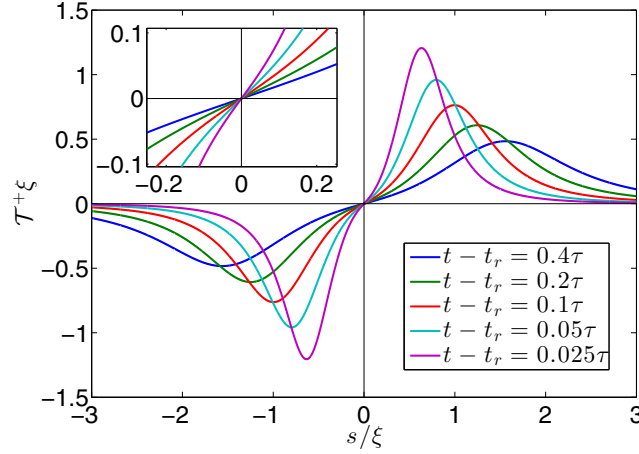
FIG. 10. Plot of the torsion versus the y coordinate, for different time steps using $\gamma = 0.01$, $\beta = 1/2$, and $a = 1$.

and

$$\kappa_{\max}^+(t) = \sqrt{\frac{4\gamma^2(1+\beta)^2[a^2(\beta-1)+2\gamma](t-t_r) - a^3(\beta-\gamma)^2(1+\gamma)^2}{a^2(\beta-\gamma)[a^2(\beta-1)+2\gamma](t-t_r)}}, \tag{C15}$$

respectively. The present calculation predicts $\kappa_{\max}^\pm(t) \propto |t - t_r|^{-1/2}$, which also corresponds to a dimensional analysis prediction. In addition, the linear approximation predicts that $\kappa_{\max}^+/\kappa_{\max}^- = (A^+/A^-)^3$ in the limit of $t \to t_r$. This nontrivial result cannot be found by dimensional arguments. Moreover, one can show that $\kappa^\pm$ presents a self-similar behavior close to the reconnection point of the form $\kappa^\pm(s,t) = \kappa_{\max}^\pm(t)\Phi^\pm(\zeta_\pm)$, where $\zeta^\pm = (s - s_r)\kappa_{\max}^\pm(t)$ and s_r is the coordinate of the reconnecting point. For small values of γ, these self-similar functions can be found to be

$$\Phi^\pm(\zeta) = \frac{1 \pm \frac{3}{2}\frac{(\beta^{\pm 1}+1)\zeta^2}{1+(\beta^{\pm 1}+1)\zeta^2}\gamma}{[1+(\beta^{\pm 1}+1)\zeta^2]^{3/2}} + O(\gamma^2) = \frac{1}{\left\{1+\left[\left(\frac{A^\mp}{A^\pm}\right)^2+1\right]\xi^2\right\}^{3/2}} + O\left(\eta^\pm\gamma^2\frac{(t-t_r)}{\tau}\right), \tag{C16}$$

where $\eta^\pm = (A^\mp/A^\pm)^2 - 1$. Remarkably, once the ratio A^+/A^- is reintroduced, γ only appears as a quadratic correction to the self-similar form. Note that within this approximation, self-similarity is destroyed when $\eta^\pm\gamma^2(t-t_r)/\tau$ is of order 1.

We note that if one chooses $\beta > \frac{a^2-2\gamma}{a^2}$, then $\frac{A^+}{A^-} = \sqrt{\frac{\beta-\gamma}{1+\gamma}}$ and

$$[\Phi^\pm(\zeta)]_{\beta>(a^2-2\gamma)/a^2} = [\Phi^\mp(\zeta)]_{\beta<(a^2-2\gamma)/a^2}. \tag{C17}$$

The former calculations were evaluated using symbolic computation software.

Finally, the torsion $\mathcal{T}^\pm(s,t)$ of the vortex line can be also computed within this approximation. It vanishes at s_r (suggesting a locally planar reconnection); however, it changes sign linearly at this point. Its slope is given by

$$\frac{d\mathcal{T}^+}{ds} = -\gamma \frac{3\sqrt{2}(1+\beta)}{\sqrt{a(\beta-\gamma)}\sqrt{(t-t_r)[a^2(1-\beta)-2\gamma]}} \tag{C18}$$

and it diverges as $\gamma|t-t_r|^{-1/2}$. The torsion thus develops shocklike structures as displayed in Fig. 10.

The inset in Fig. 10 shows the linear behavior close to the reconnection point. It is possible to prove analytically that the ratio of the slopes is given by $\frac{d\mathcal{T}^+}{ds}/\frac{d\mathcal{T}^-}{ds}|_{s=s_r} = A^+/A^-$. The full formulas for the torsion are too long to be presented here.

[1] E. R. Priest, in *Proceedings of the VIIth International Conference on Plasma Astrophysics and Space Physics, Lindau, 1998*, edited by J. Büchner, I. Axford, E. Marsch, and V. Vasyliūnas (Springer Netherlands, Dordrecht, 1999), pp. 77–100.

[2] S. Kida and M. Takaoka, Vortex reconnection, Annu. Rev. Fluid Mech. **26**, 169 (1994).

[3] J. Koplik and H. Levine, Vortex Reconnection in Superfluid Helium, Phys. Rev. Lett. **71**, 1375 (1993).

[4] X. Zhike, Y. Xiaoli, C. Xin, Y. Liheng, S. Yingna, K. Bernhard, Z. Jun, L. Zhong, B. Yi, X. Yongyuan, Y. Kai, and Z. Li, Observing the release of twist by magnetic reconnection in a solar filament eruption, Nat. Commun. **7**, 11837 (2016).

[5] F. Hussain and K. Duraisamy, Mechanics of viscous vortex reconnection, Phys. Fluids **23**, 021701 (2011).

[6] E. Fonda, D. P. Meichle, N. T. Ouellette, S. Hormoz, and D. P. Lathrop, Direct observation of Kelvin waves excited by quantized vortex reconnection, Proc. Natl. Acad. Sci. USA **111**, 4707 (2014).

[7] P. Constantin, C. Fefferman, and A. J. Majda, Geometric constraints on potentially singular solutions for the 3-D Euler equations, Commun. Part. Diff. Eq. **21**, 559 (1996).

[8] H. K. Moffatt, The interaction of skewed vortex pairs: A model for blow-up of the Navier-Stokes equations, J. Fluid Mech. **409**, 51 (2000).

[9] R. P. Feynman, in *Progress in Low Temperature Physics*, edited by C. J. Gorter (Elsevier, Amsterdam, 1955), Chap. 2, pp. 17–53.

[10] K. W. Schwarz, Three-dimensional vortex dynamics in superfluid ^{4}He: Homogeneous superfluid turbulence, Phys. Rev. B **38**, 2398 (1988).

[11] G. P. Bewley, M. S. Paoletti, K. R. Sreenivasan, and D. P. Lathrop, Characterization of reconnecting vortices in superfluid helium, Proc. Natl. Acad. Sci. USA **105**, 13707 (2008).

[12] B. P. Anderson, P. C. Haljan, C. A. Regal, D. L. Feder, L. A. Collins, C. W. Clark, and E. A. Cornell, Watching Dark Solitons Decay into Vortex Rings in a Bose-Einstein Condensate, Phys. Rev. Lett. **86**, 2926 (2001).

[13] S. Serafini, M. Barbiero, M. Debortoli, S. Donadello, F. Larcher, F. Dalfovo, G. Lamporesi, and G. Ferrari, Dynamics and Interaction of Vortex Lines in an Elongated Bose-Einstein Condensate, Phys. Rev. Lett. **115**, 170402 (2015).

[14] A. W. Baggaley, L. K. Sherwin, C. F. Barenghi, and Y. A. Sergeev, Thermally and mechanically driven quantum turbulence in helium II, Phys. Rev. B **86**, 104501 (2012).

[15] S. Nazarenko and R. West, Analytical solution for nonlinear Schrödinger vortex reconnection, J. Low Temp. Phys. **132**, 1 (2003).

[16] S. Zuccher, M. Caliari, A. W. Baggaley, and C. F. Barenghi, Quantum vortex reconnections, Phys. Fluids **24**, 125108 (2012).

[17] A. J. Allen, S. Zuccher, M. Caliari, N. P. Proukakis, N. G. Parker, and C. F. Barenghi, Vortex reconnections in atomic condensates at finite temperature, Phys. Rev. A **90**, 013601 (2014).

[18] C. Rorai, J. Skipper, R. M. Kerr, and K. R. Sreenivasan, Approach and separation of quantised vortices with balanced cores, J. Fluid Mech. **808**, 641 (2016).

[19] A. T. A. M. de Waele and R. G. K. M. Aarts, Route to Vortex Reconnection, Phys. Rev. Lett. **72**, 482 (1994).

[20] R. Tebbs, A. J. Youd, and C. F. Barenghi, The approach to vortex reconnection, J. Low Temp. Phys. **162**, 314 (2011).

[21] D. Kivotides, J. C. Vassilicos, D. C. Samuels, and C. F. Barenghi, Kelvin Waves Cascade in Superfluid Turbulence, Phys. Rev. Lett. **86**, 3080 (2001).

[22] S. Nazarenko, Kelvin wave turbulence generated by vortex reconnections, JETP Lett. **84**, 585 (2007).

[23] R. Hänninen, Kelvin waves from vortex reconnection in superfluid helium at low temperatures, Phys. Rev. B **92**, 184508 (2015).

[24] M. W. Scheeler, D. Kleckner, D. Proment, G. L. Kindlmann, and W. T. M. Irvine, Helicity conservation by flow across scales in reconnecting vortex links and knots, Proc. Natl. Acad. Sci. USA **111**, 15350 (2014).

[25] Y. Kimura and H. K. Moffatt, Reconnection of skewed vortices, J. Fluid Mech. **751**, 329 (2014).

[26] C. E. Laing, R. L. Ricca, and L. S. De Witt, Conservation of writhe helicity under anti-parallel reconnection, Sci. Rep. **5**, 9224 (2015).

[27] S. Zuccher and R. L. Ricca, Helicity conservation under quantum reconnection of vortex rings, Phys. Rev. E **92**, 061001 (2015).

[28] P. Clark di Leoni, P. D. Mininni, and M. E. Brachet, Helicity, topology, and Kelvin waves in reconnecting quantum knots, Phys. Rev. A **94**, 043605 (2016).

[29] A. Villois, G. Krstulovic, D. Proment, and H. Salman, A vortex filament tracking method for the Gross-Pitaevskii model of a superfluid, J. Phys. A: Math. Theor. **49**, 415502 (2016).

[30] N. G. Berloff and P. H. Roberts, Motion in a Bose condensate: IX. Crow instability of antiparallel vortex pairs, J. Phys. A: Math. Gen. **34**, 10057 (2001).

[31] D. Proment, M. Onorato, and C. F. Barenghi, Vortex knots in a Bose-Einstein condensate, Phys. Rev. E **85**, 036306 (2012).

[32] C. Nore, M. Abid, and M. E. Brachet, Decaying Kolmogorov turbulence in a model of superflow, Phys. Fluids **9**, 2644 (1997).

[33] A. Villois, D. Proment, and G. Krstulovic, Evolution of a superfluid vortex filament tangle driven by the Gross-Pitaevskii equation, Phys. Rev. E **93**, 061103 (2016).

[34] See Supplemental Material at http://link.aps.org/supplemental/10.1103/PhysRevFluids.2.044701 for an explanatory movie of the knot reconnection.

[35] P. Constantin, I. Procaccia, and D. Segel, Creation and dynamics of vortex tubes in three-dimensional turbulence, Phys. Rev. E **51**, 3207 (1995).

[36] S. Serafini, L. Galantucci, E. Iseni, T. Bienaimé, R. N. Bisset, C. F. Barenghi, F. Dalfovo, G. Lamporesi, and G. Ferrari, Vortex reconnections and rebounds in trapped atomic Bose-Einstein condensates, arXiv:1611.01691.

Irreversible Dynamics of Vortex Reconnections in Quantum Fluids

Alberto Villois◉

Department of Physics, University of Bath, Bath BA2 7AY, United Kingdom
and School of Mathematics, University of East Anglia, Norwich Research Park, Norwich NR4 7TJ, United Kingdom

Davide Proment◉

School of Mathematics, University of East Anglia, Norwich Research Park, Norwich NR4 7TJ, United Kingdom

Giorgio Krstulovic◉

Université Côte d'Azur, Observatoire de la Côte d'Azur, CNRS, Laboratoire Lagrange,
Bd de l'Observatoire, CS 34229, 06304 Nice cedex 4, France

We statistically study vortex reconnections in quantum fluids by evolving different realizations of vortex Hopf links using the Gross–Pitaevskii model. Despite the time reversibility of the model, we report clear evidence that the dynamics of the reconnection process is time irreversible, as reconnecting vortices tend to separate faster than they approach. Thanks to a matching theory devised concurrently by Proment and Krstulovic [Phys. Rev. Fluids **5**, 104701 (2020)], we quantitatively relate the origin of this asymmetry to the generation of a sound pulse after the reconnection event. Our results have the prospect of being tested in several quantum fluid experiments and, theoretically, may shed new light on the energy transfer mechanisms in both classical and quantum turbulent fluids.

Introduction.—Irreversibility emerges naturally in most interacting systems characterized by a huge number of degrees of freedom. Its manifestation is associated to a time-symmetry breaking: the arrow of time appears inherently defined in the dynamics and an experienced observer is able to distinguish what are *before* and *after*.

In dissipative systems the arrow of time naturally reflects the dynamics that minimizes the energy. Classical viscous fluids present valuable examples. When no external forces are applied, an initial laminar flow decays in time until its kinetic energy is totally converted into heat. A less simple example is the particle pair dispersion in turbulent flows. Although two tracers separate from each other backward and forward in time with the same Richardson scaling, their rates are different [1]: particles separate slower forward in time than backward.

Conservative (energy-preserving) systems are more subtle. The arrow of time is defined only in a statistical sense by exploiting an entropy function that approaches its extremal as time progresses. The simplest example of this kind is the free-expansion experiment of a gas: even if the gas particles interact microscopically through conservative collisions, on average their macroscopic position and velocity distribution obeys the Boltzmann kinetic equation which is time irreversible.

Quantum fluids are exotic types of fluids characterized by the total absence of viscosity, thus being conservative. Examples of such systems are superfluid liquid helium [2]

and Bose-Einstein condensates (BECs) made of dilute gases of bosons [3], Cooper-paired fermions [4], or massive photons [5]. As a consequence of the wave nature of their bosonic constituents, quantum fluids have two striking properties: vortices arise as topological defects in the order parameter and their circulation takes only discrete multiples of the quantum of circulation $\Gamma = h/m$, where h is the Planck constant and m is the boson's mass. These defects, referred to in the following as vortex filaments, present a complicated dynamics which still misses a general solution. A key point in such dynamics is the occurrence of reconnection events. A vortex reconnection is the process of interchange of two sections of different filaments; see the sketch in Fig. 1(a). It happens at small spatial and fast timescales [6], and allows the filament topology to vary.

For the sake of simplicity, we consider in this Letter a quantum fluid described by a single scalar order parameter. In the limit of zero temperature, this quantum fluid accommodates only two distinct excitation families: vortex-type excitations, in the form of filaments, and compressible density-phase excitations, that is sound waves. While the full dynamics is energy preserving, the energy may continually flow between these two excitation families. In this perspective, we provide a statistical analysis over many realizations of vortex reconnections, unveiling an inherent irreversible dynamics of the reconnection process. Moreover, we show how the linear momentum and energy transfers, from vortex-type

(a)

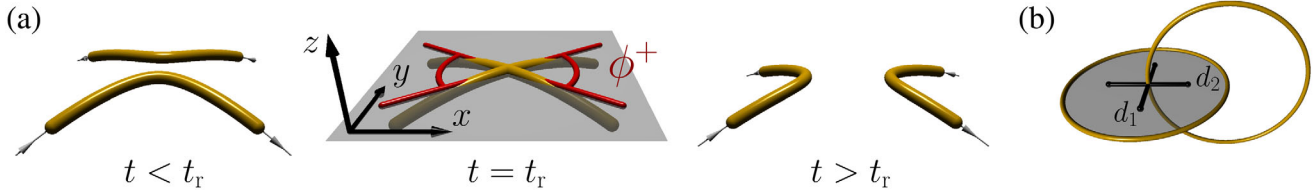$t < t_r$ $\qquad$ $t = t_r$ $\qquad$ $t > t_r$

(b)

FIG. 1. (a) Sketch of a vortex reconnection event in quantum fluids. At the reconnection time t_r the reconnecting filaments are locally tangent to the plane xOy, here depicted in gray, and form the reconnecting angle ϕ^+. The vorticity of the filaments is depicted with gray arrows. (b) The Hopf link initial condition used to create the different realizations, with visual indication of the offset parameters (d_1, d_2).

excitations to compressible density-phase excitations, are related to the geometrical parameters (macroscopic reconnection angle and concavity parameter) of the reconnecting filaments, explaining the origin of such irreversibility.

Main results.—We choose an initial configuration characterized by a Hopf link vortex filament, see Fig. 1(b), where (almost) all the superfluid kinetic energy is stored into the vortex-type excitations. Similarly to vortex knots, the Hopf links naturally decay into topologically simpler configurations [7–9] by performing a set of vortex reconnections. To study the Hopf link evolution, we use the Gross-Pitaevskii (GP) model, a nonlinear partial differential equation formally derived to mimic the order parameter ψ of a BEC made of dilute locally interacting bosons, but qualitatively able to mimic a generic quantum fluid [10]. The GP equation, cast in terms of the healing length ξ and the sound velocity c, reads

$$i\frac{\partial \psi}{\partial t} = \frac{c}{\sqrt{2}\xi}\left(-\xi^2\nabla^2\psi + \frac{m}{\rho_0}|\psi|^2\psi\right),\qquad(1)$$

where ρ_0 is the bulk superfluid density and m the mass of a boson. When the GP equation is linearized about the uniform bulk value $|\psi_0| = \sqrt{\rho_0/m}$, dispersive effects arise at scales smaller than ξ and (large-scale) sound waves effectively propagate at speed c. In this Letter lengths and times are expressed in units of ξ and $\tau = \xi/c$, respectively. Thanks to the Madelung transformation, $\psi(\mathbf{x}, t) = \sqrt{\rho(\mathbf{x}, t)/m}\exp[i\phi(\mathbf{x}, t)/(\sqrt{2}c\xi)]$, Eq. (1) can be interpreted as a model for an irrotational inviscid barotropic fluid of density ρ and velocity $\mathbf{v} = \nabla\phi$. Vortices arise as topological defects of circulation $\Gamma = h/m = 2\sqrt{2}\pi c\xi$ and vanishing density core size order of ξ [11]. In the previous formula, h is the Planck constant.

We evolve a Hopf link prepared by superimposing two rings of radius $R = 18\xi$, obtained by using a Newton-Raphson and biconjugate-gradient technique [12] to ensure a minimal amount of compressible energy; details on the numerical scheme and on the generation of the initial condition are in the Supplemental Material [13]. A set of 49 different realizations are obtained by changing the offsets (d_1, d_2) of one ring as sketched in Fig. 1(b), taking $d_i \in [-9\xi, 9\xi]$ with unit step of 3ξ. During the evolution one or

more reconnection events occur. It has been shown [14–17] that about the reconnection event, the distance between the two filaments behaves as

$$\delta^\pm(t) = A^\pm(\Gamma|t - t_r|)^{1/2},\qquad(2)$$

where $A^\pm$ are dimensionless prefactors and t_r is the reconnection time; the superscripts $-$ and $+$ label the cases *before* and *after* the reconnection, respectively. In each Hopf link realization, we carefully track [18] all reconnecting events and measure $A^\pm$. The measured values of $\delta^2(t)$ for all the 71 analyzed reconnections are shown in Fig. 2; the best-fit $A^\pm$ are plotted in red dots in the inset of Fig. 2. Remarkably, the reconnecting filaments always separate faster (or at an almost equal rate) than they approach; that is, $A^+ \geq A^-$. The clear asymmetry recorded in the δ^2 versus $t - t_r$ and in the distribution of the $A^\pm$'s is the fingerprint of the irreversible dynamics characterizing the vortex reconnection process. For completeness, we also report in the inset of Fig. 2, using different symbols, the prefactor measurements obtained in previous works [15,16], which corroborate even further our results. Finally note that in a
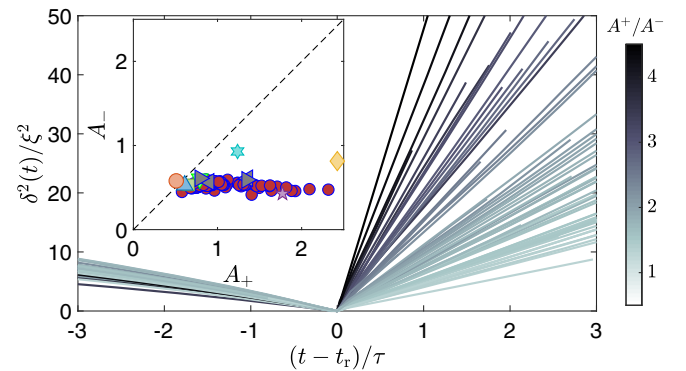
FIG. 2. Squared distances versus time of the reconnecting filaments measured in all the 49 realizations. The gray-scale color indicates the estimated value of A^+/A^- in each case. Inset: values of approach and separation prefactors A^+ and A^-. Red points correspond to data of the present work. Gray left- and right-facing triangles correspond to reconnections of free and trapped vortices, respectively, from Galantucci *et al.* [16]; other symbols from Villois *et al.* [15].

recent work [19], it has been reported that vortex reconnections in the Navier-Stokes equation also display a clear $t^{1/2}$ scaling, a coefficient $A^- \sim 0.3$–0.4 and the same time asymmetry $A^+ > A^-$. Note that the Biot-Savart (BS) analytical calculations of Ref. [20] and the local induction approximation based ones of Ref. [21] predict $A^- \sim 0.47$ and $A^- = 0.427$, respectively, which are in agreement with our GP measurements. In what follows, we quantitatively relate the asymmetry in the distribution of the prefactors with the irreversible energy transfer between the vortex-type and density or phase excitation families occurring during a reconnection event. Previous numerical studies of the GP model have indeed reported the clear emission of a sound pulse during reconnection events [22,23]. A series of snapshots showing the sound pulse emitted during the decay of the Hopf link in one of our realizations is reported in Ref. [24].

The simple linear theory neglecting the nonlinear term of the GP model [14,15], valid in the limit $\delta^\pm \to 0$, provides insight into the dynamics of reconnecting parameters as the order parameter can be found analytically. It predicts that the filaments reconnect tangent to a plane, in our reference frame the $z = 0$, see Fig. 1(a), and that the projections of the filaments onto it approach and separate following the branches of a hyperbola. The macroscopic (post) reconnection angle, formed by the hyperbola asymptotes, results in

$$\phi^+ = 2\operatorname{arccot}(A_r), \quad \text{where } A_r = A^+/A^-. \quad (3)$$

the projections of the filaments onto the orthogonal plane $y = 0$ form a parabola (not shown in here; see Ref. [24] for more details). Without any loss of generality, we set Λ/ζ the concavity of such a parabola, and we refer to Λ as the *concavity parameter*, where ζ is an arbitrary length scale, whose value is not important in the following discussion.

In all the reconnection events detected, we observe a distinct sound pulse generated after the reconnection and propagating toward the positive z axis, as shown in Figs. 3(a) and 3(b). Figure 3(c) shows the behavior of the superfluid density along the z direction versus times $t - t_r$. A (depression) sound pulse is generated soon after the reconnection and propagates toward the positive z direction at a speed qualitatively close to the speed of sound in the bulk; refer to the green dashed line $z = c(t - t_r)$, with c defined in Eq. (1). Note that the other low density regions, corresponding to the density depletions of the vortex cores, move much slower.

To explain the generation and directionality of such a pulse, we devise a novel theoretical approach, detailed in Ref. [24], and summarize in the following. Let us denote by $\mathbf{R}_1^\pm(s,t)$ and $\mathbf{R}_2^\pm(s,t)$ the reconnecting filaments, with s being their spatial parametrization variable. Far from the reconnection point (both before and after), the dynamics of the vortex filaments are mostly driven by
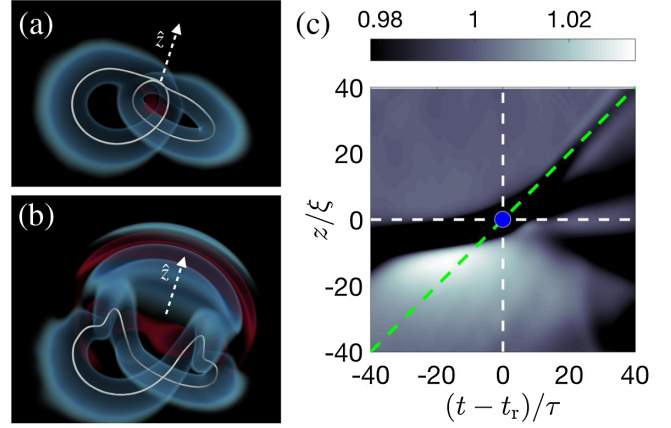

FIG. 3. Three-dimensional rendering of the density field. White contours display the vortices and density fluctuations are rendered in blue-redish colors: (a) reconnection time and (b) at $t - t_r \approx 40\tau$. (b) The positive direction of the z axis is also depicted with a white arrow. (c) Spatiotemporal plot of density along the z axis about the reconnection event denoted by the blue central point. The two dashed green lines are $z = c(t - t_r)$; here, the reconnection point (0,0) is represented by the blue dot.

the Biot-Savart model, which describes the motion of δ-supported vorticity in an incompressible inviscid flow [25]; note that this limit can be formally derived from GP [26]. In our realizations, BS is valid at distances $\delta^\pm(t) \gg \delta_{\text{lin}}$, whereas for $\delta^\pm(t) \ll \delta_{\text{lin}}$ the dynamics is determined by the linear approximation, given δ_{lin} is a crossover scale of order of the healing length. We assume both descriptions approximately valid when the filaments are at the distance $\delta^\pm(t^\pm) \approx \delta_{\text{lin}}$. This hypothesis, validated by previous GP simulations [15,16], allows us to perform an asymptotic matching.

We can therefore compute the difference, before and after the reconnection, of BS linear momentum $\Delta \mathbf{P}_{\text{fil}}$ using the positions of the filaments $\mathbf{R}_1^\pm(s,t^\pm)$ and $\mathbf{R}_2^\pm(s,t^\pm)$ coming from the linear approximation. As shown in Ref. [24], note that these depend only on the reconnection angle ϕ^+ (or equivalently A_r) and the concavity parameter Λ. Within BS, the linear momentum is given as the line integral $\mathbf{P}_{\text{fil}}(t) = (\rho_0/2)\Gamma \oint \mathbf{R}(s,t) \times d\mathbf{R}(s,t)$ [27]. As the total linear momentum of the superfluid is conserved in GP [28], the linear momentum carried by the sound pulse created after the reconnection must compensate the loss of linear momentum accounted by $\Delta \mathbf{P}_{\text{fil}}$ and reads [24]

$$\mathbf{P}_{\text{pulse}} = -\Delta \mathbf{P}_{\text{fil}} \propto (0, 0, 2 \csc \phi^+), \quad (4)$$

independently of the δ_{lin} chosen. This result is remarkable: the sound pulse linear momentum is (overall) nonzero only in the positive z direction, as observed in all our reconnection events, and its amplitude is independent of Λ and minimal for $\phi^+ = \pi/2$.
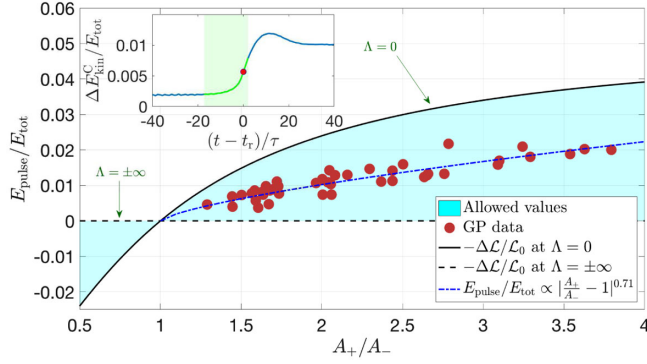
FIG. 4. Relative energy transferred to waves during the reconnection process. The cyan zone denotes the allowed values from the matching theory. Inset: relative increase of compressible kinetic energy (solid blue) about a reconnection event (denoted by the red dots) for a typical realization. The green area corresponds to the interval defined by $\delta^{\pm}(t) \leq \delta_{\mathrm{lin}} = 6\xi$.

The same matching theory can be applied to estimate the amount of energy transferred to the sound pulse. Following the standard energy splitting protocol in GP [29], the superfluid kinetic energy is decomposed into a compressible component E_{kin}^{C}, associated to sound excitations, and an incompressible component E_{kin}^{I}, associated to vortex-type excitations. In all our realizations, we observe a sharp growth of E_{kin}^{C} during each reconnection event. An example of its evolution, normalized by the total (constant) energy E_{tot}, is shown in the inset of Fig. 4: here the red dot indicates the reconnection time and the green region indicates the times when $\delta^{\pm}(t) \leq \delta_{\mathrm{lin}} = 6\xi$. The increase of E_{kin}^{C} during the reconnection event is related to the loss of incompressible kinetic energy E_{kin}^{I}. For all the reconnection events measured in our realizations, we compute the energy transferred to the sound pulse as $E_{\mathrm{pulse}} = -\Delta E_{\mathrm{kin}}^{I}$, where $\Delta E_{\mathrm{kin}}^{I} = E_{\mathrm{kin}}^{I}(t^{+}) - E_{\mathrm{kin}}^{I}(t^{-})$. Figure 4 shows the measured $E_{\mathrm{pulse}}/E_{\mathrm{tot}}$ data versus A_{r}: there is clear correlation between these two quantities, with a best-fit scaling of $E_{\mathrm{pulse}}/E_{\mathrm{tot}} \propto (A_{r} - 1)^{0.71}$.

To the simplest approximation, called local induction approximation, the BS superfluid kinetic energy is proportional to the total length of the filaments. As the representations $\mathbf{R}_{1}(s, t)$ and $\mathbf{R}_{2}(s, t)$ have infinite lengths (as in the linear regime they do not close) we choose to account only for the length of finite sections of the filaments contained in a cylinder of radius $R \gg \delta_{\mathrm{lin}}$, centered at the reconnection point and parallel to the z axis. Evaluating E_{pulse} reduces thus to the computation of the difference $\Delta\mathcal{L}(A_{r}, |\Lambda|/\zeta, \delta_{\mathrm{lin}}, R/\delta_{\mathrm{lin}})$ of the length of these sections; see [24] for more details. As the total GP energy is conserved, we have that

$$E_{\mathrm{pulse}}/E_{\mathrm{tot}} = -\Delta\mathcal{L}/\mathcal{L}_{0}, \qquad (5)$$

given $\mathcal{L}_{0}$ is the initial length of the Hopf link filament. For any given choices of δ_{lin} and R, all the admissible values of the theoretical estimation $\Delta\mathcal{L}$, rendered in cyan color in Fig. 4, are bounded between two lines obtained setting $\Lambda = 0$ (dashed line) and $|\Lambda| \to \infty$ (solid line). The GP data are all distributed within these admissible values, thus confirming the accuracy of the matching theory.

Remarkably, the estimation of E_{pulse} explains in a straightforward way the time asymmetry between the rates of approach and separation reported in Fig. 2 and its inset. Independently on the value of the concavity parameter Λ, the energy of the sound pulse is only non-negative when $A^{+} \geq A^{-}$, meaning that unless energy is externally provided to the reconnecting vortices, it is energetically impossible to have a reconnection event where $A^{+} < A^{-}$, or equivalently, where $\phi^{+} > \pi/2$.

Closing remarks.—In this Letter we reported numerical evidence of the irreversible dynamics of vortex reconnections in a scalar quantum fluid and explain its origin thanks to a matching theory developed concurrently in Ref. [24]. This theory is based on very general physical considerations and give bounds for the energy of the pulse emitted during a reconnection event. However, it cannot determine the exact value of the reconnecting angle and, thus, the one of A_{+}/A_{-}. Our results can be extended to more complicated quantum fluids where nonlocal interactions and/or higher order nonlinearities are included, like BECs with dipolar interactions, cold Fermi gases, and superfluid liquid ^{4}He.

In quantum fluid experiments, the detailed study of vortex reconnections is still in its infancy. In current BECs made of dilute gases, reconnecting vortices are created only in a nonreproducible way using fast temperature quenches [30]; however, new protocols have been proposed to create vortices in a reproducible manner [31]. In such setups, once the reconnection plane is identified, it should be feasible to measure the rates of approach and separation and detecting directionality of the sound pulse, using, for instance, Bragg spectroscopy [32]. In superfluid liquid ^{4}He experiments, vortex reconnections have been detected so far only at relatively high temperature where the normal component is non-negligible [33]. This latter may provide energy but also dissipates it through mutual friction; hence, measuring experimentally the distribution of the rates of approach and separation at different temperatures would be particularly desirable.

Finally, let us come back to the concept of irreversibility. In the realizations presented in this Letter, almost all of the superfluid kinetic energy is initially stored in the vortex-type excitations. This is likely to cause the observed statistical asymmetry in the distribution of the rates of approach and separation to be maximized. At finite temperatures or in a turbulent tangle, fluctuations can provide extra energy to reduce this asymmetry, perhaps allowing also for $\phi^{+} > \pi/2$, but the time asymmetry should in

principle remain as an inherent mechanism allowing the system to reach the equilibrium. From a fluid dynamical point of view, let us remark that vortex reconnections are allowed and regular, in classical fluids due to the presence of viscosity, while in quantum fluids thanks to a dispersive term. Showing whether the resulting dynamics of these two different fluids are equivalent or not, in the limit where their respective regularization scale tends to zero, is an appealing open problem. Comparing the results presented in this Letter with a similar study in Navier-Stokes or a carefully regularized Biot-Savart model might provide some insight on the spontaneous stochasticity and the dissipative anomaly of turbulent flows, two concepts closely related to irreversibility.

[1] J. P. Salazar and L. R. Collins, Annu. Rev. Fluid Mech. 41, 405 (2009).

[2] R. J. Donnelly, *Quantized Vortices in Helium II* (Cambridge University Press, Cambridge, England, 1991), Vol. 3.

[3] L. Pitaevskii and S. Stringari, *Bose-Einstein Condensation and Superfluidity* (Oxford University Press, New York, 2016), Vol. 164.

[4] A. J. Leggett, *Quantum Liquids: Bose Condensation and Cooper Pairing in Condensed-Matter Systems* (Oxford University Press, New York, 2006).

[5] I. Carusotto and C. Ciuti, Rev. Mod. Phys. 85, 299 (2013).

[6] Small length scales compared to the average filaments' length and fast timescales compared to the average filaments' length divided by their average speed.

[7] D. Proment, M. Onorato, and C. F. Barenghi, Phys. Rev. E 85, 036306 (2012).

[8] D. Proment, M. Onorato, and C. F. Barenghi, J. Phys. Conf. Ser. 544, 012022 (2014).

[9] D. Kleckner, L. H. Kauffman, and W. T. M. Irvine, Nat. Phys. 12, 650 (2016).

[10] A. Villois, D. Proment, and G. Krstulovic, Phys. Rev. E 93, 061103(R) (2016).

[11] L. Pitaevskii, Sov. Phys. JETP 13, 451 (1961), http://www .jetp.ac.ru/cgi-bin/e/index/e/13/2/p451?a=list.

[12] M. Abid, C. Huepe, S. Metens, C. Nore, C. T. Pham, L. S. Tuckerman, and M. E. Brachet, Fluid Dyn. Res. 33, 509 (2003).

[13] See Supplemental Material at http://link.aps.org/ supplemental/10.1103/PhysRevLett.125.164501 for specific details on the numerical scheme used, the numerical creation of the Hopf link, and the numerical analysis of each reconnection process.

[14] S. Nazarenko and R. West, J. Low Temp. Phys. 132, 1 (2003).

[15] A. Villois, D. Proment, and G. Krstulovic, Phys. Rev. Fluids 2, 044701 (2017).

[16] L. Galantucci, A. W. Baggaley, N. G. Parker, and C. F. Barenghi, Proc. Natl. Acad. Sci. U.S.A. 116, 12204 (2019).

[17] A. Enciso and D. Peralta-Salas, arXiv:1905.02467.

[18] A. Villois, G. Krstulovic, D. Proment, and H. Salman, J. Phys. A 49, 415502 (2016).

[19] J. Yao and F. Hussain, J. Fluid Mech. 900, R4 (2020).

[20] L. Boué, D. Khomenko, V. S. L'vov, and I. Procaccia, Phys. Rev. Lett. 111, 145302 (2013).

[21] S. Rica, C. R. Méc. 347, 365 (2019).

[22] M. Leadbeater, T. Winiecki, D. C. Samuels, C. F. Barenghi, and C. S. Adams, Phys. Rev. Lett. 86, 1410 (2001).

[23] S. Zuccher, M. Caliari, A. W. Baggaley, and C. F. Barenghi, Phys. Fluids 24, 125108 (2012).

[24] D. Proment and G. Krstulovic, companion paper, Phys. Rev. Fluids 5, 104701 (2020).

[25] K. W. Schwarz, Phys. Rev. B 38, 2398 (1988).

[26] M. D. Bustamante and S. Nazarenko, Phys. Rev. E 92, 053019 (2015).

[27] L. M. Pismen and L. M. Pismen, *Vortices in Nonlinear Fields: From Liquid Crystals to Superfluids, From Non-Equilibrium Patterns to Cosmic Strings* (Oxford University Press, New York, 1999), Vol. 100.

[28] This is formally true in a system which is invariant under spatial translations. We can extend this property to a finite system if we assume that the boundaries are sufficiently far from the reconnection point so that the conservation of the linear momentum is almost exact within a given volume enclosing the reconnection event.

[29] C. Nore, M. Abid, and M. Brachet, Phys. Fluids 9, 2644 (1997).

[30] S. Serafini, M. Barbiero, M. Debortoli, S. Donadello, F. Larcher, F. Dalfovo, G. Lamporesi, and G. Ferrari, Phys. Rev. Lett. 115, 170402 (2015).

[31] K. Xhani, E. Neri, L. Galantucci, F. Scazza, A. Burchianti, K. L. Lee, C. F. Barenghi, A. Trombettoni, M. Inguscio, M. Zaccanti, G. Roati, and N. P. Proukakis, Phys. Rev. Lett. 124, 045301 (2020).

[32] J. Steinhauer, R. Ozeri, N. Katz, and N. Davidson, Phys. Rev. Lett. 88, 120407 (2002).

[33] G. P. Bewley, M. S. Paoletti, K. R. Sreenivasan, and D. P. Lathrop, Proc. Natl. Acad. Sci. U.S.A. 105, 13707 (2008).

Quantum vortex reconnections mediated by trapped particles

Umberto Giuriato and Giorgio Krstulovic

Université Côte d'Azur, Observatoire de la Côte d'Azur, Laboratoire Lagrange, CNRS, Nice, France

Reconnections between quantum vortex filaments in the presence of trapped particles are investigated using numerical simulations of the Gross-Pitaevskii equation. Particles are described with classical degrees of freedom and modeled as highly repulsive potentials which deplete the superfluid. First, the case of a vortex dipole with a single particle trapped inside one of the vortices is studied. It is shown that the reconnection takes place at the position of the particle as a consequence of the symmetry breaking induced by it. The separation rate between the reconnecting points is compatible with the known dynamics of quantum vortex reconnections, and it is independent of the particle mass and size. After the reconnection, the particle is pushed away with a constant velocity, and its trajectory is deflected because of the transverse momentum exchange with the vortex filaments. The momentum exchanges between the particle, the vortex, and a density pulse are characterized. Finally, the reconnection of two linked rings, each of them with several initially randomly distributed particles, is studied. It is observed that generically, reconnections take place at the location of trapped particles. It is shown that reconnection dynamics is unaffected for light particles.

I. INTRODUCTION

One of the most striking features of superfluids is the presence of quantum vortices, thin tornadoes which arise as topological defects and nodal lines of the complex order parameter describing the system [1]. Quantum vortices have been observed in different kinds of superfluids, from atomic Bose-Einstein condensates (BECs), where their core is micrometer sized, to superfluid ^{4}He, where the core size is a few angstroms. The topological nature of quantum vortices constrains their circulation to be a discrete multiple of the quantum of circulation $\Gamma = h/m$, where h is the Planck constant and m is the mass of the bosons constituting the superfluid.

The dynamics of such vortex filaments is rich and still not fully comprehended. In particular, a fundamental phenomenon is the occurrence of reconnection events. In general, in fluid mechanics a vortex reconnection is an event in which the topology of the vorticity field is rearranged [2]. In the case of classical fluids, the presence of viscosity breaks the Kelvin circulation theorem, allowing the reconnection between vortex tubes [3]. In the case of inviscid superfluids, the vorticity is supported exclusively along the unidimensional vortex filaments, and the reconnection between them is made possible because of the vanishing density at the core of the vortices [4]. Specifically, the process of superfluid vortex reconnection consists in the local exchange of two strands of different filaments after a fast approach, allowing the topology to vary. In quantum turbulence, reconnections are also thought to be a fundamental mechanism for the redistribution of energy at scales smaller than the intervortex distance [5].

The separation $\delta(t)$ between the two reconnecting points is the simplest observable that characterizes a vortex reconnection. Given that a reconnection is an event localized in space and time, sufficiently close to the reconnection event it is expected to be fully driven by the interaction between two filaments. Assuming that at this scale the only parameter that determines the dynamics is the circulation Γ about each filament, a simple dimensional analysis suggests the following scaling for the separation rate:

$$\delta(t) = A^{\pm}(\Gamma|t - t_{\text{rec}}|)^{1/2}, \tag{1}$$

where $A^{\pm}$ are dimensionless prefactors, t_{rec} is the reconnection time, and the labels $-$ and $+$ refer, respectively, to the times before and after the reconnection event. Such scaling has been demonstrated analytically in the context of the Gross-Pitaevskii (GP) model for $\delta \to 0$ [6–8], and it has been observed to be valid even at distances that go beyond several healing lengths [7,9]. Note that previous studies reported disparate exponents that still need to be explained [10–12]. The scaling (1) has also been observed in Biot-Savart simulations [9,13,14] and superfluid helium experiments [15]. If an external driving mechanism is absent, the scaling (1) is considered a universal feature of vortex reconnections, and the filaments always approach slower than they separate, i.e., $A^+/A^- > 1$. This last observation has been explained by a novel matching theory as the consequence of an irreversible mechanism related to the sound radiated during the event [8,16].

In recent years, vortex reconnections have been directly observed in atomic BECs by means of destructive absorption imaging [17] and in superfluid helium experiments by using solidified hydrogen particles as probes [15,18]. This latter technique has become a standard tool for the investigation of the properties of superfluid helium and quantum vortices, following its first utilization in 2006 [19]. Indeed, such particles get captured by quantum vortices thanks to pressure gradients and are carried by them, unveiling in this way the dynamics of the filaments. Besides the reconnections between vortices and Kelvin waves (helicoidal displacements

that propagate along the vortex filaments), solidified hydrogen particles succeeded in revealing important differences between the statistics of classical and quantum turbulent states [20,21]. However, given that the typical size of such particles is four orders of magnitude larger than the vortex core size, it is far from trivial that they actually behave as tracers. For this reason, understanding the actual vortex-particle interactions and how particles and fluids affect each other's motions is a crucial theoretical task.

Many models have been developed and studied in this regard. The main difficulty is caused by the large extent of the scales involved in the problem, so that different phenomenological approaches need to be used. For what concerns large scales, the dynamics of particles in classical fluids has been phenomenologically adapted to the two-fluid description of a superfluid [22], and the distribution of inertial passive particles has been studied in the Hall-Vinen-Bekarevich-Khalatnikov (HVBK) model [23]. In this macroscopic approach, the vorticity is a coarse-grained field, and there is no notion of quantized vortices. Instead, in the vortex-filament model, the superfluid is modeled as a collection of filaments that evolve according to Biot-Savart integrals [1]. This method involves nonlocal contributions and a singular integral for the computation of the vortex self-induced velocity that needs to be regularized [24]. In this framework, hard spherical particles can be modeled as moving boundary conditions [25,26], although the reconnections both between vortices and between a vortex and a particle surface need to be implemented with an *ad hoc* procedure. These issues are absent in the GP model, in which the evolution of the order parameter of the superfluid is described with a nonlinear Schrödinger equation. Indeed, although the GP equation is formally derived for dilute Bose–Einstein condensates, it can be considered as a general model for low temperature superfluids, including superfluid helium. Unlike the vortex-filament method or the HVBK model, the full dynamics of vortices emerges naturally, including the reconnection events. Particles modeled as highly repulsive potentials have been successfully implemented in the GP framework, allowing for an extensive study of the capture process [27], the interaction between trapped particles and Kelvin waves [28], and the Lagrangian properties of quantum turbulence [29]. Recently, the dynamics of particles trapped inside GP vortices was also addressed in two dimensions [30].

Because the GP equation is a microscopic model, regular at the vortex core, it is the natural setting in which quantum vortex reconnections can be studied. In this work, we combine such suitability with the simplicity of modeling particles in the GP framework to study vortex reconnections in the presence of particles trapped by the filaments. We focus on two different configurations. In Sec. III we study the evolution of a dipole of two counterrotating straight vortices with a particle trapped in one of them. In Sec. IV we characterize the reconnection of two linked rings loaded with a number of particles. In the first case the reconnection is induced by the presence of the particle, and its simplicity allows for a systematic investigation of the mutual interaction between vortices and particles during the process of the reconnection. In the second case, the reconnection happens even in the absence of particles, so that how the presence of particles effectively affects the reconnection process can be addressed.

II. MODEL FOR PARTICLES AND QUANTUM VORTICES

We consider a quantum fluid with N_p spherical particles of mass M_p and radius a_p immersed in it. We describe the system by a self-consistent model based on the three-dimensional Gross-Pitaevskii equation. The particles are modeled by strong localized potentials V_p that completely deplete the superfluid up to a distance a_p from the position of their center $\mathbf{q}_i$. The dynamics of the system is governed by the following Hamiltonian:

$$
H = \int \left(\frac{\hbar^2}{2m} |\boldsymbol{\nabla}\psi|^2 - \mu|\psi|^2 \right.
$$

$$
+ \frac{g}{2}|\psi|^4 + \sum_{i=1}^{N_\mathrm{p}} V_\mathrm{p}(\mathbf{r}-\mathbf{q}_i)|\psi|^2 \bigg) d\mathbf{r}
$$

$$
+ \sum_{i=1}^{N_\mathrm{p}} \frac{\left(\mathbf{p}_i^{\mathrm{part}}\right)^2}{2M_\mathrm{p}} + \sum_{i<j}^{N_\mathrm{p}} V_\mathrm{rep}^{ij}, \tag{2}
$$

where ψ is the order parameter of the quantum and $\mathbf{p}_i^{\mathrm{part}} = M_\mathrm{p}\dot{\mathbf{q}}_i$ are the particles linear momenta. The chemical potential is denoted by μ. The nonlinear self-interaction coupling constant of the fluid is denoted by g, and m is the mass of the condensed bosons. The potential V_rep^{ij} is a repulsive potential between particles, needed to avoid an unphysical overlap, due to a short-range fluid-mediated interaction [31,32]. The equations of motion for the superfluid field ψ and the particle positions $\mathbf{q}_i = (q_{i,x}, q_{i,y}, q_{i,z})$ are

$$
i\hbar \frac{\partial \psi}{\partial t} = -\frac{\hbar^2}{2m}\nabla^2\psi + g|\psi|^2\psi - \mu\psi + \sum_{i=1}^{N_\mathrm{p}} V_\mathrm{p}(|\mathbf{x}-\mathbf{q}_i|)\psi,
$$

$$
\tag{3}
$$

$$
M_\mathrm{p}\ddot{\mathbf{q}}_i = -\int V_\mathrm{p}(|\mathbf{x}-\mathbf{q}_i|)\boldsymbol{\nabla}|\psi|^2\, d\mathbf{x} + \sum_{j\neq i}^{N_\mathrm{p}} \frac{\partial}{\partial \mathbf{q}_i} V_\mathrm{rep}^{ij}. \tag{4}
$$

We refer to [27–29,33] for further details about the model, which was recently adopted to study extensively the interaction between particles and quantum vortices.

In the absence of particles, the ground state of the system is a homogeneous flat condensate $\psi_\infty = \sqrt{\mu/g} \equiv \sqrt{\rho_\infty/m}$, with a constant mass density ρ_∞. Linearizing around this value, dispersive effects take place at scales smaller than the healing length $\xi = \sqrt{\hbar^2/2g\rho_\infty}$, while large-wavelength excitations propagate with the phonon (sound) velocity $c = \sqrt{g\rho_\infty/m^2}$. The close relation between the GP model and hydrodynamics comes from the Madelung transformation $\psi(\mathbf{x}) = \sqrt{\rho(\mathbf{x})/m}\, e^{i\frac{m}{\hbar}\phi(\mathbf{x})}$, which maps the GP (3) into the continuity and Bernoulli equations of a superfluid of density ρ and velocity $\mathbf{v}_\mathrm{s} = \boldsymbol{\nabla}\phi$. Although the superfluid velocity is described by a potential flow, vortices may appear as topological defects because the phase is not defined at the nodal lines of $\psi(\mathbf{x})$, and thus, vortices may appear to be topological defects. Each superfluid vortex carries a quantum of circulation $\Gamma = h/m = 2\pi\sqrt{2}c\xi$, and vortices are characterized by a vanishing density core size of the order of ξ.

In this work, we perform numerical simulations of the coupled differential equations (3) and (4) in a periodic cubic

box with sides $L = 128\xi$ with $N_c = 256^3$ collocation points. We use a standard pseudospectral method with a fourth-order Runge-Kutta scheme for the time step. In numerics, we measure distances in units of ξ, velocities in units of c, and times in units of $\tau = \xi/c$. As described in the Appendix and in Ref. [34], dealiasing is applied to equations (3) and (4), in such a way that they conserve the total energy H (2), the total fluid mass $N = \int |\psi|^2 \, d\mathbf{x}$, and the total momentum

$$\mathbf{p}^{\text{tot}} = \mathbf{p}^{\text{GP}} + \sum_{i=1}^{N_p} \mathbf{p}^{\text{part}}, \qquad (5)$$

where $\mathbf{p}^{\text{GP}} = i\hbar/2 \int (\psi \nabla \psi^* - \psi^* \nabla \psi) \, d\mathbf{x}$ is the momentum of the quantum fluid. If dealiasing is not carefully performed, the discrete system does not conserve momentum. In the simulations presented here the total momentum is conserved up to eight decimal digits.

We use two different particle potentials to model the particles. For the simulations with the dipole, a smoothed hat function $V_p^1(r) = \frac{V_0}{2}(1 - \tanh[\frac{r^2 - \zeta^2}{4\Delta_a^2}])$ is used. The parameters ζ and Δ_a are set to model the particle attributes. In particular, ζ fixes the width of the potential, and it is related to the particle size, while Δ_a controls the steepness of the smoothed hat function. The latter needs to be adjusted in order to avoid the Gibbs effect in the Fourier transform of V_p^1. For the simulations of the Hopf link, we use a Gaussian potential $V_p^2(r) = V_0 \exp(-r^2/2d_{\text{eff}}^2)$, where the width is fixed using the Thomas-Fermi approximation to set an approximate radius ζ of the particle as $d_{\text{eff}} = \zeta/\sqrt{2\ln(V_0/\mu)}$. Since the particle boundaries are not sharp, the effective particle radius is measured as $a_p = (3M_0/4\pi \rho_\infty)^{\frac{1}{3}}$, where $M_0 = \rho_\infty L^3 (1 - \int |\psi_p|^2 \, d\mathbf{x}/ \int |\psi_\infty|^2 \, d\mathbf{x})$ is the fluid mass displaced by the particle and ψ_p is the steady state with just one particle. Practically, given the set of numerical parameters ζ and Δ_a, the state ψ_p is obtained numerically with imaginary time evolution and the excluded mass M_0 is measured directly. We use the repulsive potential $V_{\text{rep}}^{ij} = \gamma_{\text{rep}}(2a_p/|\mathbf{q}_i - \mathbf{q}_j|)^{12}$ in order to avoid an overlap between them. The functional form of V_{rep}^{ij} is inspired by the repulsive term of the Lennard-Jones potential and the prefactor γ_{rep} is adjusted numerically so that the interparticle distance $2a_p$ minimizes the sum of V_{rep}^{ij} with the fluid mediated attractive potential [31,32].

The initial conditions for the dipole and a single ring (without particles) are obtained using the Newton-Raphson method and a biconjugate-gradient technique in order to minimize the sound emission [35]. The Hopf link of two rings is obtained by multiplying two states containing a ring each.

III. RECONNECTION OF A VORTEX DIPOLE

We start by presenting a series of numerical simulations of a dipole of two counterrotating superfluid vortices, with a single particle initially trapped inside one of them. Such a setting is useful to illustrate how a superfluid vortex reconnection can be triggered by the symmetry breaking produced by the presence of particles. Indeed, in the absence of trapped particles, the vortex dipole is a steady configuration, in which a spontaneous self-reconnection does not happen unless a Crow instability is induced [36]. At the same time, the simplicity

TABLE I. Simulation parameters for the vortex dipole reconnection experiment.

λ	d/ξ	a_p/ξ	ζ/ξ	Δ_a/ξ	V_0/μ
1	10	4.3	3.0	0.75	20
2	20	8.6	7.4	0.75	20

of the initial configuration allows for the systematic study of the mutual effects between the particle and the reconnecting filaments.

In the initial time of each simulation, the vortices are straight and aligned along the z direction. The initial velocity of the particle is set equal to the translational speed of the dipole $\mathbf{v}_d \sim (\Gamma/2\pi d)\hat{\mathbf{y}}$, where d is the distance between the two filaments and $\hat{\mathbf{y}}$ is the unit vector along the y direction [30,37]. We performed the same experiment using particles of two different sizes and for a wide range of mass densities.

It has been observed in Ref. [27] that the effective Hamiltonian describing the process of particle capture by a vortex induces a dynamics which is invariant under the following scaling transformation:

$$d \to \lambda d, \quad a_p \to \lambda a_p, \quad t \to \lambda^2 t \qquad \forall \lambda \in \mathbb{R}^+, \quad (6)$$

where d is the vortex-particle distance. In order to check if the scaling invariance (6) is valid also in the present simulations, we set the radius of the large particle exactly $\lambda = 2$ times larger than the radius of the small one. Analogously, in the case of the large particle, the vortex filaments are initially placed $\lambda = 2$ times more distant than for the small particle. If such invariance subsists, it would be an indication of the analogy between the reconnection process and the trapping mechanism. In addition, it would naturally extend the validity of the results reported below in the case of particles with larger sizes, comparable to the ones used in current experiments. Note, however, that the scaling invariance (6) neglects the density profile of the vortex core, as well as other more complex particle-vortex interactions which can become relevant when a particle is trapped, like the Magnus effect.

The parameters used for these sets of simulations are summarized in Table I [note that the repulsive potential V_{rep}^{ij} in Eq. (4) is absent because only one particle is present].

Snapshots of the typical evolution of the dipole configuration under the GP dynamics (3) and (4) are displayed in Fig. 1 for a neutral particle of size $a_p = 4.3\xi$ and initial vortex separation $d = 10\xi$. During the motion of the dipole, the particle starts to precede about the filament because of the Magnus effect [28,30,38]. At the same time, the two vortices start to bend, until the filament without a particle reconnects with the surface of the sphere at time t_{rec}^-. After the reconnection, the contact point of the free vortex separates into two branches, which then slide on the particle surface toward opposite directions. For a time window of about $\sim 20\tau$ the particle is pierced by both vortices, until the couple of pinning points above and below the particles merge and the vortices detach symmetrically. The reconnection changes the topology of the flow, so that the dipole is eventually converted into a single vortex ring (which in Fig. 1 appears to be folded on the vertical direction because of spatial periodicity). At the time
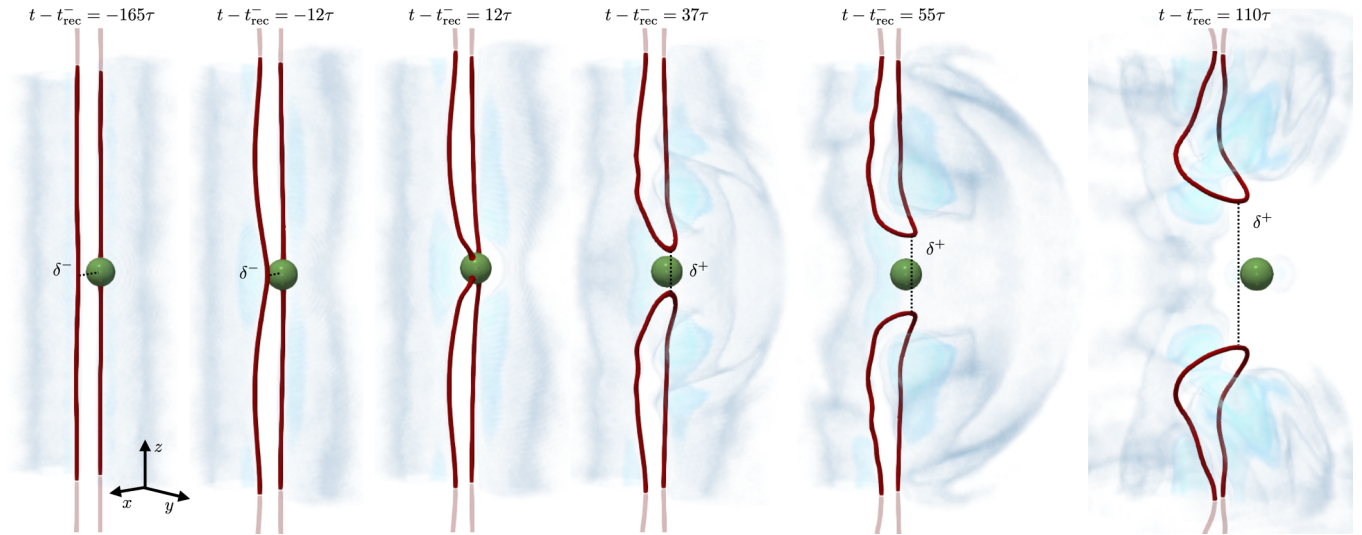
FIG. 1. Snapshots of the superfluid density and a neutral-mass particle of size $a_{\mathrm{p}} = 4.3\xi$ during the dipole reconnection (time varies from left to right). The initial distance between the vortices is $d = 10\xi$. Vortices are displayed as red isosurfaces at low density; particles are the green spheres, and sound is rendered in blue.

of the detachment, a clear spherical sound pulse is generated at the reconnection point. It expands and propagates along the y direction, which is the dipole propagation direction and coincides with the normal to the reconnection plane, in agreement with Refs. [8,16]. Simultaneously, the particle is released and abruptly accelerated. Eventually, it keeps on moving forward with a constant speed larger than the dipole velocity.

Before exploring in more detail the origin of the particle dynamics, we address the question of whether the observed reconnections induced by the particle are compatible with the standard picture of GP reconnections. In order to do so, we compute the separation $\delta(t)$ between the reconnecting points as a function of time. When the circulation Γ is the only relevant parameter driving the reconnection dynamics, $\delta(t)$ is expected to scale as Eq. (1). We operatively define the separation before the reconnection δ^- as the distance between the reconnecting point on the free vortex and the particle surface. After reconnection time t_{rec}^- between the free vortex and the sphere surface, the separation is not well defined until the particle detachment, after which δ^+ becomes simply the distance between the two extremal points of the outgoing vortex ring (see Fig. 1). The vortex filaments have been tracked using the method based on the pseudovorticity developed in [39]. Since the initial measurable value of δ^+ is of the order of the particle diameter $2a_{\mathrm{p}}$, we extrapolate the virtual original time t_{rec}^+ at which $\delta^+(t_{\mathrm{rec}}^+) = 0$, performing a linear fit of $[\delta^+(t)]^2$ and evaluating the point where it vanishes. The same protocol was used with $\delta^-(t)$ to refine the value of t_{rec}^-. The evolution of $\delta(t)$ is displayed in Fig. 2(a) for all the types of particles analyzed. In Fig. 2(b), $\delta^+(t)$ and $\delta^-(t)$ are plotted in a logarithmic scale, after rescaling the distances by a factor of λ and times by a factor of λ^2 ($\lambda = 1$ for the small particle, and $\lambda = 2$ for the large one), according to Eq. (6). It is apparent that the separation rate is independent of the particle mass and always shows a scaling compatible with $t^{1/2}$. This evidence confirms that, although the reconnection is triggered by the presence of the particle, the vortex dynamics is effectively fully governed only by the circulation.

Moreover, the scaling invariance (6) seems to be respected for the separation rate. Finally, note that the observed positive ratio between the prefactors of the separation rate (1) after and before the reconnection ($A^+/A^- \sim 5.5$) is consistent with the irreversibility of the reconnection dynamics, which is related to the conversion of energy into sound [7,8,16].
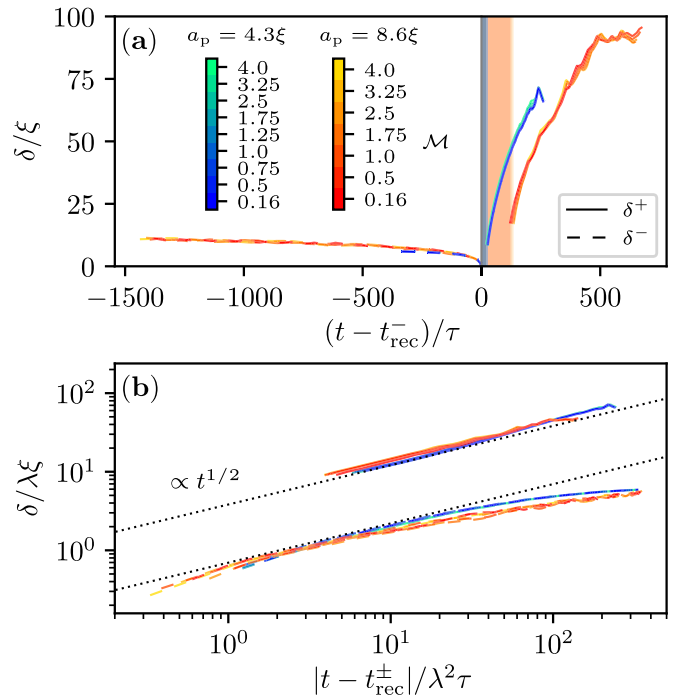
FIG. 2. (a) Distance $\delta(t)$ between reconnecting points for particles of size $a_{\mathrm{p}} = 4.3\xi$ and $a_{\mathrm{p}} = 8.6\xi$. Dashed lines correspond to δ^- before reconnection, and solid lines correspond to δ^+ after reconnection. (b) Log-Log plot of $\delta(t)$, with the rescaling (6). $\lambda = 1$ for the particle of size $a_{\mathrm{p}} = 4.3\xi$, and $\lambda = 2$ for the particle of size $a_{\mathrm{p}} = 8.6\xi$. Dotted lines indicate the scaling $t^{1/2}$.
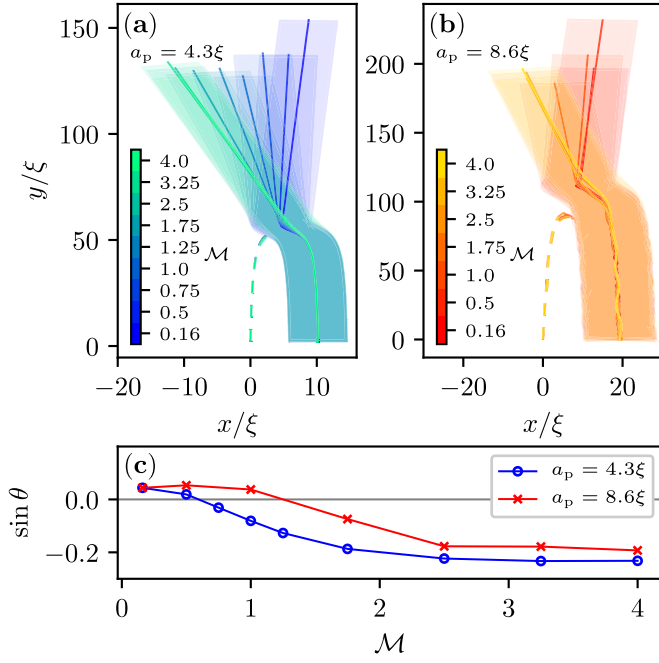
FIG. 3. Trajectories of particles of size (a) $a_{\mathrm{p}} = 4.3\xi$ and (b) $a_{\mathrm{p}} = 8.6\xi$ during the dipole reconnection. Different colors correspond to different masses, and the shaded regions indicate the area spanned by each particle. The dashed lines in corresponding colors are the trajectories of the reconnecting point of the vortex without particles at times $t < t_{\mathrm{rec}}^-$. (c) Angle of deflection of the particle trajectory after the reconnection as a function of the particle mass for both particle sizes (blue circles correspond to $a_{\mathrm{p}} = 4.3\xi$, and red crosses correspond to $a_{\mathrm{p}} = 8.6\xi$). The angle considered is with respect to the dipole propagation direction.

In Figs. 3(a) and 3(b) we show the trajectories of the particles on the plane orthogonal to the dipole for the small and large particles, respectively, and for all the different masses used. The shaded regions indicate the actual area spanned by each particle. In Figs. 3(a) and 3(b), the dashed lines show the trajectories of the reconnecting point on the vortex without the particle (initially placed at $x = 0$, $y = 0$) until it touches the particle surface at time t_{rec}^-. For the large particle one can appreciate the different Magnus precession frequencies, which are inversely proportional to the mass. We observe that the ballistic motion of the particle after the reconnection is deflected with respect to the propagation direction of the dipole, and a correlation between the particle mass and the deflection angle is apparent. In particular, the heaviest particles show a smooth trajectory and a deflection concordant with the velocity orientation at the reconnection point. Conversely, light particles slightly bounce back in the opposite direction. In Fig. 3(c) the deflection angle θ of the particle trajectory with respect to the dipole propagation direction is displayed as a function of the particle mass. As already qualitatively observed in Figs. 3(a) and 3(b), both the small and large particles (indicated, respectively, by blue circles and red crosses) deviate in a similar manner, with a deflection angle that saturates at $\sin\theta \sim -0.2$ for the largest masses. The origin of such behavior can be understood as the consequence
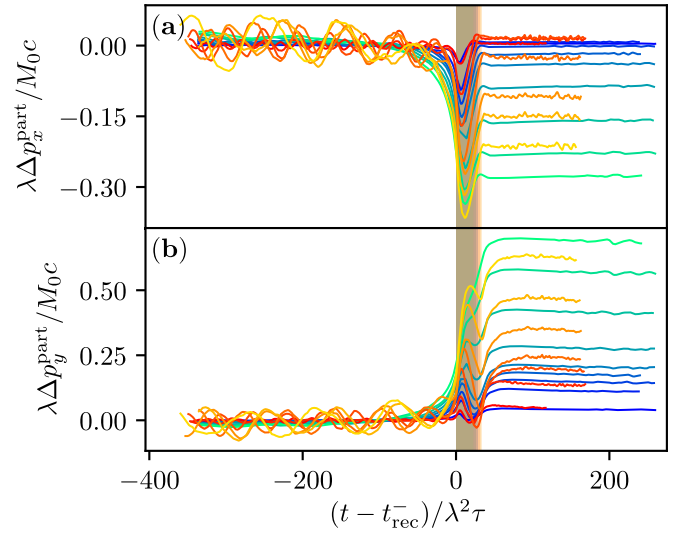

FIG. 4. (a) x component and (b) y component of the particle momentum increment with the rescaling (6) as a function of time. Different colors correspond to different particle species, with the same convention as in Fig. 2.

of a transverse momentum transfer between the vortices and the particle, which we analyze in the remainder of this section.

The x component and y component particle momentum increments $\Delta\mathbf{p}^{\mathrm{part}}(t) = \mathbf{p}^{\mathrm{part}}(t) - \mathbf{p}^{\mathrm{part}}(t = 0)$ are plotted as a function of the rescaled time, respectively, in Figs. 4(a) and 4(b). The data associated with all the species of particles analyzed are displayed using the same convention as in Fig. 3, and also the particle momentum has been rescaled as $\mathbf{p}^{\mathrm{part}} \to \mathbf{p}^{\mathrm{part}}/\lambda$, according to the transformation (6). Note that at the initial time of the simulations the particle is placed in the reference frame comoving with the dipole, so that its momentum is aligned with the propagation direction of the dipole (the y direction) and reads $\mathbf{p}^{\mathrm{part}}(t = 0) = M_{\mathrm{p}}\mathbf{v}_{\mathrm{d}} = (M_{\mathrm{p}}\Gamma/2\pi d)\hat{\mathbf{y}}$. We can clearly observe the abrupt acceleration felt by the particle in both the transverse and longitudinal directions during the reconnection event, followed after the detachment by a relaxation to a ballistic motion with constant speed. The ballistic motion is due to the absence of Stokes drag in the superfluid, and a negligible interaction with sound or with the outgoing vortex ring. The shaded area represents the time window after t_{rec}^- in which the particle is pierced by both the filaments and the vortex separation δ is undefined. Remarkably, such a window turns out to be the same in the rescaled units regardless of the particle size. Note how before the reconnection the momentum of the trapped particle oscillates weakly about a constant average because of the Magnus precession induced by the vortex [28]. If the invariance (6) really holds, the net particle momentum increment after the detachment in the rescaled units is expected to coincide for particles of different radii but the same relative mass $\mathcal{M}$. However, a small mismatch can be observed, which is probably due to the interaction between the particle and the vortex by which it is trapped before the reconnection. Such interaction indeed produces Magnus oscillations of greater amplitude for the large particle, as well as the generation of Kelvin waves along
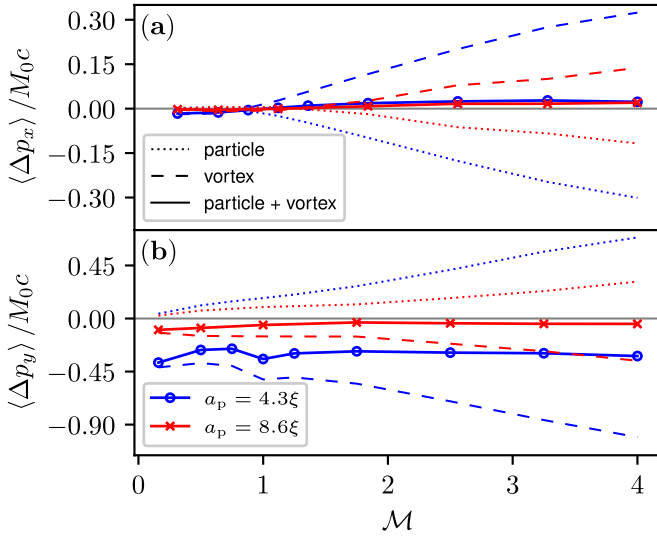
FIG. 5. (a) x component and (b) y component of the net momentum increment as a function of the particle mass for different particle sizes. Dotted lines are the particle momentum, dashed lines are the vortex ring momentum, and solid lines show the sum of the two. Blue lines refer to the small particle ($a_{\mathrm{p}} = 4.3\xi$), and red lines refer to the large one ($a_{\mathrm{p}} = 8.6\xi$).

the filament and sound radiation, which certainly corrupt the scaling invariance (6).

We eventually analyze the momentum exchange between the vortices and particle. Parametrizing the vortex ring after the reconnection as $\mathbf{R}(s, t)$, where s is a spatial parametrization variable, the linear momentum of the vortex can be expressed within the Biot-Savart framework as [40]

$$\mathbf{p}^{\mathrm{vort}} = \frac{\rho_0 \Gamma}{2} \oint \mathbf{R}(s, t) \times d\mathbf{R}(s, t), \qquad (7)$$

where the contour integral is evaluated along the ring. Note that the vortex linear momentum (7) is *de facto* a purely geometrical quantity, determined by the spatial configuration of the ring. In fact, each component of the vortex momentum can be related to the projection of the oriented area enclosed by the filament onto the corresponding direction [41]. The momentum contribution of the superfluid $\mathbf{p}_{\mathrm{GP}}$ to the total momentum in Eq. (5) contains the vortex momentum (7) and compressible waves.

The net momentum increment for the vortex is defined as $\langle \Delta \mathbf{p}^{\mathrm{vort}} \rangle = \langle \mathbf{p}^{\mathrm{vort}}(t > t_{\mathrm{rec}}) \rangle - \mathbf{p}^{\mathrm{vort}}(t = 0)$, which is analogous to the net momentum increment for the particle. In practice, the vortex momentum is computed from the filaments tracked during the GP simulation. Then it is averaged over a time window of $\sim 20\tau$ after the particle detachment, during which it remains steady. The x and y components of the net momentum increments as a function of the mass are displayed Fig. 5. The dotted lines are the particle net momentum increments, the dashed lines are the corresponding vortex net momentum increments, and the solid lines are the sum of the two. Blue lines refer to the small particle, and red lines refer to the large one.

In the x direction (perpendicular to the dipole velocity) the momentum acquired by the particle compensates almost exactly the momentum increment of the vortex, and thus,

the transfer to sound modes is negligible. On the contrary, in the y direction and, in particular, for the small particle (solid blue line with circles), we observe a net momentum transfer from the particle and the vortices to other degrees of freedom. This transfer is independent of the particle mass, and it is consistent with the observation of a sound pulse after the reconnection in Fig. 1.

IV. RECONNECTION OF TWO LINKED RINGS

In this section we study a different setting in which vortices reconnect regardless of the presence of particles. In particular, we consider as the initial configuration a Hopf link consisting of two vortex rings with radius $R = 18\xi$, which is known to spontaneously undergo reconnection. We place $N_{\mathrm{p}} = 8$ particles of size $a_{\mathrm{p}} = 3.7\xi$ randomly distributed along each ring. The initial condition is shown in the first snapshot on the left in Fig. 6. The numerical parameters for the particle potential are $V_0 = 20\mu$ and $\zeta = 3\xi$.

We set as the initial velocity of each particle the velocity of the ring by which it is trapped $\mathbf{v}_{\mathrm{ring}}$. In order to study how the presence of particles modifies the reconnection we consider three different particle masses, light ($\mathcal{M} = 0.51$), neutral ($\mathcal{M} = 1$), and heavy ($\mathcal{M} = 3.14$ and $\mathcal{M} = 12.56$). The evolution of the system for light particles ($\mathcal{M} = 0.51$) according to the GP dynamics is displayed in Fig. 6. Analogous to what was observed for the dipole, as a result of the particle-vortex interaction [27], the reconnection takes place between one trapped particle and the other filament. In the particular case of light particles, two unlinked vortex rings emerge after the reconnection: a large ring which contains the majority of the particles and a small ring with two particles still attached. Moreover, because of the violence of the event, a couple of particles get detached from the vortices.

In order to give a quantitative description, we measured the separation rate $\delta(t)$ for the different masses. They are reported in Fig. 7(a) as solid lines with markers. For comparison, Fig. 7(a) also includes the distance δ for the vortices without particles (dashed red line). Overall, if the particles are not too heavy, the reconnection remains almost unaffected by their presence. However, at very close distances a speedup takes place due to particle-vortex interactions. Conversely, in the case of heavy particles, their inertia is so large that vortices are driven by them. To illustrate this fact, we consider the fictitious case in which free heavy particles (without vortices) are set in the same positions as and with the initial velocity of the trapped ones. The distance in this case is computed as the minimal distance between the two groups of particles. Comparing this separation with that of heavy trapped particles $\mathcal{M} = 12.56$ (light green triangles), it is clear that in the latter case the ballistic motion of particles governs the dynamics.

Finally, in Figs. 7(b) and 7(c) a reconstruction of the event displayed in Fig. 6 using the tracked vortex filaments (rendered as blue solid lines) is also shown from a different perspective. For comparison, the tracked vortices corresponding to a simulation with the same initial configuration but without particles are shown as red lines. It is evident that the dynamics in the two cases are rather similar, especially before the reconnection. However, in the moments immediately prior to the reconnection one of the vortices decorated with particles shows a clear bending toward a particle set on the other
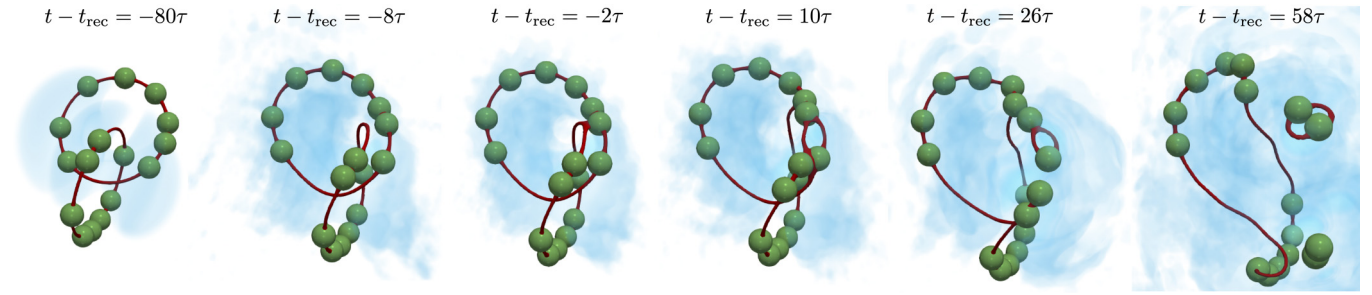
FIG. 6. Snapshots of the superfluid density and light particles ($\mathcal{M} = 0.51$) during the Hopf link reconnection (time varies from left to right). Vortices are displayed as red isosurfaces at low density; particles are the green spheres, and sound is rendered in blue.

filament. This is a clear indication of a fast acceleration, which is induced by the fluid depletion generated by the presence of the particle.

V. DISCUSSION

In this work we studied how particles trapped inside quantum vortices modify the process of vortex reconnections. We
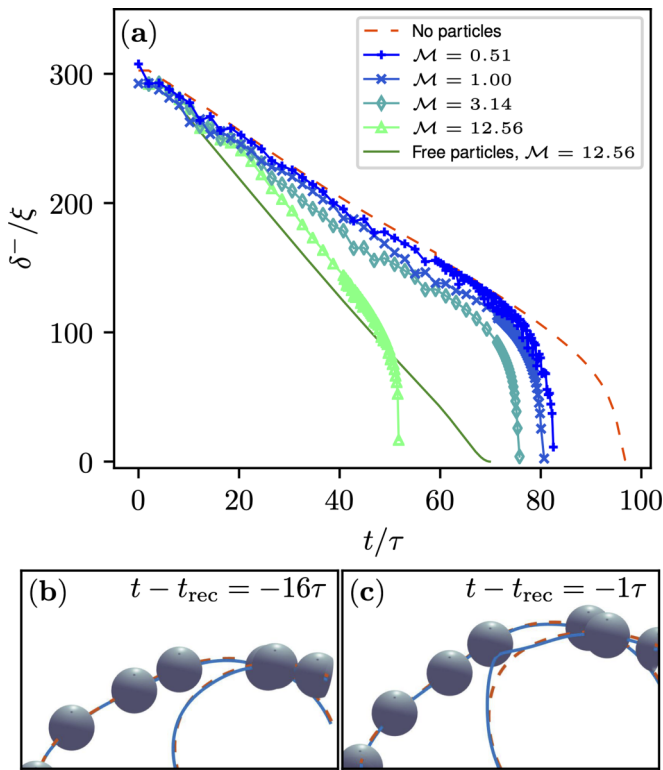

FIG. 7. (a) Separation between the reconnecting rings for different masses of the trapped particles (solid lines with markers). The red dashed line is the vortex separation in the absence of particles, and the green solid line is the separation between ballistic particles without vortices. A reconstruction of the event for light particles ($\mathcal{M} = 0.51$) using the tracked filaments (b) before and (c) at the reconnection. The filaments of the simulation with particles are displayed as blue solid lines. The filaments corresponding to a simulation with the same initial conditions but without particles are shown as red dashed lines.

have investigated two different settings: a vortex dipole with one trapped particle and a Hopf link with a number of particles randomly positioned within the vortex. Whereas in the first case the reconnection is triggered by the symmetry breaking induced by the particle, in the second one vortices reconnect regardless of the presence of particles. In the case of the dipoles, we observed that the $t^{1/2}$ temporal reconnection scaling is preserved independently of the particle mass and size. During the reconnection process, we observe a net momentum transfer from vortices to particles in both directions perpendicular to the axis of the vortex dipole. In the transverse direction with respect to the dipole initial velocity, the transfer is proportional to the mass of the particles, and it is almost exactly compensated by an equal change in the vortex momentum. In the direction of the dipole displacement, the particle speedup after reconnection is not fully compensated by the vortices. The net momentum difference is roughly independent of the mass, and it could be associated with the emission of a sound pulse, such as the one studied in [16]. In the case of the Hopf link vortex, it was observed that the reconnection process at large distances is almost unaffected by neutral or light particles. On the contrary, if particles are heavy, it is driven by the particle ballistic motion. At very close distances, the reconnection is speeded up because of the interaction between the particles and the reconnecting vortex. In general, it was also observed that reconnection takes place generically between a trapped particle and an approaching filament.

In conclusion, besides providing further insights into the current knowledge of the vortex reconnection process, our findings constitute theoretical support and a benchmark for the superfluid ^{4}He experiments at very low temperature, in which the vortices are sampled by solid particles [15,18]. In particular, as has been proved in the case of Kelvin wave tracking [28], we stress that the use of light particles is recommended for reproducing the bare vortex dynamics, provided, of course, that buoyancy effects remain negligible.

APPENDIX: DEALIASING OF THE EQUATIONS OF MOTIONS AND CONSERVATION OF THE INVARIANTS

The set of equations of motion (3) and (4) needs to be dealiased in order to conserve the total momentum (5). The equations are dealiased by performing a Galerkin truncation, which consists in keeping only the Fourier modes with wave numbers smaller than a UV cutoff $k_{\max}$. The truncated equations of motion are

$$i\hbar \frac{\partial \psi}{\partial t} = \mathcal{P}_{\mathrm{G}}\left[-\frac{\hbar^2}{2m}\nabla^2\psi - \mu\psi + g\mathcal{P}_{\mathrm{G}}\big[|\psi|^2\big]\psi + \sum_{i=1}^{N_{\mathrm{p}}} V_{\mathrm{p}}^i\psi \right],$$
(A1)

$$M_{\mathrm{p}}\ddot{\mathbf{q}}_i = -\int V_{\mathrm{p}}^i \mathcal{P}_{\mathrm{G}}\big[\nabla|\psi|^2\big]\,d\mathbf{x} + \sum_{j\neq i}^{N_{\mathrm{p}}} \frac{\partial}{\partial\mathbf{q}_i}V_{\mathrm{rep}}^{ij}, \quad \text{(A2)}$$

where $V_{\mathrm{p}}^i = V_{\mathrm{p}}(|\mathbf{x} - \mathbf{q}_i|)$ and $\mathcal{P}_{\mathrm{G}}$ is a Galerkin truncation operator. $\mathcal{P}_{\mathrm{G}}$ acts on the function $f(\mathbf{x})$ as $\mathcal{P}_{\mathrm{G}}[f(\mathbf{x})] = \sum_{\mathbf{k}} \hat{f}(\mathbf{k})e^{i\mathbf{k}\cdot\mathbf{x}}\theta_{\mathrm{H}}(k_{\max} - |\mathbf{k}|)$, where $\hat{f}(\mathbf{k})$ is the Fourier transform of $f(\mathbf{x})$ and θ_{H} is a Heaviside theta function. It is also assumed that the particle potential is always truncated: $V_{\mathrm{p}}^i = \mathcal{P}_{\mathrm{G}}[V_{\mathrm{p}}^i]$. Equations (A1) and (A2) exactly conserve all the invariants (Hamiltonian, fluid mass, and total momentum) if the 2/3 rule is used, namely, if $k_{\max} = \frac{2}{3}\frac{N_{\mathrm{res}}}{2}$, with N_{res} being the number of uniform grid points per direction [34]. For a pseudospectral code, this technique implies an extra computational cost of one extra back and forth fast Fourier transform.

[1] R. J. Donnelly, *Quantized Vortices in Helium II* (Cambridge University Press, Cambridge, 1991).

[2] S. Kida and M. Takaoka, Annu. Rev. Fluid Mech. **26**, 169 (1994).

[3] F. Hussain and K. Duraisamy, Phys. Fluids **23**, 021701 (2011).

[4] J. Koplik and H. Levine, Phys. Rev. Lett. **71**, 1375 (1993).

[5] W. F. Vinen and J. J. Niemela, J. Low Temp. Phys. **128**, 167 (2002).

[6] S. Nazarenko and R. West, J. Low Temp. Phys. **132**, 1 (2003).

[7] A. Villois, D. Proment, and G. Krstulovic, Phys. Rev. Fluids **2**, 044701 (2017).

[8] D. Proment and G. Krstulovic, arXiv:2005.02047.

[9] L. Galantucci, A. W. Baggaley, N. G. Parker, and C. F. Barenghi, Proc. Natl. Acad. Sci. USA **116**, 12204 (2019).

[10] S. Zuccher, M. Caliari, A. W. Baggaley, and C. F. Barenghi, Phys. Fluids **24**, 125108 (2012).

[11] A. J. Allen, S. Zuccher, M. Caliari, N. P. Proukakis, N. G. Parker, and C. F. Barenghi, Phys. Rev. A **90**, 013601 (2014).

[12] C. Rorai, J. Skipper, R. M. Kerr, and K. R. Sreenivasan, J. Fluid Mech. **808**, 641 (2016).

[13] M. Tsubota and H. Adachi, J. Low Temp. Phys. **162**, 367 (2011).

[14] A. W. Baggaley, L. K. Sherwin, C. F. Barenghi, and Y. A. Sergeev, Phys. Rev. B **86**, 104501 (2012).

[15] M. S. Paoletti, M. E. Fisher, and D. P. Lathrop, Phys. D (Amsterdam, Neth.), **239**, 1367 (2010).

[16] A. Villois, D. Proment, and G. Krstulovic, arXiv:2005.02048.

[17] S. Serafini, M. Barbiero, M. Debortoli, S. Donadello, F. Larcher, F. Dalfovo, G. Lamporesi, and G. Ferrari, Phys. Rev. Lett. **115**, 170402 (2015).

[18] G. P. Bewley, M. S. Paoletti, K. R. Sreenivasan, and D. P. Lathrop, Proc. Natl. Acad. Sci. USA **105**, 13707 (2008).

[19] G. P. Bewley, D. P. Lathrop, and K. R. Sreenivasan, Nature (London) **441**, 588 (2006).

[20] M. L. Mantia and L. Skrbek, Europhys. Lett. **105**, 46002 (2014).

[21] M. La Mantia and L. Skrbek, Phys. Rev. B **90**, 014519 (2014).

[22] D. R. Poole, C. F. Barenghi, Y. A. Sergeev, and W. F. Vinen, Phys. Rev. B **71**, 064514 (2005).

[23] J. I. Polanco and G. Krstulovic, Phys. Rev. Fluids **5**, 032601 (2020).

[24] K. W. Schwarz, Phys. Rev. B **38**, 2398 (1988).

[25] D. Kivotides, C. F. Barenghi, and Y. A. Sergeev, Phys. Rev. B **77**, 014527 (2008).

[26] Y. A. Sergeev and C. F. Barenghi, J. Low Temp. Phys. **157**, 429 (2009).

[27] U. Giuriato and G. Krstulovic, Sci. Rep. **9**, 4839 (2019).

[28] U. Giuriato, G. Krstulovic, and S. Nazarenko, Phys. Rev. Res. **2**, 023149 (2020).

[29] U. Giuriato and G. Krstulovic, Phys. Rev. Fluids **5**, 054608 (2020).

[30] A. Griffin, V. Shukla, M.-E. Brachet, and S. Nazarenko, Phys. Rev. A **101**, 053601 (2020).

[31] V. Shukla, M. Brachet, and R. Pandit, Phys. Rev. A **94**, 041602(R) (2016).

[32] U. Giuriato, G. Krstulovic, and D. Proment, J. Phys. A **52**, 305501 (2019).

[33] V. Shukla, R. Pandit, and M. Brachet, Phys. Rev. A **97**, 013627 (2018).

[34] G. Krstulovic and M. Brachet, Phys. Rev. E **83**, 066311 (2011).

[35] M. Abid, C. Huepe, S. Metens, C. Nore, C. T. Pham, L. S. Tuckerman, and M. E. Brachet, Fluid Dyn. Res. **33**, 509 (2003).

[36] N. G. Berloff and P. H. Roberts, J. Phys. A **34**, 10057 (2001).

[37] P. G. Saffman, *Vortex Dynamics* (Cambridge University Press, Cambridge, 1992).

[38] L. Kiknadze and Y. Mamaladze, arXiv:cond-mat/0604436.

[39] A. Villois, G. Krstulovic, D. Proment, and H. Salman, J. Phys. A **49**, 415502 (2016).

[40] L. M. Pismen, *Vortices in Nonlinear Fields: From Liquid Crystals to Superfluids, from Non-Equilibrium Patterns to Cosmic Strings*, International Series of Monographs on Physics (Oxford University Press, Oxford, 1999).

[41] S. Zuccher and R. L. Ricca, Phys. Rev. E **100**, 011101(R) (2019).

Chapter 5

Particles in superfluids

In this chapter, we provide an introduction to the dynamics of particles in low-temperature superfluids. We will briefly present different models used to describe the dynamics of particles or impurities in superfluids. Then, we will discuss the interaction between particles and Kelvin waves. Three works are included at the end of the chapter.

One of the most natural ways of studying the dynamics of a fluid is to use particles that are transported by the flow. If such particles are small enough and have the same density than the fluid, they can be considered as tracers of the flow and their velocity is simply given by the one of the flow. Their dynamics is then described by the equation

$$\frac{\mathrm{d}\mathbf{X}(t)}{\mathrm{dt}} = \mathbf{v}(\mathbf{X}(t), t), \tag{5.1}$$

where $\mathbf{v}$ is the velocity field of the flow, and $\mathbf{X}$ the position of the particle. In that way, if one can measure the instantaneous velocity of particles, one can thus infer or reconstruct the velocity field. Such an idea has been largely used in the past in classical fluids with the experimental techniques of *Particle image velocimetry* (PIV) and *Particle tracking velocimetry* (PTV) [Raf07; TB09]. Thanks to the incredibly fast cameras and powerful lasers available today, those techniques are at the heart of current experiments in classical turbulent research.

For incompressible flows, perfect tracers uniformly sample the fluid. While this is important to study the velocity field, it might not be the best property to visualise certain structures of the flow. It is well understood that particle inertia plays a crucial role in the spatial concentrations of particles [Bec+07; Cal+08; GV08; TB09]. Indeed, whereas heavy particles show a tendency to escape from vortices, light ones are captured by them [Max83]. This idea led to the visualisation of vortex filaments in the early 1990s [DCB91], and it has become now very standard.

In superfluids, the idea of using small objects to learn the properties of the flow has a long history. Early experiments in superfluid helium used ions and electron bubbles to study quantum vortices [Don91]. There is a vast number of experimental studies on the interaction of ions and quantum vortices, but the most significant breakthrough occurred in 2006. Using micrometre sized solid hydrogen particles, an experimental group in Maryland succeeded to visualise quantum vortex filaments in superfluid helium [BLS06]. Since then, particles are the main experimental tool to study the dynamics of quantum vortices and quantum turbulence. Such particles are several orders of magnitude larger than the vortex core size to be called tracers, and it is still not entirely clear how they affect quantum vortex dynamics. Address such a critical issue for current superfluid experiments is the main objective of my ongoing ANR JCJC project *Lagrangian properties and universality of quantum turbulence*.

5.1 Experimental use of particles in superfluids

As already mentioned, the experimental use of electron bubbles to infer properties of quantum vortices has a long history. Such ions get captured by vortices, and because of their charge, they can be manipulated by using an external electric field. This idea was already used in the 50's to visualise Abrikosov vortex lattices [WP74; YGP79]. Once the electrons get trapped by quantum vortices inside a rotating superfluid helium bucket, an electric field can drive them to boundaries of the experiment, where they can be used to make a "photograph" of the lattice. In such a way, the first visualisation of quantum vortices was obtained. Figure 5.1.a reproduces an experimental image published in reference [WP74].
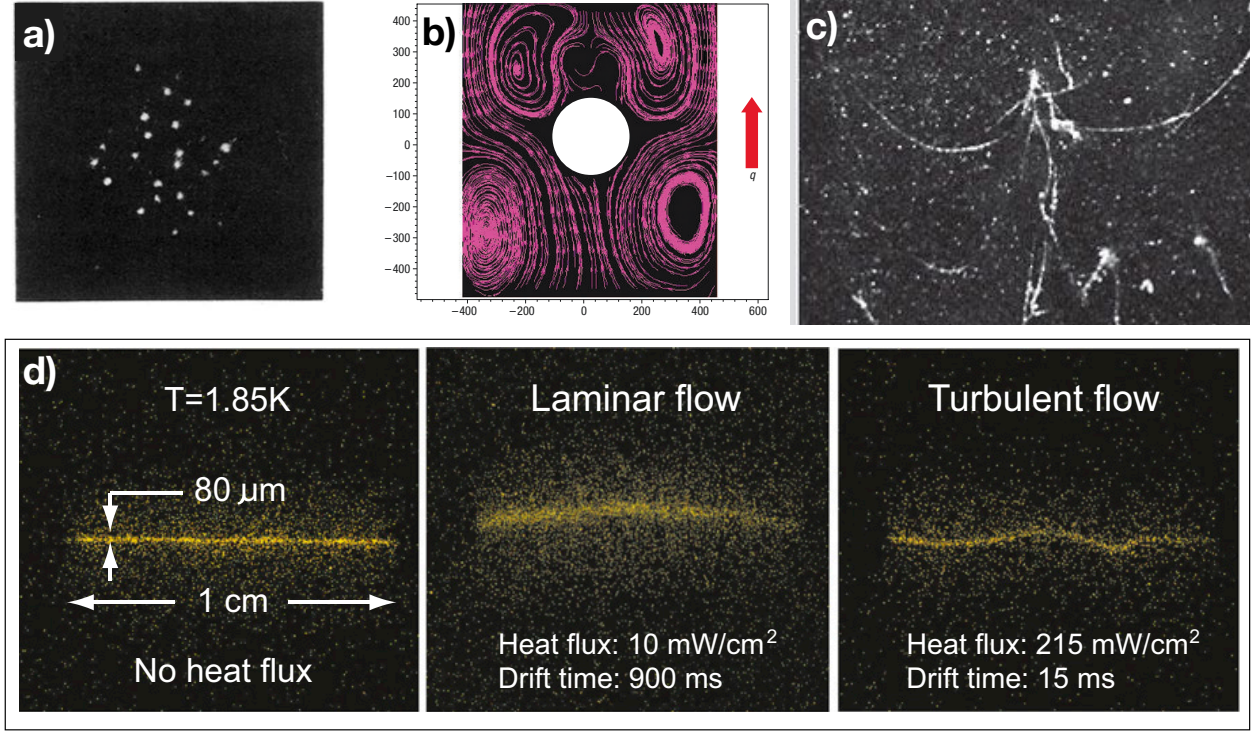

FIG. 2. Photographs of stable vortex arrays. Each photograph is a multiple exposure of 60 consecutive motion-picture frames. The length scale on the photographs is known to an accuracy of approximately 2%. The diameter of the dark circles corresponds to the 2-mm bucket diameter. The arrays were placed symmetrically within the circles. The actual location of the bucket relative to the arrays is not known. The angular velocities were (a) 0.30 sec^{-1}, (b) 0.30 sec^{-1},

Figure 5.1: **a)** Early experimental visualisations of quantum vortices in a rotating bucket. Figure reproduced from [WP74].**b)** PIV visualisation of a superfluid flow around an obstacle from T. Zhang and Van Sciver [ZV05]. **c)** First visualisation of quantum vortices using hydrogen particles by Bewley et al. [BLS06]. **d)** Fluorescence images of a thin line of He$_2^*$ tracers in thermal counterflow, from [Guo+14].

Another remarkable achievement in the use of particles for studying superfluid helium was the development of PIV in the early 2000 [Don+02; ZCV04; ZV05]. T. Zhang and Van Sciver [ZV05] succeed to visualise a superfluid flow around a cylinder, observing the appearance of stationary normal fluid eddies both downstream (at the rear) and upstream (in front) of the cylinder. However, its "pure" quantum origin was later questioned and explained in terms of classical fluids [SB09a]. A PIV visualisation of that flow is reproduced from reference [ZV05] in figure 5.1.b.

The real breakthrough, occurred in 2006 when entire vortex filaments were visualised. Bewley et al. [BLS06] injected micrometer sized hydrogen particles in a superfluid helium experiment and observed that they get trapped inside filaments. An image of quantum vortices, taken from [BLS06], is reproduced in 5.1.c. Since then, particle tracking has been used to study the dynamics of quantum vortices, including the observation of Kelvin waves [Fon+14], vortex reconnections [Bew+08; FSL19] and to unveil the differences between the velocity statistics of classical and quantum turbulent flows [Pao+08; LS14b; LS14a]. Today, different groups in Grenoble, Prague and Tallahassee use hydrogen and deuterium particles to study superfluid helium.

Finally, it is worth mentioning that a new visualisation technique was developed by W. Guo et al. [Guo+10; Gao+15] using helium excimers. By exciting or ionising helium atoms, it is possible to produce He_2^* triplets. Such molecules form bubbles of a typical size of 6 Angstroms and can be visualised by a laser-induced fluorescence technique. Above $1K$, such particles are expected to follow mainly the normal fluid and become excellent tracers of that component. Using this technique, Marakov et al. [Mar+15] succeed to estimate structure functions in turbulent counterflow. Visualisations of the flow are displayed in figure 5.1.d.

The list of references previously cited is certainly not exhaustive but gives a rough idea of some experimental techniques and the first groups that used them. We refer the reader to the review article [Guo+14] for more details on the visualisation of turbulent quantum flows.

5.2 Theoretical modelling of particles and impurities immersed in superfluids

In Chapter 2 we discussed different models that are commonly used to describe the dynamics of a superfluid. We highlighted the complexity of the system and the lack of a universal model able to describe the whole range of scales and temperatures. When trying to describe the dynamics of particles, one faces the same issue, and even further assumptions are needed. Basically, for each of the models presented in Chapter 2, there exist one or several ways of incorporating the particles dynamics. In this chapter, we will mainly discuss a simple model based on the Gross-Pitaevskii equation. This model was extensively studied in the Ph.D work of Umberto Giuriato, from which I selected three publications included at the end of the chapter. Other possible models will be briefly mentioned in Section 5.2.2.

5.2.1 Gross-Pitaevskii equation coupled with classical active particles

In this model, the idea is to introduce the particle dynamics in a self-consistent manner, taking advantage of the Hamiltonian structure of the GP equation. We start we rewriting the Gross-Pitaevskii model

$$i\hbar \frac{\partial \psi}{\partial t} = -\frac{\hbar^2}{2m} \nabla^2 \psi + g|\psi|^2 \psi - \mu \psi + V_p(\mathbf{x})\psi, \qquad (5.2)$$

where we have included the potential V_p that we assumed to be localised around $\mathbf{x} = 0$ and to have a maximum strength $V_0 > 0$ at $\mathbf{x} = 0$. The ground state of the system can be easily found within the Thomas-Fermi approximation, that consists on neglecting the kinetic term of GP. The density profile ρ_p reads

$$\rho_p(\mathbf{x}) = \rho_0 \left(1 - \frac{V_p(\mathbf{x})}{\mu}\right) \theta \left[1 - \frac{V_p(\mathbf{x})}{\mu}\right], \qquad (5.3)$$

where $\rho_0 = \mu/g$ is the bulk density value and $\theta[\ ]$ is the Heaviside function that ensures positivity. As the potential is strong, that means $V_0 \gg \mu$, the density vanishes at the centre of potential, creating a hole. This approximation, together with a numerical solution, are displayed in figure (5.2). A particle immersed in a superfluid can be seen as a hole or a complete depletion of the condensate. The potential V_p can be used to model a particle, and its support determines the particle shape. The simplest way to provide some dynamics to the particle is to add to the GP Hamiltonian the extra degrees of freedom of the particles.

We consider a set of N_p spherical particles of radius a_p and mass M_p, described by the set of coordinates $\mathbf{q}_1(t), \mathbf{q}_2(t), \ldots, \mathbf{q}_{N_p}(t)$ and velocities $\dot{\mathbf{q}}_1(t), \dot{\mathbf{q}}_2(t), \ldots, \dot{\mathbf{q}}_{N_p}(t)$. The Hamiltonian of the system consists of the GP Hamiltonian containing a potential V_p for each particle centred on their position, plus the kinetic energy of the particles. It reads

$$H = \int \left(\frac{\hbar^2}{2m}|\nabla \psi|^2 + \frac{g}{2}\left(|\psi|^2 - \frac{\mu}{g}\right)^2 + \sum_{i=1}^{N_p} V_p(|\mathbf{x} - \mathbf{q}_i|)|\psi|^2\right) d\mathbf{x} + \sum_{i=1}^{N_p} \frac{\mathbf{p}_i^2}{2M_p}, + \sum_{i<j}^{N_p} V_{rep}^{ij}, \qquad (5.4)$$
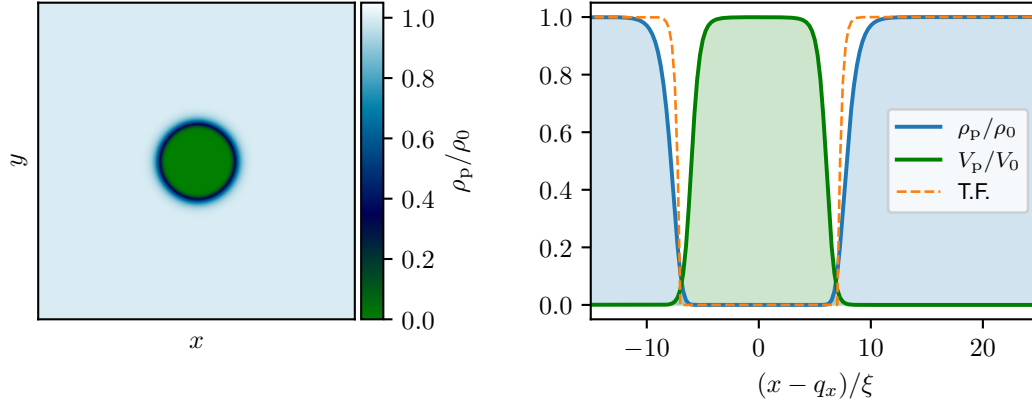
Figure 5.2: **Left:** Ground state a_p of GP equation (5.2) obtained numerically. **Right:** One dimensional cut of the ground state. The blue line shows the density profile and its compared to the Thomas-Fermi approximation (5.3) (orange dashed line). The figure also displays the normalised potential used to obtained this solution. The strength of the potential is $V_0 = 20\mu$. ξ is the healing length. Figure courtesy of U. Giuriato, taken from his Ph.D. manuscript [Giu20]

where the momenta are $\mathbf{p}_i = M_\mathrm{p}\dot{\mathbf{q}}_i$ and V_rep^{ij} is a repulsive short-range potential to mimic a hard-sphere behaviour between particles i and j. The corresponding equations of motion are directly obtained by varying the associated action, and they are given by

$$i\hbar\frac{\partial\psi}{\partial t} = -\frac{\hbar^2}{2m}\nabla^2\psi + (g|\psi|^2 - \mu)\psi + \sum_{i=1}^{N_\mathrm{p}} V_\mathrm{p}(|\mathbf{x} - \mathbf{q}_i|)\psi, \tag{5.5}$$

$$M_\mathrm{p}\ddot{\mathbf{q}}_i = -\int V_\mathrm{p}(|\mathbf{x} - \mathbf{q}_i|)\nabla|\psi|^2\,\mathrm{d}\mathbf{x} + \sum_{\substack{j\neq i}}^{N_\mathrm{p}} \frac{\partial}{\partial\mathbf{q}_i}V_\mathrm{rep}^{ij}. \tag{5.6}$$

We will refer in the following to this model as the GP-P model. This set of equation fully describes the dynamics of particles in a superfluid. Note that by definition, particles have a finite size, they are active and modify the flow. They also interact with each other through the superfluid. This model was firstly introduced by Winiecki and Adams in 2000 [WA00] to study vortex nucleation in three dimensions and later used by Shukla et al. [SBP16] in two dimensions. Although it presents some technical complications if one wants to ensure full numerical conservation of momentum (see [Giu20; GK20b]), the model remains simple and allows for simulations with a relatively large number of particles. For this reason, we have chosen this model to address several questions concerning the interaction between particles and quantum vortices.

To provide an intuition of this model, let's consider only one particle and take the limit where the potential V_p is a δ-Dirac function. In that limit, the equation for the particle simplifies to

$$M_\mathrm{p}\frac{\mathrm{d}^2\mathbf{q}}{\mathrm{d}t^2} = -c\nabla\rho(\mathbf{q}, t), \tag{5.7}$$

where c is a suitable dimensional constant which value is not essential. This Newton equation tells that particles tend to go where density, or pressure, is minimal. Particles are thus, roughly speaking, driven by Bernoulli forces what allows the use of particles for visualising quantum vortices. In work [GK19], included at the end of the chapter, we study the trapping of a particle by a quantum vortex.

We also notice that equation (5.7) is very different from the on of a tracer (5.1). At very low temperatures, because of the absence of Stokes drag, particles do not sample the superfluid velocity $\nabla\phi$ and

inertial effects fully drive their dynamics. Therefore, at low temperatures particle tracking in quantum fluids provides, at best, the dynamics of quantum vortices that is different from the ambient superfluid flow. In the included publications, we show that even though particles are not point-like, have inertia and strongly interact with quantum vortices, they can provide a lot of information on the vortices as well as opening some exciting research directions.

5.2.2 Other models for particle dynamics

Impurity field description

One of the first attempts to describe the dynamics of impurities in a superfluid was made by E.P. Gross himself in 1958 [Gro58] and shortly after resumed by Clark [Cla65] trying to provide some support for the use of electron bubbles in superfluid helium. In the Gross-Clark model, the impurity is represented by a new field φ satisfying the (linear) Schrödinger equation. The associated Hamiltonian is

$$H = \int \left(\frac{\hbar^2}{2m}|\nabla\psi|^2 + \frac{g}{2}\left(|\psi|^2 - \frac{\mu}{g}\right)^2 + \frac{\hbar^2}{2m_\mathrm{I}}|\nabla\varphi|^2 - \mu_\mathrm{I}|\varphi|^2 + g_{12}|\psi|^2|\varphi|^2 \right) \tag{5.8}$$

where m_I is the mass of the impurity, μ_I is its chemical potential and g_{12} the coupling constant between the condensate and the impurity. In this model, the impurity has the same effect that the potential V_p in the previous model. It depletes the condensate, but its shape can change in time. Several works have used this model; here we cite only two that are very relevant for this chapter. The Gross-Clark model was much later used by N. Berloff and P.H. Roberts [BR00] to study the trapping of an electron bubble by a quantum vortex and more recently by Villois and Salman [VS18] to address the vortex nucleation produced by an accelerated ion.

The model (5.8) readily generalises to the case of several impurities, and to the case where the impurity self-interacts. The last case corresponds to mixtures of different BECs. Although challenging to realise experimentally, it is particularly interesting the theoretical works by S. Rica and D.C. Roberts [RR09a; RR09b], where they considered several impurities coupled with one large condensate. For this system, the Hamiltonian is

$$H = \int \left(\frac{\hbar^2}{2m}|\nabla\psi|^2 + \frac{g}{2}|\psi|^4 + \lambda|\psi|^2\sum_{i=1}^{N_\mathrm{I}}|\varphi_i|^2 + \sum_{i=1}^{N_\mathrm{I}}\frac{\hbar^2}{2m_\mathrm{I}}|\nabla\varphi_i|^2 + \frac{\gamma_0}{2}|\varphi_i|^4 + \gamma\sum_{j\neq i}|\varphi_i|^2|\varphi_j|^2 \right). \tag{5.9}$$

In [RR09a; RR09b], S. Rica and D.C. Roberts showed that i) in the limit of large coupling λ impurities self-localise and thus can completely deplete the condensate. ii) There exists a condensate-mediated attractive force between the impurities. Such an effect was also studied in the model (5.4) by Shukla et al. [SBP16] and by U. Giuriato et al. [GKP19] in finite temperature two-dimensional superfluids.

We intuitively expect that for a mixture of two BECs, in which the mutual coupling and self-interaction constant of the impurity are large enough, the two resulting coupled GP equation should be well described by the GP-P model (5.4).

Vortex filament model

A different approach is again possible using the vortex filament method described in Section 2.2. The basic idea is to consider that the superfluid velocity field has to satisfy free-slip boundary conditions at the surface of the moving particle. Then, the particle is evolved by computing the net force exerted by the fluid on the particle. Schwarz performed the first numerical and theoretical investigations in 1974 [Sch74]. After the experimental observation of quantum vortices, this idea was resumed and developed further numerically by the Newcastle group [KBS06; KBS07; KBS08; Kiv08b; Kiv08a].

This model is costly and, as for vortex reconnections, it needs several ad-hoc patches to describe some physical aspects of the system such as the trapping of a particle by a quantum vortex. However, as

anyway the vortex filament is not intended to describe the physics of a superfluid at scales of the order of the vortex core, those issues might be not very important.

Passive particles in the Hall-Vinen-Bekarevich-Khalatnikov model

If one is interested in the large scales of finite temperature superfluids described by the HVBK equations presented in Section 2.4, it is also possible to include the particle dynamics. In this setting, the approximations are very crude, and they need to be interpreted with caution and be confronted with experimental data whenever it is possible.

Particles in finite temperature superfluid helium experience a Stokes drag associated with the viscosity of the normal fluid, while also feeling the pressure gradient forces from both fluid components. The first strong approximation is to consider that particles are much smaller than the Kolmogorov scales of the flow, so their action on the flow and any finite-size effects are neglected because the viscous term immediately damps any disturbance of the flow. Besides, we also neglect the Basset history term. Such approximations are very standard in the study of inertial particles in classical turbulence, and therefore the resulting equations for particles in the HVBK framework are a generalisation of the famous M. Maxey and J.J. Riley equations for point particles in classical fluids [Max83]. We do not provide here a derivation of their equation of motion and we refer to [ZCV04; Poo+05; SB09b] for further reading. The equations of motion for a particle immersed in a HVBK superfluid are

$$\frac{\mathrm{d}^2\mathbf{q}}{\mathrm{d}t^2} = \frac{1}{\tau_\mathrm{p}}(\mathbf{v}_\mathrm{n}(\mathbf{q}) - \frac{\mathrm{d}\mathbf{q}}{\mathrm{d}t}) + \beta\left(\frac{\rho_\mathrm{n}}{\rho}\frac{D\mathbf{v}_\mathrm{n}}{Dt} + \frac{\rho_\mathrm{s}}{\rho}\frac{D\mathbf{v}_\mathrm{s}}{Dt}\right) \tag{5.10}$$

$$\tau_\mathrm{p} = \frac{a_\mathrm{p}^2}{3\beta\nu}, \quad \beta = \frac{3\rho}{2\rho_\mathrm{p} + \rho} \tag{5.11}$$

where ρ_p is the particle density and a_p its radius. D/Dt is the corresponding material derivatives. We recall that the superfluid and normal velocities are denoted by $\mathbf{v}_\mathrm{s}$ and $\mathbf{v}_\mathrm{n}$, respectively. Besides, the total fluid density $\rho = \rho_\mathrm{n} + \rho_\mathrm{s}$ is the sum of the normal and superfluid densities. The parameter β accounts for added mass effects, while the Stokes time τ_p represents the particle response time to normal fluid fluctuations. In its definition, it appears the kinematic viscosity of helium defined as $\nu = (\rho_\mathrm{n}/\rho)\nu_\mathrm{n}$.

This model completely neglects the trapping of particles by quantum vortices and their interaction with them. Consistently with this fact, particles should be in principle smaller than the mean inter-vortex distance, so that they do not interact actively with quantised vortices, and do not get often trapped by them [SB09b]. In recent experiments, the inter-vortex distance is of the order of 10 microns [BSS14; Roc+07; Rou+14], that is comparable to both the Kolmogorov scales and to the typical size of hydrogen particles in experiments. Even though trapping is absent in the model, the term $D\mathbf{v}_\mathrm{s}/Dt$ is related to the superfluid pressure gradient, and it attracts particles towards vortices. With J. I. Polanco, we have shown that this term is dominant at low temperatures and particles indeed cluster on vortex filaments even if they are not quantised in this framework [PK20b].

5.3 Interaction between particles and Kelvin waves

One of the most striking experimental movies that were produced by the Maryland team, was the direct visualisation of vortex reconnections and Kelvin waves [Bew+08; Fon+14], that is available on youtube[1]. Particles trapped in vortices seem to follow the oscillations of Kelvin waves correctly. How is it possible that such large particles, with a size of several microns, can move without perturbing much the vortex that has a core size of the order of one Angstrom? How important is particle inertia? We address such issues in the work [GKN20] included at the end of the chapter. In this section, we take a simple model

---

[1]https://www.youtube.com/watch?v=SlXIOeOkKxU

derived in that work to further develop some concepts that are important to understand the interaction between Kelvin waves and particles.

The model developed in [GKN20] is formally valid for a particle with a size similar to the vortex core. However, we showed numerically that it still works for particles several tens of times larger than the vortex [2], showing that the model captures the main physical ingredients. We present here a simplified model that can be derived from [GKN20], that illustrates well the relevant physical process.

We consider the LIA description for the dynamics of an almost straight vortex line (see Section 3.3.1). We use the cartesian parametrisation of the filament in complex variables $s(z) = X(z) + iY(z)$ and we consider a particle at $z = 0$. We imagine the situation where a Kelvin wave pulse (or wave packet) is arriving from the left ($z < 0$) as in figure 5.3.a. The KW pulse will hit the particle, perturbing the particle
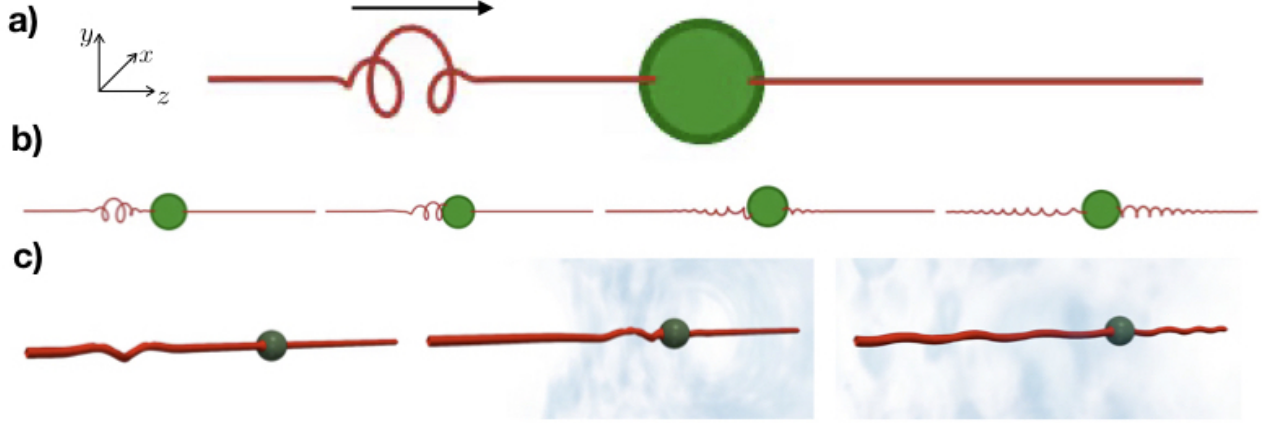

Figure 5.3: **a)** The initial configuration. A Kelvin wave pulse is moving towards a particle at rest. **b)** Evolution of the pulse. The pulse hits the particle, this one start moving and excite KWs at the other side. A fraction of KWs are transmitted, and another is reflected. **c)** Equivalent simulations with the Gross-Pitaevskii model. Simulations performed by U. Giuriato.

at rest. Once the particle starts moving, it will excite KWs on its right, as drawn in 5.3.b. From the point of view of the KW, the particle acts as a potential, where a fraction of the wave is reflected, and another one is transmitted. This idea reminds us immediately the tunnel effect of an electron. In the work [GKN20] we build this analogy mathematically. The dynamics of the system can be described by following linear equation [3]

$$ i\frac{\partial s}{\partial t} = -\frac{\Gamma\Lambda}{4\pi}\frac{\partial^2 s}{\partial z^2} + \frac{6\pi a_{\mathrm{p}}}{\Omega_{\mathrm{p}}}\delta(z)\frac{\partial^2 s}{\partial t^2}, \quad \text{with} \quad \Omega_{\mathrm{p}} = \frac{3}{2}\frac{\rho\Gamma a_{\mathrm{p}}}{M_{\mathrm{p}} + \frac{1}{2}M_0}. \tag{5.12} $$

In the previous formula, $M_0 = \rho 4\pi a_{\mathrm{p}}^3/3$ is the mass of superfluid displaced by the particle and Λ is the constant appearing in the LIA model. The frequency Ω_{p} is the result of the Magnus force acting on the trapped particle. For current experiments, it is in the range of $10 - 100$ Hz, and it could be used experimentally to determine if a particle is trapped by one or several vortices. This property is currently under experimental investigation by collaborators.

The analogy between the particle and a Kelvin wave with an electron and a δ-potential is now manifest by equation 5.12. The visualisations presented in figure 5.3.b, are actually numerical simulations of the model presented in [GKN20] and 5.3.c presents the corresponding GP numerical simulations, where we observe the discussed behaviour. To exploit further the analogy, we write the equation for an electron

---

[2]To simulate particles $\sim 10^5$ larger than the vortex core, as in current experiments, is not feasible

[3]In reference [GKN20], the equation was not written explicitly in that form, but it can be deduced taking the limits discussed in that work.

and a δ-Dirac potential

$$i\hbar\frac{\partial\psi}{\partial t} = -\frac{\hbar^2}{2m}\frac{\partial^2\psi}{\partial z^2} + U_0\delta(z)\psi. \tag{5.13}$$

We thus note that the only mathematical difference between equation (5.12) and (5.13), is the second time derivative multiplying the δ-function, that reflects the inertia of the particle. We thus infer, that an incoming Kelvin wave of frequency ω, feels the particle as an effective (particle) potential of strength

$$U_0 \propto \frac{a_{\mathrm{p}}\omega^2}{\Omega_{\mathrm{p}}}. \tag{5.14}$$

It follows that large scale (low frequency) Kelvin waves do not feel the presence of particles, and are transmitted through the particle with no significant effect. In reference [GKN20], we observe that at large scales, the Kelvin wave dispersion relation sampled by particles is the same as the theoretical one discussed in Section 3.2.

5.4 Selected publications

In this chapter we integrally include three selected publications. These works are an important part of the Ph. D. work of my student Umberto Giuriato.

- Umberto Giuriato and Giorgio Krstulovic. "Interaction between Active Particles and Quantum Vortices Leading to Kelvin Wave Generation". In: *Scientific Reports* 9.1 (Dec. 2019), p. 4839. ISSN: 2045-2322. DOI: 10.1038/s41598-019-39877-w

- Umberto Giuriato, Giorgio Krstulovic, and Sergey Nazarenko. "How Trapped Particles Interact with and Sample Superfluid Vortex Excitations". In: *Physical Review Research* 2.2 (May 11, 2020), p. 023149. ISSN: 2643-1564. DOI: 10.1103/PhysRevResearch.2.023149

- Umberto Giuriato and Giorgio Krstulovic. "Active and Finite-Size Particles in Decaying Quantum Turbulence at Low Temperature". In: *Physical Review Fluids* 5.5 (May 29, 2020), p. 054608. ISSN: 2469-990X. DOI: 10.1103/PhysRevFluids.5.054608

In the first publication, we study the capture of a particle by a quantum vortex. We build a reduced Hamiltonian model to describe the dynamics of the particle. The trapping of a particle is thus seen as a central force problem in classical mechanics. Particularly interesting is the scaling invariance

$$a_{\mathrm{p}} \to \lambda a_{\mathrm{p}}, \mathbf{q} \to \lambda\mathbf{q}, \quad \text{and} \quad t \to \lambda^2 t, \quad \text{for all } \lambda > 0, \tag{5.15}$$

found in the reduced equations describing the trapping of a particle. Such invariance could be used to justify that the current work should apply to realistic particle sizes, after a proper rescaling. Such scaling was also found to be valid in vortex reconnections in the work [GK20b], included in Chapter 4.

We also study how the vortex filament is deformed as a consequence of the long-range vortex-particle interaction. Besides, we demonstrate that when a particle moves close to a vortex, it can trigger KWs by a linear resonance. Such a mechanism could perhaps be used to excite KWs experimentally in a controlled manner.

The second publication concerns the interaction between KWs and trapped particles by the vortex. We developed there the theory presented in the previous section. The most remarkable result is the study of the KW dispersion relation sampled by the particles. Mimicking experiments, we consider an array of particles trapped in the vortex. We predict quantitatively and observe the appearance of Brillouin zones with bands and gaps. Such study naturally opens the way to investigate the propagation of KWs in disordered media and the possibility of Anderson localisation in such system.

Finally, the third work addresses the decay of a quantum turbulent tangle containing a large number of particles. We study the effect of particles on Eulerian and Lagrangian observables and discuss similarities and differences between classical and quantum Lagrangian turbulence.

SCIENTIFIC REPORTS

Interaction between active particles and quantum vortices leading to Kelvin wave generation

Umberto Giuriato & Giorgio Krstulovic

One of the main features of superfluids is the presence of topological defects with quantised circulation. These objects are known as quantum vortices and exhibit a hydrodynamic behaviour. Nowadays, particles are the main experimental tool used to visualise quantum vortices and to study their dynamics. We use a self-consistent model based on the three-dimensional Gross-Pitaevskii (GP) equation to explore theoretically and numerically the attractive interaction between particles and quantized vortices at very low temperature. Particles are described as localised potentials depleting the superfluid and following Newtonian dynamics. We are able to derive analytically a reduced central-force model that only depends on the classical degrees of freedom of the particle. Such model is found to be consistent with the GP simulations. We then generalised the model to include deformations of the vortex filament. The resulting long-range mutual interaction qualitatively reproduces the observed generation of a cusp on the vortex filament during the particle approach. Moreover, we show that particles can excite Kelvin waves on the vortex filament through a resonance mechanism even if they are still far from it.

Quantum vortices have a long history in physics of superfluids and superconductors. Already in the 40's Onsager had suggested the existence of quantised flows. This idea was further developed by Feynman by introducing the concept of quantum vortices[1]. What makes these vortices fascinating is that they appear as topological defects of the order parameter describing the system. As a consequence their charge or circulation is quantised, making them topological protected objects. Their core size varies form a few Angstroms in superfluid ^{4}He to micrometers in Bose-Einstein condensates (BECs). In systems such as ^{4}He, ^{3}He and atomic BECs, quantum vortices behave as hydrodynamic vortices, reconnecting and rearranging their topology, forming in this way complex vortex tangles. Such out-of-equilibrium state is today known as quantum turbulence[2]. In rotating BECs, quantised vortices naturally appear and they have been studied since the early 2000s[3,4]. In superfluid helium, ions and impurities have been extensively used since long time to investigate the properties of quantum vortices[1]. However, an important experimental breakthrough occurred in 2006[5], when quantum vortices were directly visualised by using micrometer-sized hydrogen particles. These impurities are trapped inside the vortex core and they can be directly visualised by using standard particle-tracking techniques, that are commonly exploited in classical hydrodynamic turbulence. Thanks to this method, quantum vortex reconnections[6] and Kelvin waves propagating along the vortex filaments[7] have been observed. In addition, the employment of particles has been helpful to enlighten similarities and differences between classical hydrodynamic and quantum turbulence[8,9]. For superfluid helium, the typical size of hydrogen particles is several orders of magnitude larger than the vortex core, whereas recent experiments have used He$_2^*$ excimers that are slightly larger than the vortex core[10]. Therefore, understanding the interaction between particles and vortices has become crucial for current experiments.

In general, utilising particles to unveil the properties of a fluid is a common technique in classical hydrodynamics. For instance, air bubbles are used to visualise classical vortices in water since the pioneering work of Couder et al. in 1991[11] and tracers (very small and neutrally-buoyant particles) are followed by using ultra-fast-cameras to determine the statistics of turbulent flows[12]. When particles are not tracers, they manifest inertia with respect to the fluid flow, deviating from its stream lines. Although complex, their dynamics is well understood in classical fluids if their size is small enough[13,14].

Université Côte d'Azur, Observatoire de la Côte d'Azur, CNRS, Laboratoire Lagrange, Bd de l'Observatoire, CS 34229, 06304 Cedex 4, Nice, France. Correspondence and requests for materials should be addressed to U.G. (email: umberto.giuriato@oca.eu) or G.K. (email: krstulovic@oca.eu)

Superfluids differ in several aspects to classical fluids. Firstly, at very low temperature, an object moving at low velocity experiences no drag. Secondly, the quantum nature of vortices makes the vorticity field (the curl of the velocity) a Dirac-δ distribution supported on the vortex filaments. Finally, at finite temperature, they are modelled by an immiscible mixture of two components: the actual superfluid and a *normal* fluid. The latter is described by the (viscous) Navier-Stokes equations. Such mixture of fluids is responsible for some quantum effects with no classical analogous such as the fountain effect and second sound[1]. The dynamics of a particle moving in a finite temperature superfluid happens to be richer than in an ordinary fluid. Its equations of motion have been generalised to the case where the flow is prescribed by the two-fluid model[15,16]. This model provides a large-scale description of a finite temperature superfluid where vortices are described with a coarse-grained field, therefore the quantised nature of superfluid vortices is missing. A different model that does account for the quantised nature of superfluid vortices, was introduced by Schwartz and it is known as the vortex filament method[17]. Also in this case, the dynamics of particles has been addressed both theoretically and numerically[18,19]. Eventually, in the limit of very low temperature, superfluids can be described by another important model, the Gross-Pitaevskii (GP) equation. This model derives from a mean field approximation of a quantum system and directly applies to weakly-interacting BECs, but it is also expected to qualitatively apply to other types of superfluids. The GP equation governs the dynamics of the macroscopic wave function of the system, hence quantum vortices are naturally included. In the GP framework, impurities and particles are often described in terms of classical fields[20–23]. In particular, it was shown by Roberts and Rica[22] that, depending on the coupling constants, the impurity field separates from the condensate and the two fields become immiscible. In this regime, an impurity can be seen as a hard-core particle described with classical (Newtonian) degrees of freedom[24–26]. Such approach is numerically much cheaper than the classical field description, and thus allow for simulations of a large number of particles[27]. It also suitable for developing analytical predictions.

In this Report we study numerically and analytically the interaction of quantum vortices and particles by using the Gross-Pitaevskii model coupled with a particle having classical degrees of freedom. We take advantage of the Hamiltonian structure of the system to derive a simplified model for the particle motion that it is then directly confronted with numerical simulations of the full GP model. In particular, we study the trapping of particles by a straight vortex, where an explicit analogy of a Newtonian central force problem can be established. The model is then generalised to describe the deformation of the vortex filament. The consequences of the long-range interaction between the particle and the filament are analytically studied and a prediction for the generation of Kelvin wave is obtained.

Results

Model for particles in a superfluid.
We consider a superfluid at very low temperature with one spherical particle of radius a_p and mass M_p immersed in it. The superfluid is described by a complex field $\psi(\mathbf{x}, t)$ and the particle classical degrees of freedom are its position $\mathbf{q} = (q_x, q_y, q_z)$ and momentum $\mathbf{p} = M_p \dot{\mathbf{q}} = (p_x, p_y, p_z)$. The dynamics of the system is governed by the following Hamiltonian:

$$H = \frac{\mathbf{p}^2}{2M_p} + \int \left(\frac{\hbar^2}{2m} |\nabla \psi|^2 + \frac{g}{2} |\psi|^4 - \mu |\psi|^2 + V_p(|\mathbf{x} - \mathbf{q}|) |\psi|^2 \right) \mathrm{d}\mathbf{x},$$

(1)

where m is the mass of the fundamental bosons constituting the superfluid, μ is the chemical potential and the coupling constant $g = 4\pi a_s \hbar^2 / m$ depends on the s-wave scattering length a_s. The potential $V_p(|\mathbf{x} - \mathbf{q}|) \gg \mu > 0$ is localised around $\mathbf{q}$ and it determines the shape of the particle. Its presence induces a full depletion of the superfluid around the position $\mathbf{q}$ up to a distance a_p. The equations of motion for the field and the particle position are directly obtained by varying (1) and read

$$i\hbar \frac{\partial \psi}{\partial t} = -\frac{\hbar^2}{2m} \nabla^2 \psi + (g|\psi|^2 - \mu)\psi + V_p(|\mathbf{x} - \mathbf{q}|)\psi,$$

$$M_p \ddot{\mathbf{q}} = -\int V_p(|\mathbf{x} - \mathbf{q}|) \nabla |\psi|^2 \, \mathrm{d}\mathbf{x}.$$

(2)

The Hamiltonian (1), the total superfluid mass $M = m \int |\psi|^2 \, \mathrm{d}\mathbf{x}$ and the total momentum $\mathbf{P} = \frac{i\hbar}{2} \int (\psi \nabla \psi^* - \psi^* \nabla \psi) \, \mathrm{d}\mathbf{x} + \mathbf{p}$ are conserved quantities. The connection of Eq. (2) with hydrodynamics is made through the Madelung transformation $\psi(\mathbf{x}) = \sqrt{\rho(x)/m} \, e^{i\frac{m}{\hbar}\phi(\mathbf{x})}$ that maps the GP model into the continuity and Bernoulli equations of a fluid of density ρ and velocity $\mathbf{v}_s = \Delta \phi$.

In absence of the particle, the GP equation has a simple steady solution corresponding to a constant flat condensate $\psi_\infty = \sqrt{\rho_\infty / m} = \sqrt{\mu/g}$. If (2) is linearised about ψ_∞, large wavelength waves propagate with the phonon (sound) velocity $c = \sqrt{g\rho_\infty / m^2}$ and dispersive effects take place at length scales smaller than the healing length $\xi = \sqrt{\hbar^2 / 2g\rho_\infty}$.

Another important steady solution corresponds to a straight quantum vortex

$$\psi_v(x, y, z) = \sqrt{\rho_v(x, y)/m} \, e^{i\frac{m}{\hbar}\phi_v(x, y)}.$$

(3)

The vortex density ρ_v vanishes at $(0, 0, z)$ and the phase is given by $\phi_v = \frac{\hbar}{m}\kappa\varphi$, with φ the angle in the (x, y) plane and κ a non-zero integer. The corresponding velocity field $\mathbf{v}_v$ satisfies
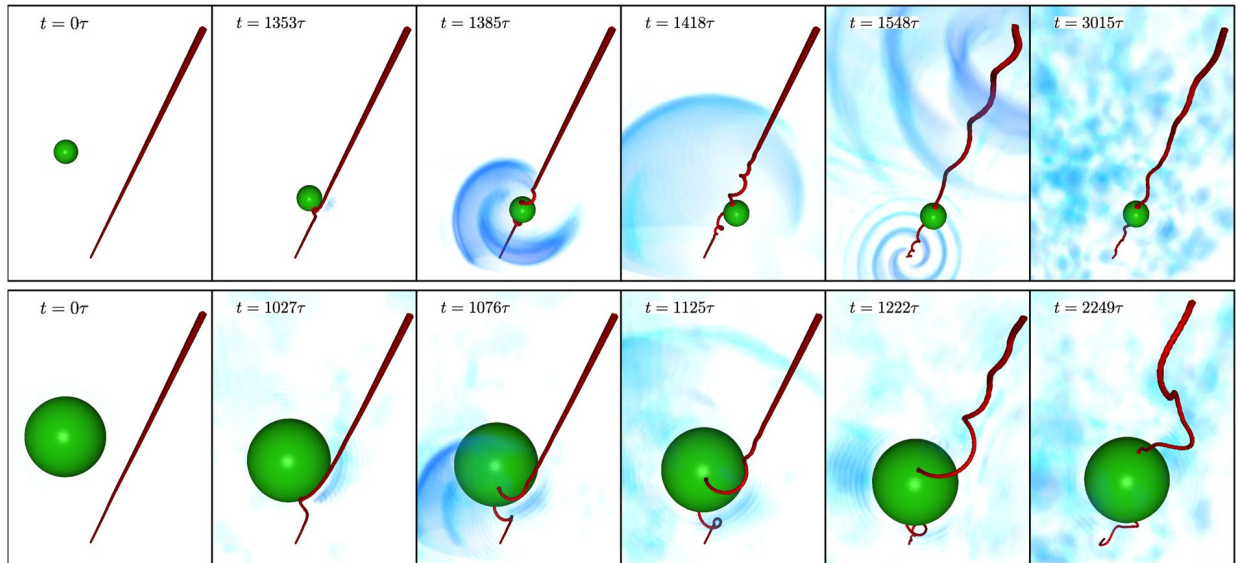
Figure 1. Snapshots of the superfluid density and a neutral-mass particle during the trapping (times varies from left to right). Vortices are displayed in red, particles in green and sound waves are rendered in blue. *Top*: small particle ($a_p = 7.6\xi$). *Bottom*: large particle ($a_p = 23.5\xi$). Images were produced with VAPOR rendering software.

$$\mathbf{v}_v = \frac{\kappa \hbar}{m} \frac{\hat{\varphi}}{|\mathbf{x}_\perp|} \text{ and } \Gamma = \frac{1}{\kappa} \oint_{\mathcal{C}} \mathbf{v}_v \cdot d\mathbf{l} = \frac{h}{m} = 2\pi\sqrt{2}\,c\xi, \tag{4}$$

where $\hat{\varphi}$ is the azimuthal versor and $\boldsymbol{x}_\perp = (x, y, 0)$. Similarly, in the following we will denote $q_\perp = (q_x, q_y, 0)$ and $q_\perp = |\mathbf{q}_\perp|$. The close path $\mathcal{C}$ surrounds the vortex, whose circulation is thus given by $\kappa\Gamma$. We will consider $\kappa = \pm 1$ because it is the only stable solution. Note that the vortex core size is given by the healing length ξ, ρ_v and $\mathbf{v}_v$ are radial functions and $\rho_v \to \rho_\infty$ away from the vortex[28].

When a particle is present, the ground state (without vortices) corresponds to a flat condensate with a strong density depletion at places where $V_p(|\mathbf{x} - \mathbf{q}|) > \mu$. A good approximation when $a_p \gg \xi$ is given by the Thomas-Fermi ground state that is obtained neglecting the kinetic term. It reads

$$\rho_p(\mathbf{x}; \mathbf{q}) = \rho_p(|\mathbf{x} - \mathbf{q}|) = \rho_\infty \left(1 - \frac{V_p(|\mathbf{x} - \mathbf{q}|)}{\mu}\right) \theta\left[1 - \frac{V_p(|\mathbf{x} - \mathbf{q}|)}{\mu}\right], \tag{5}$$

with θ the Heaviside function. The size of the particles is thus roughly determined by the relation $V_p(a_p) \approx \mu$. The results presented in this work are independent of the functional shape of V_p, provided that it is isotropic.

In numerics, we express the particle mass as $M_p = \mathcal{M}M_0$, where M_0 is the mass of the displaced superfluid. Therefore, neutral-mass particles have $\mathcal{M} = 1$, heavy particles have $\mathcal{M} > 1$ and light particles have $\mathcal{L} < 1$. Lengths are expressed in units of ξ, times in units of $\tau = \xi/c$, velocities in units of c and energies are normalised by $M_0 c^2$. Details on the numerical implementation and the particular choice of V_p are given in Methods.

Interaction between particles and quantum vortices. We begin by presenting some numerical experiments where a particle is attracted and captured by a vortex. We integrate the model (2) in a 3D periodic domain of size $L = 256\xi$ with an initial condition consisting of one particle at rest and one straight vortex initially separated by a distance $q_\perp = q_0 \gg \xi$. The domain contains image vortices in order to preserve periodicity that are not displayed in figures. Their effect on the particle has been checked to be negligible. Snapshots of the superfluid density field with the particle at different times are displayed in Fig. 1. The top row refers to a relatively small particle ($a_p = 7.6\xi$), while the bottom row to a large one ($a_p = 23.5\xi$). Both particles have a neutral relative mass $\mathcal{M} = 1$. Note that hydrogen particles used for visualization of quantum vortices in superfluid helium have a relative mass $\mathcal{M} \sim 0.7$ and a typical size of $a_p \sim 10^3 \xi$. Simulating such particle size is not achievable numerically, however a clear difference is already observed for our large particle. In both cases, the particle is attracted by the vortex. Before the merging, while the particle is moving closer to the vortex, a deformation of the vortex line is observed. Such deformation is a cusp regularised at the scale of the healing length by the dispersion of the GP equation. Initially, the cusp develops perpendicularly to the particle velocity. Later, it curves towards the particle, until the contact point the vortex separates into two branches. The two contact points then slide on the particle surface towards opposite directions. The oscillation of the trapped particle excites helicoidal waves on the filament. Such waves, that propagate along the vortex line, are known as Kelvin waves. We note that the vortex deformation is less marked for smaller particles and the amplitude of Kelvin waves increases with the particle size. A similar behaviour has been already observed in the hydrodynamical model adopted in refs[15,29,30], as well as in the

classical field impurity model studied by Berloff and Roberts[21]. The trapping process was then interpreted as a reconnection of the straight vortex with its images inside the particle, whose presence is necessary to set the boundary conditions for the flow around the particle.

The model (2) also allow us to observe the sound emitted by the particle-vortex pair during the trapping process. In a first stage, a big pulse is emitted at the moment of the trapping due to the strong acceleration experienced by the particle. In a later time, for the smaller particle a clear quadrupolar radiative pulse is observed ($t = 1548\tau$, top row of Fig. 1). Remarkably, this kind of pattern is expected in superfluids when some symmetry cancels the first order of the multipolar radiative expansion. For instance, this is the case in 2D counter-rotating vortices[31,32]. Here, the symmetry could be related to the two antisymmetric traveling waves emerging from the particle and meeting at the boundary of the periodic domain. This issue will be investigated further in a future work. Finally, the particle remains trapped inside the vortex and coexists with a bath of sound waves. For the big particle, all the phenomena are amplified. Movies of the numerical simulations can be found as a Supplementary Information.

From these simulations it is manifest that the trapping of a particle by a quantum vortex is accompanied by a myriad of complex physical phenomena. In the next sections, we take advantage of the simplicity of the model to derive effective equations for the particle and the vortex Filament dynamics.

Reduced theoretical model for the particle-vortex interaction. In the following we set the origin of the reference frame at the intersection between the unperturbed vortex line and its orthogonal plane where the particle lies. At $t = 0$, the vortex line coincides then with the z axis. To derive a simplified theory, we consider the following ansatz for the superfluid field:

$$\psi(\mathbf{x}; \mathbf{q}, \mathbf{\dot q}) = \sqrt{\frac{\rho_\infty}{m}} \sqrt{\widetilde{\rho_v}(\mathbf{x})} \sqrt{\widetilde{\rho_p}(|\mathbf{x} - \mathbf{q}|)}\, e^{i\frac{m}{\hbar}\phi(\mathbf{x}; \mathbf{q}, \mathbf{\dot q})}, \tag{6}$$

where $\widetilde{\rho_v} = \sqrt{\rho_v/\rho_\infty}$ and $\widetilde{\rho_p} = \sqrt{\rho_p/\rho_\infty}$ are the normalised ground states of an isolated vortex and an isolated particle given in (3) and (5) respectively. At first approximation, we neglect the deformation of the vortex. This last assumption is valid at the stages where the particle is attracted by the vortex, but still far from it. We will consider the vortex deformation in the last section. The ansatz (6) also neglects small density variations due to sound emission and might not be valid at the exact moment of the trapping, but it gives a good description elsewhere. The phase ϕ leads to the superfluid velocity field $\mathbf{v}_s = \nabla\phi$ and it is determined by imposing the boundary conditions around the particle and at infinity:

$$\mathbf{\dot q} \cdot \mathbf{n} = \mathbf{v}_s \cdot \mathbf{n} \quad \forall\, \mathbf{x}\ \text{s.\,t.}\, |\mathbf{x} - \mathbf{q}| = a_p \quad \text{and} \quad \mathbf{v}_s \xrightarrow[|\mathbf{x}-\mathbf{q}|\to\infty]{} \mathbf{v}_v. \tag{7}$$

where $\mathbf{n} = (\mathbf{x} - \mathbf{q})/|\mathbf{x} - q|$ and $\mathbf{v}_v$ the vortex velocity field (4). Since $\mathbf{v}_v$ describes a non-uniform irrotational flow, we have to take into account how the superfluid velocity field is modified when the particle accelerates in it. As it is done in classical fluid mechanics[13–15], we include in the superfluid velocity the corrections to the pure vortex flow $\mathbf{v}_v$ that are generated by the moving particle. We set $\mathbf{v}_s = \mathbf{v}_v + \mathbf{v}_p + \mathbf{v}_{BC}$, or in terms of the phase $\phi = \phi_v + \phi_p + \phi_{BC}$.

The potential ϕ_p describes the flow of a sphere of radius a_p moving in a uniform flow given by the relative velocity $\mathbf{\dot q} - \mathbf{v}_v(\mathbf{q})$. It reads[33]

$$\phi_p(\mathbf{x}; \mathbf{q}, \mathbf{\dot q}) = -\frac{a_p^3}{2|\mathbf{x} - \mathbf{q}|^3}(\mathbf{x} - \mathbf{q}) \cdot (\mathbf{\dot q} - \mathbf{v}_v(\mathbf{q})). \tag{8}$$

The potential ϕ_{BC} is in principle determined by the condition at the particle boundary $\nabla\phi_{BC} \cdot \mathbf{n} = [\mathbf{v}_v(\mathbf{q} + a_p\mathbf{n}) - \mathbf{v}_v(\mathbf{q})] \cdot \mathbf{n}$. In practice, it is obtained by a Taylor expansion of the vortex velocity flow around the particle and hence ϕ_{BC} is expressed in terms of its gradients[13–15]. This flow gives a contribution of order

$$\varepsilon = a_p \frac{|\nabla\mathbf{v}_v(\mathbf{q})|}{|\mathbf{v}_v(\mathbf{q})|} = \frac{a_p}{q_\perp} \ll 1, \tag{9}$$

where we have used $|\mathbf{v}_v(\mathbf{q})| \sim 1/q_\perp$. We include in our calculations ϕ_{BC} up to $\mathcal{O}(\varepsilon^2)$.

In order to express the Hamiltonian (1) only in terms of q and $\dot q$ we split it as $H = K + H_{hydro}^{GP} + H_{int}^{GP} + H_p^{GP} + H_{qnt}^{GP}$, where

$$K = \frac{1}{2}M_p\mathbf{\dot q}^2, \quad H_{hydro}^{GP} = \frac{1}{2}\int \rho\mathbf{v}_s^2 d\mathbf{x}, \quad H_{int}^{GP} = \frac{g}{2m^2}\int \rho^2 d\mathbf{x},$$

$$H_p^{GP} = \frac{1}{m}\int (V_p - \mu)\rho\, d\mathbf{x}, \quad H_{qnt}^{GP} = \frac{\Gamma^2}{8\pi^2}\int (\nabla\sqrt{\rho})^2 d\mathbf{x}. \tag{10}$$

We use the ansatz (6) to explicitly perform the space integrals. From (5), we observe that for a strong localised potential $V_p \gg \mu$ the field $1 - \widetilde{\rho_p}(x)$ is supported on a ball of center q and radius a_p, up to a layer of size ξ. We use this fact to reduce the domain of integration. Inside this ball and if $\varepsilon \ll 1$, we can assume that $\widetilde{\rho_v}(\mathbf{x}) \approx \widetilde{\rho_v}(q_\perp)$ and $\mathbf{v}_v(\mathbf{x}) \approx \mathbf{v}_v(q_\perp)$. All the integrations can be then carried out. Details on these computations are given in Methods. The Hamiltonian components (10) eventually read

$$H_{\text{hydro}}^{\text{GP}} \approx \overline{H}_{\text{hydro}}^{GP} - \frac{(1+C)M_0\Gamma^2}{8\pi^2 q_\perp^2}\tilde{\rho}_v(q_\perp) - \frac{\Gamma^2 a_p^2}{20\pi^2 c^2 q_\perp^4}\tilde{\rho}_v(q_\perp) + E_{\text{add}},$$

with

$$E_{\text{add}} = \frac{1}{2}C\tilde{\rho}_v(q_\perp)M_0\dot{\mathbf{q}}^2, \tag{11}$$

$$H_{\text{int}}^{\text{GP}} \approx \overline{H}_{\text{int}}^{\text{GP}} - \frac{1}{2}M_0 c^2 \tilde{\rho}_v^2(q_\perp), \quad H_p^{\text{GP}} \approx \overline{H}_p^{\text{GP}} + M_0 c^2 \tilde{\rho}_v^2(q_\perp), \quad H_{\text{qnt}}^{\text{GP}} \approx \overline{H}_{\text{qnt}}^{\text{GP}} \tag{12}$$

where $C = 1/2$ and overbars denote constants at the leading order. E_{add} is the classical added mass energy in three dimensions[33] modified by the density profile. Gathering all the terms, we obtain the reduced Hamiltonian (RH)

$$H_{\text{red}}[\mathbf{q}, \mathbf{p}] = \overline{H}^{\text{GP}} + \frac{\mathbf{p}^2}{2M_{\text{eff}}} + M_0 c^2 \left[-\frac{1}{2}\tilde{\rho}_v^2(q_\perp) + \tilde{\rho}_v(q_\perp) \right.$$
$$\left. -\frac{(1+C)\Gamma^2}{8\pi^2 c^2 q_\perp^2}\tilde{\rho}_v(q_\perp) - \frac{\Gamma^2 a_p^2}{20\pi^2 c^2 q_\perp^4}\tilde{\rho}_v(q_\perp) \right]. \tag{13}$$

In (13) the added mass has been absorbed in the effective particle mass $M_{\text{eff}} = M_p + C\tilde{\rho}_v M_0 = (\mathcal{M} + C\tilde{\rho}_v)M_0$ and the particle momentum has been redefined as $\mathbf{p} = M_{\text{eff}}\dot{\mathbf{q}}$. Note that, as $\tilde{\rho}_v$ only depends on $q_\perp$, the coordinate q_z of the particle is cyclic and can be trivially integrated. The dynamics thus simplifies to a motion in the plane perpendicular to the vortex. The reduced model (13), therefore describes a classical central force problem in two dimensions with a potential given by its last term. Note that the same calculations can be performed in two dimensions, by redefining the phase (8) which leads to the constant $C = 1$.

The reduced Hamiltonian (13) can be further simplified using the asymptotic behaviour of $\tilde{\rho}_v$. At large distances, $\tilde{\rho}_v \sim 1 - \xi^2/q_\perp^2 - 2\xi^4/q_\perp^4 + O(\xi^6/q_\perp^6)$, hence at the leading order $H_p^{\text{GP}} \approx -H_{\text{int}}^{\text{GP}}$ and the main contribution comes only from $H_{\text{hydro}}^{\text{GP}}$. Finally, at lowest order, we obtain the effective Hamiltonian (EH) for the particle dynamics

$$H_{\text{eff}}[\mathbf{q}, \mathbf{p}] = \frac{\mathbf{p}^2}{2M_{\text{eff}}} + U(q_\perp), \quad U(q_\perp) = -\frac{(1+C)M_0\Gamma^2}{8\pi^2 q_\perp^2}, \text{ and}$$
$$M_{\text{eff}} = M_p + CM_0 = (\mathcal{M} + C)M_0. \tag{14}$$

The equations of motion for the particle position are then:

$$(\mathcal{M} + C)\ddot{\mathbf{q}}_\perp = -\frac{(1+C)\Gamma^2}{4\pi^2 q_\perp^4}\mathbf{q}_\perp, \qquad \ddot{q}_z = 0, \tag{15}$$

Note that the added mass effect is suppressed for neutral-mass particles having $\mathcal{M} = 1$ and the particle size explicitly appears only at high order terms. The attractive force scaling as $q_\perp^{-3}$ was first proposed by Donnelly[34] as the result of a pressure gradient. Equation (15) has been also studied for neutral-mass particles in the framework of pure hydrodynamical models[15,16].

Finally, note that if we replace in (13) the density by its leading order $\tilde{\rho}_v = 1$, then the associated equations of motion are invariant under the following scaling transformation:

$$\mathbf{q} \to \lambda\mathbf{q}, \quad a_p \to \lambda a_p, \quad t \to \lambda^2 t \qquad \forall \lambda \in \mathbb{R}^+ \tag{16}$$

Such invariance will be also preserved in terms coming from higher orders in ε.

Numerical measurements and comparison with theory. We compare now our reduced model to the numerical experiment presented in Fig. 1. We first consider a small neutral-mass particle of size $a_p = 2.7\xi$. For this particle, the condition (9) is valid for a wide range of separations and the deformation of the vortex during the particle approach is negligible. We measured the variation of the different components of the Hamiltonian (10) as a function of distance between the particle and the vortex. Figure 2a displays such energies (markers) compared to the respective theoretical predictions (lines).

The striped region identifies the particle radius a_p/ξ where the particle and the vortex overlap. Since the added mass energy E_{add} (11) only modifies the particle inertia but has no effect in determining the force in the r.h.s. of (15), we subtract it from the hydrodynamic component $H_{\text{hydro}}^{\text{GP}}$ and the total GP energy $H^{\text{GP}} = H - K$. We have used the Padé approximation given in Methods as an analytical expression for the vortex density profile $\tilde{\rho}_v$, so that both asymptotics (large and short vortex-particle separations) are reproduced. Even if our model is not supposed to be quantitatively accurate for $q_\perp \sim a_p$, we can still observe a quite good agreement. Remarkably, the hypothesis that leads to neglect H_q^{GP} is perfectly valid up to a distance about twice of the particle radius. Moreover, $H_p^{\text{GP}} \approx -H_{\text{int}}^{\text{GP}}$ and thus during the particle approach $H^{\text{GP}} \approx H_{\text{hydro}}^{\text{GP}}$. Figure 2b shows in a $\log - \log$ plot the absolute value of the measured energies for large distances. Clearly, all the energy contributions follow the predicted $q_\perp^{-2}$ scaling, as long as the vortex-particle separation is large. We have checked that the data in Fig. 2 are almost independent of
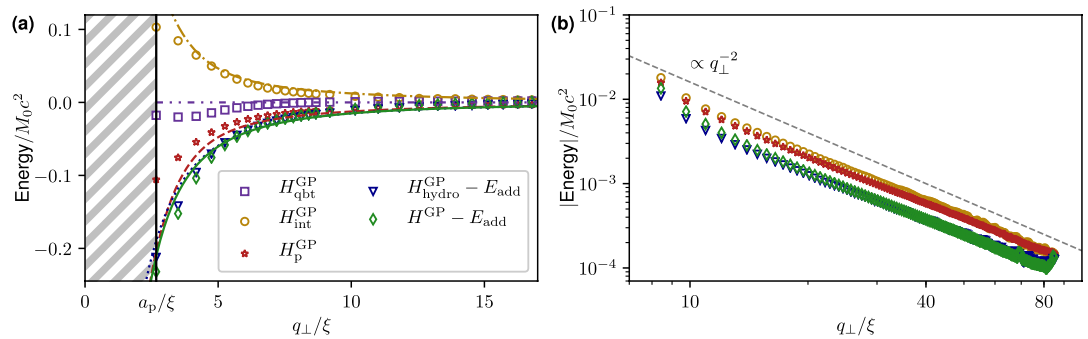
Figure 2. (a) Different energies as a function of the vortex-particle distance $q_\perp/\xi$ during the approach of a particle with size $a_p = 2.7\xi$. The initial separation is $q_\perp = 45.3\xi$ and the particle has zero velocity. Markers are numerical data and lines theoretical curves of corresponding colours. (b) Same energies as in (a) in $(log - log)$ scale). Initial $q_\perp = 85.1\xi$ and initial velocity $\dot{q}_\perp = -0.04c$.
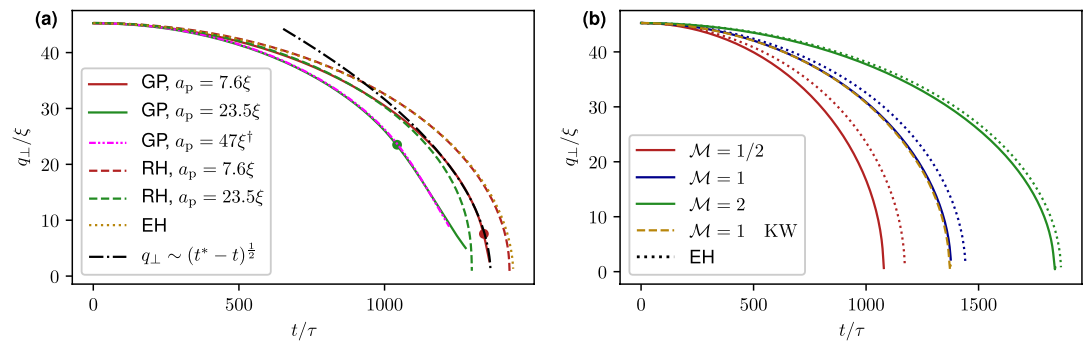
Figure 3. (a) Measured vortex-particle separation as a function of time for neutral-mass ($\mathcal{M} = 1$) particles of different sizes moving towards a straight vortex (solid lines). The initial condition is $q_\perp = 45.3\xi$ and $q = 0$. Round markers indicate the corresponding trapping times. †The pink dash-dot-dotted line refers to a big particle initially at $q_\perp = 90.6\xi$ rescaled using Eq. (16) with $\lambda = 2$. The figure also displays the predictions RH (13) in dashed lines of the corresponding colours, the theoretical prediction (17) of the effective model EH (dotted golden line) and the scaling $q \sim (t^* - t)^{\frac{1}{2}}$, obtained by fitting the numerical data (dash-dotted black line). (b) The same as (a) but for particles with $a_p = 2.7\xi$ and different masses. Data from GP simulation are displayed in solid lines whereas the predictions (17) are in dotted lines. The dashed golden line refers to a GP simulation with a vortex containing Kelvin waves of *rms* amplitude 0.5ξ.

the particle mass. Discrepancies between data and theory might be due to sound radiation or to sub-leading terms in the boundary conditions of the superfluid velocity. We conclude that the effective potential energy is relatively well described by $U(q_\perp)$ in Eqs (14) and (15) gives a good approximation for the motion of the particle.

Equation (15) can be straightforwardly integrated and the solution for the particle-vortex distance reads

$$q_\perp(t) = \sqrt{\frac{2E_\perp}{M_{eff}}t^2 + q_0^2 + q_0\dot{q}_0 t},$$

(17)

where $q_0 = q_\perp(t=0)$, $\dot{q}_0 = \dot{q}_\perp(t=0)$ and $E_\perp = H_{eff}[\mathbf{q}(t=0), \mathbf{p}(t=0)] - p_z^2/2M_{eff}$ is the conserved energy in the effective model. In the case of a neutral-mass particle with zero initial velocity Eq. (17) reduces to the one derived by Barenghi et al.[30]. In Fig. 3 the prediction (17) and the one obtained numerically from RH (13) are compared with numerical data.

Figure 3a shows the particle-vortex distance for neutral-mass particles of different sizes initially located at a distance $q_0 = 45.3\xi$. The markers denote the capture times, after which particles keep moving inside the vortex. The assumption (9) is ideally satisfied for point-like particles but it reasonably applies as long as the particle radius is sufficiently small compared to its distance to the vortex. Indeed, for the particle $a_p = 7.6\xi$ the accordance with theory is good, while for the one having $a_p = 23.5\xi$ is just qualitative. For such particle, the full reduced Hamiltonian gives a better description. In addition, the motion curve of a particle of radius $a_p = 2 \times 23.5\xi$, initially located at $2q_0$ is in good agreement (pink dashed-dot-dotted curve) with the scaling relation (16). It is interesting to note that close to the capture time the particle-vortex separation scales as
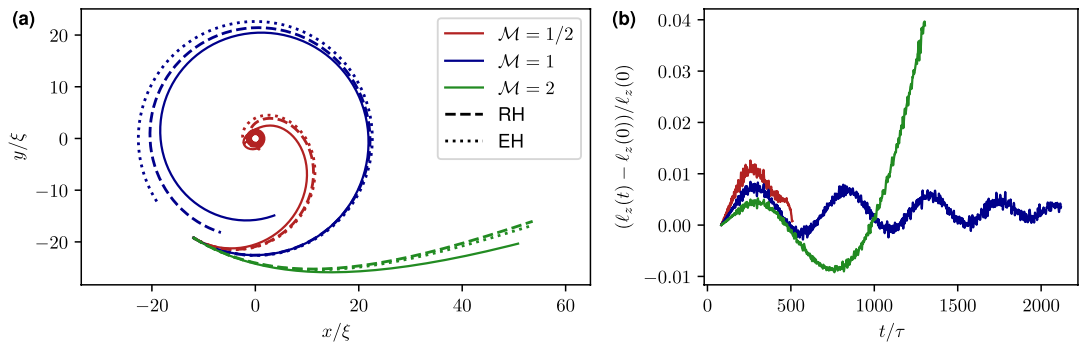
Figure 4. (**a**) Trajectories of small particles ($a_p = 2.7\xi$) with $\dot{\mathbf{q}}_\perp(t=0) = \mathbf{v}_v(q_\perp)$ and $q_\perp(t=0) = 22.6\xi$. GP data are displayed in solid lines, predictions of EH (14) in dotted lines and the predictions of RH (13) in dashed lines of the corresponding colours. (**b**) Relative variation of angular momentum as a function of time for the same simulations of (**a**).

$$q(t) \xrightarrow[t \to t^{*-}]{} \left(\frac{1 + C}{\pi^2(\mathcal{M} + C)} \right)^{1/4} \sqrt{\Gamma(t^* - t)}, \quad \text{with} \quad t^* = \frac{q_0^2}{\Gamma} \sqrt{\frac{4\pi^2(\mathcal{M} + C)}{1 + C}}, \tag{18}$$

where we have set $\dot{\mathbf{q}}(t=0) = 0$ for sake of simplicity. In Fig. 3a such scaling is also apparent up to a separation of $q \sim 30\xi$ for the particle with $a_p = 7.6\xi$ (dotted-dashed line). The capture time t^* predicted by the effective model is compatible with the one observed in the GP simulation with a relative error of 5%. The scaling (18), that is also observed in vortex reconnections[35], suggests the idea that the trapping process could be seen as reconnection of the vortex with its images inside the particle. Finally, in Fig. 3b the vortex-particle separation has been measured for a small particle ($a_p = 2.7\xi$) with the same initial condition but with different masses. Remarkably, the heavier the particle, the better the agreement with theory. This could due to the fact that light particles are more sensitive to sound waves and compressible effects not taken into account in the theory. For completeness, we also show the case of a vortex filament perturbed with small-amplitude Kelvin waves (dashed golden line). As expected, the effect of Kelvin waves is sub-leading and no difference is appreciable with respect to the unperturbed case.

It is well known in classical hydrodynamics that light particles go into vortices whereas the heavy ones escape from them[11]. The same situation takes place for a particle in a superfluid, even if there is no Stokes drag at zero temperature. Indeed, as a central force problem, the effective Hamiltonian (14) conserves the angular momentum $\ell_z = M_{\text{eff}}(\mathbf{q}_\perp \times \dot{\mathbf{q}}_\perp) \cdot \hat{z}$. This conserved quantity leads to the emergence of a repulsive potential $\ell_z^2 / 2M_{\text{eff}} q_\perp^2$ in the effective Hamiltonian for $q_\perp$. Therefore there exists a critical angular momentum $\ell_{\text{crit}} = \sqrt{(1 + C)(\mathcal{M} + C)} M_0 \Gamma / 2\pi$ such that for $\ell_z < \ell_{\text{crit}}$ particles collapse into the vortex and escape from it for $\ell_z > \ell_{\text{crit}}$. Now, if the particle is initially at rest in the reference frame moving with vortex flow, i.e. $\dot{\mathbf{q}}_\perp = \mathbf{v}_v(q_\perp)$, the condition on the critical value of ℓ_z is expressed in terms of the mass, as $\mathcal{M} < 1$ for trapping and $\mathcal{M} > 1$ for escaping. At $\mathcal{M} = 1$ the model (14) predicts a closed circular orbit, i.e. a particle tracing the flow. However, this orbit is unstable and modified by high order terms (see Methods) that lead to a collapse also in this case. The three situations $\mathcal{M} = 1$ and $\mathcal{M} > 1$ are manifest in Fig. 4a, where we display the trajectories of a small particle ($a_p = 2.7\xi$) with initial velocity $\dot{\mathbf{q}}_\perp = \mathbf{v}_v(q_\perp)$ but different masses. For the $\mathcal{M} = 1$ case the prediction given by (13) works better than the leading order solution. This is consistent with the fact that the terms proportional to $q_\perp^{-2}$ cancel for $\ell_z = \ell_{\text{crit}}$, so that the next-to-leading order becomes predominant.

Figure 4b shows that the angular momentum is conserved up to 4%. Note that the escaping particle feels the attraction of image vortices in the periodic box that break down the conservation of ℓ_z.

Generation of cusps and Kelvin waves on the vortex filament. We now address the effect of the particle on the vortex filament. As the vortex remains almost straight, it can be parametrised as $\mathbf{R}(z) = (\mathbf{s}(z), z)$, where $\mathbf{s}(z)$ is a bi-dimensional vector. The ansatz (6) can be generalised by replacing $\mathbf{x}_\perp$ in ρ_v and ϕ_v by $\mathbf{x}_\perp - \mathbf{R}(z)$. Assuming $|\mathbf{s}(z)| \ll q_\perp$ and small deflections $|\partial_z \mathbf{s}| \ll 1$, all the calculations made in the previous section to reduce the Hamiltonian can be performed in the same way if we keep only contributions at the first order in $\mathbf{s}(z)$. The vortex deformation appears in the term $\overline{H}^{\text{GP}}$ in (13) and simply corresponds to the Local Induced Approximation (LIA) Hamiltonian[28] (see Methods). The effective vortex-particle Hamiltonian (14) becomes

$$H_{\text{v-p}}[\mathbf{q}, \mathbf{p}, \mathbf{s}] = \frac{\mathbf{p}_{\text{eff}}^2}{2M_{\text{eff}}} + \frac{\Gamma^2 \rho_\infty}{8\pi} \int_0^L \left[-\mathbf{s} \cdot \Lambda \frac{\partial^2 \mathbf{s}}{\partial z^2} - \frac{(1 + C)M_0}{\rho_\infty \pi |\mathbf{q}_\perp - \mathbf{s}(z)|^2} \delta(z - q_z) \right] dz, \tag{19}$$

where from now on $q_\perp = (q_x, q_y)$. In principle Λ is a non-local operator yielding the correct Kelvin wave dispersion relation[28]. For the moment, we treat it as a constant. Up to a logarithmic correction, this is equivalent to consider the limit of large-scale vortex deformations. Although rough, such approximation provides a qualitatively
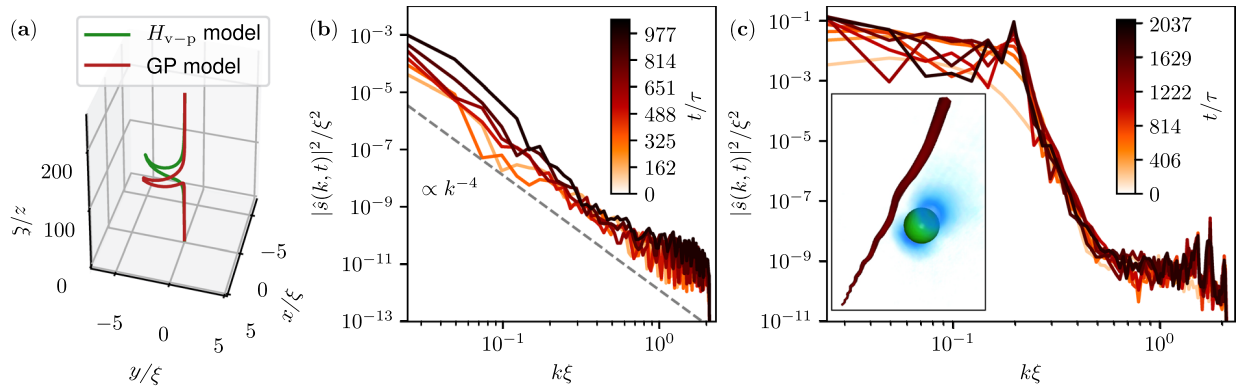
Figure 5. (**a**) Cusp generated during the trapping of a neutral-mass particle of size $a_p = 7.6\xi$ at the capture time t^*. The initial particle condition is $q_\perp = 45.3\xi$ and $q = 0$. Red solid line is the vortex line tracked during GP simulation, whereas green solid line is $s(z, t^*)$ computed with the dynamics (20, 21). (**b**) Spectrum of vortex displacement measured from GP simulation at different times during the trapping of a particle. The parameters are the same as in (**a**). (**c**) Spectrum of vortex displacement measured from GP simulation during the motion of a particle. The parameters for the particle are $a_p = 7.6\xi$, $q_\perp(t=0) = 22.6\xi$, $q_\perp(t=0) = \mathbf{v}_v(q_\perp)$ and $\dot{q}_z = 0.27c$ (see Methods). The inset shows the superfluid density and the particle where Kelvin waves are clearly present on the vortex filament.

good description of the vortex dynamics. The equations of motion coupling the vortex filament and the particle are thus found to be:

$$(\mathcal{M} + C)\ddot{\mathbf{q}}_\perp = -\frac{(1 + C)\Gamma^2}{4\pi^2 |\mathbf{q}_\perp - \mathbf{s}(q_z)|^4}(\mathbf{q}_\perp - \mathbf{s}(q_z)),$$

$$(\mathcal{M} + C)\ddot{q}_z = \frac{(1 + C)\Gamma^2}{4\pi^2 |\mathbf{q}_\perp - \mathbf{s}(q_z)|^4}(\mathbf{q}_\perp - \mathbf{s}(q_z)) \cdot \frac{\partial s}{\partial z}\Big|_{z=q_z}$$

$$(20)$$

$$\kappa \frac{\partial \mathbf{s}}{\partial t} = \hat{z} \times \left[\frac{\Lambda\Gamma}{4\pi}\frac{\partial^2 \mathbf{s}}{\partial z^2} + \frac{(1 + C)M_0\Gamma}{\rho_\infty 4\pi^2 |\mathbf{q}_\perp - \mathbf{s}(z)|^4}(\mathbf{q}_\perp - \mathbf{s}(z))\delta(z - q_z)\right], \text{ with } \kappa = \pm 1,$$

$$(21)$$

where $(\hat{z} \times \mathbf{A})_i = \varepsilon_{ij}A_j$, with ε_{ij} the Levi-Civita symbol. The l.h.s of Eq. (21) can be straightforwardly derived following the calculations performed in refs[36,37]. Note that the r.h.s of equation for $\ddot{q}_z$ is negligible in the limit $|\partial_z \mathbf{s}| \ll 1$ and $|\mathbf{q}| \gg |\mathbf{s}|$. In Eq. (21) a point force is exerted by the particle giving rise to the deformation of the vortex line, while the dispersive term leads to Kelvin wave propagation. This simplified model reproduces the generation of a cusp similar to the one observed in the numerical simulations of the full GP model, as apparent in Fig. 5a.

In previous works, such cusp-shaped deformations have been interpreted as the result of the vortex reconnection with the images inside the particle[21]. Such effect is not taken into account in our model and the formation of a cusp is the result of a simple action-reaction mechanism between the particle and the vortex. In addition, the curvature of the vortex filament during the trapping is not well described by the universal theoretical prediction for pure vortex reconnections obtained by Villois *et al.*[35] (data not shown).

From the particle-vortex model (20,21) we can extract further analytical predictions. Since $|\mathbf{s}| \ll \mathbf{q}_\perp$, we can set $\mathbf{q}_\perp - \mathbf{s} \approx \mathbf{q}_\perp$ in the model. The particle thus decouples from the vortex and just drives the forcing acting on it. We write $\mathbf{s}(z,t)$ and $\mathbf{q}(t)$ in complex variables as $s(z) = s_x(z, t) + is_y(z, t)$ and $q(t) = |q(t)|e^{i\Omega_q(t)t}$, and linearise (21) for small s. The equation now reads

$$\frac{\partial \hat{s}_k}{\partial t} = -i\kappa\frac{\Gamma\Lambda_k}{4\pi}k^2\hat{s}_k + i\frac{F_0}{|q(t)|^3}e^{-i(\Omega_q(t) + k\dot{q}_z)t} \text{ with } F_0 = \kappa\frac{(1 + C)M_0\Gamma}{4\pi^2\rho_\infty},$$

$$(22)$$

where $\hat{s}_k$ is the Fourier transform of $s(z)$ and k a wave-vector. We have now phenomenologically included the non-local operator Λ_k that in Fourier space reads $\Lambda_k = 2(1 - \sqrt{1 - ka_0K_0(ka_0)/K_1(ka_0)})/(a_0k)^2$, with K_n the modified Bessel function of order n and $a_0 = 1.1265\xi$. The operator Λ_k has been defined in order to obtain the correct Kelvin wave relation dispersion $\omega_k^{KW} = \kappa\Gamma\Lambda_k k^2/4\pi$ computed in refs[28,38] and the cut-off a_0 has been fixed to satisfy the known GP small-k asymptotic expansion[38]. First, let us consider the case of radial approach ($\Omega_q = 0$) with vertical velocity $\dot{q}_z = 0$. Integrating Eq. (22), it follows that the spectrum of the vortex displacement obeys the scaling $|\hat{s}_k|^2 \sim k^{-4}$ at large scales, up to a logarithmic correction. Such scaling corresponds to the deformation of the vortex line which starts to develop already at the early times of the trapping process. We compute the spectra using the tracked vortex lines obtained from GP simulations by using the method explained in refs[39,40]. They present a good agreement with theory (see Fig. 5b). Finally, if $\dot{q}_z \neq 0$ or $\Omega_q \neq 0$, the particle-vortex model predicts the generation of Kelvin waves when the particle is still distant. Indeed, when the particle is far from the vortex,

the time dependence of $|q(t)|$ and the one of $\Omega_q(t)$ are much slower than the one of $s(t)$ and they can be treated as constants in Eq. (22). Therefore, the model (22) predicts a linear resonance if $\omega_k^{\text{KW}} = \Omega_q + k\dot{q}_z$. As a consequence, any motion of the particle not purely radial generates waves on the filament. In order to check this claim, we performed a GP simulation with a particle orbiting around the vortex while moving parallel to it. A movie of the simulation is available as Supplementary Information. The corresponding vortex displacement spectrum is presented in Fig. 5c, where the development of a resonance is clearly visible. The resonant mode predicted by the model (22) is $k\xi = 0.24$, compatible with the position of the observed peak. In the inset a snapshot of the superfluid density shows the corresponding Kelvin waves generated on the filament. Actually, all the small-k modes of the filament are growing during the first stages of particle motion. Indeed, the forcing driven by the particle produces an oscillation in time of such modes, with low frequency and high amplitude. Note that the considerations made from Eq. (22) could be in principle formalised using a multi-time asymptotic expansion.

Discussion

We have studied the interaction of a particle and a quantum vortex in a self-consistent framework given by the particle-superfluid Hamiltonian (1). The superfluid is described by the Gross-Pitaevskii equation and the particle through classical degrees of freedom. This minimal system is able to extend results obtained in more complex models[21,30] with a much lower numerical cost. The simplicity of the model allowed us to derive the reduced Hamiltonian (13) for the particle dynamics, that also includes corrections due to the vortex density profile. Similar theoretical computations can be straightforwardly performed in the case of non-local models of superfluids, that are more adequate for describing superfluid helium. In such models, the vortex density profile shows oscillations as a function of the distance to the core[41,42], which could have some impact on the dynamics of small and light particles. In our derivation, we have neglected acoustic radiation and interaction of vortices with with sound waves. Compressibility effects of this kind might be also important for light particles and they could be included, in principle, generalising the ansatz (6). The Gross-Pitaevskii model used in this work has a very simple equation of state valid in the weak coupling limit. When the coupling is not so weak, like in superfluid helium, the equation of state can be easily modified changing the type of non-linearity of the model to account for the effect of beyond-mean-field quantum fluctuations[43,44]. It would be interesting to study how these fluctuations modify the particle dynamics. In the same spirit, at extremely low temperatures, quantum fluctuations could excite low-amplitude Kelvin waves[45]. However, we expect this effect to be negligible as it was shown in Fig. 3b.

The vortex-particle interaction leads to the trapping of the particle by the vortex. The bounded state with a particle trapped inside a vortex line possesses an energy lower that the state in which the vortex and the particle are far apart. This energy gap, known as substitution energy, was first computed by Parks and Donelly[46]. It simply corresponds to the vortex kinetic energy contained in the volume occupied by the particle. We have checked that this estimate gives the good order of magnitude for the incompressible kinetic energy difference. However, it overestimates it as it does not account for dynamical processes like the generation of Kelvin waves after the capture. The substitution energy was then used in ref.[46] to assess the life time of a Brownian ion inside a vortex in presence of an electric field. The model used in this Report can be trivially extended to describe a charged particle by adding an external potential, and similar considerations could be easily rephrased. We have observed that the vortex considerably stretches while the particle is pulled out from it by an external force (data not shown). Therefore, even at zero temperature, the energy needed to remove a particle can be much larger than the substitution energy. The release of a particle from a vortex is an interesting problem for traditional and modern experiments with superfluids. We plan to use the model studied here to study this issue in a future work.

We have observed a non-trivial dynamics of vortex filament if a particle moves around it. The vortex dynamics has been included in the effective model (19), and we explained the motion of the vortex as the result of a mutual long-range interaction between the particle and the vortex itself. Moreover, we highlighted that long-range particle-vortex interaction is sufficient to generate Kelvin waves on the filament even if the particle never touches the vortex. It would be interesting to include such a simple interaction term in the vortex filament model, to study the effect of a large number of particles. In this regard, note that the model (2) can be trivially extended to include many particles, both at zero and finite temperature[27]. It is then natural to use it for studying the effect of particles in a quantum turbulent regime. Indeed, it is still not clear how the dynamics of active particles modify the evolution and decay of complex tangle of quantised vortex lines. Addressing such issues is fundamental for current experiments, since particles are nowadays the main tool for tracking and visualising vortices in superfluid helium.

Methods

Numerical methods and parameters. Equations (2) are solved with a standard pseudo-spectral code and a 4th order Runge-Kutta scheme for the time stepping in a domain of size L with N_p mesh points per dimension. We set $c = \rho_\infty = 1$. The steady states for the particle and the vortex are prepared separately by performing imaginary time evolution of the GP equation and then they are multiplied to obtain the wished initial condition. To impose the initial flow around the particle, the initial condition is evolved for a short time ($\sim 40\tau$) using GP without the particle dynamics. In Fig. 5c, the target velocity in the z component is reached by adding an external force $\mathbf{F} = (0, 0, 2 \times 10^{-3} M_0 c^2/\xi)$ that then is switched off.

The particle potential is a smoothed hat-function $V_p(r) = \frac{V_0}{2}\left(1 - \tanh\left[\frac{r^2 - \eta^2}{4\Delta l^2}\right]\right)$ and the mass displaced by the particle is measured as $M_0 = \rho_\infty L^3 (1 - \int |\psi_p|^2 \, d\mathbf{x} / \int |\psi_\infty|^2 \, d\mathbf{x})$, where ψ_p is the steady state with just one particle. Since the particle boundaries are not sharp, we measure the particle radius as $a_p = (3M_0/4\pi\rho_\infty)^{\frac{1}{3}}$ for given values of the numerical parameters η and Δl. For all the particles $V_0 = 20$. The parameters used are the following. For $a_p = 2.7\xi$: $N_p = 512$, $\eta = \xi$ and $\Delta l = 0.75\xi$. For $a_p = 7.6\xi$: $N_p = 256$, $\eta = 2\xi$ and $\Delta l = 2.5\xi$. For $a_p = 23.5\xi$: $N_p = 256$,

$\eta = 20\xi$ and $\Delta l = 4\xi$. Finally, for $a_p = 47\xi$: $N_p = 512$, $\eta = 43\xi$ and $\Delta l = 5\xi$. Only for the last case $L = 512\xi$, while for all the others $L = 256\xi$.

In theoretical predictions we have used the Padé approximation $\widetilde{\rho}_v = \bar{r}^2(a_1 + a_2\bar{r}^2 + a_3\bar{r}^4)/(1 + b_1\bar{r}^2 + b_2\bar{r}^4 + a_3\bar{r}^6)$ where $\bar{r} = |\mathbf{x}|/\xi$. The coefficients are: $a_1 = 0.340038$, $a_2 = 0.0360207$, $a_3 = 0.000985125$, $b_1 = 0.355931$, $b_2 = 0.037502$.

Derivation of the reduced model for the particle trapping.

We report here the calculations leading to the reduced Hamiltonian (13). We denote by an overbar some constants that at the leading order are independent of $\mathbf{q}$. The quantum energy term $H_{\text{qnt}}^{\text{GP}}$ contains gradients of the density and it is sub-leading when $|\mathbf{q}| \gg a_p > \xi$. We thus we set $H_{\text{qnt}}^{\text{GP}} \approx \overline{H}_{\text{qnt}}^{\text{GP}}$. As discussed in the text, $1 - \widetilde{\rho}_p(x)$ is supported on a ball of center q and radius a_p denoted by $\mathbb{B}(\mathbf{q}, a_p)$. At the leading order we also have $\widetilde{\rho}_p^2 \approx \widetilde{\rho}_p$, and $H_{\text{int}}^{\text{GP}}$ can be computed as

$$
\begin{aligned}
H_{\text{int}}^{\text{GP}} &\approx \frac{g\rho_\infty}{2m^2} \int (1 - (1 - \widetilde{\rho}_p))\widetilde{\rho}_v^2 \, d\mathbf{x} \\
&= \overline{H}_{\text{int}}^{\text{GP}} - \frac{g\rho_\infty^2}{2m^2} \int (1 - \widetilde{\rho}_p)\widetilde{\rho}_v^2 \, d\mathbf{x} \\
&\approx \overline{H}_{\text{int}}^{\text{GP}} - \frac{g\rho_\infty^2}{2m^2} \int_{\mathbb{B}(\mathbf{q},a_p)} \widetilde{\rho}_v^2 \, d\mathbf{x} \\
&\approx \overline{H}_{\text{int}}^{\text{GP}} - \frac{1}{2}M_0 c^2 \widetilde{\rho}_v^2(q_\perp).
\end{aligned}
\tag{23}
$$

where we have treated $\widetilde{\rho}_v$ as constant inside $\mathbb{B}(\mathbf{q}, a_p)$, recognised the displaced superfluid mass $M_0 = \rho_\infty \int_{\mathbb{B}} d\mathbf{x}$ and used the definition of the speed of sound. A similar calculation can be performed for the the term H_p^{GP}:

$$
\begin{aligned}
H_p^{\text{GP}} &\approx \overline{H}_p^{\text{GP}} - \frac{\mu\rho_\infty}{m} \int (1 - \widetilde{\rho}_p)\widetilde{\rho}_v \, d\mathbf{x} \\
&\approx \overline{H}_p^{\text{GP}} - \frac{\mu\rho_\infty}{m} \int_{\mathbb{B}\mathbf{q},a_p} \widetilde{\rho}_v \, d\mathbf{x} \approx \overline{H}_p^{\text{GP}} + M_0 c^2 \widetilde{\rho}_v(q_\perp).
\end{aligned}
\tag{24}
$$

In the first equality we used the Thomas-Fermi approximation (5) and again $\widetilde{\rho}_p^2 \approx \widetilde{\rho}_p$.

To compute the hydrodynamic term $H_{\text{hydro}}^{\text{GP}}$ we write $\mathbf{v}_s^2 = \mathbf{v}_v^2 + \mathbf{v}_p \cdot (2\mathbf{v}_v + \mathbf{v}_p) + \mathbf{v}_{\text{BC}} \cdot (2\mathbf{v}_v + 2\mathbf{v}_p + \mathbf{v}_{\text{BC}})$ and consider the contribution of the three addends differently. Firstly we have

$$
\begin{aligned}
H_{\text{hydro}}^{\text{GP}(v)} &= \frac{1}{2}\int \rho \mathbf{v}_v^2 \, d\mathbf{x} = \overline{H}_{\text{hydro}}^{\text{GP}} - \frac{\rho_\infty}{2}\int (1 - \widetilde{\rho}_p)\widetilde{\rho}_v \mathbf{v}_v^2 \, d \\
&\approx \overline{H}_{\text{hydro}}^{\text{GP}} - \frac{M_0 \widetilde{\rho}_v(q_\perp)}{2}\mathbf{v}_v(q_\perp)^2 = \overline{H}_{\text{hydro}}^{\text{GP}} - \frac{\Gamma^2 M_0 \widetilde{\rho}_v(q_\perp)}{8\pi^2 q_\perp^2}.
\end{aligned}
\tag{25}
$$

The second term is computed integrating by parts, using the incompressibility of the flows and neglecting the gradients of ρ_v:

$$
\begin{aligned}
H_{\text{hydro}}^{\text{GP}(p)} &= \frac{\rho_\infty}{2}\int \widetilde{\rho}_p \widetilde{\rho}_v \nabla\phi_p \cdot (2\mathbf{v}_v + \mathbf{v}_p) \, d\mathbf{x} \\
&\approx \frac{\rho_\infty}{2}\int_{\mathbb{B}^c(\mathbf{q},a_p)} \widetilde{\rho}_v \nabla\phi_p \cdot (2\mathbf{v}_v + \mathbf{v}_p) d\mathbf{x} \\
&\approx -\frac{\rho_\infty a_p^2}{2}\oint_{\partial\mathbb{B}(\mathbf{q},a_p)} \widetilde{\rho}_v \phi_p (2\mathbf{v}_v + \mathbf{v}_p) \cdot \hat{n} d\Omega,
\end{aligned}
\tag{26}
$$

where $\mathbb{B}^c(\mathbf{q}, a_p)$ is the complement of $\mathbb{B}(\mathbf{q}, a_p)$ and $\partial\mathbb{B}(\mathbf{q}, a_p)$ its boundary. For $\varepsilon \ll 1$ (see Eq. (9)), in the last integral ρ_v and $\mathbf{v}_v$ can be evaluated at q. The angular integral is then computed exactly and it gives $H_{\text{hydro}}^{\text{GP}(vp)} = \frac{M_0 \widetilde{\rho}_v(\mathbf{q})}{2}C(\dot{\mathbf{q}}^2 - \mathbf{v}_v^2)$, with $C = 1/2$.

The velocity $\mathbf{v}_{\text{BC}}$ is obtained at order ε^2 from the potential $\phi_{\text{BC}} = \frac{1}{2}e_{ij}x'_i x'_j$, where $e_{ij}(q) = (\partial_i v_v^j + \partial_j v_v^i)/2$ is the strain rate tensor evaluated at the particle position. Following the same procedure of (26), we see that the only non-zero contribution is given by

$$
\begin{aligned}
H_{\text{hydro}}^{\text{GP}(\text{BC})} &= -\frac{\rho_\infty a_p^2}{2}\oint_{\partial\mathbb{B}(\mathbf{q},a_p)} \widetilde{\rho}_v \varphi_{\text{BC}} \mathbf{v}_{\text{BC}} \cdot \hat{n} d\Omega \\
&= -\frac{\rho_\infty a_p^5}{4}\widetilde{\rho}_v \, e_{ij}e_{rs}\oint \hat{n}_i\hat{n}_j\hat{n}_r\hat{n}_s d\Omega \\
&= -\frac{M_0 \widetilde{\rho}_v a_p^2}{10}(e_{ij})^2 = -\frac{M_0 \Gamma^2 \widetilde{\rho}_v a_p^2}{20\pi^2 q_\perp^4}.
\end{aligned}
\tag{27}
$$

We have used $\oint \hat{n}_i \hat{n}_j \hat{n}_r \hat{n}_s d\Omega = (\delta_{ij}\delta_{rs} + \delta_{ir}\delta_{js} + \delta_{is}\delta_{ir})\Omega_d/d(d+2)$, where Ω_d is the surface of the unit sphere in d dimensions. The total hydrodynamic kinetic term is the just given by $H_{hydro}^{GP} = H_{hydro}^{GP(v)} + H_{hydro}^{GP(p)} + H_{hydro}^{GP(BC)}$.

Note that at the order $\xi^4/q_\perp^4$ for large vortex-particle separations, the reduced Hamilonian (13) becomes

$$H_{red}[\mathbf{q}, \mathbf{p}] = \overline{H}^{GP} + \frac{\mathbf{p}^2}{2M_{eff}} + M_0 c^2 \left[\frac{1}{2} - \frac{(1+C)\xi^2}{q_\perp^2} + \frac{(10C + 5 - 4(a_p/\xi)^2)}{10} \frac{\xi^4}{q_\perp^4} \right],$$

(28)

where the term proportional to $\xi^4/q_\perp^4$ turns out to be repulsive if $a_p^2 < \frac{5}{4}(1 + 2C)\xi^2$.

Vortex deformation. We can give a rough derivation of the effective vortex-particle Hamiltonian (19) by assuming a small deformation of the vortex line. Similarly to the previous calculations, we neglect the gradients of $\widetilde{\rho}_p$. At the leading order, the terms H_{hydro}^{GP} and H_{qnt}^{GP} are the only contributing to H_{v-p}. For distant particles, the only component of the superfluid velocity modified by the vortex displacement is $\mathbf{v}_v$. The new contributions to the energy coming from the products of $\mathbf{v}_v$ and the other velocity fields vanish after angular integration. We thus need to compute the term $\mathbf{v}_v(|\mathbf{x} - \mathbf{R}(z)|)^2 = \nabla_\perp \phi_v(\mathbf{x}_\perp - \mathbf{s}(z))^2 + (\nabla_\perp \phi_v(|\mathbf{x}_\perp - \mathbf{s}(z)|) \cdot \partial_z \mathbf{s}(z))^2$ where now $\mathbf{x}_\perp = (x, y)$ and $\nabla_\perp = (\partial_x, \partial_y)$. The first term leads directly to the potential (11) evaluated at $\mathbf{q}_\perp - \mathbf{s}(q_z)$. The second term is treated by using the fact that $1 - \widetilde{\rho}_p$ is practically supported on $\mathbb{B}(\mathbf{q}, a_p)$ and $\widetilde{\rho}_p = 1 - (1 - \widetilde{\rho}_p)$. We need to compute

$$
\begin{aligned}
H_{LIA}^{GP} &\approx \frac{\rho_\infty}{2} \int \widetilde{\rho}_v(|\mathbf{x}_\perp - \mathbf{s}(z)|)(\nabla_\perp \phi_v(|\mathbf{x}_\perp - \mathbf{s}(z)|) \cdot \partial_z \mathbf{s}(z))^2 \, d\mathbf{x} \\
&\quad - \frac{\rho_\infty}{2} \int_{\mathbb{B}(\mathbf{q},a_p)} \widetilde{\rho}_v(|\mathbf{x}_\perp - \mathbf{s}(z)|)(\nabla_\perp \phi_v(|\mathbf{x}_\perp - \mathbf{s}(z)|) \cdot \partial_z \mathbf{s}(z))^2 \, d\mathbf{x} \\
&\approx \frac{\rho_\infty}{2} \int_0^L \partial_z s_i(z) \partial_z s_j(z) \left(\int \widetilde{\rho}_v(x_\perp) v_v^i(x_\perp) v_v^j(x_\perp) d\mathbf{x}_\perp \right) dz \\
&\quad + \frac{M_0}{2} \widetilde{\rho}_v(q_\perp)(\mathbf{v}_v(q_\perp) \cdot \partial_z \mathbf{R}(z))^2
\end{aligned}
$$

(29)

$$\approx \frac{\rho_\infty}{4} \int_0^L (\partial_z \mathbf{s}(z))^2 \left(\int \widetilde{\rho}_v(x_\perp) \mathbf{v}_v(x_\perp)^2 d\mathbf{x}_\perp \right) dz = \frac{\rho_\infty \Gamma^2 \Lambda_{hydro}}{8\pi} \int_0^L (\partial_z \mathbf{s}(z))^2 dz,$$

(30)

where we have neglected the second term in (29) as it subdominant. The constant Λ_{hydro} is given by the radial integral

$$
\begin{aligned}
\Lambda_{hydro} &= \int_0^{L_d} \frac{\widetilde{\rho}_v(r)}{r} dr = \int_0^\xi \frac{\widetilde{\rho}_v(r)}{r} dr \\
&\quad + \int_\xi^\infty \frac{\widetilde{\rho}_v(r) - 1}{r} dr + \log \frac{L_d}{\xi} + O((L_d/\xi)^2) \\
&= \log \frac{L_d}{\xi} - 0.3978 + O((L_d/\xi)^2),
\end{aligned}
$$

(31)

where L_d is a cut-off of the order of the inter-vortex distance. The last integral has been performed numerically using $\widetilde{\rho}_v$ obtained by imaginary time evolution of the GP equation in a infinite domain. The quantum energy term H_{qnt}^{GP} gives a contribution equal to (30) but with the constant Λ_{hydro} replaced by $\Lambda_{qnt} = \frac{1}{4} \int_0^\infty \left(\frac{d\widetilde{\rho}_v}{dr} \right)^2 \frac{r}{\widetilde{\rho}_v} dr = 0.2854$.

Finally, in Eq. (19) the constant is $\Lambda = \Lambda_{hydro} + \Lambda_{qnt}$. This oversimplified derivation does not recover the full dispersion relation of Kelvin waves as it neglects non-linear interactions and the 3D modifications of v_v due to vortex deformations. For a more accurate discussion see refs[28,38,47].

Data Availability

The datasets generated and analysed during the current study are available from the corresponding authors on request.

References

1. Donnelly, R. J. *Quantized vortices in helium II*, vol. 2 (Cambridge University Press, 1991).
2. Barenghi, C. F., Skrbek, L. & Sreenivasan, K. R. Introduction to quantum turbulence. *Proceedings of the National Academy of Sciences* **111**, 4647–4652, https://doi.org/10.1073/pnas.1400033111 (2014).
3. Madison, K. W., Chevy, F., Wohlleben, W. & Dalibard, J. Vortex formation in a stirred bose-einstein condensate. *Phys. Rev. Lett.* **84**, 806–809, https://doi.org/10.1103/PhysRevLett.84.806 (2000).
4. Abo-Shaeer, J. R., Raman, C., Vogels, J. M. & Ketterle, W. Observation of vortex lattices in bose-einstein condensates. *Science* **292**, 476–479, https://doi.org/10.1126/science.1060182 (2001).
5. Bewley, G. P., Lathrop, D. P. & Sreenivasan, K. R. Superfluid helium: Visualization of quantized vortices. *Nature* **441**, 588 (2006).
6. Bewley, G. P., Paoletti, M. S., Sreenivasan, K. R. & Lathrop, D. P. Characterization of reconnecting vortices in superfluid helium. *Proceedings of the National Academy of Sciences* **105**, 13707–13710, https://doi.org/10.1073/pnas.0806002105 (2008).
7. Fonda, E., Meichle, D. P., Ouellette, N. T., Hormoz, S. & Lathrop, D. P. Direct observation of kelvin waves excited by quantized vortex reconnection. *Proceedings of the National Academy of Sciences* **111**, 4707–4710, https://doi.org/10.1073/pnas.1312536110 (2014).

8. Paoletti, M. S., Fisher, M. E., Sreenivasan, K. R. & Lathrop, D. P. Velocity statistics distinguish quantum turbulence from classical turbulence. *Phys. Rev. Lett.* **101**, 154501, https://doi.org/10.1103/PhysRevLett.101.154501 (2008).

9. La Mantia, M. & Skrbek, L. Quantum turbulence visualized by particle dynamics. *Phys. Rev. B* **90**, 014519, https://doi.org/10.1103/PhysRevB.90.014519 (2014).

10. Zmeev, D. E. *et al.* Excimers he$^*_2$ as tracers of quantum turbulence in ^{4}He in the $t = 0$ limit. *Phys. Rev. Lett.* **110**, 175303, https://doi.org/10.1103/PhysRevLett.110.175303 (2013).

11. Douady, S., Couder, Y. & Brachet, M. E. Direct observation of the intermittency of intense vorticity filaments in turbulence. *Phys. Rev. Lett.* **67**, 983–986, https://doi.org/10.1103/PhysRevLett.67.983 (1991).

12. Toschi, F. & Bodenschatz, E. Lagrangian properties of particles in turbulence. *Annual review of fluid mechanics* **41**, 375–404 (2009).

13. Maxey, M. R. & Riley, J. J. Equation of motion for a small rigid sphere in a nonuniform flow. *The Physics of Fluids* **26**, 883–889, https://doi.org/10.1063/1.864230 (1983).

14. Auton, T. R., Hunt, J. C. R. & Prud'Homme, M. The force exerted on a body in inviscid unsteady non-uniform rotational flow. *Journal of Fluid Mechanics* **197**, 241–257, https://doi.org/10.1017/S0022112088003246 (1988).

15. Poole, D. R., Barenghi, C. F., Sergeev, Y. A. & Vinen, W. F. Motion of tracer particles in he ii. *Phys. Rev. B* **71**, 064514, https://doi.org/10.1103/PhysRevB.71.064514 (2005).

16. Sergeev, Y. A. & Barenghi, C. F. Particles-vortex interactions and flow visualization in 4he. *Journal of Low Temperature Physics* **157**, 429, https://doi.org/10.1007/s10909-009-9994-8 (2009).

17. Schwarz, K. W. Three-dimensional vortex dynamics in superfluid ^{4}He: Homogeneous superfluid turbulence. *Phys. Rev. B* **38**, 2398–2417, https://doi.org/10.1103/PhysRevB.38.2398 (1988).

18. Schwarz, K. W. Spherical probes and quantized vortices: Hydrodynamic formalism and simple applications. *Phys. Rev. A* **10**, 2306–2317, https://doi.org/10.1103/PhysRevA.10.2306 (1974).

19. Kivotides, D., Barenghi, C. F. & Sergeev, Y. A. Collision of a tracer particle and a quantized vortex in superfluid helium: Self-consistent calculations. *Phys. Rev. B* **75**, 212502, https://doi.org/10.1103/PhysRevB.75.212502 (2007).

20. Astrakharchik, G. E. & Pitaevskii, L. P. Motion of a heavy impurity through a bose-einstein condensate. *Phys. Rev. A* **70**, 013608, https://doi.org/10.1103/PhysRevA.70.013608 (2004).

21. Berloff, N. G. & Roberts, P. H. Capture of an impurity by a vortex line in a bose condensate. *Phys. Rev. B* **63**, 024510, https://doi.org/10.1103/PhysRevB.63.024510 (2000).

22. Rica, S. & Roberts, D. C. Induced interaction and crystallization of self-localized impurity fields in a bose-einstein condensate. *Phys. Rev. A* **80**, 013609, https://doi.org/10.1103/PhysRevA.80.013609 (2009).

23. Villois, A. & Salman, H. Vortex nucleation limited mobility of free electron bubbles in the gross-pitaevskii model of a superfluid. *Phys. Rev. B* **97**, 094507, https://doi.org/10.1103/PhysRevB.97.094507 (2018).

24. Winiecki, T. & Adams, C. S. Motion of an object through a quantum fluid. *EPL (Europhysics Letters)* **52**, 257 (2000).

25. Shukla, V., Brachet, M. & Pandit, R. Sticking transition in a minimal model for the collisions of active particles in quantum fluids. *Phys. Rev. A* **94**, 041602, https://doi.org/10.1103/PhysRevA.94.041602 (2016).

26. Shukla, V., Pandit, R. & Brachet, M. Particles and fields in superfluids: Insights from the two-dimensional gross-pitaevskii equation. *Phys. Rev. A* **97**, 013627, https://doi.org/10.1103/PhysRevA.97.013627 (2018).

27. Giuriato, U., Krstulovic, G. & Proment, D. Clustering and phase transitions in a 2d quantum fluid with impurities. *arXiv preprint arXiv:1807.08721* (2018).

28. Pismen, L. M. *Vortices in nonlinear fields: from liquid crystals to superfluids, from non-equilibrium patterns to cosmic strings*, vol. 100 (Oxford University Press, 1999).

29. Kivotides, D., Barenghi, C. F. & Sergeev, Y. A. Numerical calculation of the interaction of superfluid vortices and a rigid sphere. *Journal of Low Temperature Physics* **144**, 121–134, https://doi.org/10.1007/s10909-006-9253-1 (2006).

30. Barenghi, C. F., Kivotides, D. & Sergeev, Y. A. Close approach of a spherical particle and a quantised vortex in helium ii. *Journal of Low Temperature Physics* **148**, 293–297, https://doi.org/10.1007/s10909-007-9387-9 (2007).

31. Barenghi, C. F., Parker, N., Proukakis, N. & Adams, C. Decay of quantised vorticity by sound emission. *Journal of Low Temperature Physics* **138**, 629–634, https://doi.org/10.1007/s10909-005-2272-5 (2005).

32. Krstulovic, G., Brachet, M. & Tirapegui, E. Radiation and vortex dynamics in the nonlinear schrödinger equation. *Phys. Rev. E* **78**, 026601, https://doi.org/10.1103/PhysRevE.78.026601 (2008).

33. Batchelor, G. K. *An Introduction to Fluid Dynamics*. Cambridge Mathematical Library (Cambridge University Press, 2000).

34. Donnelly, R. J. Theory of the interaction of ions and quantized vortices in rotating helium ii. *Phys. Rev. Lett.* **14**, 39–41, https://doi.org/10.1103/PhysRevLett.14.39 (1965).

35. Villois, A., Proment, D. & Krstulovic, G. Universal and nonuniversal aspects of vortex reconnections in superfluids. *Phys. Rev. Fluids* **2**, 044701, https://doi.org/10.1103/PhysRevFluids.2.044701 (2017).

36. Nemirovskii, S. K. Thermodynamic equilibrium in the system of chaotic quantized vortices in a weakly imperfect bose gas. *Theoretical and Mathematical Physics* **141**, 1452–1460, https://doi.org/10.1023/B:TAMP.0000043860.52270.0c (2004).

37. Bustamante, M. D. & Nazarenko, S. Derivation of the biot-savart equation from the nonlinear schrödinger equation. *Phys. Rev. E* **92**, 053019, https://doi.org/10.1103/PhysRevE.92.053019 (2015).

38. Roberts, P. H. On vortex waves in compressible fluids. ii. the condensate vortex. *Proceedings of the Royal Society of London A: Mathematical, Physical and Engineering Sciences* **459**, 597–607, https://doi.org/10.1098/rspa.2002.1033 (2003).

39. Krstulovic, G. Kelvin-wave cascade and dissipation in low-temperature superfluid vortices. *Phys. Rev. E* **86**, 055301, https://doi.org/10.1103/PhysRevE.86.055301 (2012).

40. Villois, A., Krstulovic, G., Proment, D. & Salman, H. A vortex filament tracking method for the gross–pitaevskii model of a superfluid. *Journal of Physics A: Mathematical and Theoretical* **49**, 415502 (2016).

41. Berloff, N. G. & Roberts, P. H. Motions in a bose condensate: Vi. vortices in a nonlocal model. *Journal of Physics A: Mathematical and General* **32**, 5611 (1999).

42. Reneuve, J., Salort, J. & Chevillard, L. Structure, dynamics, and reconnection of vortices in a nonlocal model of superfluids. *Phys. Rev. Fluids* **3**, 114602, https://doi.org/10.1103/PhysRevFluids.3.114602 (2018).

43. Berloff, N. G., Brachet, M. & Proukakis, N. P. Modeling quantum fluid dynamics at nonzero temperatures. *Proceedings of the National Academy of Sciences*, https://doi.org/10.1073/pnas.1312549111 (2014).

44. Adhikari, S. & Salasnich, L. Vortex lattice in the crossover of a bose gas from weak coupling to unitarity. *Scientific reports* **8**, 8825 (2018).

45. Krstulovic, G. & Brachet, M. Anomalous vortex-ring velocities induced by thermally excited kelvin waves and counterflow effects in superfluids. *Phys. Rev. B* **83**, 132506, https://doi.org/10.1103/PhysRevB.83.132506 (2011).

46. Parks, P. E. & Donnelly, R. J. Radii of positive and negative ions in helium ii. *Phys. Rev. Lett.* **16**, 45–48, https://doi.org/10.1103/PhysRevLett.16.45 (1966).

47. Laurie, J., L'vov, V. S., Nazarenko, S. & Rudenko, O. Interaction of kelvin waves and nonlocality of energy transfer in superfluids. *Phys. Rev. B* **81**, 104526, https://doi.org/10.1103/PhysRevB.81.104526 (2010).

Acknowledgements

Author Contributions

U.G. performed the numerical simulations and analysed the data. U.G. and G.K. developed the theory and wrote the manuscript.

Additional Information

Supplementary information accompanies this paper at https://doi.org/10.1038/s41598-019-39877-w.

Competing Interests: The authors declare no competing interests.

Publisher's note: Springer Nature remains neutral with regard to jurisdictional claims in published maps and institutional affiliations.

How trapped particles interact with and sample superfluid vortex excitations

Umberto Giuriato ●* and Giorgio Krstulovic ●

Université Côte d'Azur, CNRS, OCA, Laboratoire Lagrange, Boulevard de l'Observatoire CS 34229 - F 06304 NICE Cedex 4, France

Sergey Nazarenko ●

Université Côte d'Azur, Institut de Physique de Nice (INPHYNI), CNRS UMR 7010, Parc Valrose, 06108 Nice Cedex 2, France

Particles have been used for more than a decade to visualize and study the dynamics of quantum vortices in superfluid helium. In this work we study how the dynamics of a collection of particles set inside a vortex reflects the motion of the vortex. We use a self-consistent model based on the Gross-Pitaevskii equation coupled with classical particle dynamics. We find that each particle oscillates with a natural frequency proportional to the number of vortices attached to it. We then study the dynamics of an array of particles trapped in a quantum vortex and use particle trajectories to measure the frequency spectrum of the vortex excitations. Surprisingly, due to the discreetness of the array, the vortex excitations measured by the particles exhibit bands, gaps, and Brillouin zones, analogous to the ones of electrons moving in crystals. We then establish a mathematical analogy where vortex excitations play the role of electrons and particles that of the potential barriers constituting the crystal. We find that the height of the effective potential barriers is proportional to the particle mass and the frequency of the incoming waves. We conclude that large-scale vortex excitations could be in principle directly measured by particles and novel physics could emerge from particle-vortex interaction.

DOI: [10.1103/PhysRevResearch.2.023149](https://doi.org/10.1103/PhysRevResearch.2.023149)

I. INTRODUCTION

When a fluid composed of bosons is cooled down, a spectacular phase transition takes place. The system becomes superfluid and exhibits exotic physical properties. Unlike any classical fluid, a superfluid flows with no viscosity. This is an intriguing example of the manifestation of pure quantum-mechanical effects on a macroscopic level. The first discovered superfluid is liquid helium ^{4}He in its so-called phase II, below the critical temperature $T_\lambda \simeq 2.17$ K. In one of the first attempts of describing the behavior of superfluid helium, London suggested that superfluidity is intimately linked to the phenomenon of Bose-Einstein condensation (BEC) [1]. In the same years, Landau and Tisza independently put forward a phenomenological two-fluid model, wherein superfluid helium can be regarded as a physically inseparable mixture of two components: a normal viscous component that carries the entire entropy and an inviscid component with zero entropy [2,3].

Because of its intrinsic long-range order, a superfluid can be described by a macroscopic complex wave function. A stunning quantum-mechanical constraint is that vortices

appear as topological defects of such order parameter. In three dimensions, such defects are unidimensional structures, usually referred to as quantum vortices. Indeed, the circulation (contour integral) of the flow around a vortex must be a multiple of the Feynman-Onsager quantum of circulation h/m, where h is the Planck constant and m is the mass of the Bosons constituting the fluid [4]. Such peculiarity is necessary to ensure the monodromy of the wave function. In superfluid helium, quantum vortices have a core size on the order of an angstrom. At low temperatures, below 1 K, the normal component is negligible and vortices are stable and do not decay by any diffusion process, unlike their classical counterparts. The understanding of superfluid vortex dynamics has a direct impact on many interesting, complex nonequilibrium multiscale phenomena, such as turbulence [5–7].

Most of the experimental knowledge on superfluid vortices is based on indirect measurement of their properties. The early efforts in the observation of quantized vortices were made in the framework of rotating superfluid helium, by using electron bubbles (ions) as probes [8]. Since then, impurities have been extensively used to unveil the dynamics of superfluid vortices. An important breakthrough occurred in 2006, when micrometer-sized hydrogen ice particles were used to directly visualize superfluid helium vortices [9]. Thanks to pressure gradients, particles get trapped inside quantum vortices and are subsequently carried by them. Hence, it has been possible to observe vortex reconnections and Kelvin waves (helicoidal displacements that propagate along the vortex line) by means of standard particle-tracking techniques [10]. Furthermore, the particle dynamics unveiled important differences between

---

*Corresponding author: umberto.giuriato@oca.eu

velocity statistics of quantum and classical turbulent states [11,12]. In experiments, such particles are used as tracers, despite their very large size compared to the vortex core. Therefore, it is of the utmost importance that the mechanisms driving their dynamics are fully comprehended. Specifically, how well is vortex dynamics reflected by the motion of the particles trapped in it? How much does their presence in the core modify the propagation of Kelvin waves? Would they affect the reconnection rates?

Describing the interaction of particles with isolated vortex lines or complex quantum vortex tangles is not an easy task. Depending on the scale of interest, there are different theoretical and numerical models that can be adopted. A big effort has been made in adapting the standard dynamics of particles in classical fluids to the case of superfluids described by two-fluid models [13,14]. This is a macroscopic model in which vorticity is a coarse-grained field and therefore there is no notion of quantized vortices. A medium-scale description is given by the vortex filament model, where the superfluid is modeled as a collection of lines that evolve following Biot-Savart integrals. In this approximation, circulation of vortices is by construction quantized but reconnections are absent and have to be implemented via some *ad hoc* mechanism. Finite-size particles can be studied in the vortex filament framework but the resulting equations are numerically costly and limited [15]. A microscopic approach consists in describing each impurity by a classical field in the framework of the Gross-Pitaevskii model [16–18]. In principle, such method is valid for weakly interacting BECs, and is numerically and theoretically difficult to handle if one wants to consider more than just a few particles. In the same context, an alternative possibility is to assume classical degrees of freedom for the particles, while the superfluid is still a complex field obeying the Gross-Pitaevskii equation. This idea of modeling particles as simple classical hard spheres has been shown to be both numerically and analytically very powerful [19–22]. In particular, such minimal and self-consistent model allows for simulating a relatively large number of particles, and describes well the particle-vortex interaction [22]. Although formally valid for weakly interacting BECs, it is expected to give a good qualitative description of superfluid helium.

In this paper we investigate how particles trapped in quantum vortices interact with vortex excitations and in particular how well they can be used to infer properties of superfluid vortices. We use the Gross-Pitaevskii equation coupled with inertial and active particles obeying classical dynamics to answer this question. We first address how the Magnus force acting on trapped particles induces oscillations at a certain natural frequency. This quantity may be experimentally measured to determine the number of vortices composing a polarized bundle (see a discussion later in this paper). Second, in order to understand the effect of particle inertia, we analyze the spectrum of vortex excitations in the case when a continuous distribution of mass is contained inside the vortex core. Then, we study an array of particles trapped inside a vortex, in a setting similar to the one observed in experiments. Surprisingly, the dispersion relation of vortex waves measured by the particles is found to contain band gaps and the periodicity typically observed in the energy spectra of solids. We explain the numerical observation applying the concepts used in the

standard Kronig-Penney model [23,24], which describes the motion of electrons in a unidimensional crystal. Finally, based on our results, we discuss in which regimes particles could be reliably used to sample vortex excitations.

II. THEORETICAL BACKGROUND

A. Model for superfluid vortices and active particles

We consider a superfluid at very low temperature containing N_p spherical particles of mass M_p and radius a_p. We describe the system by a self-consistent model based on the three-dimensional Gross-Pitaevskii equation. The particles are modeled by strong localized potentials V_p, which completely deplete the superfluid up to a distance a_p from their center position $\mathbf{q}_i$. Particles have inertia and obey a Newtonian dynamics. The Hamiltonian of the system is

$$H = \int \left(\frac{\hbar^2}{2m}|\nabla\psi|^2 + \frac{g}{2}|\psi|^4 + \sum_{i=1}^{N_p} V_p(\mathbf{r}-\mathbf{q}_i)|\psi|^2 \right) d\mathbf{r}$$
$$+ \sum_{i=1}^{N_p} \frac{\mathbf{p}_i^2}{2M_p} + \sum_{i<j}^{N_p} V_{rep}^{ij}, \qquad (1)$$

where ψ is the wave function that describes the superfluid and m is the mass of the condensed bosons interacting with an s-wave scattering length a_s, so that the coupling constant is $g = 4\pi a_s \hbar^2/m$. The potential $V_{rep}^{ij} = \varepsilon(r_0/|\mathbf{q}_i-\mathbf{q}_j|)^{12}$ is a repulsive potential of radius r_0 between particles. See Refs. [20,22] and the next section for further details about the model. The equations of motion for the superfluid field ψ and the particle positions $\mathbf{q}_i = (q_{i,x}, q_{i,y}, q_{i,z})$ are

$$i\hbar\frac{\partial\psi}{\partial t} = -\frac{\hbar^2}{2m}\nabla^2\psi + (g|\psi|^2 - \mu)\psi + \sum_{i=1}^{N_p} V_p(|\mathbf{x}-\mathbf{q}_i|)\psi,$$
$$(2)$$

$$M_p\ddot{\mathbf{q}}_i = -\int V_p(|\mathbf{x}-\mathbf{q}_i|)\nabla|\psi|^2 d\mathbf{x} + \sum_{j\neq i}^{N_p} \frac{\partial}{\partial\mathbf{q}_i}V_{rep}^{ij}. \quad (3)$$

This model has been successfully used to study vortex nucleation [19] and trapping of particles by quantum vortices [22]. We denote by GP the Gross-Pitaevskii model without particles and by GP-P the full coupled system (2) and (3).

In the absence of particles, the chemical potential μ fixes the value of the condensate ground state $\psi_\infty = \sqrt{\rho_\infty/m} = \sqrt{\mu/g}$. Linearizing around this value, wave excitations are described by the Bogoliubov dispersion relation

$$\Omega_B(k) = c|\mathbf{k}|\sqrt{1 + \frac{\xi^2|\mathbf{k}|^2}{2}}, \qquad (4)$$

where $\mathbf{k}$ is the wave number of the excitation. Large-wavelength excitations propagate with the phonon (sound) velocity $c = \sqrt{g\rho_\infty/m^2}$, while at length scales smaller than the healing length $\xi = \sqrt{\hbar^2/2g\rho_\infty}$ excitations behave as free particles.

The close relation between the GP model and hydrodynamics comes from the Madelung transformation $\psi(\mathbf{x}) = \sqrt{\rho(\mathbf{x})/m}\, e^{i\frac{m}{\hbar}\phi(\mathbf{x})}$, which maps the GP (2) into the continuity

and Bernoulli equations of a superfluid of density ρ and velocity $\mathbf{v}_s = \nabla\phi$. Although the superfluid velocity is potential, the phase is not defined at the nodal lines of $\psi(\mathbf{x})$ and thus vortices may appear as topological defects. The simplest case corresponds to a straight quantum vortex given by

$$\psi_v(x, y, z) = \sqrt{\rho_v(x, y)/m}\, e^{i\frac{m}{\hbar}\phi_v(x,y)}, \tag{5}$$

where $\rho_v(x, y)$ vanishes at the vortex core line $(0, 0, z)$. The core size of a vortex is on the order of the healing length ξ and the phase $\phi_v = \frac{n_v \hbar}{m}\varphi$, with φ the angle in the (x, y) plane, ensures the monodromy of the solution (5) only if n_v is an integer number. The corresponding velocity field is $\mathbf{v}_v = \frac{n_v \hbar}{m}\frac{\hat{\varphi}}{|\mathbf{x}_\perp|}$, where $\hat{\varphi}$ is the azimuthal unit vector and $\mathbf{x}_\perp = (x, y, 0)$. The circulation along a closed path $\mathcal{C}$ surrounding the vortex is therefore quantized:

$$\Gamma = \oint_{\mathcal{C}} \mathbf{v}_v \cdot d\mathbf{l} = n_v \frac{h}{m} = 2\pi n_v \sqrt{2}c\xi. \tag{6}$$

Actually, for $|n_v| > 1$ vortices are structurally unstable and split into single-charged vortices. We shall consider only $n_v = \pm 1$ vortices. Note that the Bogoliubov spectrum (3) obtained in the GP framework describes well the excitations of atomic BECs, but does not match the one observed in superfluid helium. In particular, the dispersion relation never changes convexity and the roton minimum is absent. Nevertheless, the hydrodynamic description of vortices and of their large-scale excitations (summarized in the following section) is similar both in helium and in the GP model.

B. Frequency spectrum of superfluid vortex excitations

Excitations are present in quantum vortices because of thermal, quantum, or turbulent fluctuations. They are waves propagating along the vortex line with a certain frequency $\Omega_v(k)$, where k is the (one-dimensional) wave number of the excitation. At scales larger than the vortex core size ($k\xi \ll 1$), such excitations are known as Kelvin waves (KWs) and they play the important role of carrying energy toward the smallest scales of a superfluid [25]. At such scales, the dynamics of a vortex line can be described by the vortex filament model, according to which the motion of the filament is determined by the self-induced velocity $\mathbf{v}_{si}$ of the line on itself [8]. This model involves nonlocal contributions and a singular integral that needs to be regularized [26]. Note that this model has also been derived at large scales also in the framework of the GP equation [27]. The simplest approximation that can be done is the well-known local-induction approximation (LIA), where only the contribution to $\mathbf{v}_{si}$ due to the local curvature at each point of the filament is considered. Such approximation is valid when the curvature is much larger than the vortex core size. The LIA model reads [28]

$$\dot{\mathbf{s}}(\zeta, t) = \mathbf{v}_{si}(\zeta, t), \quad \mathbf{v}_{si}(\zeta, t) = \frac{\Gamma}{4\pi}\Lambda \frac{\partial \mathbf{s}}{\partial \zeta} \times \frac{\partial^2 \mathbf{s}}{\partial \zeta^2}, \tag{7}$$

where $\mathbf{s}(\zeta, t)$ is the curve that parametrizes the filament, and ζ is the arclength. The parameter $\Lambda > 0$ is in principle a nonlocal operator yielding the correct Kelvin wave dispersion relation. At a first approximation and for the sake of simplicity in analytical treatments, it can be considered as a constant. In the case of small displacements of a straight filament oriented

along the z axis, the vortex line can be parametrized as $s(z, t) = s_x(z, t) + i s_y(z, t)$. At the leading order (7) reduces to

$$\dot{s}(z, t) = v_{si}(z, t), \quad v_{si}(z, t) = i\frac{\Gamma}{4\pi}\Lambda \frac{\partial^2}{\partial z^2}s(z, t). \tag{8}$$

The LIA equation (8) admits solutions in the form of helicoidal waves propagating along the vortex line with a dispersion relation

$$\Omega_{\text{LIA}}(k) = -\frac{\Gamma\Lambda}{4\pi}k^2. \tag{9}$$

A better description of vortex waves was formally derived from the Euler equations for an ideal incompressible fluid by Sir W. Thomson (Lord Kelvin) [29] in the case of a hollow vortex, namely if the vorticity is concentrated in a thin tube of radius a_0. In this case the frequency of propagation is given by the well-known Kelvin wave dispersion relation

$$\Omega_{\text{KW}}(k) = \frac{\Gamma}{2\pi a_0^2}\left[1 - \sqrt{1 + a_0|k|\frac{K_0(a_0|k|)}{K_1(a_0|k|)}}\right], \tag{10}$$

where $K_n(x)$ is the modified Bessel function of order n and a_0 depends on the model of the vortex core. It has been shown by Roberts [30] that the small wave number limit of expression (10) is valid also for large-scale waves propagating along the superfluid vortex described by the GP equation:

$$\Omega_v(k) \xrightarrow[k\xi \ll 1]{} \Omega_{\text{KW}}(ka_0 \to 0) = -\frac{\Gamma}{4\pi}k^2\left(\ln\frac{2}{a_0|k|} - \gamma_E\right), \tag{11}$$

where $a_0 = 1.1265\xi$ and $\gamma_E \sim 0.5772$ is the Euler-Mascheroni constant. On the other hand, at small scales the excitations of a quantum vortex behave as (GP) free particles and the dispersion relation is simply given by [30]

$$\Omega_v(k) \xrightarrow[k\xi \gg 1]{} -\Omega_B(k\xi \to \infty) = -\frac{\Gamma}{4\pi}k^2. \tag{12}$$

Note that all the frequencies (9)–(12) have an opposite sign with respect to the circulation Γ; namely KWs rotate opposite to the vortex flow $\mathbf{v}_v$. Since there is not an analytic expression for the full dispersion relation of vortex excitations of the GP model, in the numerics presented in this work we use a fit of the dispersion relation that matches both asymptotic (10) and (12). It reads

$$\Omega_v^{\text{fit}}(k) = \Omega_{\text{KW}}(k)\left[1 + \epsilon_{\frac{1}{2}}(a_0|k|)^{\frac{1}{2}} + \epsilon_1(a_0|k|) + \frac{1}{2}(a_0|k|)^{\frac{3}{2}}\right]. \tag{13}$$

The dimensionless parameters $\epsilon_{\frac{1}{2}} = -0.20$ and $\epsilon_1 = 0.64$ are obtained from the measured dispersion relation of a bare vortex tracked in a GP simulation without particles. In Fig. 1 the spatiotemporal spectrum of a bare GP vortex is compared with the result of the fit (solid green line), together with the asymptotics. Note that in Eq. (13) we used the full Kelvin wave frequency relation (10) (dashed cyan line) instead of the asymptotic (11) (dotted yellow line). This is because its large-k limit $\Omega_{\text{KW}}(k) \sim \frac{\Gamma}{2\pi a_0^2}(a_0|k|)^{\frac{1}{2}}$ can be straightforwardly adjusted to obtain the free particle dispersion relation (12) (dash-dotted magenta line).
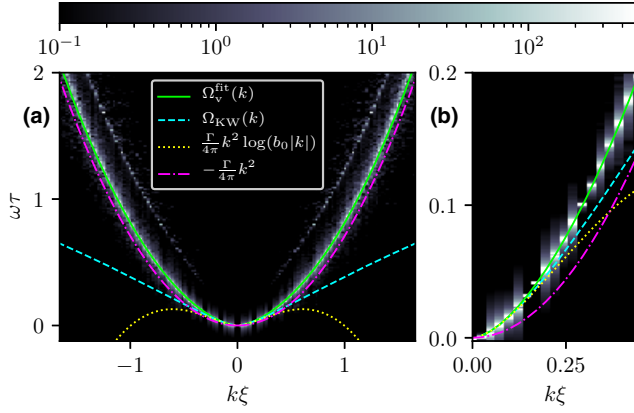
FIG. 1. (a) Spatiotemporal spectrum of a GP bare vortex loaded with small-amplitude Kelvin waves. Solid green line is the fit (13). Dashed cyan line is KW dispersion relation (10). Dotted yellow line is the small-k asymptotic (11), with $b_0 = a_0 e^{\gamma_E}/2$. Magenta dash-dotted line is the large-k asymptotic (12). The resolution of the simulation is $N_\perp = N_\parallel = 256$ in a computational domain of size $L_\perp = L_\parallel = 256\xi$. (b) A zoom close to small wave numbers.

III. MOTION OF PARTICLES TRAPPED BY QUANTUM VORTEX

We are interested in the behavior of particles captured by quantum vortices. Since hydrogen and deuterium particles used to visualize vortices in superfluid helium experiments are considerably larger than the vortex core (typically $a_p \sim 10^4\xi$) they could be captured not by an isolated vortex but by bundles of many polarized vortices. In such complex system, the large particle size and inertia might affect the vortex dynamics. It is then natural to try to understand how the dynamics of vortices is modified by the presence of the particles, or in other terms, how well particles track superfluid vortices.

An amazing piece of experimental evidence is that trapped particles distribute themselves at an almost equal spacing (see for instance Ref. [10]). In this work we do not address the physical origins of this distribution, but we adopt it as a hypothesis for setting the initial condition of our simulations.

We start our discussion by presenting the settings of the GP-P model in our simulations. The GP-P equations are integrated in a 3D periodic domain of dimensions $L_\perp \times L_\perp \times L_\parallel$. The initial conditions consist of a perturbed straight vortex containing small-amplitude vortex excitations. The vortex is loaded with a number of particles and then evolved under GP-P dynamics. The computational domain contains three other image vortices in order to preserve periodicity. Only one vortex contains particles whereas the three others are bare. We have used resolutions up to $256 \times 256 \times 1024$ and 512^3 collocation points. We express the particle mass as $M_p = \mathcal{M} M_p^0$, where M_p^0 is the mass of the displaced superfluid. Therefore, light, neutral, and heavy particles have $\mathcal{M} < 1$, $\mathcal{M} = 1$, and $\mathcal{M} > 1$, respectively. Lengths are expressed in units of ξ, times in units of $\tau = \xi/c$, and velocities in units of c. Further details on the numerical implementation are given in Appendix A.
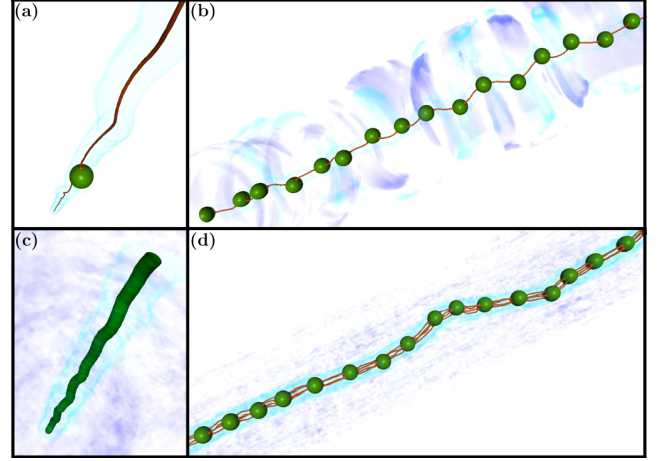

FIG. 2. Visualization of particles trapped by superfluid vortices from GP simulations. Vortices are displayed in red, particles in green, and sound waves are rendered in blue. (a) A single particle of size $a_p = 13.1\xi$ trapped in a vortex filament. (b) An array of particles of size $a_p = 13.1\xi$ and relative distance $d = 51.2\xi$. (c) A wire made of 50 overlapping particles of size 2.7ξ trapped in a vortex filament. (d) An array of particles of size $a_p = 13.1\xi$ trapped in a bundle of 4 vortex filaments. Movies of the simulations are available in the Supplemental Material [34].

Figure 2 displays the four different configurations studied in this work. Figure 2(a) shows one particle moving in a quantum vortex which clearly induces KWs on the filament. Figure 2(b) displays an array of particles initially set at equal distances. We have checked that provided that particles are distant enough, they remain equally distributed along the vortex, with very small fluctuations along its axis. Figure 2(c) displays a snapshot in the case where particles strongly overlap creating an almost continuous distribution of mass inside the vortex. Producing this state is possible by properly adjusting the repulsive potential V_{rep}^{ij} in Eq. (3). The purpose of studying this configuration is twofold. First, from the theoretical point of view it will provide an easier way to describe the role of the particle mass in the vortex dynamics and its effect on vortex excitations. On the other hand, such setting is similar to recent experiments that study the nanowire formation by the coalescence of gold nanofragments on quantum vortices [31] or experiments with vibrating wires inside quantum vortices in superfluid ^{3}He and ^{4}He [32,33]. Finally, Fig. 2(d) displays a bundle of four equally charged vortices loaded with an array of particles. In all cases, we clearly see the interaction between particles and vortices producing sound (phonon) and Kelvin waves. Movies of the simulations are available in the Supplemental Material [34].

A. Natural frequency of particles trapped by superfluid vortices

We first consider the dynamics of a particle trapped by an almost straight superfluid vortex. At the leading order this is the classical hydrodynamical problem of a moving sphere with nonzero circulation in an ideal fluid. The main force acting on the particle is the Magnus force, which arises from the pressure distribution generated at the boundary of the particle in such configuration [35,36]. We introduce the

complex variable $q(t) = q_x(t) + iq_y(t)$ for the center of the particle in the plane orthogonal to the vortex filament, and $v = v_x + iv_y$ for the velocity of the ambient superfluid flow. In these variables, the equation of motion for the particle in the absence of any external force is [36]

$$\ddot{q}(t) = i\Omega_{\mathrm{p}}[\dot{q}(t) - v], \quad \Omega_{\mathrm{p}} = \frac{3}{2}\frac{\rho\Gamma a_{\mathrm{p}}}{M_{\mathrm{p}}^{\mathrm{eff}}}, \qquad (14)$$

where $M_{\mathrm{p}}^{\mathrm{eff}} = M_{\mathrm{p}} + \frac{1}{2}M_{\mathrm{p}}^0 = (\mathcal{M} + \frac{1}{2})M_{\mathrm{p}}^0$ is the effective mass of the particle and $M_{\mathrm{p}}^0 = \frac{4}{3}\pi\rho a_{\mathrm{p}}^3$ is the displaced mass of the fluid. In Eq. (14), the fluid is assumed to be incompressible with density $\rho \sim \rho_\infty$, which is a good approximation when the particle size is larger than the healing length. From (14) we can derive the temporal spectrum of the particle position

$$|\hat{q}(\omega)|^2 = \frac{\Omega_{\mathrm{p}}^2|\hat{v}(\omega)|^2}{\omega^2(\omega - \Omega_{\mathrm{p}})^2}, \qquad (15)$$

where $\hat{q}(\omega) = \int q(t)e^{-i\omega t}\,dt$ and $\hat{v}(\omega) = \int v(t)e^{-i\omega t}\,dt$. The vortex line tension, which is responsible for the propagation of Kelvin waves [37], is implicitly contained in the superfluid flow v in Eq. (14). It generates particle oscillations in the rotation direction opposite to the flow generated by the vortex. However, from Eq. (15) we see that the particle motion is dominated by a precession with frequency Ω_{p}, which has the same sign of Γ and therefore has the same direction of the vortex flow. Such frequency is the natural frequency of the particle: expressing it as a function of $\mathcal{M}$ we get

$$\Omega_{\mathrm{p}} = \frac{9}{4\pi}\frac{\Gamma}{a_{\mathrm{p}}^2(2\mathcal{M} + 1)}. \qquad (16)$$

For current experiments using particles as probes, such characteristic frequency is of order 10–100 Hz, which is actually measurable [38].

We have performed a series of numerical experiments with particles trapped in a superfluid vortex excited with small-amplitude Kelvin waves. Measurements of temporal spectra (15) for particles characterized by different values of Ω_{p} are reported in Fig. 3. In the x axis of the plot we have the angular frequencies with the same sign of Γ. The different natural frequencies have been obtained varying the mass and the size of the particles. The observed peak at Ω_{p} is well predicted by Eq. (15). The natural frequency is also observed for particles in the particle-array configuration. In particular, if particles are attached to a bundle of N_{v} quantum vortices instead of a single filament, the corresponding characteristic frequency is N_{v} times larger. The case of a bundle of $N_{\mathrm{v}} = 4$ is also reported in Fig. 3, in a remarkable agreement with theory. This has an important experimental implication. Measuring the natural frequency Ω_{p} could give an independent estimate of the circulation (and therefore of the number of vortices) in the bundles visualized by the particles in superfluid helium experiments.

Note that in general the vortex line tension could have a nontrivial coupling with the particles and lead to a modification of the precession frequency Ω_{p}. Indeed, in the idealized derivation of Eq. (14), it is assumed that the particle center coincides with the center of a straight vortex line. In principle, one should solve Eq. (14) together with the equation of motion of the vortex, taking into account the proper boundary
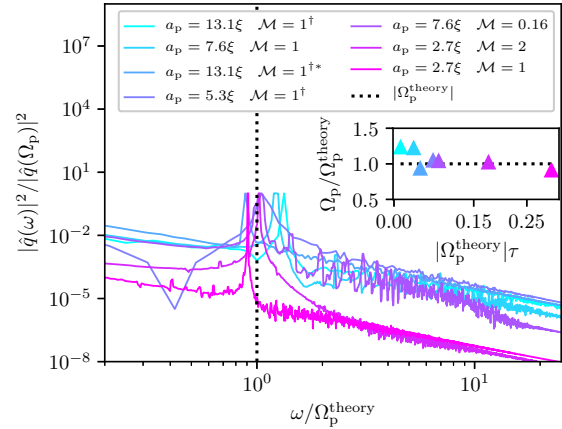

FIG. 3. Temporal spectra of the particle positions for different values of the natural frequency Ω_{p}, obtained varying mass and size of the particles. The expected natural frequency $|\Omega_{\mathrm{p}}^{\mathrm{theory}}|$ (16) is the dotted vertical line. Inset: Comparison of the measured natural particle frequency with the theory. A dagger (†) indicates that the particle considered belongs to a particle array. An asterisk (∗) indicates that the particle considered is trapped in a bundle of 4 vortices.

conditions between a sphere and a vortex filament [26], which will include restoring forces maintaining the particle trapped. Accounting for such phenomena might lead to a more accurate prediction of the precession frequency. However, the GP system naturally contains all these effects. Therefore, given the agreement between the prediction (16) and GP numerical simulations, we conclude that the modification of the particle natural frequency Ω_{p} due to the coupling at the particle-vortex boundary is a negligible effect. The simple formula (16) can be thus safely used as a first estimate in current experiments.

B. Dispersion relation of a massive quantum vortex

As already mentioned above, in order to study the dynamics of an array of particles and their interaction with vortex waves in a setting like Figs. 2(b) or 2(d), it is instructive to first analyze the case of a massive quantum vortex, as the one in Fig. 2(c). Our considerations are necessary to give a picture of the role of inertia in the propagation of vortex wave excitations. They are not meant to model a real wire, for which some results are well known in literature [39,40] and which has been used to measure the quantized circulation in superfluid helium [41,42]. We consider a wire of length L_{w}, radius a_{w}, and mass M_{w}, filling a superfluid vortex. The effective mass is $M_{\mathrm{w}}^{\mathrm{eff}} = M_{\mathrm{w}} + M_{\mathrm{w}}^0$ and the displaced mass is now $M_{\mathrm{w}}^0 = \rho L_{\mathrm{w}}\pi a_{\mathrm{w}}^2$. Since such wire possesses a circulation, each mass element is driven by the Magnus force as in Eq. (14), but with a different prefactor [35]

$$\Omega_{\mathrm{w}} = \frac{\rho\Gamma L_{\mathrm{w}}}{M_{\mathrm{w}}^{\mathrm{eff}}}, \qquad (17)$$

which arises because of the geometrical difference between a spherical particle and a cylinder. We allow the wire to deform, which means that the complex variable q is now a function of the z component too. Such physical system is analogous to a massive quantum vortex with a finite size core, which is already well known in literature [39,40], and it has

been used to measure the quantized circulation in superfluid helium [41,42]. If the curvature radius is much greater than the wire radius and the healing length, the flow velocity v can be approximated by the self-induced velocity of the vortex filament on itself. In the LIA approximation, the self-induced velocity is simply given by v_{si} in Eq. (8). The dynamics of the wire is therefore driven by the equation

$$\ddot{q}(z,t) = i\Omega_w \left[\dot{q}(z,t) - i\frac{\Gamma}{4\pi}\Lambda\frac{\partial^2}{\partial z^2}q(z,t) \right]. \quad (18)$$

In this simplified model, we are neglecting modes propagating along the wire due to elastic tension and the wave number dependence of the added mass. This choice is done because we want to focus on the inertial effects that will be relevant in the case of a particle array, developed in the following section. Equation (18) allows as a solution linear circularly polarized waves in the form $q(z,t) = q_0 e^{i(\Omega_M^\pm t - kz)}$, where the frequency is given by

$$\Omega_M^\pm(k) = \frac{\Omega_w}{2} \pm \frac{1}{2}\sqrt{\Omega_w^2 + \frac{\Omega_w \Gamma \Lambda}{\pi}k^2}. \quad (19)$$

More generally, one can consider a phenomenological extrapolation based on a more realistic model for the self-induced velocity of the vortex in Eq. (18), so that the dispersion relation of waves propagating along the wire is generalized as

$$\Omega_M^\pm(k) = \frac{1}{2}\left[\Omega_w \pm \sqrt{\Omega_w^2 - 4\Omega_w\Omega_v(k)}\right], \quad (20)$$

where $\Omega_v(k)$ is the *bare* vortex wave frequency and depends on the model chosen for the self-induced velocity. We will refer to (20) as the "massive vortex wave" dispersion relation. In the LIA approximation we have $\Omega_v(k) = \Omega_{LIA}(k)$ (9) and we recover Eq. (19), but a more accurate result is expected if the wave propagation is instead described by $\Omega_{KW}(k)$ or by the measured dispersion relation $\Omega_v^{fit}(k)$ (13). Note that the zero mode of the branch Ω_M^+ coincides with Ω_w and does not vanish even if $M_w = 0$ because of the added mass M_p^0. This is related to the fact that the wire possesses an effective inertia because during its motion it has to displace some fluid [39,43]. In the limit $k\xi \ll 1$, the result (20) can be obtained from the one derived in Ref. [40] using fluid dynamic equations to study ions in superfluid helium.

We build numerically a massive vortex placing a large number of small overlapping particles along a vortex filament. We set the repulsion between particles at a radius $r_0 = 2L_w/(N_p a_p)$ (see Appendix A), so that they are kept at constant distance $r_0/2$. Such system mimics a continuum of matter with total mass given by the sum of all particle masses $M_w = N_p M_p = N_p M_p^0 \mathcal{M}$. We have checked that the repulsion among particles leads to matter sound waves with frequencies that are subleading with respect to other terms present in Eq. (18). We initially excite the system with small-amplitude Kelvin waves and we let it evolve under GP-P dynamics. Figure 2(c) shows a typical snapshot of the system but in the case of a larger initial perturbation (in order to enhance visibility). We then use the particle positions to construct the spatiotemporal spectrum $S_q(k,\omega) \sim |\hat{q}(k,\omega)|^2$, with $\hat{q}(k,\omega)$ the time and space Fourier transform of $q(z,t)$ (see Appendix B for further details). Density plots of $S_q(k,\omega)$ are displayed
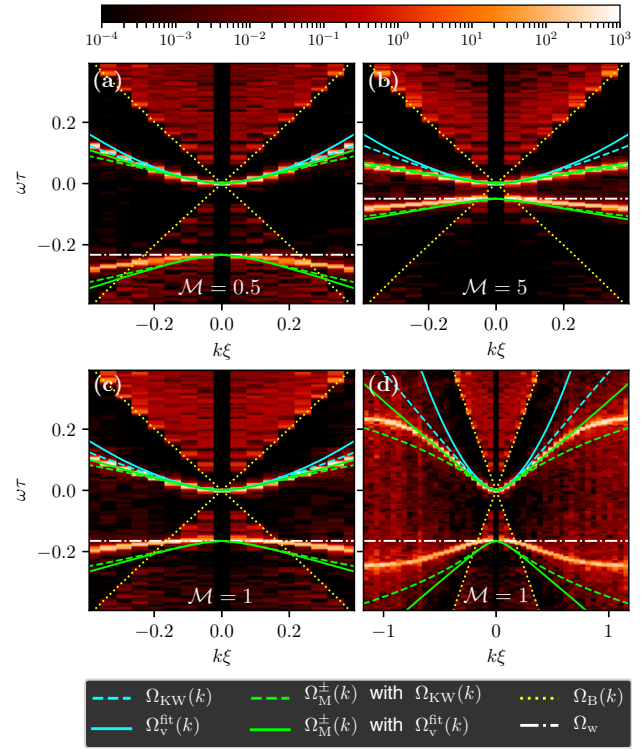

FIG. 4. Spatiotemporal spectra of massive vortices for different masses. The vortex length is $L_w = 128\xi$ and there are $N_p = 50$ particles of radius $a_p = 2.7\xi$, with repulsion radius $r_0 = 2L_w/(N_p a_p)$. Dotted yellow line is the Bogoliubov dispersion relation $\Omega_B(k)$ (4). Dashed cyan line is low-k KW dispersion relation $\Omega_{KW}(k)$ (10). Solid cyan line is full fitted vortex wave dispersion relation $\Omega_v^{fit}(k)$ (13). Dash-dotted green lines are massive vortex wave dispersion relation $\Omega_M(k)$ (20) computed using low-k KW dispersion relation. Solid green lines are massive vortex wave dispersion relation computed using full fitted vortex wave dispersion relation. Dotted horizontal white line is the natural frequency Ω_w (17). The other parameters of the simulations are $L_\perp = L_\parallel = 128\xi$ and $N_\perp = N_\parallel = 256$. (a) $\mathcal{M} = 0.5$; (b) $\mathcal{M} = 5$; (c) $\mathcal{M} = 1$; (d) same as (c), but displaying the full range.

in Fig. 4 for different values of the particle mass. For a better presentation, we have chosen $\Gamma < 0$ so that vortex wave frequencies lie in the upper plane. This convention will be adopted also in the following section.

We first observe that the massive vortex is able to capture the Bogoliubov dispersion relation $\Omega_B(\mathbf{k})$ (4) due to the presence of excitations in the superfluid, as displayed by yellow dotted lines in Fig. 4. The bare Kelvin wave dispersion relation $\Omega_{KW}(k)$ and the measured bare vortex frequency spectrum $\Omega_v^{fit}(k)$ are displayed by the cyan dashed and solid lines, respectively. They coincide in the limit $k\xi \ll 1$, as expected. The corresponding massive vortex wave predictions (20) are also displayed in green dashed and solid lines. For low masses, the effect of inertia is negligible, so that massive vortex wave (20) and bare vortex wave (13) predictions are similar. As the mass increases, the wire inertia becomes important and the measured frequencies of the wire excitations decrease at small scales, in good agreement with the massive vortex wave

prediction. The model (20) is not expected to give a good explanation for the negative branches, as it neglects the details of the internal structure of the wire, as well as the dependence on the wave number of the effective mass. Such features, which are out of the scope of the present work, are taken into account in Ref. [40] in the case of an elastic and massive hollow vortex (with no notion of the free-particle behavior of vortex excitations at small scales). The predicted natural frequency of the wire $\Omega_W = |\Omega_M^+(0)|$ is clearly reproduced by the numerical measurements and it does not become infinite when $\mathcal{M} \to 0$ because of the added mass effect. For completeness, Fig. 4(d) displays the dispersion relation over the full accessible range of wave numbers. The dispersion curves are bent due to the discreteness of the wire at scales of order $k\xi \sim 0.8$. Note that the KW dispersion relation (dashed cyan line) seems to be very similar to the fitted one (solid cyan line). However, the difference between the two is apparent in Fig. 4(d). Moreover, it is clear how the massive vortex wave dispersion relation computed using $\Omega_v(k) = \Omega_v^{fit}(k)$ (solid green line) fits the data for all the masses analyzed. In particular, in Fig. 4(d), it is shown that it can predict the dispersion relation of a massive vortex wire with relative mass $\mathcal{M} = 1$ up to a wave number $k\xi \sim 0.7$. This is not the case for the massive vortex wave dispersion relation computed using $\Omega_v(k) = \Omega_{KW}(k)$ (dashed green line). We thus conclude that the main effect of the inertia of the particles constituting the wire is to modify the frequency spectrum of vortex waves, as follows from simple hydrodynamical considerations.

C. Frequency gaps and Brillouin zones for an array of trapped particles

Now we shall address the main question of this work. How well do particles, seating in a quantum vortex, track vortex waves? In order to study this problem, we consider an array of particles as the one displayed in Fig. 2(b). Particles are placed in a quantum vortex, initially separated by a distance d. The system is excited by superimposing small-amplitude KWs. We can build a discrete spatiotemporal spectrum $S_q(k, \omega)$ of the measured vortex excitations by using the displacement of particles in the plane perpendicular to the vortex. In Figs. 5(a) and 5(c) we display the particle spatiotemporal spectra for an array of $N_p = 20$ particles of size $a_p = 2.7\xi$ with masses $\mathcal{M} = 5$ and $\mathcal{M} = 1$, respectively, placed at a distance $d = 12.8\xi$. The Bogoliubov waves are still weakly sampled by the particles, as displayed by yellow dotted lines. Surprisingly, a higher-frequency branch appears. Such pattern is similar to those observed in the typical energy spectra of crystals [24]. Particles are actually able to sample the vortex excitations only in the first Brillouin zone; namely they cannot see wave numbers larger than π/d. However, spatiotemporal spectra can be also computed by directly using the superfluid wave function. Performing the time and space Fourier transform of ψ we define the spectrum $S_\psi(k, \omega) = |\hat{\psi}(k_x = 0, k_y = 0, k, \omega)|^2$. The corresponding spectra S_ψ are shown in Figs. 5(b) and 5(d) where wave numbers go now up to $kd \sim 10$, giving access to all the small scales solved by the numerical simulations. Several Brillouin zones are clearly appreciated, as well as the opening of band gaps in the dispersion relation. At the same time, Bogoliubov modes
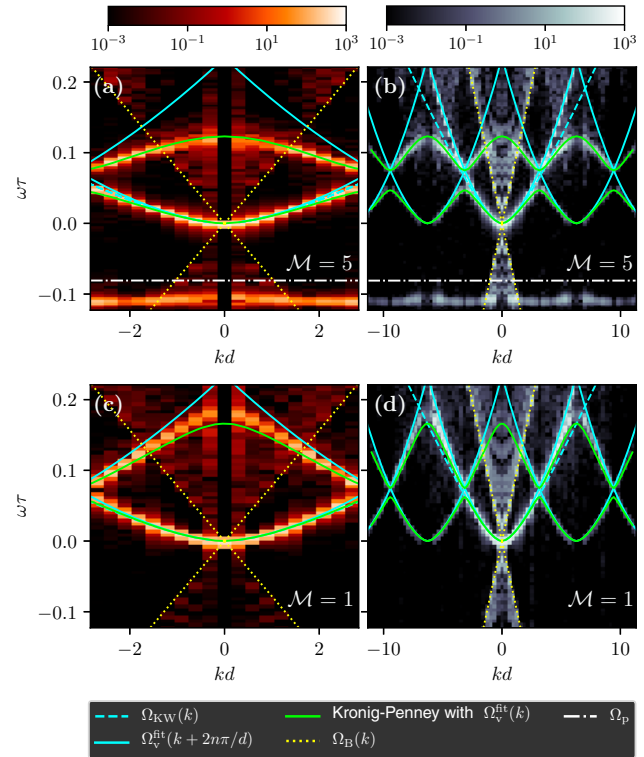

FIG. 5. Spatiotemporal spectra computed from the particle positions (left) and from the wave function ψ (right) for an array of particles with mass $\mathcal{M} = 5$ (top) and $\mathcal{M} = 1$ (bottom). Solid green lines are the contour plot of the dispersion relation (22) computed with Ω_v^{fit} (13). Dashed cyan line is low-k KW dispersion relation $\Omega_{KW}(k)$ (10). Solid cyan line is the fitted vortex wave dispersion relation (13). Dotted yellow line is Bogoliubov dispersion relation $\Omega_B(k)$ (4). Dash-dotted horizontal white line is the predicted natural frequency Ω_p. The other parameters of the particles are $d = 12.8\xi$, $a_p = 2.7\xi$, $r_0 = 4a_p$. The size of the computational box is $L_\perp = L_\parallel = 256\xi$, with $N_\perp = N_\parallel = 512$ collocation points.

can be observed and also bare vortex waves. The latter belong to the image vortices in the computational domain, where no particles have been attached.

The presence of particles clearly affects the propagation of waves along the vortex line inducing high-frequency excitations not only for small but also for large wavelengths. The intuitive idea is that when a vortex wave reaches a particle, it is partially reflected or transmitted, depending on the mass and the size of the particles, and eventually on its own frequency. This reminds us of the standard quantum-mechanical problem of an electron described by the (linear) Schrödinger equation hitting a potential barrier. Furthermore, if particles are set at almost equal distances, the system is similar to an electron propagating in a periodic array of potential barriers, as in the Kronig-Penney model [23,24]. In order to apply quantitatively this intuition and explain the opening of band gaps in the dispersion relation of vortex wave excitations, we start by considering an artificial system made of segments of bare quantum vortex of length $(d - L_w)$, alternated with massive vortex wires of length L_w. A sketch of the problem is given in Fig. 6(a). To recover the excitations in the case of the
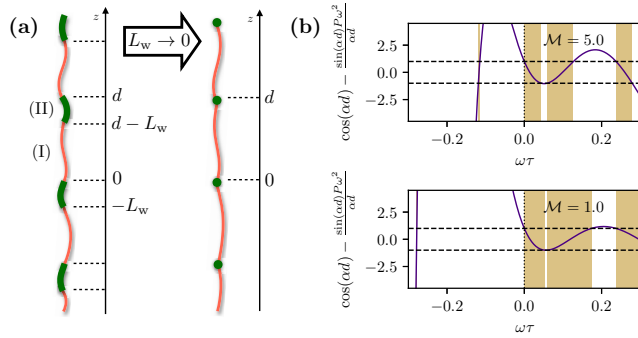
FIG. 6. (a) Sketch of the lattice vortex wave model. Bare vortex segments are in red and massive vortex segments are in green. (b) Right-hand side of Eq. (22) computed with LIA as a function of $\omega\tau$ for an array of particles with radius $a_p = 2.7\xi$ and mass $\mathcal{M} = 5$. Bands of allowed frequencies are displayed in gold. (c) The same as (b) but for particles with mass $\mathcal{M} = 1$.

particle array, we will later take the limit $L_w \to 0$, keeping the mass of the wires equal to the effective mass of the particles. The resulting effective theory must be intended as an asymptotic limit of the actual system for long waves $ka_p \ll 1$, in which the nonlinear interactions of the vortex excitations are neglected and the complexity of the vortex-particle boundary is ignored. The accuracy of such model has to be checked by comparing its predictions with the results of the GP simulations. The motion of the bare vortices is driven by the self-induced velocity that leads to the propagation of vortex waves, while the wires are driven by the Magnus force. For the sake of simplicity, we first consider the LIA approximations (8) and (18), respectively. The dynamics is thus given in each zone by

$$\dot{q}(z,t) = i\frac{\Gamma}{4\pi}\Lambda\frac{\partial^2}{\partial z^2}q(z,t) \quad (I),$$

$$\ddot{q}(z,t) = i\Omega_w\left[\dot{q}(z,t) - i\frac{\Gamma}{4\pi}\Lambda\frac{\partial^2}{\partial z^2}q(z,t)\right] \quad (II), \quad (21)$$

where (I) is the region $0 < z < d - L_w$ and (II) is the region $d - L_w < z < d$. Note that the use of LIA in the system (21) is rather qualitative, given the high level of complexity of the problem. In particular it ignores the nonlocal dynamics of the vortex, does not reproduce the good dispersion relation of vortex excitations, and may not be able to take into account the exact boundary condition between the particles and the vortex. However, it allows us to introduce some general physical concepts and perform a fully analytical treatment of the problem. The effective model will be then generalized in order to take into account a more realistic description of vortex waves and provide quantitative predictions. The dispersion relation can be found borrowing standard techniques from solid state physics, in particular by adapting the solution of the Kronig-Penny model [23,24]. We look for a wave solution $q(z,t) = \Phi(z)e^{i\omega t}$, where the spatial function $\Phi(z)$ can be written in the form $\Phi(z) = e^{ikz}u(z)$ according to the Bloch theorem, where $u(z)$ is a periodic function of period d [44]. The key point is the imposition of continuity and smoothness of the function $\Phi(z)$ as well as periodicity of

$u(z)$ and its derivative. These constraints lead to an implicit equation relating the frequency of the excitations ω, the wave number k, and all the physical parameters. The full derivation is explained in Appendix C. The last step in order to describe the excitations of the particle array is to take the limit $L_w \to 0$ at constant M_{eff}. The dispersion relation is finally determined by the implicit equation

$$\cos(kd) = \cos(\alpha_\omega d) - \frac{\sin(\alpha_\omega d)}{\alpha_\omega d}P\omega^2, \qquad (22)$$

where $P = 3\pi da_p/\Lambda\Gamma\Omega_p$ and α_ω satisfies the equation $\Omega_{LIA}(\alpha_\omega) = \omega$:

$$\alpha_\omega = \sqrt{-\frac{4\pi\omega}{\Gamma\Lambda}}. \qquad (23)$$

In Figs. 6(b) and 6(c) the right-hand side of Eq. (22) is plotted as a function of $\omega\tau$ for heavy and light small particles (that is, low and high Ω_p). The curve must be equal to $\cos(kd)$ and this selects the only allowed frequencies (displayed in gold). It is exactly the same mechanism that leads to the formation of energy bands in crystals [24].

The previous calculations can be directly generalized for more realistic wave propagators (see Appendix C). In particular, if we consider a dispersion relation $\Omega_v(k)$ for the vortex excitations, the only change in the result (22) is the functional dependence of α_ω (23), which must satisfy $\Omega_v(\alpha_\omega) = \omega$. Furthermore, the constant P becomes independent of any adjustable parameter: $P = 3\pi da_p/\Gamma\Omega_p$. We consider the dispersion relation $\Omega_v^{fit}(\omega)$ (13) that matches large- and small-scale excitations and we invert it numerically to find α_ω.

In Fig. 5 the contour plot of the theoretical prediction (22) obtained this way is compared with the numerical data (solid green lines), exhibiting a remarkable agreement with the observed excited frequencies. From Fig. 6(b), we remark that the only allowed negative frequencies lie in a thin band around Ω_p. This is also in qualitative agreement with the data. Note that the bare Kelvin wave dispersion relation (10) (dashed cyan line) and the fitted bare vortex wave dispersion relation (13) (solid cyan line) are very similar in Fig. 5. The reason is that the smallest scale that can be solved by the considered array of particles is $k\xi = 0.25$ (i.e., $kd = \pi$), and for wave numbers smaller than this value $\Omega_v^{fit}(k)$ tends to $\Omega_{KW}(k)$ by construction.

In order to make a closer connection with experiments, we now describe an array of larger particles of size $a_p = 13.1\xi$ and relative mass $\mathcal{M} = 1$ set in a single quantum vortex and in a bundle composed of four vortices. The corresponding spatiotemporal spectra $S_p(k,\omega)$ are displayed in Fig. 7. In principle such setting should not be well described by our theoretical approach. However, the excitation curves can be reproduced by using the model before the limit $L_w \to 0$ (C6) and phenomenologically replacing $L_w = 2a_p$ while keeping $\Omega_w^{eff} = \Omega_p^{eff}$. The agreement is remarkably good, considering the rough modeling that has been done. The case of a bundle in Fig. 7(b) is even more striking. At large scales, we could expect that such system is analogous to a hollow vortex with four quanta of circulation and some effective core size. We have estimated the effective core size by measuring the mean
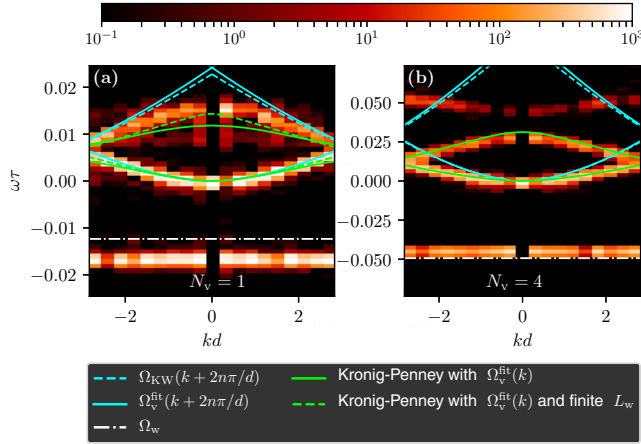
FIG. 7. Spatiotemporal spectra computed from the particle positions for an array of large particles of radius $a_p = 13.1\xi$ and mass $\mathcal{M} = 1$ placed at a distance $d = 51.2\xi$. The repulsion radius is $r_0 = 2a_p$. Solid green lines are the contour plot of the dispersion relation (22) computed with Ω_v^{fit}. Dashed cyan line is low-k KW dispersion relation $\Omega_{KW}(k)$. Solid cyan line is the fitted vortex wave dispersion relation. Dash-dotted horizontal white line is the predicted natural frequency Ω_p. (a) Particles set in a single vortex. Dashed greed line is the dispersion relation (C6) before the limit computed using a finite $L_w = 2a_p$. For the LIA calculations $\Lambda = 2.6$. (b) Particles set in a bundle of 4 vortices. The dispersion relation (22) has been computed using Ω_v^{fit} with an effective core size of $a_0 = 12\xi$ (see text). The other parameters of the simulations are $L_\perp = 1024\xi$, $L_\parallel = 256\xi$, and $N_\perp = 1024$, $N_\parallel = 256$.

distance between the vortices. The theoretical prediction (22) combined with this phenomenological approach still impressively matches the numerical data.

IV. DISCUSSION

In this work we have presented a theoretical and numerical study of the interaction between quantum vortices and a number of particles trapped in them. We have first pointed out that a trapped particle oscillates with a well-defined natural frequency that depends on its mass and the circulation of the flow surrounding it. Because of the typical values of particle parameters used in current superfluid helium experiments, such frequency should be measurable. This measurement can thus provide an independent way of estimating the number of vortices constituting the bundles at which particles are attached.

Based on the experimental evidence that particles spread along quantum vortices keeping a relatively constant interparticle distance, we have studied how the particles modify the vortex excitations. The most exciting result of this work is the strong analogy with solid state physics. Here, particles play the role of ions in the periodic structure of a crystal and vortex excitations that of the electrons. When an electron propagates, it feels the ions as the presence of a periodic array of potential barriers. One of the simplest and idealized descriptions of this physical phenomenon is the Kronig-Penney model, where the barriers have a constant height U_0. Similarly, vortex waves propagate and interact with particles and we have shown that a

similar theoretical approach can be used. The main difference is that the constant height of the barriers in the standard Kronig-Penney model induces constant shift of the energy (frequency here). As a consequence, the lowest energy level in a crystal is different from zero (unlike the case of free electrons). Instead, in the vortex case, the interaction potential is due to the Magnus force and depends on the frequency. Comparing the models, we can then establish a mathematical analogy (see Eq. (22) and Refs. [23,24]) by noticing that the effective potential in the case of vortex excitations is given by

$$U_0 \sim \omega^2/\Omega_p \propto \omega^2 M_p^{eff}. \tag{24}$$

The height of the potential is thus proportional to the squared frequency of the incoming wave and to the particle mass. In particular, for very low frequencies the presence of particles does not perturb much the vortices and large-scale Kelvin waves could be tracked by directly measuring the particle dynamics. Moreover, we observe that for particles with a higher natural frequency Ω_p (namely lighter and smaller particles), the value of U_0 and of P in Eq. (22) decrease. As a consequence, the bands of allowed frequencies are broadened. Ideally, in the limiting case of particles with zero mass, the natural frequency is infinite and P and U_0 vanish. Therefore Eq. (22) gets simplified dramatically and becomes $\cos(kd) = \cos(\alpha_\omega d)$. This implies

$$\omega(k) = \Omega_v\left(k + \frac{2n\pi}{d}\right), \quad n \in \mathbb{Z}, \tag{25}$$

which is just the vortex wave dispersion relation, but repeated with period $k_d = 2\pi/d$. In other words, light and small particles can follow the filament without modifying the vortex waves. On the contrary, particle inertia reduces the excited frequencies (in absolute value) of vortex excitations. This fact (actually coming from simple linear physics) should be taken into account when one tries to measure the Kelvin waves experimentally.

In this work we did not take into account the relevance of buoyancy effects for light and heavy particles. We can estimate it by comparing the buoyancy force $F_b = (M_p - M_0)\tilde{g}$, where $\tilde{g} \sim 9.8$ m/s^2 is the gravitational acceleration, with the Magnus force that drives the particles $F_M = \frac{3}{2}\rho\Gamma a_p u$, where u is the typical particle velocity estimated as $u \sim \Omega_p a_p$. It turns out that $F_b/F_M = C(\mathcal{M} - 1)(2\mathcal{M} + 1)$, where $C = \frac{32}{81}\pi^2\frac{\tilde{g}a_p^3}{\Gamma^2}$. This expression strongly depends on the particle size. For instance, given that the quantum of circulation in superfluid helium is $\Gamma \sim 10^{-7}$ m^2/s, we get that $C \sim 4 \times 10^{-3}$ for a particle of size $a_p = 1$ μm and therefore the buoyancy is negligible. However C becomes of order 1 for a particle of size $a_p = 7$ μm. We conclude that small and light particles would be the most suitable for tracking the vortex excitations.

Several questions can be immediately raised. If particles are not actually equally distributed along the vortex but instead they present some randomness, vortex waves will then propagate in a disordered medium. It will be natural then to study the possibility of Anderson localization in such a system [45,46]. Such situation could perhaps appear if the vortex lines are excited by external means, for instance close to the onset of the Donnelly-Glaberson instability [47,48].

The physical system studied in this work is a first idealized picture of what happens in real superfluid helium experiments. The most evident difference is that the size of particles is typically orders of magnitude larger than the vortex core size ($a_p \sim 10^4 \xi$). However, the prediction (22) comes from an asymptotic theory in which $ka_p \ll 1$ and particles can be considered pointlike, independently of the functional form of $\Omega_v(k)$. Therefore, we expect that our result should still apply for wavelengths larger than the particle size. Such long waves are indeed observed in experiments [10]. In particular, the fact that particle inertia does not affect the (low) frequency Kelvin waves should be still valid. A more quantitative prediction for vortices in He II would be always Eq. (22), but with α_ω such that $\omega = \Omega_{He}(\alpha_\omega)$, where $\Omega_{He}(k)$ is the true vortex excitation dispersion relation in superfluid helium. In any case all the main conclusions remain valid, since the analogy with a crystal is independent of $\Omega_v(k)$. Moreover, the behavior at large scales is expected to work quantitatively also for superfluid helium vortices because $\Omega_{He}(ka_0 \to 0) \sim \Omega_{KW}(ka_0)$.

Furthermore, we have used arrays of particles with all identical masses. Instead, in actual experiments there is not a perfect control on the mass and size of particles. In particular, the mass distribution of particles could be polydispersed. In this case, new gaps in the dispersion relation are opened revealing much more complex configurations. A preliminary numerical study confirms this behavior and it will be reported in a future work. In any case, the basic interaction between one particle and vortex waves remains the same regardless of the presence of some disorder. Therefore, large-scale Kelvin waves are not disturbed by the particles. Studying in detail the effects of different species of particles trapped in a vortex can be done systematically in the same spirit of the effective theory developed in the present work, for example adapting tight-binding models [24] to the vortex-particles system. We think that this is a worthy research direction that could establish new and deeper connections with concepts already known in solid state physics, introducing a plethora of novel phenomena in the framework of quantum fluids.

Last but not least, note that the basic equations considered in this work to build up the effective model are based on classical hydrodynamics. Therefore, one could expect that most of the phenomenology remains valid in a classical fluid provided that a mechanism to sustain a vortex exists. Such mechanism could be for instance provided by two corotating propellers at moderate speeds. Since these systems are achievable in much less extreme conditions than in cold superfluid helium and because the manipulation of particle parameters is much simpler, it could be possible to build analogs of solid state physics phenomena by using classical fluid experiments.

ACKNOWLEDGMENTS

APPENDIX A: NUMERICAL SCHEME AND PARAMETERS

Equations (2) and (3) are solved with a standard pseudospectral code and a fourth-order Runge-Kutta scheme for the time stepping in a 3D periodic domain of dimensions $L_\perp \times L_\perp \times L_\parallel$ with $N_\perp \times N_\perp \times N_\parallel$ collocation points. We set $c = \rho_\infty = 1$.

The ground states with particles and straight vortices are prepared separately by performing imaginary-time evolution of the GP equation. In order to have an initial state with zero global circulation (and therefore ensure periodic boundary conditions) we need to add in the computational box three image vortices with alternating charges. The state with bundles of $N_v = 4$ vortices [Fig. 2(d)] is prepared imposing a phase jump of $2N_v\pi$ around a vortex (including its images). Then, imaginary-time evolution of the GP equation is performed for a time $\sim 150\tau$, so that the vortex filaments separate and the bundles form. KWs are generated from the state with straight vortices slightly shifting each xy plane of the computational domain. Then the states with KWs and particles are multiplied to obtain the desired initial condition. Just one vortex filament is loaded with particles, while the three other images remain bare. The initial condition is evolved for a short time ($\sim 40\tau$) using GP without the particle dynamics in order to adapt the system.

The particle potential is a smoothed hat function $V_p(r) = \frac{V_0}{2}(1 - \tanh[\frac{r^2 - \eta^2}{4\Delta l^2}])$ and the mass displaced by the particle is measured as $M_w^0 = \rho_\infty L_\perp L_\parallel^2 (1 - \int |\psi_p|^2 \, d\mathbf{x} / \int |\psi_\infty|^2 \, d\mathbf{x})$, where ψ_p is the steady state with just one particle. Since the particle boundaries are not sharp, we measure the particle radius as $a_p = (3M_p^0/4\pi\rho_\infty)^{\frac{1}{3}}$ for given values of the numerical parameters η and Δl. For all the particles $V_0 = 20$. The parameters used are the following: for $a_p = 2.7\xi$, $\eta = \xi$ and $\Delta l = 0.75\xi$; for $a_p = 7.6\xi$, $\eta = 2\xi$ and $\Delta l = 2.5\xi$; and for $a_p = 13.1\xi$, $\eta = 10\xi$ and $\Delta l = 2.8\xi$.

The parameter r_0 of the potential $V_{rep}^{ij} = \varepsilon(r_0/|\mathbf{q}_i - \mathbf{q}_j|^{12})$ is the radius of the repulsion between particles. The parameter ε is fixed numerically in order to impose an exact balance between the repulsive force and the GP force $-\int V_p(|\mathbf{x} - \mathbf{q}_i|)\nabla|\psi|^2 \, d\mathbf{x}$ in the ground state with two particles placed at distance $2a_p$ when $r_0 = 2a_p$. The parameters used for the repulsion are the following: for the wires in Fig. 4, $r_0 = 2L_w/(N_p a_p)$ and $\varepsilon = 4.4 \times 10^{-5}$; for the array of particles in Fig. 5, $r_0 = 4a_p$ and $\varepsilon = 4.4 \times 10^{-5}$; and for the array of particles in Fig. 7, $r_0 = 2a_p$ and $\varepsilon = 1.7 \times 10^{-3}$.

APPENDIX B: SPATIOTEMPORAL SPECTRA

We use the particle positions to define the spatiotemporal spectra of vortex excitations by computing

$$S_q(k, \omega) = C_q \left| \int \sum_{j=1}^{N_p} q(z_j, t) e^{-i(kz_j + \omega t)} dt \right|^2, \quad \text{(B1)}$$

where z_j is the z component of the particle j. Similarly, the spatiotemporal spectrum of the superfluid wave function is defined as

$$S_\psi(k, \omega) = C_\psi \left| \int \psi(x, y, z, t) e^{-i(kz + \omega t)} \, dx \, dy \, dz \, dt \right|^2. \quad \text{(B2)}$$

Note that in Eq. (B2) an average of ψ in the x and y directions is implicit. The normalization constants C_q and C_ψ are set such that the full (k, ω) integrals of the spatiotemporal spectra are 1. In order to enhance the small-scale excitations, in the density plots shown in the present work, both the spectra (B1) and (B2) are further normalized with the frequency-averaged spectra, respectively $\int S_q(k, \omega) \, d\omega$ and $\int S_\psi(k, \omega) \, d\omega$. All the color maps shown in the present work are in log scale.

APPENDIX C: DERIVATION OF THE KRONIG-PENNEY DISPERSION RELATION FOR VORTEX WAVES

We look for a linear wave solution $q(z, t) = \Phi(z) e^{i\omega t}$ of the system (21) and in particular we want to know which frequencies ω are excited. The function $\Phi(z)$ must satisfy the system

$$\frac{\partial^2}{\partial z^2} \Phi(z) + \alpha_\omega^2 \Phi(z) = 0 \quad \text{(I)},$$

$$\frac{\partial^2}{\partial z^2} \Phi(z) + \beta_\omega^2 \Phi(z) = 0 \quad \text{(II)}, \quad \text{(C1)}$$

where α_ω and β_ω are such that

$$\Omega_{\text{LIA}}(\alpha_\omega) = \omega, \quad \Omega_{\text{LIA}}(\beta_\omega) = \omega - \frac{\omega^2}{\Omega_{\text{w}}}, \quad \text{(C2)}$$

which means

$$\alpha_\omega = \sqrt{-\frac{4\pi \omega}{\Gamma \Lambda}}, \quad \beta_\omega = \sqrt{\frac{4\pi}{\Gamma \Lambda} \left(\frac{\omega^2}{\Omega_{\text{w}}} - \omega \right)}. \quad \text{(C3)}$$

Since the system (C1) is a linear and homogeneous differential equation with periodic coefficients of period d, it admits a solution in the form $\Phi(z) = e^{ikz} u(z)$, where $u(z)$ is a periodic function of period d. The solutions of (C1) in the two regions (I) and (II) are

$$\Phi_{\text{I}}(z) = e^{ikz} u_{\text{I}}(z) = e^{ikz} [A e^{i(\alpha_\omega - k)z} + B e^{-i(\alpha_\omega + k)z}],$$

$$\Phi_{\text{II}}(z) = e^{ikz} u_{\text{II}}(z) = e^{ikz} [C e^{i(\beta_\omega - k)z} + D e^{-i(\beta_\omega + k)z}]. \quad \text{(C4)}$$

The coefficients A, B, C, D are fixed by imposing continuity and smoothness of the function $\Phi(z)$ and periodicity of $u(z)$ and its derivative:

$$\Phi_{\text{I}}(0) = \Phi_{\text{II}}(0),$$

$$\Phi'_{\text{I}}(0) = \Phi'_{\text{II}}(0),$$

$$u_{\text{I}}(d - L_{\text{w}}) = u_{\text{II}}(-L_{\text{w}}),$$

$$u'_{\text{I}}(d - L_{\text{w}}) = u'_{\text{II}}(-L_{\text{w}}). \quad \text{(C5)}$$

The system (C5) is a homogeneous linear system for the variables A, B, C, D. It admits nontrivial solutions only if the determinant of the coefficients is equal to zero. This implies

the following condition:

$$\cos(kd) = \cos(\beta_\omega L_{\text{w}}) \cos[\alpha_\omega(d - L_{\text{w}})]$$
$$- \frac{\alpha_\omega^2 + \beta_\omega^2}{2\alpha_\omega \beta_\omega} \sin(\beta_\omega L_{\text{w}}) \sin[\alpha_\omega(d - L_{\text{w}})], \quad \text{(C6)}$$

which determines implicitly the dispersion relation $\omega(k)$. Such expression is structurally identical to the standard Kronig-Penney condition but the functions α_ω and β_ω are different. The limit $L_{\text{w}} \to 0$ is applied to Eq. (C6), substituting at the same time the mass of the massive vortex segment $M_{\text{w}}^{\text{eff}}$ with the mass of the particle $M_{\text{p}}^{\text{eff}}$. In this way the system becomes a vortex filament loaded with massive point particles (see Fig. 6). The limit implies $\beta_\omega \to \infty$, $\beta_\omega L_{\text{w}} \to 0$, $\sin(\beta_\omega L_{\text{w}}) \sim \beta_\omega L_{\text{w}}$, $\alpha_\omega \ll \beta_\omega$, and $\beta_\omega^2 L_{\text{w}} \sim 6\pi a_{\text{p}} \omega^2 / \Lambda \Gamma \Omega_{\text{p}}$, so that Eq. (C6) becomes Eq. (22).

The previous result can be extended to the case of more realistic vortex waves with some caveat. We can formally rewrite the model (21) as

$$\dot{q}(z, t) = i \hat{\mathcal{L}}_{\text{v}}[q(z, t)] \quad \text{(I)},$$
$$\ddot{q}(z, t) = i \Omega_{\text{w}} \{ \dot{q}(z, t) - i \hat{\mathcal{L}}_{\text{v}}[q(z, t)] \} \quad \text{(II)}, \quad \text{(C7)}$$

where $\hat{\mathcal{L}}_{\text{v}}$ is the linear nonlocal differential operator that generates the vortex wave dispersion relation $\Omega_{\text{v}}(k)$. Namely, calling $s(z, t) = \sum_k s_k(t) e^{ikz}$ the wave operator simply reads

$$\hat{\mathcal{L}}_{\text{v}}[s(z, t)] = \sum_k \Omega_{\text{v}}(k) s_k(t) e^{ikz}. \quad \text{(C8)}$$

The system (C1) thus becomes

$$\hat{\mathcal{L}}_{\text{V}}[\Phi(z)] - \omega \Phi(z) = 0 \quad \text{(I)},$$

$$\hat{\mathcal{L}}_{\text{V}}[\Phi(z)] - \left(\omega - \frac{\omega^2}{\Omega_{\text{v}}} \right) \Phi(z) = 0 \quad \text{(II)}. \quad \text{(C9)}$$

The functions (C4) are still a solution of (C9), but now α_ω and β_ω are defined as

$$\Omega_{\text{v}}(\alpha_\omega) = \omega, \quad \Omega_{\text{v}}(\beta_\omega) = \left(\omega - \frac{\omega^2}{\Omega_{\text{w}}} \right). \quad \text{(C10)}$$

In general such equations cannot be inverted explicitly, but α_ω and β_ω can be found numerically. In particular the inversion is intended with respect to $\Omega_{\text{v}}(k > 0)$. The functions α_ω and β_ω are well defined (at least for $\omega/\Gamma > 0$) because any model for the self-induced velocity of a vortex generates a dispersion relation $\Omega_{\text{v}}(k)$ that is monotonically increasing for positive k. For evaluating the limit $L_{\text{w}} \to 0$, $M_{\text{w}}^{\text{eff}} \to M_{\text{p}}^{\text{eff}}$, we note that $\lim_{L_{\text{w}} \to 0} \Omega_{\text{v}}(\beta_\omega) = \infty$. Therefore, we can explicitly use the asymptotics of $\Omega_{\text{v}}(k)$ for large k, which is just the free particle dispersion relation (12) and can be inverted explicitly:

$$\beta_\omega \xrightarrow[L_{\text{w}} \to 0]{} \sqrt{\frac{4\pi \omega^2}{\Gamma \Omega_{\text{w}}}}, \quad \text{(C11)}$$

so that $\beta_\omega^2 L_{\text{w}} \sim 6\pi a_{\text{p}} / \Gamma \Omega_{\text{p}}$. In this way we recover Eq. (22), with α_ω defined as in (C10) and the amplification factor P is now independent of any free parameter:

$$P = \frac{3\pi d a_{\text{p}}}{\Gamma \Omega_{\text{p}}}. \quad \text{(C12)}$$

[1] F. London, Nature (London) **141**, 643 (1938).

[2] L. Landau, Phys. Rev. **60**, 356 (1941).

[3] L. Tisza, Nature (London) **141**, 913 (1938).

[4] R. Feynman, Prog. Low Temp. Phys. **1**, 17 (1955).

[5] W. Vinen and J. Niemela, J. Low Temp. Phys. **128**, 167 (2002).

[6] M. S. Paoletti and D. P. Lathrop, Annu. Rev. Condens. Matter Phys. **2**, 213 (2011).

[7] C. F. Barenghi, L. Skrbek, and K. R. Sreenivasan, Proc. Natl. Acad. Sci. USA **111**, 4647 (2014).

[8] R. J. Donnelly, *Quantized Vortices in Helium II*, Vol. 2 (Cambridge University Press, Cambridge, 1991).

[9] G. P. Bewley, D. P. Lathrop, and K. R. Sreenivasan, Nature (London) **441**, 588 (2006).

[10] E. Fonda, D. P. Meichle, N. T. Ouellette, S. Hormoz, and D. P. Lathrop, Proc. Natl. Acad. Sci. USA **111**, 4707 (2014).

[11] M. S. Paoletti, M. E. Fisher, K. R. Sreenivasan, and D. P. Lathrop, Phys. Rev. Lett. **101**, 154501 (2008).

[12] M. La Mantia and L. Skrbek, Phys. Rev. B **90**, 014519 (2014).

[13] D. R. Poole, C. F. Barenghi, Y. A. Sergeev, and W. F. Vinen, Phys. Rev. B **71**, 064514 (2005).

[14] Y. A. Sergeev and C. F. Barenghi, J. Low Temp. Phys. **157**, 429 (2009).

[15] C. F. Barenghi, D. Kivotides, and Y. A. Sergeev, J. Low Temp. Phys. **148**, 293 (2007).

[16] G. E. Astrakharchik and L. P. Pitaevskii, Phys. Rev. A **70**, 013608 (2004).

[17] S. Rica and D. C. Roberts, Phys. Rev. A **80**, 013609 (2009).

[18] A. Villois and H. Salman, Phys. Rev. B **97**, 094507 (2018).

[19] T. Winiecki and C. S. Adams, Europhys. Lett. **52**, 257 (2000).

[20] V. Shukla, M. Brachet, and R. Pandit, Phys. Rev. A **94**, 041602(R) (2016).

[21] U. Giuriato, G. Krstulovic, and D. Proment, J. Phys. A: Math. Theor. **52**, 305501 (2019).

[22] U. Giuriato and G. Krstulovic, Sci. Rep. **9**, 4839 (2019).

[23] R. D. L. Kronig, W. G. Penney, and R. H. Fowler, Proc. R. Soc. London, Ser. A **130**, 499 (1931).

[24] C. Kittel, P. McEuen, and P. McEuen, *Introduction to Solid State Physics*, Vol. 8 (Wiley, New York, 1976).

[25] W. F. Vinen, Phys. Rev. B **64**, 134520 (2001).

[26] K. W. Schwarz, Phys. Rev. B **38**, 2398 (1988).

[27] M. D. Bustamante and S. Nazarenko, Phys. Rev. E **92**, 053019 (2015).

[28] R. J. Arms and F. R. Hama, Phys. Fluids **8**, 553 (1965).

[29] S. W. Thomson, The London, Edinburgh, and Dublin Philosophical Magazine and Journal of Science **10**, 155 (1880).

[30] P. H. Roberts, Proc. R. Soc. London, Ser. A **459**, 597 (2003).

[31] E. B. Gordon, M. E. Stepanov, M. I. Kulish, A. V. Karabulin, V. I. Matyushenko, and I. I. Khodos, Laser Phys. Lett. **16**, 026002 (2018).

[32] R. J. Zieve, Y. Mukharsky, J. D. Close, J. C. Davis, and R. E. Packard, Phys. Rev. Lett. **68**, 1327 (1992).

[33] L. Hough, L. A. K. Donev, and R. J. Zieve, Phys. Rev. B **65**, 024511 (2001).

[34] See Supplemental Material at http://link.aps.org/supplemental/10.1103/PhysRevResearch.2.023149 for movies of the simulations.

[35] G. K. Batchelor, *An Introduction to Fluid Dynamics*, Cambridge Mathematical Library (Cambridge University Press, Cambridge, 2000).

[36] L. Kiknadze and Y. Mamaladze, arXiv:cond-mat/0604436.

[37] E. B. Sonin, *Dynamics of Quantised Vortices in Superfluids* (Cambridge University Press, Cambridge, 2016).

[38] M. Gibert (private communication, 2019).

[39] H. E. Hall, W. F. Vinen, and D. Shoenberg, Proc. R. Soc. Lond. A **238**, 215 (1997).

[40] A. L. Fetter and K. Harvey, Phys. Rev. A **4**, 2305 (1971).

[41] P. W. Karn, D. R. Starks, and W. Zimmermann, Phys. Rev. B **21**, 1797 (1980).

[42] J. C. Davis, J. D. Close, R. Zieve, and R. E. Packard, Phys. Rev. Lett. **66**, 329 (1991).

[43] T. Simula, Phys. Rev. A **97**, 023609 (2018).

[44] G. Floquet, Annales scientifiques de l'école Normale Supérieure **12**, 47 (1883).

[45] P. W. Anderson, Phys. Rev. **109**, 1492 (1958).

[46] B. Kramer and A. MacKinnon, Rep. Prog. Phys. **56**, 1469 (1993).

[47] D. K. Cheng, M. W. Cromar, and R. J. Donnelly, Phys. Rev. Lett. **31**, 433 (1973).

[48] W. I. Glaberson, W. W. Johnson, and R. M. Ostermeier, Phys. Rev. Lett. **33**, 1197 (1974).

Active and finite-size particles in decaying quantum turbulence at low temperature

Umberto Giuriato ●* and Giorgio Krstulovic ●

Université Côte d'Azur, Observatoire de la Côte d'Azur, CNRS, Laboratoire Lagrange, Nice, France

The evolution of a turbulent tangle of quantum vortices in the presence of finite-size active particles is studied by means of numerical simulations of the Gross-Pitaevskii equation. Particles are modeled as potentials depleting the superfluid and described with classical degrees of freedom following a Newtonian dynamics. It is shown that particles do not modify the building-up and the decay of the superfluid Kolmogorov turbulent regime. It is observed that almost the totality of particles remains trapped inside quantum vortices, although they are occasionally detached and recaptured. The statistics of this process is presented and discussed. The particle Lagrangian dynamics is also studied. At large timescales, the velocity spectrum of particles is reminiscent of a classical Lagrangian turbulent behavior. At timescales faster than the turnover time associated with the mean intervortex distance, the particle motion is dominated by oscillations due to the Magnus effect. For light particles, a nonclassical scaling of the spectrum arises. The particle velocity and acceleration probability distribution functions are then studied. The decorrelation time of the particle acceleration is found to be shorter than in classical fluids, and related to the Magnus force experienced by the trapped particles.

I. INTRODUCTION

When a fluid is stirred, energy is injected into the system exciting structures at different scales. In particular, in three-dimensional classical flows, the energy supplied at large scales is transferred toward small scales in a cascade process. Eventually, it reaches the smallest scales of the system, where dissipation acts efficiently. In the presence of a very large separation between the injection and dissipation scale, this cascade scenario proposed by Richardson leads to a fully developed turbulent state that can be described by the Kolmogorov phenomenology [1]. Kolmogorov turbulence is expected to be universal, and it is in fact commonly observed in nature, industrial applications, and in more exotic flows such as superfluids.

A superfluid is a peculiar flow, whose origin is a consequence of quantum mechanics. At finite temperature, a superfluid is considered to be a mixture of two components: the normal fluid, which can be described by the Navier-Stokes equations, and the superfluid component with zero viscosity [2]. At very low temperatures, the normal component can be neglected and the fluid becomes completely inviscid. As a consequence, an object moving at low velocities does not experience any drag from the fluid. However, when the object exceeds a critical velocity, quantum vortices are

---

*Corresponding author: umberto.giuriato@oca.eu

nucleated [3,4]. Quantum vortices (or superfluid vortices) are the most fundamental hydrodynamical excitations of a superfluid. They are topological defects (and nodal lines) of the macroscopic wave function describing the system, and as a consequence their circulation is quantized. In superfluid helium, the core size of quantum vortices is of the order of 1 Å. Despite the lack of viscosity, quantum vortices can reconnect and change their topology (see, for instance, [5–8]), unlike classical (prefect) fluids.

When energy is injected in a low-temperature superfluid at scales much larger than the mean intervortex distance ℓ, a classical Kolmogorov regime is expected. Such a behavior has been observed numerically [9–11] and experimentally [12,13]. Indeed, at such scales the quantum nature of vortices is not important and the superfluid behaves like a classical fluid. At the scales of the order of ℓ and smaller, the isolated nature of quantized vortices becomes relevant. The system keeps transferring energy toward small scales but through different nonclassical mechanisms [14]. An example of such mechanisms is the turbulent Kelvin wave cascade. Kelvin waves are helical oscillations propagating along quantum vortices, and the energy can be carried toward small scales thanks to nonlinear wave interactions. This energy cascade has been successfully described in the framework of weak-wave turbulence theory [15,16]. The resulting theoretical predictions have been observed numerically in vortex-filament and Gross-Pitaevskii numerical simulations [17–19].

Flow visualization is certainly a fundamental issue in every fluid dynamics experiment. Among the techniques that have been developed to sample a fluid, particle image velocimetry (PIV) and particle tracking velocimetry (PTV) are two of the most common methods [20]. The use of particles as probes has also been adapted to the study of cryogenic flows, in particular in superfluid helium ^{4}He experiments [21], where micrometer-sized hydrogen and deuterium particles have been used. For instance, hydrogen ice particles have been successfully employed to visualize isolated or reconnecting vortex lines [22], as well as the propagation of Kelvin waves [23]. Moreover, the observation of power-law tails in the probability density of the particle velocity is an important difference with respect to classical turbulent states [24–26]. Similar deviations from classical behaviors have recently been reported also for the acceleration statistics [26,27]. Particles in such experiments typically have a size that can rise up to several microns, which is many orders of magnitude larger than the size of the vortex core in superfluid helium. For instance, the solidified hydrogen particles produced in the experiments [22,23] are slightly smaller than 2.7 μm, while in [25,26] their size is between 5 and 10 μm. Although it has been seen that particles unveil the dynamics of quantum vortices, it is not yet clear how much they affect the dynamics of quantum turbulent flows.

Several theoretical efforts have been made in the past decade in order to clarify what is the dynamics of particles in a superfluid and how particles interact with quantum vortices. For example, the vortex-filament (VF) method can be coupled with the classical hydrodynamical equations of a sphere, allowing us to study different specific problems. The interaction between one particle and one vortex has been addressed [28,29], as well the backreaction of tracers in a thermal counterflow [30,31]. In the context of finite-temperature superfluids, the spatial statistics of particles have been recently addressed in simulations of the Hall-Vinen-Bekarevich-Khalatnikov (HVBK) model [32].

Finally, since the work of Winiecki and Adams [4], particles described by classical degrees of freedom have been implemented self-consistently in the framework of the Gross-Pitaevskii (GP) equation [33–37]. Although the GP model is formally derived for dilute Bose-Einstein condensates, it is considered a general tool for the study of superfluid dynamics at very low temperature. Indeed, unlike the VF method or the HVBK model, it naturally contains quantum vortices as topological defects of the order parameter. It was found analytically and confirmed numerically that the GP model can reproduce the process of trapping of large active inertial particles by straight vortex lines [34], in accordance with hydrodynamical calculations [28,29]. In this framework, the interplay between many trapped particles and Kelvin waves has also been investigated [36].

In the present work, we study the influence of particles on quantum turbulent flows at very low temperature by using the GP model coupled with classical particles. In particular, we study the evolution of a free decaying superfluid turbulent vortex tangle loaded with finite-size active

particles. We consider spherical particles of different masses and having a diameter up to 20 core sizes. Such a size is about 1000 times smaller than that of solidified particles used in superfluid helium experiments. Nevertheless, it is slightly smaller than or comparable to the mean intervortex distance in our simulations, similar to current experiments. We also study the different regimes of the turbulent evolution from the Lagrangian point of view. The paper is organized as follows. In Sec. II we describe the Gross-Pitaevskii model coupled with classical particles. We also review the standard properties of the model and give the basic definitions used later to analyze the flow. We also describe the numerical method used in this work. Then, in Sec. III, we present our main results. In particular, in Sec. III A we address whether the presence of particles affects the scales of the flow at which Kolmogorov turbulence takes place. Section III B is devoted to a study of the particle dynamics inside the vortex tangle, their trapping by vortices, and their dynamics at scales larger and smaller than the intervortex distance. Particle velocity and acceleration statistics are then presented in Sec. III C. Finally, Sec. IV contains our conclusions.

II. MODEL FOR PARTICLES IN A LOW-TEMPERATURE SUPERFLUID

A. Gross-Pitaevskii equation coupled with particles

We describe a superfluid of volume V at low temperature by using the complex field ψ, which obeys the GP dynamics. We consider N_p particles in the system. Each particle is characterized by the position of its center of mass $\mathbf{q}_i$ and its classical momentum $\mathbf{p}_i$. The presence of a particle of size a_p generates a superfluid depletion in a spherical region of radius a_p. This effect is reproduced by coupling the superfluid field with a strong localized potential V_p, which has a fixed shape and is centered at the position $\mathbf{q}_j(t)$.

All the particles considered have the same size, as well as the same mass M_p. The Hamiltonian of the system is given by

$$H = \int \left(\frac{\hbar^2}{2m}|\boldsymbol{\nabla}\psi|^2 + \frac{g}{2}\left(|\psi|^2 - \frac{\mu}{g}\right)^2 + \sum_{i=1}^{N_p} V_p(|\mathbf{x} - \mathbf{q}_i|)|\psi|^2 \right) d\mathbf{x} + \sum_{i=1}^{N_p} \frac{\mathbf{p}_i^2}{2M_p}, + \sum_{i<j}^{N_p} V_{\text{rep}}^{ij}, \quad (1)$$

where m is the mass of the bosons constituting the superfluid, and g is the nonlinear coupling constant between the bosons, related to the s-wave scattering length a_s so that $g = 4\pi a_s \hbar^2/m$. The chemical potential is denoted by μ. The particle interaction potential V_{rep}^{ij} is responsible for short-range repulsion between particles, so that they behave as hard spheres and do not overlap. A detailed discussion on the inclusion of this short-range repulsion and the effect on the particle collisions in the model (1) can be found in [33]. The equations of motion that govern the superfluid field and the particle positions are obtained varying the Hamiltonian (1):

$$i\hbar \frac{\partial \psi}{\partial t} = -\frac{\hbar^2}{2m}\nabla^2 \psi + (g|\psi|^2 - \mu)\psi + \sum_{i=1}^{N_p} V_p(|\mathbf{x} - \mathbf{q}_i|)\psi, \quad (2)$$

$$M_p \ddot{\mathbf{q}}_i = -\int V_p(|\mathbf{x} - \mathbf{q}_i|)\boldsymbol{\nabla}|\psi|^2 \, d\mathbf{x} + \sum_{j\neq i}^{N_p} \frac{\partial}{\partial \mathbf{q}_i} V_{\text{rep}}^{ij}. \quad (3)$$

This model has been successfully used to study vortex nucleation [4], trapping of particles by quantum vortices [34], and the interaction between particles trapped inside quantum vortices and Kelvin waves [36]. We denote by GP the Gross-Pitaevskii model without particles, and by GP-P the full coupled system (2) and (3).

In the case in which particles are absent, the chemical potential μ fixes the value of the ground state of the system $\psi_\infty = \sqrt{\rho_\infty/m} = \sqrt{\mu/g}$. Large-wavelength perturbations around this state are sound waves that propagate with the speed of sound $c = \sqrt{g\rho_\infty/m^2}$, while they become dispersive at length scales smaller than the healing length $\xi = \sqrt{\hbar^2/2g\rho_\infty}$.

The GP model describes a superfluid with zero viscosity. Using the Madelung transformation $\psi(\mathbf{x}) = \sqrt{\rho(\mathbf{x})/m}\, e^{i\frac{m}{\hbar}\phi(\mathbf{x})}$, the GP equation (2) is mapped into the continuity and Bernoulli equations of a superfluid of density ρ and velocity $\mathbf{v}_s = \nabla\phi$. A superfluid flow is potential, but the phase is not defined at the nodal lines of $\psi(\mathbf{x})$. Therefore, the vorticity is concentrated along these filaments, which are the topological defects usually called quantum vortices. The effective size of the quantum vortex core coincides with the healing length ξ, and the contour integral of the superfluid velocity around a single vortex filament is the Feynman-Onsager quantum of circulation $\kappa = h/m = 2\pi\sqrt{2}c\xi$.

Using the Madelung transformation and the Helmholtz decomposition, the kinetic term of the superfluid energy density is decomposed into incompressible, compressible, and quantum energy [9]:

$$E_{\text{kin}}^{\text{GP}} = \frac{\hbar^2}{2mV} \int |\nabla\psi|^2 \, d\mathbf{x} = E_{\text{kin}}^{\text{I}} + E_{\text{kin}}^{\text{C}} + E^{\text{Q}}$$

$$= \frac{1}{2V} \int \left([(\sqrt{\rho}\mathbf{v}_s)^{\text{I}}]^2 + [(\sqrt{\rho}\mathbf{v}_s)^{\text{C}}]^2 + \frac{\kappa^2}{4\pi^2}[\nabla\sqrt{\rho}]^2 \right) d\mathbf{x}, \tag{4}$$

where $(\sqrt{\rho}\mathbf{v}_s)^{\text{I}} = \mathcal{P}_{\text{I}}[\sqrt{\rho}\mathbf{v}_s]$ and $(\sqrt{\rho}\mathbf{v}_s)^{\text{C}} = \mathbf{v}_s - (\sqrt{\rho}\mathbf{v}_s)^{\text{I}}$, the operator $\mathcal{P}_{\text{I}}[\cdot]$ being the projector onto the space of divergence-free fields. The other energies of the superfluid are the internal energy $E_{\text{int}} = (2V)^{-1} \int g(\rho/m - \mu/g)^2 \, d\mathbf{x}$, where the energy of the ground state is subtracted, and the interaction energy with the particles $E_{\text{P}}^{\text{GP}} = V^{-1} \int \sum_i^{N_{\text{p}}} V_{\text{p}}(|\mathbf{x} - \mathbf{q}_i|)\rho \, d\mathbf{x}$, so that the total energy is given by $E_{\text{tot}} = E_{\text{kin}}^{\text{GP}} + E_{\text{int}} + E_{\text{P}}^{\text{GP}}$. From these definitions follow the corresponding energy spectra defined in terms of the Fourier transform of the fields [9].

B. Numerical methods and parameters

In the simulations presented in this work, we solve the system (2) and (3) in a cubic periodic box of side $L = 341\xi$ with $N_{\text{c}} = 512^3$ collocation points by using a standard pseudospectral method. We use a fourth-order Runge-Kutta scheme for the time-stepping and the standard 2/3 rule for the dealiasing. In numerics, we fix $c = 1$ and $\psi_\infty = 1$.

To produce a homogeneous and isotropic tangle of quantized vortex lines, we impose an initial Arnold-Beltrami-Childress (ABC) flow, following the procedure described in [38]. In particular, we use a superposition of $k = 1 \times 2\pi/L$ and $k = 2 \times 2\pi/L$ basic ABC flows: $\mathbf{v}_{\text{ABC}} = \mathbf{v}_{\text{ABC}}^{(1)} + \mathbf{v}_{\text{ABC}}^{(2)}$, with

$$\mathbf{v}_{\text{ABC}}^{(k)} = [B\cos(ky) + C\sin(kz)]\hat{x} + [C\cos(kz) + A\sin(kx)]\hat{y} + [A\cos(kx) + B\sin(ky)]\hat{z}, \tag{5}$$

and the parameters $A = 0.5196$, $B = 0.5774$, and $C = 0.6351$. The basic ABC flow is a stationary (periodic) solution of the Euler equation with maximal helicity. The resulting wave function contains a tangle whose nodal lines follow the ABC vortex lines. The initial mean intervortex distance is $\ell(t = 0) \sim 25\xi$. As the flow is prepared by minimizing the energy, most of the energy of the system is in the incompressible part of the energy and resulting from the vortex configuration.

The ground state for the particles consists in a number of particles (we use $N_{\text{p}} = 200$ and 80) of the same size and mass, randomly distributed in the computational box. Particles are initially at rest. This state is prepared using the imaginary-time evolution of Eq. (2). Then, the initial condition for the simulations is obtained by multiplying the wave function associated with the ABC flow and the wave function associated with the particle ground state. An example of an initial field containing particles is displayed in Fig. 1(d).

Because of the presence of a healing layer, the particle boundary is never sharp, independently of the functional form of the potential V_{p}. The superfluid field vanishes in the region where $V_{\text{p}} > \mu$, and at the particle boundary the fluid density passes from zero to the bulk value ρ_∞ in approximately one healing length. The potential used to model each particle is a smoothed hat-function $V_{\text{p}}(r) = \frac{V_0}{2}(1 - \tanh[\frac{r^2 - \zeta^2}{4\Delta_a^2}])$, where the parameters ζ and Δ_a are set to model the
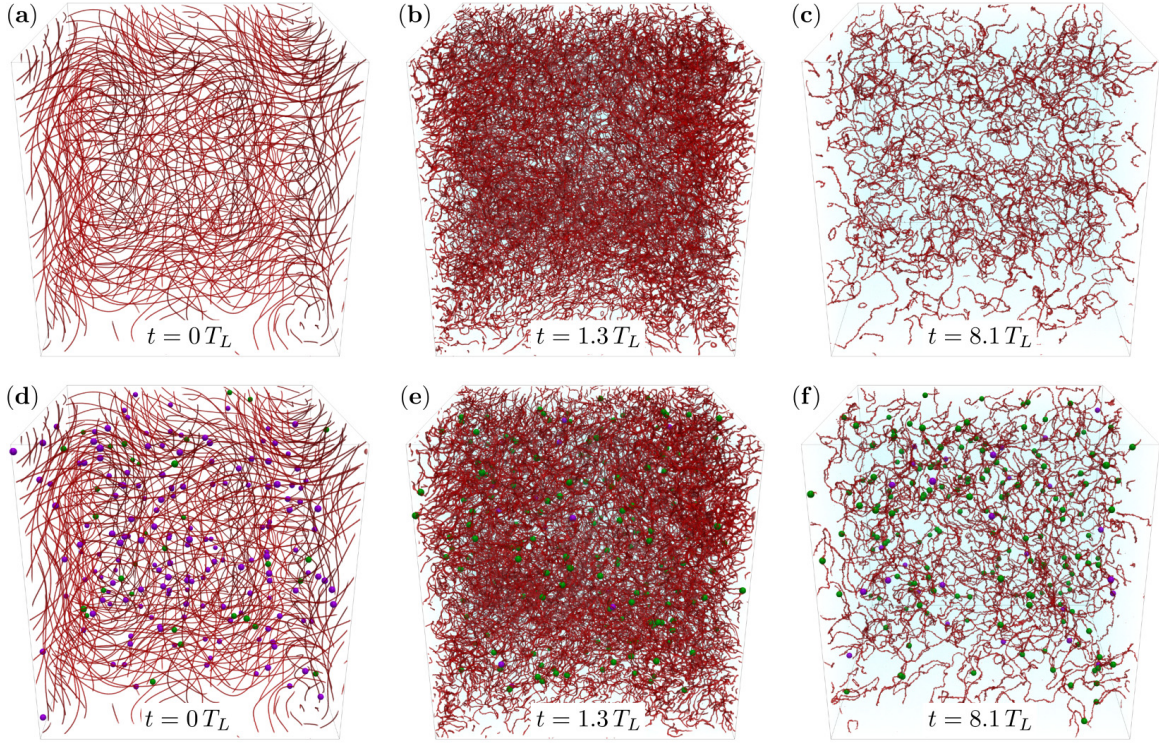
FIG. 1. Visualizations of the superfluid vortex tangle. Vortices are represented as isosurfaces in red of the density field ($\rho = 0.15\rho_\infty$), sound is rendered in blue, trapped particles in green, and free particles in purple. The upper row is without particles, the lower row is with 200 neutrally buoyant particles of radius $a_\mathrm{p} = 4\xi$. (a,d) The ABC initial states. (b,e) The most turbulent regime ($t = 1.3T_L$). (c,f) A late time ($t = 8.1T_L$). T_L denotes the large-eddy-turnover time (see the text).

particle. Their values are listed in Table I. In particular, ζ fixes the width of the potential and it is related to the particle size, while Δ_a controls the steepness of the smoothed hat-function. The latter needs to be adjusted in order to avoid the Gibbs effect in the Fourier transform of V_p. Since the particle boundaries are not sharp, the effective particle radius is defined as $a_\mathrm{p} = (3M_0/4\pi\rho_\infty)^{\frac{1}{3}}$, where $M_0 = \rho_\infty L^3(1 - \int |\psi_\mathrm{p}|^2\, d\mathbf{x}/ \int |\psi_\infty|^2\, d\mathbf{x})$ is the fluid mass displaced by the particle and ψ_p is the steady state with just one particle. Practically, given the set of numerical parameters ζ and Δ_a, the state ψ_p is obtained numerically with imaginary-time evolution and the excluded mass M_0 is measured directly. Particles attract each other by a short-range fluid mediated interaction

TABLE I. Simulation parameters.

Run	N_p	a_p	$\mathcal{M}$	ζ	Δ_a	V_0/μ	γ/μ
I	0						
II	200	4.0ξ	0.125	1.5ξ	1.2ξ	20.0	1.4×10^{-4}
III	200	4.0ξ	0.25	1.5ξ	1.2ξ	20.0	1.4×10^{-4}
IV	200	4.0ξ	1.0	1.5ξ	1.2ξ	20.0	1.4×10^{-4}
V	200	4.0ξ	2.0	1.5ξ	1.2ξ	20.0	1.4×10^{-4}
VI	80	10.0ξ	1.0	8.0ξ	2.0ξ	20.0	5.8×10^{-4}
VII	200	10.0ξ	0.125	8.0ξ	2.0ξ	20.0	5.8×10^{-4}
VIII	200	10.0ξ	0.25	8.0ξ	2.0ξ	20.0	5.8×10^{-4}
IX	200	10.0ξ	1.0	8.0ξ	2.0ξ	20.0	5.8×10^{-4}

[33,35], thus we use the repulsive potential $V_{\rm rep}^{ij} = \gamma(2a_{\rm p}/|\mathbf{q}_i - \mathbf{q}_j|)^{12}$ in order to avoid an overlap between them. The functional form of $V_{\rm rep}^{ij}$ is inspired by the repulsive term of the Lennard-Jones potential, and the prefactor γ is adjusted numerically so that the interparticle distance $2a_{\rm p}$ minimizes the sum of $V_{\rm rep}^{ij}$ with the fluid-mediated attractive potential [33,35]. We express the particle mass as $M_{\rm p} = \mathcal{M}M_0$, where M_0 is the mass of the superfluid displaced by the particle. Namely, heavy particles have $\mathcal{M} > 1$ and light particles have $\mathcal{M} < 1$. In Table I all the parameters for the particles used in the simulations presented in this work are reported. In the following, we will refer to each simulation specifying the size and the mass of the particles used.

Note that although the model (1) is a minimal model for implementing particles in the GP framework, we cannot add to the system an arbitrary number of particles. Indeed, since particles have a finite size, they occupy a volume at the expense of the superfluid field, and packing effects could become important if the filling fraction is too high. Moreover, the potential $V_{\rm p}$ must be updated at each time step, which is numerically costly. Finally, note that the the evaluation of the force term (3) acting on particles requires us to know the value of the fields at intermesh points. When the number of particles in the simulation is not large, the force $\mathbf{f}_i^{\rm GP}(\mathbf{q}_i) = -(V_{\rm p} * \boldsymbol{\nabla}\rho)[\mathbf{q}_i]$ (3) can be computed with spectral accuracy using a Fourier interpolation. Such a method has been used in [34–36], where the particle dynamics is extremely sensitive. In this work, the use of a Fourier interpolation for each particle is numerically unaffordable, due to the large number of particles involved and the resolutions used. Instead, we use a fourth-order B-spline interpolation method, which has been shown to be highly accurate with a reduced computational cost [39] and particularly well adapted for pseudospectral codes. Indeed, the use of a Fourier interpolation to evaluate the three-dimensional force for $N_{\rm p}$ particles requires $\sim 3N_{\rm p}N_{\rm c}$ operations and evaluations of complex exponentials ($N_{\rm c} = 512^3$ in the present work). Such a cost quickly becomes too expensive at high resolutions and/or a large number of particles. On the contrary, B-spline interpolation requires just one fast Fourier transform of a field per component, and an interpolation using only four neighboring grid points per dimension [39]. Such a scheme saves a factor $\sim N_{\rm p}$ of computational cost compared to Fourier interpolation. Note that in the previous discussion, we have not taken into consideration parallelization issues, where local schemes (B-splines) are much more advantageous than global ones (Fourier transforms). Nevertheless, some issues with physical quantities at small scales arising from the B-spline interpolation are discussed in the Appendix.

III. PARTICLES IMMERSED IN A TANGLE OF SUPERFLUID VORTICES

Superfluid turbulence in the context of the GP model has been studied extensively [9,11,38,40,41]. In general, quantum turbulence develops from an initial state with a vortex configuration where the incompressible kinetic energy is mainly contained at large scale. During the evolution, vortex lines move, interact among themselves, and reconnect, creating complex vortex tangles. Through this process, sound is produced and incompressible kinetic energy is irreversibly converted into quantum, internal, and compressible kinetic energy. Eventually, the compressible energy produced in the form of acoustic fluctuations starts to dominate, thermalizes, and acts as a thermal bath providing an effective dissipation acting on the vortices. As a consequence, vortices shrink and eventually disappear through mutual friction effects following Vinen's decay law [19,42]. In particular, it has been shown that the decrease of the incompressible kinetic energy behaves in a similar manner to decaying classical turbulence [9]. To make a connection with decaying classical Kolmogorov turbulence, the incompressible energy dissipation or dissipation rate is usually defined in the context of GP turbulence as

$$\epsilon = -\frac{dE_{\rm kin}^{\rm I}}{dt}. \tag{6}$$

As in decaying Navier-Stokes turbulence, in GP the most turbulent stage is achieved around the time when this quantity is maximal. About this time, the classical picture holds and the incompressible
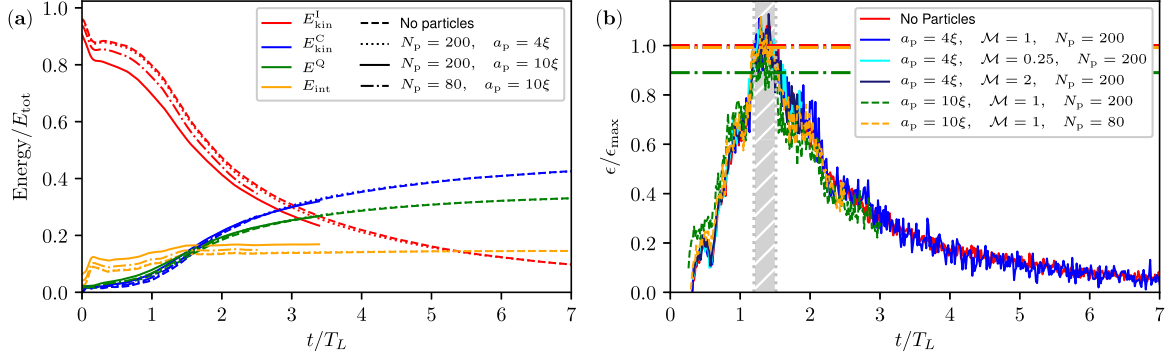
FIG. 2. (a) Time evolution of the superfluid energy components in the cases with no particles (dashed line), 200 small particles (dotted line), 200 large particles (solid line), and 80 large particles (dash-dotted line). (b) Incompressible energy dissipation rate for different numbers of particles with different sizes and different masses (solid lines). Dash-dotted horizontal lines of the corresponding colors indicate the value of the maximum of dissipation, obtained averaging over the shaded region. The dissipation is expressed in units of its maximum $\epsilon_{\max}$ in the case without particles.

energy spectrum satisfies the Kolmogorov prediction

$$E_{\text{kin}}^{\text{I}} = C\epsilon^{2/3}k^{-5/3},$$

where C is the Kolmogorov constant, the value of which has been found to be close to 1 in GP turbulence [11,38,41].

The first purpose of this work is to check whether and to what extent the presence of particles in the system modifies Kolmogorov turbulence. We add to the ABC initial condition a number of randomly distributed particles and let the system evolve under the dynamics (2) and (3). In Figs. 1(a), 1(b) and 1(c), the three stages of the evolution (initial condition, turbulent vortex tangle, and residual filaments in a bath of sound, respectively) are visualized in the case of 200 neutrally buoyant particles of radius 4ξ. See the supplemental material [43] for movies of this simulation and others with particles of a different size. Trapped particles by vortices are displayed in green, whereas free ones are displayed in purple. The algorithm to distinguish a trapped particle from a free one is based on the circulation around it and it is discussed in Sec. III B.

In Fig. 1 we observe that the building up and decay of the turbulent tangle is not strongly modified by the presence of particles. Moreover, it can be noticed how during the first stages of the evolution of the system the majority of particles gets trapped into the vortices. At zero temperature, as there is no normal component in the flow, no drag is experienced by the particles and their motion is completely driven by the pressure gradients. As a consequence, they are attracted by quantum vortices [28,34,44]. During the turbulent regime, violent and strongly nonlinear events like reconnections dominate the vortex dynamics and the flow evolution. A fundamental question is whether and how much the hydrodynamical attraction between vortices and particles is sufficient to keep them attached to the filaments. Indeed, since quantum vortices are actually the main actors of turbulence in superfluid, if particles are really able to follow them in this regime, it is a good indication that they are suitable for use as probes.

In the following subsection, we will quantitatively study the effect of particles on quantum turbulent flows. We will first focus on the large scales of the flow, where Kolmogorov turbulence takes place. Then the particle dynamics and their statistics will be addressed.

A. The effect of particles on Kolmogorov superfluid turbulence

We shall start our analysis by comparing the temporal evolution of global quantities. In Fig. 2(a) the time evolution of the different components of the energy is displayed. Times are expressed in
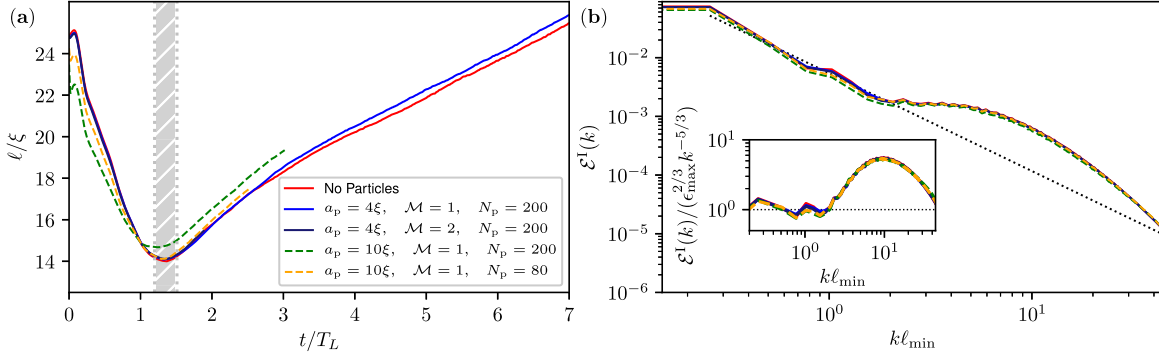
FIG. 3. (a) Time evolution of the mean intervortex distance for different numbers of particles of different sizes and different masses. (b) Incompressible energy spectrum for different numbers of particles of different sizes and different masses. Inset: Compensated incompressible energy spectrum. Solid lines refer to particles of size $a_p = 4\xi$, dashed lines refer to particles of size $a_p = 10\xi$. The dotted line is the classical scaling $\epsilon_{max} k^{-5/3}$. The spectrum is computed averaging over times in the shaded region.

units of the large-eddy-turnover time defined as $T_L = L/2v_{rms}$, where $v_{rms} = \sqrt{2E_{kin}^I(t=0)/3}$ is the root-mean-square velocity associated with the initial vortex tangle, and $L/2$ is its characteristic length scale. We compare the case in which no particles are present in the flow to the cases having particles of different sizes and of relative mass $\mathcal{M} = 1$. The net transfer of incompressible energy toward compressible, quantum, and internal energy is qualitatively unchanged in the various cases. The only difference is a slightly lower value of the incompressible energy in the case of large particles, in favor of the internal energy of the superfluid. Such an effect is more evident if the number of large particles is increased, and could be related to an increment of the filling fraction Φ, namely the fraction of the total volume occupied by the particles. In fact, for $N_p = 200$ particles of radius $a_p = 4\xi$ the filling fraction is $\Phi = 0.1\%$, for $N_p = 80$ particles of radius $a_p = 10\xi$ it is $\Phi = 0.8\%$, and for $N_p = 200$ particles of radius $a_p = 10\xi$ we have $\Phi = 2.1\%$. The kinetic and repulsion energies of the particles, as well as the particle-vortex interaction E_P^{GP}, are negligible compared with the other energies throughout the duration of the simulations (data not shown).

The dissipation rate of the incompressible kinetic energy is reported in Fig. 2(b) for particles of different masses and different sizes. The dissipation increases in the early stages when the energy begins to be transferred to the smaller scales, it reaches a maximum when all the scales are excited, and then it starts to decay since no forcing is sustaining the turbulence. We observe that the evolution of the dissipation is clearly not significantly modified by the presence of particles. In particular, the value of the maximum of dissipation, which is the signature of the most turbulent state reached by the tangle, is slightly lower only in the case in which many large particles are moving in the system. In particular for this case, it is about 90% of ϵ_{max}, the value measured in the case with no particles. The shaded region in Fig. 2(b) represents the most turbulent time of the simulations. We consider that in this short stage the system is in a quasisteady state, and we perform the temporal average of certain physical quantities in order to improve statistical convergence.

Another important quantity that is not affected much by the interplay between tangle and particles is the mean intervortex distance ℓ, whose time evolution is reported in Fig. 3(a). The mean intervortex distance is then estimated as $\ell = \sqrt{V/L_v}$, where L_v is the total vortex length in the system. This latter is estimated using the method introduced in [9], where L_v is shown to be related to the proportionality constant between the incompressible momentum density $J^I(k)$ of the flow and the spectrum of a two-dimensional point-vortex $J_{vort}^{2D}(k)$:

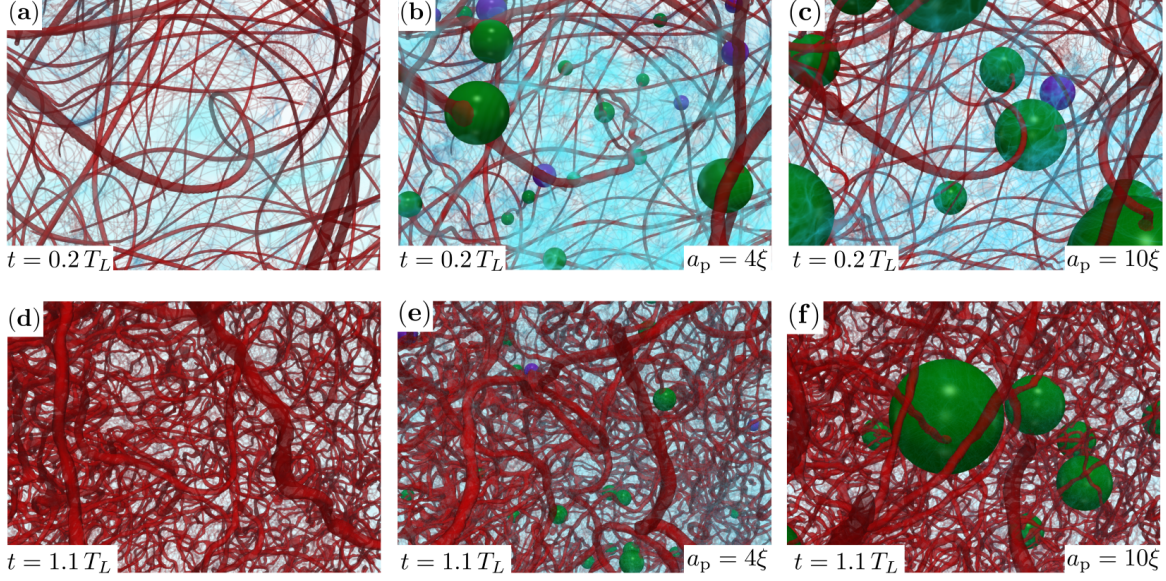$$\frac{L_v}{2\pi} = \frac{\sum_k J^I(k)}{\int J_{vort}^{2D}(k)\,dk}. \tag{7}$$

FIG. 4. Closeup of the superfluid vortex tangle at the early stage of the simulation (upper row: $t = 0.27 T_L$) and during the turbulent regime (lower row: $t = 1.1 T_L$) for the cases with no particles [left column (a),(d)], small particles [central column (b),(e): $a_{\rm p} = 4\xi$], and large particles [right column (c),(f): $a_{\rm p} = 10\xi$]. Vortices are represented as isosurfaces of the density field ($\rho = 0.15\rho_\infty$) and rendered in red, sound is rendered in blue, trapped particles in green, and free particles in purple.

The spectra of momentum densities are the angle average of the norm in Fourier space of the momentum density $\mathbf{J} = \rho \mathbf{v}_{\rm s}$, and the incompressible part is obtained projecting onto the space of divergence-free fields. We have checked the validity of this formula by using the vortex filament tracking method described in [45] at some checkpoints.

In the turbulent regime, where the dissipation gets its maximum, the total length of the entangled vortices is also larger by a factor 4 compared to the initial condition, and the distance between the filaments is minimum. The value $\ell_{\rm min} \sim 14\xi$ of the intervortex distance in this regime will be used as a characteristic small length scale of the Kolmogorov turbulent regime. Such length is smaller than the diameter of the largest particles considered ($2a_{\rm p} = 20\xi$), but nevertheless this has no appreciable repercussions on the behavior of the observables studied. Furthermore, as shown in Fig. 3(c), the scaling of the incompressible energy spectrum $\mathcal{E}^{\rm I}(k)$ averaged around the maximum of dissipation is unaltered by particles in the system. Figure 3(b) displays the incompressible energy spectrum. It is apparent that the scaling of the spectrum is always compatible with classical turbulence at scales larger than the intervortex distance, and the way in which the energy is accumulated at smaller scales is not modified by the particles. In the inset of Fig. 3(b), the spectrum is compensated by the Kolmogorov prediction $\mathcal{E}^{\rm I}(k) = C\epsilon_{\rm max}^{2/3} k^{-5/3}$ for classical hydrodynamic turbulence. The dotted horizontal black line shows that the value of the constant C in the Kolmogorov law is a number of order 1 for superfluid turbulence.

The only appreciable difference observed between the case with and without particles is that in the early stages of the evolution, the trapping of particles perturbs the vortex filaments and excites Kelvin waves. A comparison between the volume renderings can be seen in the upper row of Fig. 4. Such perturbations propagate during the evolution of the tangle. At the times when turbulence is developed, the details of the vortex configurations are completely different (see the lower row of Fig. 4). Nevertheless, the statistical properties of the system in this regime remain unchanged. We stress that the intervortex distance in quantum turbulence experiments lies typically in the range 10–100 μm, which is equal to or slightly larger than the particle size [24,25,27]. In this sense, the simulations presented here are compatible with the experimental parameters. They thus support
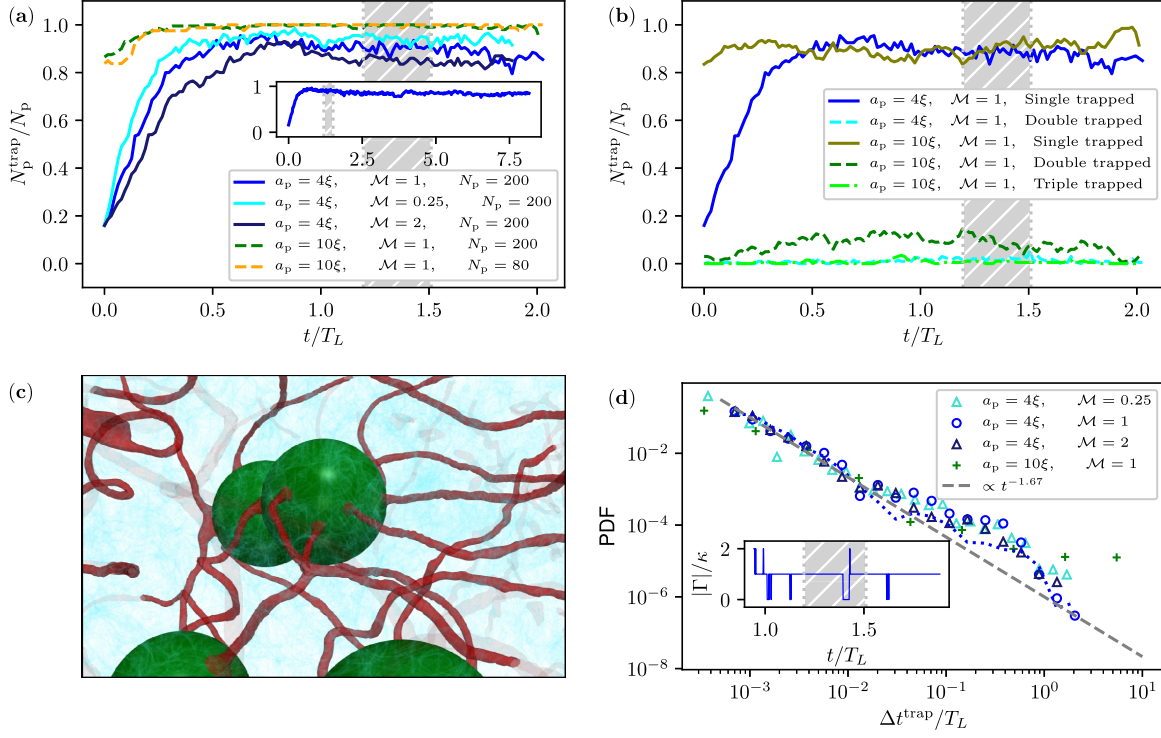
FIG. 5. (a) Fraction of trapped particles as a function of time for different numbers of particles of different sizes and different masses. Inset: The same for longer time in the case of 200 neutrally buoyant particles of size $a_p = 4\xi$. (b) Comparison between the fraction of multiply trapped particles as a function of time for neutrally buoyant particles. (c) Volume rendering of large particles ($a_p = 10\xi$) multiply trapped by quantum vortices. Vortices are rendered in red, sound in blue, particles in green. (d) Probability density function of the continuous time spent by particles inside vortices for different species of particles. The dotted blue line corresponds to the same simulation of blue circles (particles with size a_p and mass $\mathcal{M} = 1$) but averaged over the full simulation times. Inset: Absolute value of the circulation around a single particle of size $a_p = 4\xi$ and mass $\mathcal{M} = 1$ as a function of time. The PDF is computed averaging over times in the shaded region.

the belief that active particles have effectively no influence on the typical development and decay of quantum turbulence. This numerical fact helps to validate past and future experiments that use particles as probes of superfluids.

On the other hand, because of the lack of a Stokes drag in the system, particles cannot be treated as simple tracers of the superfluid velocity $\mathbf{v}_s$. Nevertheless, if they remain trapped inside the vortices they can track the evolution of the vortex filaments, which are the structures that effectively become turbulent. With the purpose of characterizing this scenario, in the next subsection we investigate the motion of particles once they are immersed in a tangle of quantum vortices.

B. Motion of particles in the superfluid vortex tangle

Looking at the time evolution of the vortex tangle (see Fig. 1 and movies in the supplemental material), the first thing that is apparent is how particles quickly get trapped into vortex filaments. This dynamics is expected and it has been studied in the case in which vortices move slowly [34]. It is a consequence of the pressure gradients. However, it is less obvious if such behavior remains dominant when turbulence take place and reconnections become frequent.

We study the evolution of particles and compute whether they are free or trapped by vortices. The temporal evolution of the fraction of trapped particles is displayed in Fig. 5(a) for all runs. This measurement is made by computing the circulation $\Gamma = \oint_C \mathbf{v}_s \cdot d\mathbf{x}$ of the superfluid velocity $\mathbf{v}_s$

along contours $\mathcal{C}$ encircling each particle, and counting for which particles it is different from zero. Specifically, we compute the circulation along many parallel square contours of side $2(a_{\mathrm{p}} + \Delta_x)$ around each particle, where Δ_x is the grid spacing. If the circulation around at least one of these contours is different from zero, the particle is considered as trapped [46]. For practical reasons, due to the parallelization of the numerical code, we consider only contours perpendicular to the z axis of the computational box. As a consequence, the protocol is not able to grasp vortices that are crossing the particles exactly on a plane perpendicular to the z axis. This means that our estimation of the fraction of trapped particles is effectively a lower bound. However, it should be noticed that this pathological situation is an extremely rare situation that does not change the conclusions of our analysis.

In the initial condition the particles are placed randomly in the computational box. It happens then that some of them are already positioned inside a vortex. In the case of particles with a size comparable to the intervortex distance, the majority of particles are in this situation. In the first stages of the evolution of the flow, the number of trapped particles increases rapidly until it becomes stationary always at times much smaller than one T_L. The time needed to reach a stationary state depends slightly on the mass of the particles, as well as the fraction of trapped particles once a steady regime is reached. The steady value of $N_{\mathrm{p}}^{\mathrm{trap}}/N_{\mathrm{p}}$ is between 80% and 90% for small particles ($2a_{\mathrm{p}} < \ell$), while on average the totality of particles of size $2a_{\mathrm{p}} \sim \ell$ is found to be trapped by vortices, independently of the filling fraction. When the system reaches the most turbulent regime (indicated by the shaded region), the fraction of trapped particles does not undergo any appreciable changing. In the inset of Fig. 5(a), $N_{\mathrm{p}}^{\mathrm{trap}}/N_{\mathrm{p}}$ is also shown for late times in the case of small particles of relative mass $\mathcal{M} = 1$. It manifestly remains stable. This means that even when the density of vortex lines is decaying (along with the intensity of turbulence), the particles stay trapped inside vortices. Note that in this work we are dealing with homogeneous and isotropic decaying quantum turbulence at low temperature. We mention that the fraction of trapped particles measured in thermal counterflow simulated by means of the VF method is lower that the one observed here [31].

The circulation around each superfluid vortex filament is equal to a single quantum of circulation κ. As a consequence, measuring the circulation along a closed line $\mathcal{C}$ allows us to count the number of filaments in the region delimited by the line, provided that the quanta of circulation around every filament have the same sign. This is true also if the vortices are trapping particles, because their topological nature does not change. In Fig. 5(b) we show again the fraction of trapped particles, but now separating the number of particles trapped by multiple vortices. It turns out that at least the 5–10 % of the particles with size $2a_{\mathrm{p}} \sim \ell$ are always attached to at least two different filaments. Sometimes even more vortices pass simultaneously through the same particle, as can be visualized in the volume plot of Fig. 5(c).

Once a particle is trapped by a vortex, it can experience violent events, for instance during vortex reconnections. In such circumstances, such a particle could be detached and expelled from the vortex until it will eventually get trapped by another vortex of the tangle. We compute the probability density function (PDF) of the continuous time intervals Δt_{trap} spent by the particles inside the vortices regime. The PDFs for particles of different sizes and masses are displayed in Fig. 5(d). For all the species of particles examined, the probability distribution seems to follow roughly a power-law scaling in time $\sim(\Delta t_{\mathrm{trap}})^{-\alpha}$, with $\alpha \sim 1.67$. The PDF certainly vanishes much slower than an exponential decay at large Δt^{trap}, which would typically result from a standard escape problem over energy barriers. We checked that the intermittency of the circulation and the shape of the trapping time PDF are not characteristic of the most turbulent regime, since they persist also at the late times of the simulations [see the dotted blue line in Fig. 5(d)]. Therefore, many particles spend a time at least of the order of the simulation time ($\sim 10 T_L$) inside a vortex filament, i.e., the typical escape time from the vortices is virtually infinite. This observation is exemplified in the inset of Fig. 5(d), where the evolution of the circulation around a single-small neutral particle is reported (the qualitative behavior is the same for the other particles). It is also clear that the time spent by the particles with zero circulation around them (namely free from vortices) is short. Since
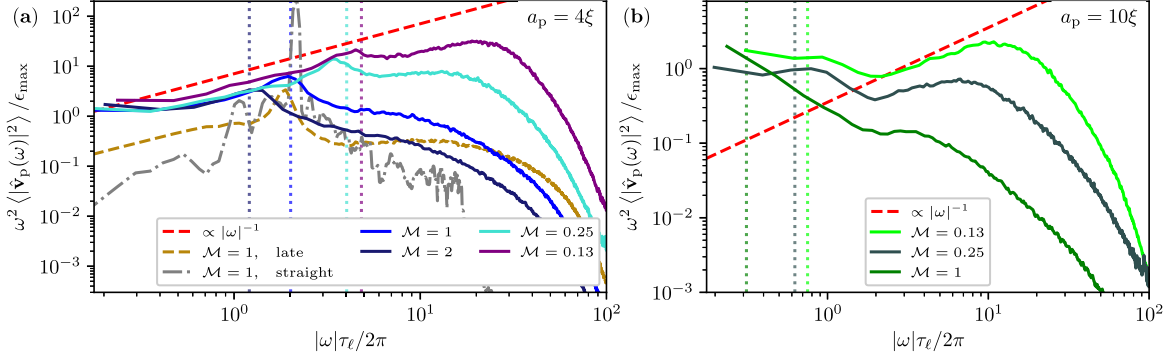
FIG. 6. Frequency spectrum of the particle velocity for particles of different masses and different sizes, compensated with the prediction for the Lagrangian spectrum in classical turbulence $\propto \epsilon/\omega^2$: (a) small particles with $a_{\mathrm{p}} = 4\xi$; (b) large particles with $a_{\mathrm{p}} = 10\xi$. The dash-dotted gray line is the frequency spectrum of a single small particle trapped in a straight vortex slightly perturbed. Dotted lines of corresponding colors are the prediction for the particle natural frequency Ω_{p}. The dashed red line is the scaling due to vortex reconnection or Kelvin waves $\propto |\omega|^{-1}$. The dashed golden line is the spectrum evaluated at late times in the simulation ($6T_L < \tau < 7T_L$).

we established that particles immersed in a tangle spend most of the time inside vortex filaments, in the following we study their motion once they get trapped.

At large scales, the vortex tangle seems to behave as a classical hydrodynamic turbulent system. Therefore, the first natural question is whether the particles can trace such large-scale fluctuations. In classical turbulence, it is well known that the Lagrangian velocity spectrum scales as

$$\langle |\hat{\mathbf{v}}_{\mathrm{p}}(\omega)|^2 \rangle = B\epsilon\omega^{-2}, \tag{8}$$

where B is a constant of order unity and $\hat{\mathbf{v}}_{\mathrm{p}}(\omega)$ is the Fourier transform of the Lagrangian particle velocity $\mathbf{v}_{\mathrm{p}}(t)$ [47,48]. Such scaling is valid in the inertial range $2\pi/T_L \ll \omega \ll 2\pi/\tau_\eta$, where τ_η is the Kolmogorov timescale. In our case, we build an analog of the Kolmogorov time scale under the assumptions that the dissipation rate ϵ_{max} is the only important physical parameter in the classical turbulence regime and that the Kolmogorov turbulent cascade ends at the intervortex distance ℓ_{min}. Therefore, we define the smallest timescale of the classical turbulence regime as $\tau_\ell = (\ell_{\mathrm{min}}^2/\epsilon_{\mathrm{max}})^{1/3}$, and we expect classical turbulent phenomenology to hold for times $\tau_\ell \ll t \ll T_L$. In Fig. 6, the measurement of the frequency spectrum of the particle velocity $\langle |\hat{\mathbf{v}}_{\mathrm{p}}(\omega)|^2 \rangle = \langle |\int \dot{\mathbf{q}}(t)e^{-i\omega t}\,dt|^2 \rangle$ during the turbulent regime is shown for different species of particles, compensated with the classical scaling $\epsilon_{\mathrm{max}}\omega^{-2}$. Note that the average that defines the spectrum is meant over different realizations. In numerics we average over all the particle trajectories during the turbulent regime. At frequencies $\omega < \tau_\ell/2\pi$, the spectra approach a plateau of value 1, confirming that particles sample well the flow and their behavior is described by the standard classical turbulence picture at large scales. Note that the classical temporal inertial range of our simulations is pretty small, since $T_L \sim 5\tau_\ell$. For comparison, we also present the velocity spectrum of a particle of size $a_{\mathrm{p}} = 4\xi$ and mass $\mathcal{M} = 1$, computed in a temporal window at much later times, when Kolmogorov turbulence has decayed and only a few vortices are left. Note that a ω^{-2} scaling of the Lagrangian velocity spectrum has also been observed in numerical simulations of the vortex filament model [49], although not in the Kolmogorov inertial range and not related to the energy dissipation rate nor to Kolmogorov turbulence.

As expected, in our simulations no Kolmogorov scaling is observed at small timescales. Indeed, one of the most striking features of quantum turbulence is the crossover between the classical Kolmogorov regime and the physics taking place at scales smaller than the mean intervortex distance. Unlike classical turbulence (see, for instance, [47]), there is still a nontrivial scaling at

timescales shorter than τ_ℓ. Such a difference is a consequence of the quantum nature of the system, here manifested by the presence of quantized vortices.

When a particle is trapped by a vortex, the superfluid flow turns around it. As a consequence, while the particle moves, it experience a Magnus force. This lift force is simply expressed as $\mathbf{F}_{\text{Magnus}} = \frac{3}{2}\rho_\infty a_p \boldsymbol{\Gamma} \times (\dot{\mathbf{q}} - \mathbf{v}_s)$, where the circulation vector $\boldsymbol{\Gamma}$ is oriented along the vortex filament, and the superfluid velocity $\mathbf{v}_s$ contains the contributions of the mean flow and the vortex motion [36,50]. The Magnus effect induces a precession of the particle about the filament with the characteristic angular velocity

$$\Omega_p = \frac{3}{2}\frac{\rho_\infty a_p}{M_p^{\text{eff}}}\Gamma, \tag{9}$$

where the particle effective mass $M_p^{\text{eff}} = M_p + \frac{1}{2}M_0 = (\mathcal{M} + \frac{1}{2})M_0$ takes into account the added mass effect due to the mass of the superfluid displaced by the particle M_0. As mentioned in [36], for current experiments with hydrogen particles in superfluid helium, this frequency is of order 10–100 Hz. If the Magnus force is the main force acting on a trapped particle, the Newton equation $M_p^{\text{eff}}\ddot{\mathbf{q}} = \mathbf{F}_{\text{Magnus}}$ implies the following expression for the frequency spectrum of the particle velocity:

$$\langle|\hat{\mathbf{v}}_p(\omega)|^2\rangle = \frac{\Omega_p^2}{\Gamma^2(\omega - \Omega_p)^2}\langle|\boldsymbol{\Gamma} \times \hat{\mathbf{v}}_s(\omega)|^2\rangle. \tag{10}$$

Independently of the external superfluid velocity, the expression (11) predicts that the spectrum $\langle|\hat{\mathbf{v}}_p(\omega)|^2\rangle$ must be peaked around the natural frequency of trapped particles $\omega = \Omega_p$. Such behavior has been studied in detail in the case of particles trapped inside slightly perturbed straight vortex filaments [36]. The spectrum of this simple configuration is also reported for comparison in Fig. 6(a) for a small particle of relative unit mass. A clear bump in the frequency spectrum, corresponding to Ω_p, is still visible when particles are immersed in a complex quantum vortex tangle. For the large particles, the presence of a peak is less evident because the natural frequency is lower, and therefore a longer sampling (in time) would be necessary to resolve it properly ($2\pi/\Omega_p = 0.7T_L$ for the particles of size $a_p = 10\xi$ and mass $\mathcal{M} = 1$). Moreover, as large particles are multiply trapped by many vortices, the resulting motion is certainly more complex than a precession with a single characteristic angular frequency of one single vortex. The broadness of the peak around the Magnus frequency for the small particles in Fig. 10(a) could also be related to this fact.

At small timescales, a different scaling of the velocity spectrum is observed for the light particles, now in agreement with $\langle|\hat{\mathbf{v}}_p(\omega)|^2\rangle \propto |\omega|^{-1}$. This behavior is consistent with the fact that at scales smaller than the intervortex distance, the typical velocities of a superfluid turbulent tangle are supposed to scale as $v_{\text{fast}}(t) \propto \sqrt{\kappa/|t - t_0|}$, because the circulation becomes the only relevant physical parameter, and the motion of vortices is dominated by their mutual advection and reconnections. In this scenario, if particles are sufficiently light to be able to follow the fast vortex dynamics, we can substitute $\langle|\hat{\mathbf{v}}_p(\omega)|^2\rangle \sim \hat{v}_{\text{fast}}^2(\omega) \propto \kappa|\omega|^{-1}$. Another effect that could contribute to the same result is the attraction of particles by the vortices, since the scaling in time of the particle-vortex distance is the same as that of vortex reconnection [34]. Note that for the heaviest particles, such fast scaling is absent since their reaction is probably too slow to be sensible to the fast fluctuations of the tangle.

C. Particle velocity and acceleration statistics

Unlike classical turbulence, where the statistics of the one-point particle velocity v is known to be Gaussian [1], experiments in superfluid helium using hydrogen and deuterium particles as tracers have reported long tails, with a v^{-3} power-law scaling in their velocity distribution [24–26]. Such scaling has been related to the singular velocity field of quantized vortices [51,52]. At low temperatures, as Stokes drag is negligible, particles should not move with the superfluid flow
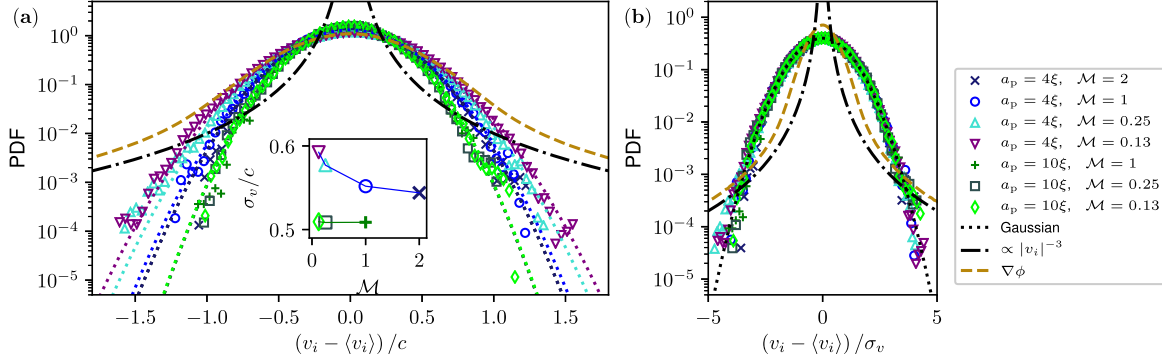
FIG. 7. (a) Probability density function of the single-component particle velocity, for different species of particles. The dotted golden line is the Eulerian velocity field $\nabla\phi$, corresponding to the simulation without particles at the time $1.4\,T_L$. The data for the particles are averaged in time between $t = 1.2T_L$ and $1.6T_L$. Inset: Standard deviation of the particle velocity as a function of the particle mass. (b) The same as (a) but with the velocities normalized by the standard deviation σ_v. Dotted lines are Gaussian, dash-dotted line is a power-law scaling $|v_i|^{-3}$.

and such scaling can be understood as a consequence of quantum vortex reconnections sampled by trapped particles [7,24]. Furthermore, in Ref. [25], by using particle tracking velocimetry in counterflow turbulence, it was shown that while varying the sampling scale, the velocity PDFs continuously change from Gaussian statistics to power-law tails, the crossover taking place at scales of the order of the intervortex distance. In this final subsection we present measurements of particle velocity and acceleration statistics within the GP-P model.

We start the discussion by presenting the Eulerian velocity field. Formally, the velocity of the superfluid is simply given by $\nabla\phi$. This field contains the density fluctuations, as well as the divergence of the vortex velocity flow close to its core. This divergence leads to the well-observed v^{-3} scaling of velocity PDF [51,53,54]. The PDF of $\nabla\phi$ is displayed in Fig. 7. We turn now to analyze the particle velocity PDFs. We compute the velocity PDFs for all runs in the turbulent regime. Data are filtered with a Gaussian convolution in order to smooth out the noisy oscillations at frequencies $\omega < \omega_{\mathrm{noise}} = 50\,(2\pi/\tau_\ell)$ (see Appendix). In Fig. 7 the PDF of the single-component velocity is plotted for all the species of analyzed particles. In Fig. 7(a), velocities are expressed in terms of the speed of sound c, whereas in Fig. 7(b) they are normalized by their root-mean-squared values. The root-mean-squared values are displayed in the inset of Fig. 7(a) as a function of the mass for the two particle sizes. It is apparent from Fig. 7(b) that the particle statistics exhibits a Gaussian distribution. Note that Gaussian velocity statistics was also observed in thermal counterflow simulations of the vortex filament method with tracers particles [30]. The absence of power-law tails could be a consequence of weak statistical sampling of large velocity fluctuations due to the low number of particles present in the system and/or by compressible effects of the GP model. We will comment more about this in Sec. IV.

We would like to remark here that high-frequency fluctuations are strongly sensitive to numerical artifacts. In the Appendix, inspired by the experimental results of Ref. [25], we have computed the velocity PDFs of the velocity fluctuations filtered at a given frequency ω_c. The frequency was varied from values lower to larger than $2\pi/\tau_\ell$. For one simulation we have compared two different interpolation methods to evaluate the force term in Eq. (3) needed to drive the particles. It turns out that for the fourth-order B-spline method, the velocity PDFs start to develop tails while the filtering scale is varied, eventually leading to a v^{-3} scaling. However, when using Fourier interpolation, which is an exact evaluation (up to spectral convergence of the pseudospectral code) of the force term, the PDFs do not develop any tail and remain Gaussian. We have decided to keep this example with spurious numerical effects in the Appendix, as it might be useful for future numerical studies
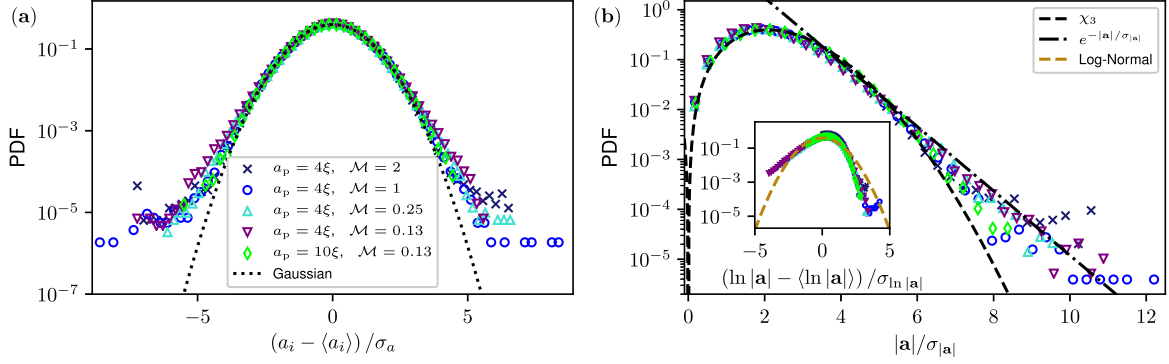
FIG. 8. (a) Probability density functions of the single-component particle acceleration. (b) Probability density functions of the norm of the particle acceleration. The dotted line is a Gaussian, the dashed line is a χ_3 distribution, and the dash-dotted line is an exponential tail $e^{-|\mathbf{a}|/\sigma_{|\mathbf{a}|}}$. Inset: Probability density functions of the natural logarithm of the norm of the particle acceleration. The dashed golden line is a log-normal distribution.

and data analysis of similar problems. We have checked that the results presented in the paper are independent of the interpolation scheme.

We turn now to study the acceleration statistics. As displayed in Fig. 8(a), the PDF of the acceleration presents some deviations from a Gaussian distribution at large values. The norm of the acceleration has also an exponential tail for $|\mathbf{a}| > \sigma_{|\mathbf{a}|}$, as displayed in Fig. 8(b). The core of the PDF in this case is a χ_3 distribution, which is expected for the norm of a vector with Gaussian components. In classical Lagrangian turbulence, the norm of the particle acceleration is observed to obey a log-normal distribution [55]. In the inset of Fig. 8(b), we compare our data with such distribution. For the lightest and smallest particle, the small accelerations appear to be more probable than in the classical case. Note that, as pointed out in [55], small values of the acceleration are very sensible to experimental (numerical) errors. By contrast, the large accelerations are less probable than a log-normal distribution. This observation is compatible with classical numerical calculations in the framework of the viscous vortex filament model, in which it has been shown that, because of inertia, solid particles undergo less rapid changes of velocity than fluid particles [56].

Finally, in Fig. 9, we show the two-point correlator of the particle acceleration, defined as

$$\rho^a(t) = \frac{\langle a_i(t_0) a_i(t_0 + t) \rangle - \langle a_i(t_0) \rangle \langle a_i(t_0 + t) \rangle}{\sigma_a(t_0) \sigma_a(t_0 + t)}. \tag{11}$$
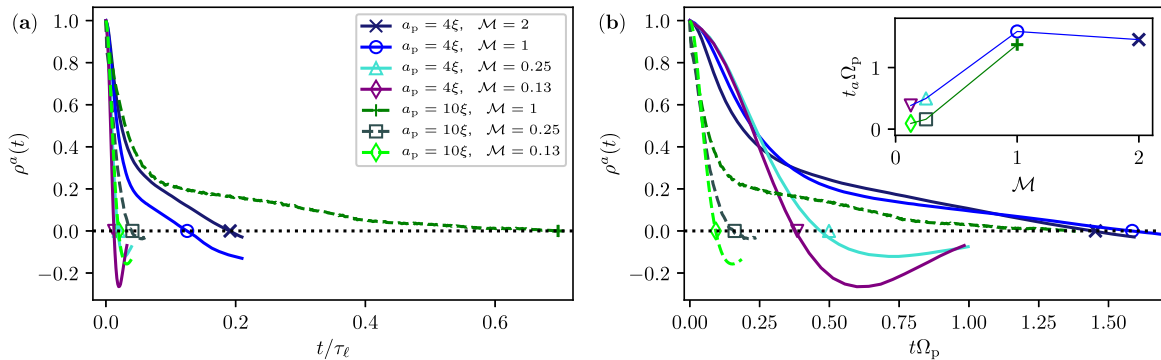
FIG. 9. Acceleration two-point correlator, plotted vs time normalized by the dissipation timescale τ_ℓ (a), and by the Magnus natural frequency $1/\Omega_\mathrm{p}$. (b) Markers indicate the time of acceleration decorrelation t_a. Inset: t_a normalized by $1/\Omega_\mathrm{p}$ as a function of the particle relative mass.

In classical Lagrangian turbulence, the decorrelation time t_a [such that $\rho^a(t_a) = 0$] is related to the Kolmogorov timescale $t_a = 2\tau_\eta$ [57]. This is not the case in quantum turbulence. Figure 9(a) displays the autocorrelation $\rho^a(t)$ for all the simulations. It is apparent that the acceleration decorrelates much faster than τ_ℓ, the equivalent of the Kolmogorov timescale in our system. This fact is a consequence of the myriad of physical phenomena taking place at smaller scales. As most particles are trapped by vortices, they oscillate at the Magnus frequency Ω_p in Eq. (9). If time is normalized by Ω_p (9), then $t_a\Omega_p$ becomes of order 1, at least for the heaviest particles [see Fig. 9(b) and the inset therein]. For the lightest particles, the decorrelation time is even lower, meaning that they are sensible to other mechanisms, such as reconnection events between vortex filaments and Kelvin wave excitations at even smaller scales.

IV. DISCUSSION

In this work, we used the Gross-Pitaevskii model to study free decaying quantum turbulence at zero temperature in the presence of finite-size active particles. We considered different families of spherical particles having sizes smaller than and of the order of the mean intervortex distance. We first performed a standard analysis of the observables commonly used for studying Kolmogorov turbulence, such as the energy decomposition, the temporal evolution of mean energy, the rate of incompressible kinetic energy, and the mean intervortex distance. Although particles are active and get captured by vortices generating Kelvin waves, there is not a significant impact at scales larger than the intervortex distance, where Kolmogorov turbulence takes place. Monitoring the motion of the particles in the system, we confirmed their tendency to remain trapped into vortex filaments during the evolution of the tangle, with intermittent episodes of detachment and recapture. This behavior is independent of the vortex line density. We also found that particles can be easily captured simultaneously by several quantum vortices.

We also studied turbulence from the Lagrangian point of view. In particular, we computed the power spectra of the particle velocities. At large scales the particle dynamics is compatible with that of Lagrangian tracers in classical turbulence, while at short timescales the Magnus precession around the filaments caused by the vortex circulation is dominating the motion. Such information can be extracted consistently both in the frequency spectrum of the velocity and in the decay time of the correlation of the acceleration. Furthermore, if particles are light enough, faster frequencies are also excited. This suggests (as intuitively expected) that light particles can be more sensitive to the small-scale fluctuations of the flow.

Finally, we investigated the particle velocity statistics. The distribution of the particle velocity is Gaussian, in contrast with the power-law scaling $|v_i|^{-3}$ recently observed in superfluid helium experiments [24,25]. There are several reasons why power-law tails are absent in our simulations. First, since the simulation of each particle has an important numerical cost, the number of particles is restricted only to a couple of hundred. Due to this issue, vortex reconnections might be unlikely sampled by the sparse distribution of particles. Note also that, as particles have a finite size, increasing their number keeping the size of the system constant will increase substantially the filling fraction. In this case, turbulence could even be prevented by the presence of particles. Although interesting, this limit is beyond the scope of this work. Secondly, the GP model is compressible, and particles moving at large velocities are slowed down by vortex nucleations. This certainly reduces large velocity fluctuations, perhaps limiting the development of power-law tails. It would be interesting to address such issues in generalized GP models, including a roton minimum and high-order nonlinearities. Moreover, our simulations are by definition at zero temperature, and particles do not follow the singular superfluid velocity field because of the lack of viscosity in the system. Indeed, in the GP model the pressure gradients that drive the particle dynamics are always regular because of the vanishing density at the vortex cores, unlike other models such as the vortex filament method. As a consequence, the divergence of the superfluid velocity along the vortex lines cannot be experienced by the particles. Conversely, at finite temperature the superfluid and the normal component can be locked thanks to mutual friction. In this case, since particles

would sample the normal fluid velocity because of Stokes drag, they might be able to sample the $1/r$ flow around a quantum vortex. Finally, we observed that fast velocity fluctuations are highly sensitive to interpolation and filtering methods that could even lead to power-law tails. These tails are completely spurious, and special care is needed while analyzing numerical or experimental data.

APPENDIX: NUMERICAL ARTIFACTS ON THE PARTICLE VELOCITY STATISTICS: COMPARISON BETWEEN B-SPLINE AND SPECTRAL INTERPOLATION METHODS

As explained in the main text, we evaluate the force $\mathbf{f}_i^{\mathrm{GP}} = -(V_\mathrm{p} * \nabla \rho)[\mathbf{q}_i]$ (3) at the particle position $\mathbf{q}_i$ using a B-spline interpolation method [39] at each time step. Such a method is precise and computationally cheap, but it turns out to present some issues that we have to take care of. To check the reliability of the method, we rerun a simulation using Fourier interpolation for one species of particles in the time window corresponding to the turbulent regime. Fourier interpolation is exact in the sense that it uses the information of the full three-dimensional field, which is resolved with spectral accuracy (i.e., discretization errors are at most exponentially small with the number of discretization points). The numerical cost of this method is that of one Fourier transform (per particle). In Fig. 10 the velocity and acceleration spectra computed using B-spline and Fourier interpolation methods are compared. Clearly, the B-spline interpolation introduces nonphysical fast oscillations, but at the frequencies $\omega < \omega_{\mathrm{noise}} = 50(2\pi/\tau_\ell)$ the behavior of the spectra is unchanged. Nevertheless, some differences in the features of particle statistics are still visible at fast timescales once the noise is filtered out.

We use a Gaussian convolution to perform a filtering of the velocity time series for each particle in the frequency window $\omega_c < \omega < \omega_{\mathrm{noise}}$, where ω_c is a variable infrared cutoff frequency. Then we compute the PDF of the filtered velocity for different values of ω_c. Such PDFs are shown in Fig. 11 comparing the simulations in which Fourier and B-spline interpolation are used for the same species of particle. Surprisingly, only in the latter case do we observe power-law tails for the fast oscillation distributions. Such PDFs are similar to the ones observed experimentally [24,25], but in the present case they are just a consequence of numerical artifacts.
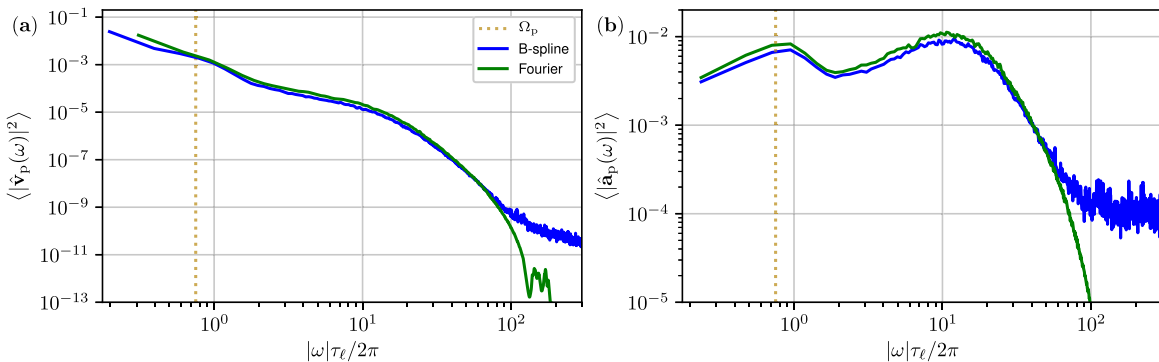
FIG. 10. Velocity spectra (a) and the acceleration spectra (b) for particles of size $a_\mathrm{p} = 10\xi$ and mass $\mathcal{M} = 0.13$, evolved using B-spline interpolation (blue lines) and spectral Fourier interpolation (green lines). The spectra are averaged over particles and over the times $1.3 T_L < t < 1.5 T_L$.
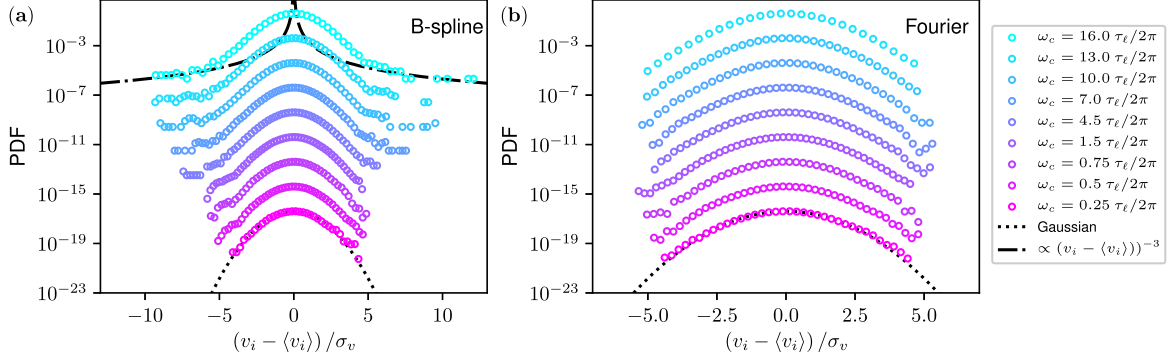
FIG. 11. Probability density function of the velocity filtered in the frequency window $\omega_c < \omega < \omega_{\text{noise}}$ for different values of ω_c. Data refer to particles of size $a_{\text{p}} = 10\xi$ and mass $\mathcal{M} = 0.13$. The dotted line is a Gaussian distribution, and the dash-dotted line is a power-law scaling $0.002(v_i - \langle v_i \rangle)^{-3}$. The data are averaged over particles and over the times $1.3 T_L < t < 1.5 T_L$. Different PDFs are shifted for visualization. (a) Particle force interpolated with the B-spline method. (b) Particle force interpolated with the Fourier method.

[1] U. Frisch and A. N. Kolmogorov, *Turbulence: The Legacy of AN Kolmogorov* (Cambridge University Press, Cambridge, 1995).

[2] R. J. Donnelly, *Quantized Vortices in Helium II* (Cambridge University Press, Cambridge, 1991), Vol. 2.

[3] T. Frisch, Y. Pomeau, and S. Rica, Transition to Dissipation in a Model of Superflow, Phys. Rev. Lett. **69**, 1644 (1992).

[4] T. Winiecki and C. S. Adams, Motion of an object through a quantum fluid, Europhys. Lett. **52**, 257 (2000).

[5] J. Koplik and H. Levine, Vortex Reconnection in Superfluid Helium, Phys. Rev. Lett. **71**, 1375 (1993).

[6] G. P. Bewley, M. S. Paoletti, K. R. Sreenivasan, and D. P. Lathrop, Characterization of reconnecting vortices in superfluid helium, Proc. Natl. Acad. Sci. USA **105**, 13707 (2008).

[7] A. Villois, D. Proment, and G. Krstulovic, Universal and nonuniversal aspects of vortex reconnections in superfluids, Phys. Rev. Fluids **2**, 044701 (2017).

[8] L. Galantucci, A. W. Baggaley, N. G. Parker, and C. F. Barenghi, Crossover from interaction to driven regimes in quantum vortex reconnections, Proc. Natl. Acad. Sci. USA **116**, 12204 (2019).

[9] C. Nore, M. Abid, and M. E. Brachet, Decaying Kolmogorov turbulence in a model of superflow, Phys. Fluids **9**, 2644 (1997).

[10] A. W. Baggaley, J. Laurie, and C. F. Barenghi, Vortex-Density Fluctuations, Energy Spectra, and Vortical Regions in Superfluid Turbulence, Phys. Rev. Lett. **109**, 205304 (2012).

[11] V. Shukla, P. D. Mininni, G. Krstulovic, P. C. di Leoni, and M. E. Brachet, Quantitative estimation of effective viscosity in quantum turbulence, Phys. Rev. A **99**, 043605 (2019).

[12] J. Maurer and P. Tabeling, Local investigation of superfluid turbulence, Europhys. Lett. **43**, 29 (1998).

[13] J. Salort, C. Baudet, B. Castaing, B. Chabaud, F. Daviaud, T. Didelot, P. Diribarne, B. Dubrulle, Y. Gagne, F. Gauthier, A. Girard, B. Hébral, B. Rousset, P. Thibault, and P.-E. Roche, Turbulent velocity spectra in superfluid flows, Phys. Fluids **22**, 125102 (2010).

[14] W. F. Vinen, Decay of superfluid turbulence at a very low temperature: The radiation of sound from a kelvin wave on a quantized vortex, Phys. Rev. B **64**, 134520 (2001).

[15] V. S. L'vov and S. Nazarenko, Weak turbulence of kelvin waves in superfluid he, Low Temp. Phys. **36**, 785 (2010).

[16] J. Laurie, V. S. L'vov, S. Nazarenko, and O. Rudenko, Interaction of kelvin waves and nonlocality of energy transfer in superfluids, Phys. Rev. B **81**, 104526 (2010).

[17] G. Krstulovic, Kelvin-wave cascade and dissipation in low-temperature superfluid vortices, Phys. Rev. E **86**, 055301(R) (2012).

[18] A. W. Baggaley and J. Laurie, Kelvin-wave cascade in the vortex filament model, Phys. Rev. B **89**, 014504 (2014).

[19] A. Villois, D. Proment, and G. Krstulovic, Evolution of a superfluid vortex filament tangle driven by the Gross-Pitaevskii equation, Phys. Rev. E **93**, 061103(R) (2016).

[20] F. Toschi and E. Bodenschatz, Lagrangian properties of particles in turbulence, Annu. Rev. Fluid Mech. **41**, 375 (2009).

[21] W. Guo, M. La Mantia, D. P. Lathrop, and S. W. Van Sciver, Visualization of two-fluid flows of superfluid helium-4, Proc. Natl. Acad. Sci. USA **111**, 4653 (2014).

[22] G. P. Bewley, D. P. Lathrop, and K. R. Sreenivasan, Superfluid helium: Visualization of quantized vortices, Nature (London) **441**, 588 (2006).

[23] E. Fonda, D. P. Meichle, N. T. Ouellette, S. Hormoz, and D. P. Lathrop, Direct observation of kelvin waves excited by quantized vortex reconnection, Proc. Natl. Acad. Sci. USA **111**, 4707 (2014).

[24] M. S. Paoletti, M. E. Fisher, K. R. Sreenivasan, and D. P. Lathrop, Velocity Statistics Distinguish Quantum Turbulence from Classical Turbulence, Phys. Rev. Lett. **101**, 154501 (2008).

[25] M. L. Mantia and L. Skrbek, Quantum, or classical turbulence?, Europhys. Lett. **105**, 46002 (2014).

[26] M. La Mantia and L. Skrbek, Quantum turbulence visualized by particle dynamics, Phys. Rev. B **90**, 014519 (2014).

[27] M. La Mantia, D. Duda, M. Rotter, and L. Skrbek, Lagrangian accelerations of particles in superfluid turbulence, J. Fluid Mech. **717**, R9 (2013).

[28] Y. A. Sergeev and C. F. Barenghi, Particles-vortex interactions and flow visualization in 4he, J. Low Temp. Phys. **157**, 429 (2009).

[29] C. F. Barenghi, D. Kivotides, and Y. A. Sergeev, Close approach of a spherical particle and a quantised vortex in helium II, J. Low Temp. Phys. **148**, 293 (2007).

[30] Y. Mineda, M. Tsubota, Y. A. Sergeev, C. F. Barenghi, and W. F. Vinen, Velocity distributions of tracer particles in thermal counterflow in superfluid ^{4}He, Phys. Rev. B **87**, 174508 (2013).

[31] E. Varga, C. F. Barenghi, Y. A. Sergeev, and L. Skrbek, Backreaction of tracer particles on vortex tangle in helium ii counterflow, J. Low Temp. Phys. **183**, 215 (2016).

[32] J. I. Polanco and G. Krstulovic, Inhomogeneous distribution of particles in coflow and counterflow quantum turbulence, Phys. Rev. Fluids **5**, 032601 (2020).

[33] V. Shukla, M. Brachet, and R. Pandit, Sticking transition in a minimal model for the collisions of active particles in quantum fluids, Phys. Rev. A **94**, 041602(R) (2016).

[34] U. Giuriato and G. Krstulovic, Interaction between active particles and quantum vortices leading to kelvin wave generation, Sci. Rep. **9**, 4839 (2019).

[35] U. Giuriato, G. Krstulovic, and D. Proment, Clustering and phase transitions in a 2d superfluid with immiscible active impurities, J. Phys. A **52**, 305501 (2019).

[36] U. Giuriato, G. Krstulovic, and S. Nazarenko, How trapped particles interact with and sample superfluid vortex excitations, Phys. Rev. Research **2**, 023149 (2020).

[37] A. Griffin, S. Nazarenko, V. Shukla, and M.-E. Brachet, The vortex-particle magnus effect, arXiv:1909.11010.

[38] P. Clark di Leoni, P. D. Mininni, and M. E. Brachet, Dual cascade and dissipation mechanisms in helical quantum turbulence, Phys. Rev. A **95**, 053636 (2017).

[39] M. A. T. van Hinsberg, J. H. M. Thije Boonkkamp, F. Toschi, and H. J. H. Clercx, On the efficiency and accuracy of interpolation methods for spectral codes, SIAM J. Sci. Comput. **34**, B479 (2012).

[40] N. Sasa, T. Kano, M. Machida, V. S. L'vov, O. Rudenko, and M. Tsubota, Energy spectra of quantum turbulence: Large-scale simulation and modeling, Phys. Rev. B **84**, 054525 (2011).

[41] G. Krstulovic, Grid superfluid turbulence and intermittency at very low temperature, Phys. Rev. E **93**, 063104 (2016).

[42] W. F. Vinen, Mutual friction in a heat current in liquid helium ii iii. theory of the mutual friction, Proc. R. Soc. London, Ser. A **242**, 493 (1957).

[43] See Supplemental Material at http://link.aps.org/supplemental/10.1103/PhysRevFluids.5.054608 for movies of the simulations.

[44] N. G. Berloff and P. H. Roberts, Capture of an impurity by a vortex line in a Bose condensate, Phys. Rev. B **63**, 024510 (2000).

[45] A. Villois, G. Krstulovic, D. Proment, and H. Salman, A vortex filament tracking method for the gross-pitaevskii model of a superfluid, J. Phys. A **49**, 415502 (2016).

[46] The circulation measured with this method is subjected to a numerical error coming from the grid spacing. Such error is removed in postprocessing, knowing that Γ can only be an integer multiple of κ. Furthermore, extremely high values of Γ have been removed since they are related to the ill-defined situation in which a topological defect is placed at the boundary $\mathcal{C}$.

[47] P. K. Yeung, Lagrangian characteristics of turbulence and scalar transport in direct numerical simulations, J. Fluid Mech. **427**, 241 (2001).

[48] H. Tennekes, J. L. Lumley, J. Lumley *et al.*, *A First Course in Turbulence* (MIT Press, Cambridge, 1972).

[49] D. Kivotides, Y. A. Sergeev, and C. F. Barenghi, Dynamics of solid particles in a tangle of superfluid vortices at low temperatures, Phys. Fluids **20**, 055105 (2008).

[50] L. Kiknadze and Y. Mamaladze, The magnus (kutta-jukovskii) force acting on a sphere, arXiv:cond-mat/0604436.

[51] A. C. White, C. F. Barenghi, N. P. Proukakis, A. J. Youd, and D. H. Wacks, Nonclassical Velocity Statistics in a Turbulent Atomic Bose-Einstein Condensate, Phys. Rev. Lett. **104**, 075301 (2010).

[52] M. S. Paoletti and D. P. Lathrop, Quantum turbulence, Annu. Rev. Condens. Matter Phys. **2**, 213 (2011).

[53] A. W. Baggaley and C. F. Barenghi, Quantum turbulent velocity statistics and quasiclassical limit, Phys. Rev. E **84**, 067301 (2011).

[54] V. Shukla, M. Brachet, and R. Pandit, Turbulence in the two-dimensional fourier-truncated gross-pitaevskii equation, New J. Phys. **15**, 113025 (2013).

[55] N. Mordant, A. M. Crawford, and E. Bodenschatz, Three-Dimensional Structure of the Lagrangian Acceleration in Turbulent Flows, Phys. Rev. Lett. **93**, 214501 (2004).

[56] D. Kivotides, C. F. Barenghi, A. J. Mee, and Y. A. Sergeev, Interaction of Solid Particles with a Tangle of Vortex Filaments in a Viscous Fluid, Phys. Rev. Lett. **99**, 074501 (2007).

[57] P. K. Yeung and S. B. Pope, Lagrangian statistics from direct numerical simulations of isotropic turbulence, J. Fluid Mech. **207**, 531 (1989).

Chapter 6

Conclusions and perspectives

In this manuscript, I have presented some of my contributions to the field of superfluids. I have chosen to discuss three topics that I find particularly relevant for the current state of experiments with superfluid helium and BECs. Some of those works have an interesting connection with classical flows.

I discussed Kelvin waves in Chapter 3. I found helpful, in particular for students and researchers wishing to learn more about them, to start the chapter by reproducing the key steps of the original work of Lord Kelvin, but using a modern notation. Later in that chapter, I tried to roughly explain how the wave turbulence theory can be applied to explain the transfer of energy toward the smallest scales of the system. Kelvin waves are typically associated with superfluids (not by Lord Kelvin of course), and much less studied in classical fluids. Certainly, they are less important in classical turbulent flows, as there is no notion of inter-vortex distance. On the other hand, it is not difficult to experimentally produce vortex filaments, where the propagation of Kelvin might be relevant. The predictions concerning Kelvin waves are actually based on classical hydrodynamics, so they should apply in classical fluids provided that dissipation is small enough and that we look at scales much larger than the vortex core. We are now investigating such issues numerically with J.I. Polanco. It would be, of course, a great achievement to be able to study Kelvin waves deeply in superfluids. The observation of Kelvin waves in helium [Fon+14] was an important achievement, but quantitative measurements were rather scarce. In addition, the use of particles opens many questions, as discussed in the included publication [GKN20] in Chapter 5. I will come back to this point later. Finally, concerning BECs, there is a long path to be able to study Kelvin waves experimentally. Still, the experimental advances made in the last years, in particular by the Trento group, are quite encouraging. Finding a clean and controlled manner of exciting Kelvin waves is the main difficulty to overcome. Numerical simulations and a good understanding of the physics of Kelvin waves can really help to design new experiments.

The second topic addressed in this manuscript is quantum vortex reconnections, that is presented in Chapter 4. I tried in this chapter to keep a connection with classical fluid. I am convinced that superfluids, at least from a theoretical point of view, can be used to understand many things of classical fluids in the limit of infinite Reynolds numbers. Reconnections are smooth processes in the Gross-Pitaevskii equation, as they are regularised by dispersion, and so they are in Navier-Stokes thanks to viscosity. In figure 4.6, I compared visualisations of the reconnection of a Hopf linked ring, for superfluids, Navier-Stokes and hyper-viscous Navier-Stokes. The goal of this qualitative figure was to show that superfluids and classical fluids are very similar, both dissipate a "piece" of vortex length by the mechanisms allowed by the system. It is thus natural to study in classical fluids, the limit of large rings and vanishing viscosity, and see how the dissipative anomaly manifests in this physical problem. A bit in the same spirit, figure 4.5 displays some hints of an intrinsic irreversible process of vortex reconnections. As mentioned in the text, the same behaviour was recently observed in Navier-Stokes simulations [YH20b]. Again, does this temporal asymmetry persists for infinite Reynolds numbers? Is this behaviour—trajectories approaching a singular point by an attractive manifold, that once they pass the singular event (reconnection), separate in a stochastic manner—somehow akin to spontaneous stochasticity? This behaviour reminds the approach by T. Drivas

and A. Mailybaev [DM18] of spontaneous stochasticity in non-Lipschitz ordinary differential equations. Understanding how the process of vortex reconnections depends on the regularisation mechanism of the system, might provide some insights on the limit of infinite Reynolds numbers. Although such studies are numerically demanding, I believe that is today possible to address many of these questions with a renewed regard.

The initial motivation to study the dynamics of particles in superfluid was their use in current experiments. Some of the works performed during the Ph.D of U. Giuriato are presented in Chapter 5. I have to recognise that I was relatively sceptical that using particles, with a size of some micrometres, to study the dynamics of vortices in superfluid helium, could provide trustful information on the vortex dynamics, in particular at low temperatures. I was nevertheless enthusiastic about understanding how experimental measurements will be affected, how to interpret them, and especially, I was looking forward to finding some new physics. The works I included in that chapter address such issues, from the simple trapping of a particle to Lagrangian turbulence, demonstrating how particles could be used safely, even to determine the dispersion relation of Kelvin waves. I find particularly remarkable, the mathematical analogy between Kelvin waves interacting with particles and electrons propagating in a crystal, developed in the included work [GKN20] and explained in Section 5.3. This work has several interesting continuations. The model (5.12), describing the interaction between a particle and Kelvin waves, results very appealing for students. Its simplicity allows undergraduate students to address open scientific questions, as little prior mathematical and physical knowledge (just a first course on quantum mechanics and some basic notions of fluid dynamics) is required to deal with the equation. Indeed, an undergraduate student in Chile (supervised by G. Düring, PUC) is currently studying how trapped particles exchange momentum with Kelvin waves. In [GKN20], we restricted the study to an array of equidistant trapped particles. The appearance of Brillouin zones with band and gaps in the Kelvin wave dispersion relation was quite surprising to us. The following obvious question is to understand what happens in the presence of some disorder (e.g. particles masses, initial distances, etc.). It is natural to expect Anderson localisation, thought the answer is not trivial as the disorder is not quenched and it is correlated with the incoming waves. Such questions might be certainly almost impossible to address with current experimental technics in superfluids, but they are certainly of great theoretical interest. Besides, as mentioned in [GKN20], the main physics leading to the appearance of band gaps is based on hydrodynamic equations that should apply for very large classical vortices, provided that some external mechanism stabilises them. In that manner, a classical vortex filament loaded with particles could be used as a classical analogue of a quantum system.

This HDR manuscript did not cover many important topics. For instance, I omitted to discuss some recent results obtained in collaboration with J.I Polanco in the framework of the HVBK model (see Section 2.4). We found that a very large counterflow can induce an abrupt transition from three- to two-dimensional turbulence [PK20a], including the emergence of an inverse energy cascade in three-dimensional flows. Such finding could be used, for instance, to study (quasi) two-dimensional turbulence in three-dimensional experiments, instead of using superfluid helium films, that are too complex from the experimental point of view.

Another important open issue related to the large scale description of superfluids is the problem of boundary conditions. The HVBK equations, might (or might not) be a good large scale model for finite temperature superfluids far away from boundaries (as often in theoretical physics), but close to boundaries, its validity is less clear. Such a question is of crucial importance for industrial applications using superfluid helium for cooling sensitive devices. The normal fluid has to satisfy the no-slip boundary conditions, as any viscous fluid. For the superfluid component, there is not a simple answer. In the idealised case of a perfectly smooth surface, as the superfluid is non-viscous, the boundary conditions should be then free-slip. However, at the scale of quantum vortices, the surface is rough, and vortex nucleations should take place dissipating some of the superfluid energy [FPR92]. At the scales at which HVBK is valid, it is thus not clear, which are the proper boundary conditions. Non-trivial modelling and the use of numerical simulations of different equations, valid at different scales, might provide some insights to this question. Undoubtedly, any theoretical result should be confronted with experimental

data. Such understanding will also allow for studying the generation of superfluid turbulence by grids or oscillating objects that are today very often used in superfluid helium experiments.

In the general description of the Gross-Pitaevskii model in Section 2.1, I discussed the different types of waves present in BECs (Bogoliubov waves). It is obvious that such waves can interact non-linearly, and wave turbulent states can emerge. If the amplitude of the waves is small, the theory of weak wave turbulence, briefly explained in Section 3.3.3, can be there applied. To be fair, a proper discussion on weak wave turbulence in BECs deserves at least a full chapter, as depending on the strength of the condensate, the interaction can be three or for waves, with direct and inverse cascades. Here, I just refer to the books [ZLF12; Naz11] for a theoretical description and to the works [NO06; PNO09] for numerical studies. We should remark that this kind of (density) wave turbulence is very different from the one mainly discussed in this manuscript. First of all, it is assumes that there are no vortices in the system (otherwise the theory breaks down) and the cascades (and the physics) at scales smaller than the coherence length are very important. There has been enormous progress from the experimental side. Experimentalists are now able to confine BECs in squared traps, which is very suitable to compare with theory. By "shaking" such traps, wave turbulence cascades have been observed [Nav+16]. As part of the SIMONS Collaboration Wave Turbulence, we are currently studying different aspects of the weak wave turbulence cascade in BECs, from both theoretical and numerical sides.

I have not discussed at all the issue of intermittency. The first experiments with superfluids did not find any differences between classical and superfluid turbulence [MT98]. Such behaviour was also observed in more recent experiments, almost twenty years later [Rus+17]. On the other hand, numerical simulations of HVBK-based shell models found that depending on temperature, intermittency can be either enhanced [Bou+13b] or reduced [SP16]. Some years later, DNS of the HVBK model [Bif+18] provided some support to the findings of [Bou+13b] and recent experiments seems to be in agreement with it [Bao+18]. In the case of low-temperature superfluids (GP), I showed that intermittency is strongly enhanced [Krs16]. While there is a global consensus that second-order structure functions should obey the Kolmogorov prediction (up to eventual intermittency corrections), it is not fully clear why it should be the case for high order moments. In classical fluid, there is not a first principle theory able to explain the multifractality of intermittency [Fri95]. It is believed that vortex filaments are one of the most dissipative structures of classical turbulence, and their contribution is very important for high order statistics. Such an idea is behind the construction of the She-Leveque model for intermittency [SL94], that is known to fit well the scaling exponents. In this model, to fix some recursion relations, a scaling associated with vortex filaments is used for moments of order tending to infinity. In that spirit, as vortex filaments are the essence of quantum turbulence, it is thus natural to think that high-order statistics of superfluid turbulent fields might differ from the classical ones. Whether or not, this difference becomes visible at orders that are possible to investigate numerically or experimentally, it is a different question. I believed that the Gross-Pitaevskii model, although limited to low-temperature superfluids, is the correct framework to address such issues, as quantum vortex filaments are naturally included. One issue that could be somehow easier to address in low-temperature superfluids than in classical flows is the statistics of circulation. There has been a renewed interest in classical fluids concerning how the circulation scales with the size of the loops in the inertial range of turbulence. In [ISY19], it was found that the circulation statistics are intermittent, although they exhibit a simpler (bi-fractal) behaviour than the velocity increments. We have studied that problem in low-temperature superfluids with N.P Müller and J.I. Polanco [MPK20]. We have observed that superfluids present the same property, including the intermittent statistics of circulation in the classical range. As we have largely discussed, the circulation around quantum vortices is discrete. Although for loops with size laying in the inertial range the total number of vortices crossing the loops can be very large, that number is still discrete and it is the sum of the circulation of many individual vortices. This fact suggests that some tools of statistical physics, such as Markov chains or the large deviation theory might help to comprehend the problem. If such an approach is successful, one could hope that this understanding could be extrapolated to classical fluids, as in the inertial range both systems share the same statistics.

As a summary, I have presented in this manuscript many aspects of the dynamics of superfluids that I find very passionating. Superfluid turbulence is a very rich system, with many open questions waiting to be answered. I also believe that superfluid turbulence, can teach us many things about classical fluids and it can be considered as the skeleton of fully developed turbulence.

Appendix A

Numerical tools for superfluids

A.1   Vortex Tracking algorithm

Some questions concerning the dynamics of quantum vortices need to have access to direct information of the vortex lines, such as their position, curvature, torsion, etc. The Gross-Pitaevskii equation does not provide such information, and it has to be extracted numerically from the wave function.

We developed a robust and accurate algorithm to track vortex lines of a periodic wave function ψ, with no prior knowledge of vortex configuration. This algorithm was an important generalisation of the one used in [Krs12] to study Kelvin waves. The full details of the algorithm and the case studies to check its validity can be found in [Vil+16]. We recall here briefly the basic ideas. A quantised vortex line is defined by the nodal lines of the wave function. In three dimensions, this corresponds to a curve defined by

$$Re[\psi(x, y, z)] = Im[\psi(x, y, z)] = 0 \tag{A.1}$$

The algorithm is based on a Newton-Raphson method to find zeros of ψ on a plane and on the knowledge of the *pseudo-vorticity* field $\mathbf{J} = 2\hbar \nabla Re[\psi] \times \nabla Im[\psi]$, that is always tangent to the lines, to follow vortex lines.

Starting from a point $\mathbf{x_0}$, where the density $|\psi|^2$ is below a given small threshold (therefore very close to a vortex), we define the orthogonal plane to the vortex line using $\mathbf{J}(\mathbf{x_0})$. The plane is then spanned by the two directors $\hat{\mathbf{u}}_1$ and $\hat{\mathbf{u}}_2$ as illustrated in Fig.A.1.
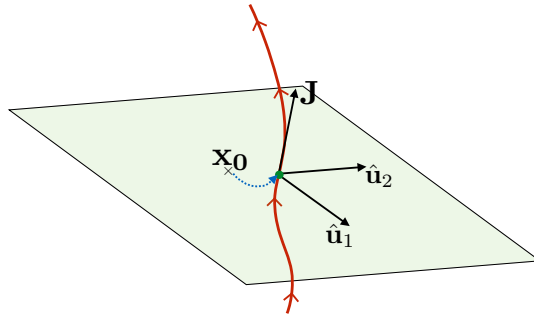
Figure A.1: Sketch of the plane on which the Newton-Raphson method is implemented.

The point $\mathbf{x_0}$ is the first approximation to the vortex position in that plane. A better approximation for the true point $\mathbf{x}_v$, where the vortex line crosses the plane is then given by $\mathbf{x_1} = \mathbf{x_0} + \delta \mathbf{x}$. Here the increment $\delta \mathbf{x}$ is obtained using the Newton-Raphson formula:

$$0 = \begin{pmatrix} Re[\psi(\mathbf{x_0} + \delta\mathbf{x})] \\ Im[\psi(\mathbf{x_0} + \delta\mathbf{x})] \end{pmatrix} \approx \begin{pmatrix} Re[\psi(\mathbf{x_0})] \\ Im[\psi(\mathbf{x_0})] \end{pmatrix} + D\psi(\mathbf{x_0}) \cdot \delta\mathbf{x} \tag{A.2}$$

where $D\psi(\mathbf{x_0})$ is the Jacobian matrix expressed as

$$D\psi = \begin{pmatrix} \nabla Re[\psi] \cdot \hat{\mathbf{u}}_1 & \nabla Re[\psi] \cdot \hat{\mathbf{u}}_2 \\ \nabla Im[\psi] \cdot \hat{\mathbf{u}}_1 & \nabla Im[\psi] \cdot \hat{\mathbf{u}}_2 \end{pmatrix}. \tag{A.3}$$

The increment is therefore found to be $\delta\mathbf{x} = -D\psi(\mathbf{x_0})^{-1} \cdot (Re[\psi(\mathbf{x_0})], Im[\psi(\mathbf{x_0})])^T$. The Jacobian matrix $D\psi$ is a non-singular 2×2 matrix, so its inverse can be computed with its explicit formula. We underline that the method requires the evaluation of the the wave function and the Jacobian (A.2) at intermesh points. Making use of the spectral representation of ψ, we can compute spatial derivatives of the field ψ on those points with the accuracy of spectral methods. As the number of interpolations is small, the evaluation of the fields on those points can be done by direct evaluation of the Fourier sum. Alternatively, if high accuracy is not necessary, some other interpolation schemes can be used to speed up the algorithm. This process can be iterated until the exact vortex location $\mathbf{x}_v$ is determined upon a selected convergence precision.

To track the next vortex point, we use as new initial guess $\mathbf{x_0} = \mathbf{x}_v + \zeta\mathbf{J}$, which is obtained evolving along the pseudo-vorticity by a small step ζ, typically of the order of, or smaller than a healing length. The process is repeated until the entire line is tracked and closed. Once the line is completely tracked, the process is repeated with another line until the whole domain has been fully explored.

The numerical cost of tracking can be very high for dense tangles, especially at large resolutions if one needs the full spectral accuracy provided by Fourier interpolation. Each Fourier interpolation requires the evaluation of $N_x \times N_y \times N_z$ complex exponentials, so that for a vortex filament roughly having a length of $N_v\xi$, the numerical cost is of order $N_v \times N_x \times N_y \times N_z$. Thanks to parallel computing, many processors share this numerical cost, so it remains still affordable even for very long vortices. Such accuracy is needed, for instance, to study Kelvin waves and vortex reconnections. Note that if instead of Fourier interpolation, one uses a local scheme, the cost is substantially reduced.

The previous algorithm is very general and does not assume any prior knowledge of the vortex geometry. In the case of an almost straight vortex, considering the cartesian parametrisation of the vortex $\mathbf{s}(z) = (X(z), Y(z), z)$, the tracking can be reduced to a N_z two-dimensional tracking problems. This simplification allows for a fast tracking of the filaments, even using Fourier interpolation. I introduced this idea in [Krs12], and we have implemented it in FROST (see Section A.3). It is fast enough to be used to determine the spatio-temporal spectra of Kelvin waves [GK19].

A.2 De-aliasing of the Gross-Pitaevskii equation and conservation of invariants

Very often in physics, we are concerned with phenomena taking place at scales much smaller than the system size. In such cases, the physics might be independent of the boundary conditions we impose on the partial differential equation (PDE) describing the system. Such is the case of homogenous turbulence, where inertial scales are independent of the large scale forcing or boundary conditions. In those cases, it is very convenient to assume periodic boundary conditions, so that we can make use of Fourier transforms. The advantage of expressing fields in Fourier space is that differential operators become diagonal. However, on the other hand, non-linear terms become convolutions, that are very expensive to compute. To avoid this computational cost, one uses pseudo-spectral codes, where linear terms are computed in Fourier space while the non-linear ones are evaluated in physical space. Using Fast Fourier Transforms (FFT), passing from physical to Fourier space only costs $\sim N^D \log N$ operations, where N is the number of grid points in one direction and D is the dimension of the system. Note that by definition, a Fourier transform costs N^{2D} operations. Steven Orszag pioneered the study of pseudo-spectral codes, in particular in the field of classical turbulence [Ors69]. We refer to the book [GO09] for further details on pseudo-spectral codes.

Pseudo-spectral codes have the advantage that they approximate solutions of a PDE with spectral accuracy. That means that errors due discretisation are exponentially small and decrease at least as $e^{-c/N}$

(actually one should formally say they are smaller than any power of $1/N$). The reason is that analytic functions decrease very fast in Fourier space, so if N is large enough to ensure *spectral convergence*, a pseudo-spectral code is more accurate that any finite difference scheme.

There is one important extra property of pseudo-spectral codes. For many systems, the discrete equations (of the pseudo-spectral approach), also conserve the corresponding (discrete) invariants of the original PDE. To ensure this, one needs to perform a proper de-aliasing of the fields, that corresponds to kill certain Fourier modes. We explain in the following the origin of aliasing and how to deal with it to conserve the invariants.

For the sake of simplicity, we consider one dimensional 2π-periodic functions. It follows that the wave vectors are integers. To fix the notation, we write a function f in Fourier space as

$$f(x) = \sum_k \hat{f}_k e^{ikx}, \quad \text{and} \quad \hat{f}_k = \frac{1}{2\pi} \int f(x) e^{-ikx} \mathrm{d}x. \tag{A.4}$$

We recall the Parseval theorem, which demonstration is a simple exercise in this case. The theorem states that

$$\frac{1}{2\pi} \int f(x)g(x)\mathrm{d}x = \sum_k \hat{f}_k \hat{g}_{-k}. \tag{A.5}$$

In general, to demonstrate some conservation laws of a PDE, one needs to perform integrations by parts. Even in the case where Fourier transforms are truncated (because of discretisation), integration by parts always hold because of Parseval theorem:

$$\int f'(x)g(x)\mathrm{d}x = 2\pi \sum_k \left(ik\hat{f}_k\right)\hat{g}_{-k} = -2\pi \sum_k \hat{f}_k\left(-ik\hat{g}_{-k}\right) = -\int f(x)g'(x)\mathrm{d}x. \tag{A.6}$$

However, one also needs to be able to apply the Leibniz rule

$$(fg)' = f'g + fg'. \tag{A.7}$$

This rule, it of course holds if we consider the full expansion in the Fourier transform, but it might break down if it is truncated. In order to illustrate this, let's compute the Fourier transform of $(f'g+fg')-(fg)'$. A straightforward calculation gives

$$\widehat{f'g + fg' - (fg)'}_k = \sum_{p,q} i\hat{f}_p\hat{g}_q(p + q - k) \int e^{i(p+q-k)x}\frac{\mathrm{d}x}{2\pi}. \tag{A.8}$$

As $\int e^{i(p+q-k)x}\frac{\mathrm{d}x}{2\pi} = \delta_{p+q,k}$, the right hand side is zero and the Leibniz rule is demonstrated for all wave vectors k.

Let's now consider that the functions are discrete, and N collocation points are used. The Fourier transforms are now discrete and read

$$f(x_j) = f_j = \sum_{k=-N/2+1}^{N/2} \hat{f}_k e^{i\frac{(j-1)2\pi}{N}}, \quad \text{and} \quad \hat{f}_k = \frac{1}{N}\sum_{j=0}^{N-1} f_j e^{-ik\frac{(j-1)2\pi}{N}}\mathrm{d}x. \tag{A.9}$$

Note that wave vectors satisfy $|k| <= N/2$. For the discrete fields, equation becomes

$$\widehat{f'g + fg' - (fg)'}_k = \sum_{p,q} i\hat{f}_p\hat{g}_q(p + q - k)\frac{1}{N}\sum_j e^{i(p+q-k)\frac{(j-1)2\pi}{N}} = \sum_{p,q} i\hat{f}_p\hat{g}_q(p + q - k)\delta_{p+q,k}^{(N)}, \tag{A.10}$$

where $\delta_{i,j}^{(N)}$ is the Kronecker delta modulo N. The right hand side does not always vanish. For instance, if $k = -N/3 + 2, p = q = N/3 + 1$ we have that $\delta_{p+q,k}^{(N)} = 1$ but $(p + q - k) = N \neq 0$ and the Leibniz rule

break downs. To solve this problem, one can impose a Galerkin truncation and keep only wavenumber smaller than then cut-off $k_{\max} = N/3$. We define the Galerkin projector in Fourier space as

$$\mathcal{P}_{\mathrm{G}}[\hat{f}_k] = \theta(k_{\max} - k)\hat{f}_k \tag{A.11}$$

with $\theta(\cdot)$ the Heaviside theta function. The Galerkin projector was introduced in Section 2.1.4 to define the Projected Gross-Pitaevskii equation.

We say that a function is de-aliased if $\mathcal{P}_{\mathrm{G}}[f] = f$. Note that, if f and g are de-aliased, we have that

$$\overline{f'g + fg' - \mathcal{P}_{\mathrm{G}}[fg]'}_k = 0 \tag{A.12}$$

because $|p + q - k| < N$ by construction.

The previous property can be used to solve PDEs and ensures the conservation of invariants by adequately applying the Galerkin projector to the non-linear terms. However, it is important to remark that $N - 2k_{\max} = N/3$ are set to zero, so $1/3$ of the resolution is lost. De-aliasing the fields at $2/3$ of the maximum wavenumber $N/2$ (i.e. at $k_{\max} = N/3$) is known as the 2/3-rule. It is widely known and used in the community of classical fluid dynamics, whereas rarely considered in the community of superfluids.

As an application, let's consider the projected Gross-Pitaevskii equation in one dimension

$$i\hbar\frac{\partial\psi}{\partial t} = \mathcal{P}_{\mathrm{G}}\left[-\frac{\hbar^2}{2m}\partial_{xx}\psi + g\mathcal{P}_{\mathrm{G}}[|\psi|^2]\psi\right], \tag{A.13}$$

As a PDE, the GP equation conserves the momentum $P = \frac{i\hbar}{2}\int(\psi\partial_x\psi^* - \psi^*\partial_x\psi)\mathrm{d}x$. Using the projected GP equation (A.13), we obtain after direct algebra

$$\frac{\mathrm{d}P}{\mathrm{d}t} = \frac{g}{2}\int\left\{\mathcal{P}_{\mathrm{G}}[|\psi|^2]\left(\psi\partial_x\psi^* + \psi^*\partial_x\psi\right) + \psi\partial_x\left(\mathcal{P}_{\mathrm{G}}[|\psi|^2]\psi^*\right) + \psi^*\partial_x\left(\mathcal{P}_{\mathrm{G}}[|\psi|^2]\psi\right)\right\}\mathrm{d}x. \tag{A.14}$$

where the contribution coming from the kinetic terms vanishes by integration by parts (using (A.6)). We also used the property

$$\int\mathcal{P}_G\left[\mathcal{P}_{\mathrm{G}}[|\psi|^2]\psi\right]\partial_x\psi^*\mathrm{d}x = \int\mathcal{P}_{\mathrm{G}}[|\psi|^2]\psi\mathcal{P}_G\left[\partial_x\psi^*\right]\mathrm{d}x = \int\mathcal{P}_{\mathrm{G}}[|\psi|^2]\psi\partial_x\psi^*\mathrm{d}x,$$

because of the Parseval theorem and the fact that ψ is de-aliased ($\mathcal{P}_G[\psi] = \psi$). The Leibniz rule for de-aliased fields implies

$$\psi\partial_x\psi^* + \psi^*\partial_x\psi = \partial_x\mathcal{P}_G\left[|\psi|^2\right] \tag{A.15}$$
$$\partial_x\left(\mathcal{P}_{\mathrm{G}}[|\psi|^2]\psi\right) = \psi\partial_x\mathcal{P}_{\mathrm{G}}[|\psi|^2] + \mathcal{P}_{\mathrm{G}}[|\psi|^2]\partial_x\psi. \tag{A.16}$$

Using the previous two identities in (A.14) and collecting terms we obtain

$$\frac{\mathrm{d}P}{\mathrm{d}t} = g\int\left\{\mathcal{P}_{\mathrm{G}}[|\psi|^2]\partial_x|\psi|^2 + |\psi|^2\partial_x\mathcal{P}_{\mathrm{G}}[|\psi|^2]\right\}\mathrm{d}x = 0, \tag{A.17}$$

where we have used again an integration by parts to show that the r.h.s vanishes. If ψ is not de-aliased or the Galerkin projector is not applied as in equation (A.13), identities (A.15-A.16) are not valid, and $\frac{\mathrm{d}P}{\mathrm{d}t} \neq 0$ for the discrete system.

The GP equation has a quite remarkable structure. Even if de-aliasing is not applied at all, it can be shown that the energy and the number of particles are still conserved. For finite temperature studies, the use of a proper de-aliasing is crucial to conserve momentum. For (standard) GP, spurious effect, such as the change of a ring or dipole size during the evolution, can appear if de-aliasing is not performed. However, the error in the conservation of momentum decreases if the resolution is increased (when $k_{\max} \to \infty$!).

We introduced the de-aliasing scheme (A.13) in [KB11b] to study thermal counterflow. Such a scheme has the advantage of preserving the Hamiltonian structure of the system. Note that, it requires the computations of an extra FFT back and forth to evaluate the non-linear term. A different approach is to compute the non-linear term without the Galerkin projector and perform only the truncation to the right hand side of the equation at $k_{\max} = N/4$. With this approach, one half of the resolution is lost.

A.3   FROST: Full solveR Of Superfluid Turbulence

Most of the scientific results presented in this manuscript have been obtained using to the code FROST, that I have been developing over the last eight years. This code is written in modern Fortran language and takes advantage of the state-of-the-art machines having several thousands of processors. My students Umberto Giuriato and Nicolas P. Müller have enormously contributed to the development of the code. Umberto has developed the particle dynamics in the GP model and the Stochastic-Real-Ginzburg-Landau equation for studying thermal states. Nicolas has developed the generalised GP model, that includes non-local interactions and high order terms. He was also involved in the implementation of a hybrid OpenMP/MPI parallelisation scheme. Finally, Alberto Villois during a stay in Nice, implemented the three-dimensional vortex tracking on the code.

The solver integrates in two and three dimensions different equations that share a similar structure with the Gross-Pitaevskii equation. The solver, the temporal scheme and the dimension are set at compilation time. The possible solvers are:

GP: Gross-Pitaevskii equation. It includes different types of external potentials, order and type of non-linearity and a non-local interaction term. It also integrates GP in a rotating frame. If particles are set on, it integrates the GP-P model with particles. Several standard initial conditions are already implemented.

ADGP: Advected-Dissipative GP. It solves GP in a co-moving frame, and different types of dissipation are included. The advection velocity can be either constant or chosen among many already implemented velocity fields.

RGL: Real-Ginzburg-Landau or GP in imaginary time. This solver is used to generate ground states.

ARGL: Advected-Real-Ginzburg-Landau. This solver is used to generate ground states in a Galilean-transformed frame of reference. It is used for instance to generate turbulent states such as quantum Taylor-Green or ABC flows.

SRGL: Stochastic-Real-Ginzburg-Landau. This solver generates thermal states. Temperature, chemical potential are given as parameters.

SARGL: Stochastic-Advected-Real-Ginzburg-Landau. This solver generates thermal states, including a counterflow velocity.

NEWTON: A Newton-Raphson method to find steady states of the GP equation in a co-moving frame. It uses a biconjugate gradient stabilised method (BiCGSTAB) to solve the associated linear problem. This solver is used for instance to find dipoles and vortex ring that are perfect steady solutions of GP and to follow stable and unstable branches of solutions.

The solver computes several diagnostics on-the-fly, such as the hydrodynamic energies and spectra, and the regularised helicity. It produces outputs to generate spatio-temporal spectra. If turned on, it also performs on-the-fly full three-dimensional vortex tracking, two-dimensional tracking for almost straight vortices and the evaluation of energy and mass fluxes on spheres.

Finally, the code is fully parallelised in slabs using the Message Passing Interface (MPI) library. Such parallelisation is efficient, simple and sufficient for most applications. For very large resolutions, we have partially implemented a hybrid scheme that uses, in addition, the OpenMP shared memory library. This scheme allows to use more processors at fixed resolutions. It has been tested up to 16000 cores, showing a good scaling.

Many parts of the code still need a considerable amount of work to be freely distributed, in particular the documentation. It is nevertheless available upon request.

Bibliography

[Abo+01] J. R. Abo-Shaeer et al. "Observation of Vortex Lattices in Bose-Einstein Condensates". In: *Science* 292.5516 (Apr. 20, 2001), pp. 476–479. ISSN: 0036-8075, 1095-9203. DOI: 10.1126/science.1060182.

[AI75]   P. W. Anderson and N. Itoh. "Pulsar Glitches and Restlessness as a Hard Superfluidity Phenomenon". In: *Nature* 256.5512 (July 1975), pp. 25–27. ISSN: 0028-0836, 1476-4687. DOI: 10.1038/256025a0.

[AM38]   J. F. Allen and A. D. Misener. "Flow of Liquid Helium II". In: *Nature* 141.3558 (Jan. 1938), pp. 75–75. ISSN: 0028-0836, 1476-4687. DOI: 10.1038/141075a0.

[And+95] M. H. Anderson et al. "Observation of Bose-Einstein Condensation in a Dilute Atomic Vapor". In: *Science* 269.5221 (July 14, 1995), pp. 198–201. ISSN: 0036-8075, 1095-9203. DOI: 10.1126/science.269.5221.198.

[Bag+12] A. W. Baggaley et al. "Thermally and Mechanically Driven Quantum Turbulence in Helium II". In: *Physical Review B* 86.10 (Sept. 4, 2012), p. 104501. ISSN: 1098-0121, 1550-235X. DOI: 10.1103/PhysRevB.86.104501.

[Bal04]   Sébastien Balibar. "Looking Back at Superfluid Helium". In: *Poincaré Seminar 2003*. Ed. by Jean Dalibard, Bertrand Duplantier, and Vincent Rivasseau. Basel: Birkhäuser Basel, 2004, pp. 17–29. ISBN: 978-3-7643-7116-6 978-3-0348-7932-3. DOI: 10.1007/978-3-0348-7932-3_2.

[Bal07]   Sébastien Balibar. "The Discovery of Superfluidity". In: *Journal of Low Temperature Physics* 146.5-6 (Feb. 13, 2007), pp. 441–470. ISSN: 0022-2291, 1573-7357. DOI: 10.1007/s10909-006-9276-7.

[Bao+18] S. Bao et al. "Statistics of Turbulence and Intermittency Enhancement in Superfluid He 4 Counterflow". In: *Physical Review B* 98.17 (Nov. 26, 2018), p. 174509. ISSN: 2469-9950, 2469-9969. DOI: 10.1103/PhysRevB.98.174509.

[BB11]   Andrew W. Baggaley and Carlo F. Barenghi. "Spectrum of Turbulent Kelvin-Waves Cascade in Superfluid Helium". In: *Physical Review B* 83.13 (Apr. 8, 2011), p. 134509. ISSN: 1098-0121, 1550-235X. DOI: 10.1103/PhysRevB.83.134509.

[BBP14]   N. G. Berloff, M. Brachet, and N. P. Proukakis. "Modeling Quantum Fluid Dynamics at Nonzero Temperatures". In: *Proceedings of the National Academy of Sciences* 111 (Supplement_1 Mar. 25, 2014), pp. 4675–4682. ISSN: 0027-8424, 1091-6490. DOI: 10.1073/pnas.1312549111.

[BD77]   James S. Brooks and Russell J. Donnelly. "The Calculated Thermodynamic Properties of Superfluid Helium-4". In: *Journal of Physical and Chemical Reference Data* 6.1 (Jan. 1977), pp. 51–104. ISSN: 0047-2689, 1529-7845. DOI: 10.1063/1.555549.

[Bec+07] J. Bec et al. "Heavy Particle Concentration in Turbulence at Dissipative and Inertial Scales". In: *Physical Review Letters* 98.8 (Feb. 21, 2007), p. 084502. ISSN: 0031-9007, 1079-7114. DOI: 10.1103/PhysRevLett.98.084502.

[Ber04]   Natalia G Berloff. "Padé Approximations of Solitary Wave Solutions of the Gross–Pitaevskii Equation". In: *Journal of Physics A: Mathematical and General* 37.5 (Feb. 6, 2004), pp. 1617–1632. ISSN: 0305-4470, 1361-6447. DOI: `10.1088/0305-4470/37/5/011`.

[Bew+08]   G. P. Bewley et al. "Characterization of Reconnecting Vortices in Superfluid Helium". In: *Proceedings of the National Academy of Sciences* 105.37 (Sept. 16, 2008), pp. 13707–13710. ISSN: 0027-8424, 1091-6490. DOI: `10.1073/pnas.0806002105`.

[BHP16]   Michael P. Brenner, Sahand Hormoz, and Alain Pumir. "Potential Singularity Mechanism for the Euler Equations". In: *Physical Review Fluids* 1.8 (Dec. 28, 2016), p. 084503. ISSN: 2469-990X. DOI: `10.1103/PhysRevFluids.1.084503`.

[Bif+18]   L. Biferale et al. "Turbulent Statistics and Intermittency Enhancement in Coflowing Superfluid He 4". In: *Physical Review Fluids* 3.2 (Feb. 21, 2018), p. 024605. ISSN: 2469-990X. DOI: `10.1103/PhysRevFluids.3.024605`.

[Bif+19]   L. Biferale et al. "Strong Anisotropy of Superfluid ^{4}He Counterflow Turbulence". In: *Physical Review B* 100.13 (Oct. 28, 2019), p. 134515. DOI: `10.1103/PhysRevB.100.134515`.

[BL14]   Andrew W. Baggaley and Jason Laurie. "Kelvin-Wave Cascade in the Vortex Filament Model". In: *Physical Review B* 89.1 (Jan. 9, 2014), p. 014504. ISSN: 1098-0121, 1550-235X. DOI: `10.1103/PhysRevB.89.014504`.

[BLS06]   Gregory P. Bewley, Daniel P. Lathrop, and Katepalli R. Sreenivasan. "Visualization of Quantized Vortices". In: *Nature* 441.7093 (June 2006), pp. 588–588. ISSN: 0028-0836, 1476-4687. DOI: `10.1038/441588a`.

[Bou+11]   Laurent Boué et al. "Exact Solution for the Energy Spectrum of Kelvin-Wave Turbulence in Superfluids". In: *Physical Review B* 84.6 (Aug. 23, 2011), p. 064516. ISSN: 1098-0121, 1550-235X. DOI: `10.1103/PhysRevB.84.064516`.

[Bou+13a]   Laurent Boué et al. "Analytic Solution of the Approach of Quantum Vortices Towards Reconnection". In: *Physical Review Letters* 111.14 (Oct. 2, 2013), p. 145302. ISSN: 0031-9007, 1079-7114. DOI: `10.1103/PhysRevLett.111.145302`.

[Bou+13b]   Laurent Boué et al. "Enhancement of Intermittency in Superfluid Turbulence". In: *Physical Review Letters* 110.1 (Jan. 4, 2013), p. 014502. ISSN: 0031-9007, 1079-7114. DOI: `10.1103/PhysRevLett.110.014502`.

[Bou+15]   Laurent Boué et al. "Energy and Vorticity Spectra in Turbulent Superfluid ^{4}He from $T=0$ to T_λ". In: *Physical Review B* 91.14 (Apr. 1, 2015), p. 144501. DOI: `10.1103/PhysRevB.91.144501`.

[BR00]   Natalia G. Berloff and Paul H. Roberts. "Capture of an Impurity by a Vortex Line in a Bose Condensate". In: *Physical Review B* 63.2 (Dec. 20, 2000), p. 024510. ISSN: 0163-1829, 1095-3795. DOI: `10.1103/PhysRevB.63.024510`.

[BR99]   Natalia G Berloff and Paul H Roberts. "Motions in a Bose Condensate: VI. Vortices in a Nonlocal Model". In: *Journal of Physics A: Mathematical and General* 32.30 (July 30, 1999), pp. 5611–5625. ISSN: 0305-4470, 1361-6447. DOI: `10.1088/0305-4470/32/30/308`.

[BSS14]   C. F. Barenghi, L. Skrbek, and K. R. Sreenivasan. "Introduction to Quantum Turbulence". In: *Proceedings of the National Academy of Sciences* 111 (Supplement_1 Mar. 25, 2014), pp. 4647–4652. ISSN: 0027-8424, 1091-6490. DOI: `10.1073/pnas.1400033111`.

[BY07]   Natalia G. Berloff and Anthony J. Youd. "Dissipative Dynamics of Superfluid Vortices at Nonzero Temperatures". In: *Physical Review Letters* 99.14 (Oct. 5, 2007), p. 145301. ISSN: 0031-9007, 1079-7114. DOI: `10.1103/PhysRevLett.99.145301`.

[Cal+08]   Enrico Calzavarini et al. "Dimensionality and Morphology of Particle and Bubble Clusters in Turbulent Flow". In: *Journal of Fluid Mechanics* 607 (July 25, 2008), pp. 13–24. ISSN: 0022-1120, 1469-7645. DOI: 10.1017/S0022112008001936.

[CC13]   Iacopo Carusotto and Cristiano Ciuti. "Quantum Fluids of Light". In: *Reviews of Modern Physics* 85.1 (Feb. 21, 2013), pp. 299–366. ISSN: 0034-6861, 1539-0756. DOI: 10.1103/RevModPhys.85.299.

[Che+06]   Shiyi Chen et al. "Is the Kelvin Theorem Valid for High Reynolds Number Turbulence?" In: *Physical Review Letters* 97.14 (Oct. 4, 2006), p. 144505. ISSN: 0031-9007, 1079-7114. DOI: 10.1103/PhysRevLett.97.144505.

[Chi+10]   Cheng Chin et al. "Feshbach Resonances in Ultracold Gases". In: *Reviews of Modern Physics* 82.2 (Apr. 29, 2010), pp. 1225–1286. ISSN: 0034-6861, 1539-0756. DOI: 10.1103/RevModPhys.82.1225.

[Cla65]   R.C. Clark. "Self-Trapped Electrons in Liquid Helium II". In: *Physics Letters* 16.1 (May 1965), pp. 42–43. ISSN: 00319163. DOI: 10.1016/0031-9163(65)90395-1.

[CMB15]   P. Clark di Leoni, P. D. Mininni, and M. E. Brachet. "Spatiotemporal Detection of Kelvin Waves in Quantum Turbulence Simulations". In: *Physical Review A* 92.6 (Dec. 28, 2015), p. 063632. ISSN: 1050-2947, 1094-1622. DOI: 10.1103/PhysRevA.92.063632.

[CMB16]   P. Clark di Leoni, P. D. Mininni, and M. E. Brachet. "Helicity, Topology, and Kelvin Waves in Reconnecting Quantum Knots". In: *Physical Review A* 94.4 (Oct. 3, 2016), p. 043605. ISSN: 2469-9926, 2469-9934. DOI: 10.1103/PhysRevA.94.043605.

[Da 06]   Luigi Sante Da Rios. "Sul moto d'un liquido indefinito con un filetto vorticoso di forma qualunque". In: *Rendiconti del Circolo Matematico di Palermo* 22.1 (Dec. 1906), pp. 117–135. ISSN: 0009-725X, 1973-4409. DOI: 10.1007/BF03018608.

[Dal+99]   Franco Dalfovo et al. "Theory of Bose-Einstein Condensation in Trapped Gases". In: *Reviews of Modern Physics* 71.3 (Apr. 1, 1999), pp. 463–512. ISSN: 0034-6861, 1539-0756. DOI: 10.1103/RevModPhys.71.463.

[DCB91]   S. Douady, Y. Couder, and M. E. Brachet. "Direct Observation of the Intermittency of Intense Vorticity Filaments in Turbulence". In: *Physical Review Letters* 67.8 (Aug. 19, 1991), pp. 983–986. ISSN: 0031-9007. DOI: 10.1103/PhysRevLett.67.983.

[DM18]   Theodore D. Drivas and Alexei A. Mailybaev. ""Life after Death" in Ordinary Differential Equations with a Non-Lipschitz Singularity". In: (June 23, 2018). Comment: 27 pages, 8 figures. arXiv: 1806.09001 [math-ph].

[DMB01]   M. J. Davis, S. A. Morgan, and K. Burnett. "Simulations of Bose Fields at Finite Temperature". In: *Physical Review Letters* 87.16 (Sept. 27, 2001), p. 160402. ISSN: 0031-9007, 1079-7114. DOI: 10.1103/PhysRevLett.87.160402.

[Don+02]   R. J. Donnelly et al. "The Use of Particle Image Velocimetry in the Study of Turbulence in Liquid Helium". In: *Journal of Low Temperature Physics* 126.1/2 (2002), pp. 327–332. ISSN: 00222291. DOI: 10.1023/A:1013745118386.

[Don91]   Russell J. Donnelly. *Quantized Vortices in Helium II*. Cambridge University Press, Mar. 7, 1991. 368 pp. ISBN: 978-0-521-32400-7.

[Dub19]   Bérengère Dubrulle. "Beyond Kolmogorov Cascades". In: *Journal of Fluid Mechanics* 867 (May 25, 2019), P1. ISSN: 0022-1120, 1469-7645. DOI: 10.1017/jfm.2019.98.

[dWA94]   A. T. A. M. de Waele and R. G. K. M. Aarts. "Route to Vortex Reconnection". In: *Physical Review Letters* 72.4 (Jan. 24, 1994), pp. 482–485. ISSN: 0031-9007. DOI: 10.1103/PhysRevLett.72.482.

[ED15] Gregory L. Eyink and Theodore D. Drivas. "Spontaneous Stochasticity and Anomalous Dissipation for Burgers Equation". In: *Journal of Statistical Physics* 158.2 (Jan. 2015), pp. 386–432. ISSN: 0022-4715, 1572-9613. DOI: 10.1007/s10955-014-1135-3.

[EL20] V.B. Eltsov and V. S. L'vov. "Amplitude of Waves in the Kelvin-Wave Cascade". In: *JETP Letters* (Mar. 30, 2020). ISSN: 0021-3640, 1090-6487. DOI: 10.1134/S0021364020070012.

[Eyi08] Gregory L. Eyink. "Dissipative Anomalies in Singular Euler Flows". In: *Physica D: Nonlinear Phenomena* 237.14-17 (Aug. 2008), pp. 1956–1968. ISSN: 01672789. DOI: 10.1016/j.physd.2008.02.005.

[Fey55] R.P. Feynman. "Chapter II Application of Quantum Mechanics to Liquid Helium". In: *Progress in Low Temperature Physics*. Vol. 1. Elsevier, 1955, pp. 17–53. ISBN: 978-0-444-53307-4. DOI: 10.1016/S0079-6417(08)60077-3.

[FGV01] G. Falkovich, K. Gaw\ c{e}dzki, and M. Vergassola. "Particles and Fields in Fluid Turbulence". In: *Reviews of Modern Physics* 73.4 (Nov. 19, 2001), pp. 913–975. ISSN: 0034-6861, 1539-0756. DOI: 10.1103/RevModPhys.73.913.

[FM96] Charles Fefferman† and Andrew J. Majda‡. "Geometric Constraints on Potentially". In: *Communications in Partial Differential Equations* 21.3-4 (Jan. 1996), pp. 559–571. ISSN: 0360-5302, 1532-4133. DOI: 10.1080/03605309608821197.

[Fon+14] E. Fonda et al. "Direct Observation of Kelvin Waves Excited by Quantized Vortex Reconnection". In: *Proceedings of the National Academy of Sciences* 111 (Supplement_1 Mar. 25, 2014), pp. 4707–4710. ISSN: 0027-8424, 1091-6490. DOI: 10.1073/pnas.1312536110.

[FPR92] T. Frisch, Y. Pomeau, and S. Rica. "Transition to Dissipation in a Model of Superflow". In: *Physical Review Letters* 69.11 (Sept. 14, 1992), pp. 1644–1647. ISSN: 0031-9007. DOI: 10.1103/PhysRevLett.69.1644.

[Fri95] Uriel Frisch. *Turbulence: The Legacy of A.N. Kolmogorov*. 1st ed. Cambridge University Press, Nov. 30, 1995. ISBN: 978-0-521-45103-1 978-1-139-17066-6 978-0-521-45713-2. DOI: 10.1017/CBO9781139170666.

[FSL19] Enrico Fonda, Katepalli R. Sreenivasan, and Daniel P. Lathrop. "Reconnection Scaling in Quantum Fluids". In: *Proceedings of the National Academy of Sciences* 116.6 (Feb. 5, 2019), pp. 1924–1928. ISSN: 0027-8424, 1091-6490. DOI: 10.1073/pnas.1816403116.

[Gal+19] Luca Galantucci et al. "Crossover from Interaction to Driven Regimes in Quantum Vortex Reconnections". In: *Proceedings of the National Academy of Sciences* 116.25 (June 18, 2019), pp. 12204–12211. ISSN: 0027-8424, 1091-6490. DOI: 10.1073/pnas.1818668116.

[Gal+20] Luca Galantucci et al. "A New Self-Consistent Approach of Quantum Turbulence in Superfluid Helium". In: *The European Physical Journal Plus* 135.7 (2020). DOI: 10.1140/epjp/s13360-020-00543-0.

[Gao+15] J. Gao et al. "Producing and Imaging a Thin Line of He$\overset{\ast}{}_2$ Molecular Tracers in Helium-4". In: *Review of Scientific Instruments* 86.9 (Sept. 2015), p. 093904. ISSN: 0034-6748, 1089-7623. DOI: 10.1063/1.4930147.

[Giu20] Umberto Giuriato. "Dynamics of Active Particles in Superfluids and Their Interaction with Quantum Vortices". Ph. D. Physics. Ph. D. Physics. Université Côte d'Azur, Nov. 20, 2020.

[GK19] Umberto Giuriato and Giorgio Krstulovic. "Interaction between Active Particles and Quantum Vortices Leading to Kelvin Wave Generation". In: *Scientific Reports* 9.1 (Dec. 2019), p. 4839. ISSN: 2045-2322. DOI: 10.1038/s41598-019-39877-w.

[GK20a] Umberto Giuriato and Giorgio Krstulovic. "Active and Finite-Size Particles in Decaying Quantum Turbulence at Low Temperature". In: *Physical Review Fluids* 5.5 (May 29, 2020), p. 054608. ISSN: 2469-990X. DOI: 10.1103/PhysRevFluids.5.054608.

[GK20b]   Umberto Giuriato and Giorgio Krstulovic. "Quantum vortex reconnections mediated by trapped particles". In: *Physical Review B* 102 (9 Sept. 2020), p. 094508. DOI: 10.1103/PhysRevB.102.094508.

[GKN20]   Umberto Giuriato, Giorgio Krstulovic, and Sergey Nazarenko. "How Trapped Particles Interact with and Sample Superfluid Vortex Excitations". In: *Physical Review Research* 2.2 (May 11, 2020), p. 023149. ISSN: 2643-1564. DOI: 10.1103/PhysRevResearch.2.023149.

[GKP19]   Umberto Giuriato, Giorgio Krstulovic, and Davide Proment. "Clustering and Phase Transitions in a 2D Superfluid with Immiscible Active Impurities". In: *Journal of Physics A: Mathematical and Theoretical* 52.30 (July 26, 2019), p. 305501. ISSN: 1751-8113, 1751-8121. DOI: 10.1088/1751-8121/ab2607.

[GO09]   David Gottlieb and Steven A. Orszag. *Numerical Analysis of Spectral Methods: Theory and Applications*. Nachdr. CBMS-NSF Regional Conference Series in Applied Mathematics 26. Literaturverz. S. 164 - 167. Philadelphia, Pa: Soc. for Industrial and Applied Mathematics, 2009. 170 pp. ISBN: 978-0-89871-023-6.

[GP58]   V L Ginzburg and L P Pitaevskii. "On the Theory of Superfluidity". In: *Journal of Experimental and Theoretical Physics* 34.5 (Jan. 11, 1958), p. 1240.

[Gri07]   Axel Griesmaier. "Generation of a Dipolar Bose–Einstein Condensate". In: *Journal of Physics B: Atomic, Molecular and Optical Physics* 40.14 (July 28, 2007), R91–R134. ISSN: 0953-4075, 1361-6455. DOI: 10.1088/0953-4075/40/14/R01.

[Gro58]   E.P Gross. "Classical Theory of Boson Wave Fields". In: *Annals of Physics* 4.1 (May 1958), pp. 57–74. ISSN: 00034916. DOI: 10.1016/0003-4916(58)90037-X.

[Guo+10]   W. Guo et al. "Visualization Study of Counterflow in Superfluid He 4 Using Metastable Helium Molecules". In: *Physical Review Letters* 105.4 (July 19, 2010), p. 045301. ISSN: 0031-9007, 1079-7114. DOI: 10.1103/PhysRevLett.105.045301.

[Guo+14]   W. Guo et al. "Visualization of Two-Fluid Flows of Superfluid Helium-4". In: *Proceedings of the National Academy of Sciences* 111 (Supplement_1 Mar. 25, 2014), pp. 4653–4658. ISSN: 0027-8424, 1091-6490. DOI: 10.1073/pnas.1312546111.

[GV08]   Susumu Goto and J. C. Vassilicos. "Sweep-Stick Mechanism of Heavy Particle Clustering in Fluid Turbulence". In: *Physical Review Letters* 100.5 (Feb. 8, 2008), p. 054503. ISSN: 0031-9007, 1079-7114. DOI: 10.1103/PhysRevLett.100.054503.

[HB00]   Cristián Huepe and Marc-Etienne Brachet. "Scaling Laws for Vortical Nucleation Solutions in a Model of Superflow". In: *Physica D: Nonlinear Phenomena* 140.1-2 (June 2000), pp. 126–140. ISSN: 01672789. DOI: 10.1016/S0167-2789(99)00229-8.

[HD11]   Fazle Hussain and Karthik Duraisamy. "Mechanics of Viscous Vortex Reconnection". In: *Physics of Fluids* 23.2 (Feb. 2011), p. 021701. ISSN: 1070-6631, 1089-7666. DOI: 10.1063/1.3532039.

[Hod+01]   E. Hodby et al. "Vortex Nucleation in Bose-Einstein Condensates in an Oblate, Purely Magnetic Potential". In: *Physical Review Letters* 88.1 (Dec. 19, 2001), p. 010405. ISSN: 0031-9007, 1079-7114. DOI: 10.1103/PhysRevLett.88.010405.

[Ido+00]   Olusola C. Idowu et al. "Local Normal-Fluid Helium II Flow Due to Mutual Friction Interaction with the Superfluid". In: *Physical Review B* 62.5 (Aug. 1, 2000), pp. 3409–3415. ISSN: 0163-1829, 1095-3795. DOI: 10.1103/PhysRevB.62.3409.

[ISY19]   Kartik P. Iyer, Katepalli R. Sreenivasan, and P. K. Yeung. "Circulation in High Reynolds Number Isotropic Turbulence Is a Bifractal". In: *Physical Review X* 9.4 (Oct. 4, 2019), p. 041006. DOI: 10.1103/PhysRevX.9.041006.

[JR82]   C A Jones and P H Roberts. "Motions in a Bose Condensate. IV. Axisymmetric Solitary Waves". In: *Journal of Physics A: Mathematical and General* 15.8 (Aug. 1, 1982), pp. 2599–2619. ISSN: 0305-4470. DOI: 10.1088/0305-4470/15/8/036.

[Kap38]   P. Kapitza. "Viscosity of Liquid Helium below the λ-Point". In: *Nature* 141.3558 (Jan. 1938), pp. 74–74. ISSN: 0028-0836, 1476-4687. DOI: 10.1038/141074a0.

[KB11a]   Giorgio Krstulovic and Marc Brachet. "Anomalous Vortex-Ring Velocities Induced by Thermally Excited Kelvin Waves and Counterflow Effects in Superfluids". In: *Physical Review B* 83.13 (Apr. 21, 2011), p. 132506. ISSN: 1098-0121, 1550-235X. DOI: 10.1103/PhysRevB.83.132506.

[KB11b]   Giorgio Krstulovic and Marc Brachet. "Energy Cascade with Small-Scale Thermalization, Counterflow Metastability, and Anomalous Velocity of Vortex Rings in Fourier-Truncated Gross-Pitaevskii Equation". In: *Physical Review E* 83.6 (June 16, 2011), p. 066311. ISSN: 1539-3755, 1550-2376. DOI: 10.1103/PhysRevE.83.066311.

[KBS00]   D. Kivotides, C. F. Barenghi, and David C. Samuels. "Triple Vortex Ring Structure in Superfluid Helium II". In: *Science* 290.5492 (Oct. 27, 2000), pp. 777–779. ISSN: 00368075, 10959203. DOI: 10.1126/science.290.5492.777.

[KBS06]   Demosthenes Kivotides, Carlo F. Barenghi, and Yuri A. Sergeev. "Numerical Calculation of the Interaction of Superfluid Vortices and a Rigid Sphere". In: *Journal of Low Temperature Physics* 144.4-6 (Dec. 5, 2006), pp. 121–134. ISSN: 0022-2291, 1573-7357. DOI: 10.1007/s10909-006-9253-1.

[KBS07]   Demosthenes Kivotides, Carlo F. Barenghi, and Yuri A. Sergeev. "Collision of a Tracer Particle and a Quantized Vortex in Superfluid Helium: Self-Consistent Calculations". In: *Physical Review B* 75.21 (June 7, 2007), p. 212502. ISSN: 1098-0121, 1550-235X. DOI: 10.1103/PhysRevB.75.212502.

[KBS08]   Demosthenes Kivotides, Carlo F. Barenghi, and Yuri A. Sergeev. "Interactions between Particles and Quantized Vortices in Superfluid Helium". In: *Physical Review B* 77.1 (Jan. 28, 2008), p. 014527. ISSN: 1098-0121, 1550-235X. DOI: 10.1103/PhysRevB.77.014527.

[KBT08]   Giorgio Krstulovic, Marc Brachet, and Enrique Tirapegui. "Radiation and Vortex Dynamics in the Nonlinear Schrödinger Equation". In: *Physical Review E* 78.2 (Aug. 1, 2008), p. 026601. ISSN: 1539-3755, 1550-2376. DOI: 10.1103/PhysRevE.78.026601.

[Ker18]   Robert M Kerr. "Trefoil Knot Timescales for Reconnection and Helicity". In: *Fluid Dynamics Research* 50.1 (Feb. 1, 2018), p. 011422. ISSN: 0169-5983, 1873-7005. DOI: 10.1088/1873-7005/aa8163.

[KI13]   Dustin Kleckner and William T. M. Irvine. "Creation and Dynamics of Knotted Vortices". In: *Nature Physics* 9.4 (Apr. 2013), pp. 253–258. ISSN: 1745-2473, 1745-2481. DOI: 10.1038/nphys2560.

[Kiv+01]   D. Kivotides et al. "Kelvin Waves Cascade in Superfluid Turbulence". In: *Physical Review Letters* 86.14 (Apr. 2, 2001), pp. 3080–3083. ISSN: 0031-9007, 1079-7114. DOI: 10.1103/PhysRevLett.86.3080.

[Kiv08a]   Demosthenes Kivotides. "Motion of a Spherical Solid Particle in Thermal Counterflow Turbulence". In: *Physical Review B* 77.17 (May 12, 2008), p. 174508. ISSN: 1098-0121, 1550-235X. DOI: 10.1103/PhysRevB.77.174508.

[Kiv08b]   Demosthenes Kivotides. "Normal-Fluid Velocity Measurement and Superfluid Vortex Detection in Thermal Counterflow Turbulence". In: *Physical Review B* 78.22 (Dec. 1, 2008), p. 224501. ISSN: 1098-0121, 1550-235X. DOI: 10.1103/PhysRevB.78.224501.

[KL93]   Joel Koplik and Herbert Levine. "Vortex Reconnection in Superfluid Helium". In: *Physical Review Letters* 71.9 (Aug. 30, 1993), pp. 1375–1378. ISSN: 0031-9007. DOI: 10.1103/PhysRevLett.71.1375.

[Krs05]   Giorgio Krstulovic. "Dinámica de Vórtices En La Ecuación de Schródinger No Lineal". Memoria Ingeniería Matemática. Memoria Ingeniería Matemática. Santiago, Chile, Jan. 8, 2005.

[Krs12]   Giorgio Krstulovic. "Kelvin-Wave Cascade and Dissipation in Low-Temperature Superfluid Vortices". In: *Physical Review E* 86.5 (Nov. 9, 2012), p. 055301. ISSN: 1539-3755, 1550-2376. DOI: 10.1103/PhysRevE.86.055301.

[Krs16]   Giorgio Krstulovic. "Grid Superfluid Turbulence and Intermittency at Very Low Temperature". In: *Physical Review E* 93.6 (June 8, 2016), p. 063104. ISSN: 2470-0045, 2470-0053. DOI: 10.1103/PhysRevE.93.063104.

[KS04]   Evgeny Kozik and Boris Svistunov. "Kelvin-Wave Cascade and Decay of Superfluid Turbulence". In: *Physical Review Letters* 92.3 (Jan. 22, 2004), p. 035301. ISSN: 0031-9007, 1079-7114. DOI: 10.1103/PhysRevLett.92.035301.

[KS05]   Evgeny Kozik and Boris Svistunov. "Scale-Separation Scheme for Simulating Superfluid Turbulence: Kelvin-Wave Cascade". In: *Physical Review Letters* 94.2 (Jan. 18, 2005), p. 025301. ISSN: 0031-9007, 1079-7114. DOI: 10.1103/PhysRevLett.94.025301.

[KT94]   S Kida and M Takaoka. "Vortex Reconnection". In: *Annual Review of Fluid Mechanics* 26.1 (Jan. 1994), pp. 169–177. ISSN: 0066-4189, 1545-4479. DOI: 10.1146/annurev.fl.26.010194.001125.

[Lah+09]   T Lahaye et al. "The Physics of Dipolar Bosonic Quantum Gases". In: *Reports on Progress in Physics* 72.12 (Dec. 1, 2009), p. 126401. ISSN: 0034-4885, 1361-6633. DOI: 10.1088/0034-4885/72/12/126401.

[Lan41]   L. Landau. "Theory of the Superfluidity of Helium II". In: *Physical Review* 60.4 (Aug. 15, 1941), pp. 356–358. ISSN: 0031-899X. DOI: 10.1103/PhysRev.60.356.

[Lau+10]   Jason Laurie et al. "Interaction of Kelvin Waves and Nonlocality of Energy Transfer in Superfluids". In: *Physical Review B* 81.10 (Mar. 26, 2010), p. 104526. ISSN: 1098-0121, 1550-235X. DOI: 10.1103/PhysRevB.81.104526.

[Le 91]   Michel Le Bellac. *Quantum and Statistical Field Theory*. Oxford ; New York: Oxford University Press, 1991. 592 pp. ISBN: 978-0-19-853929-2 978-0-19-853964-3.

[LLL11]   Lev Davidovi**v**c Landau, Evgenij M. Lif**v**sic, and Lev Davidovich Landau. *Fluid Mechanics*. 2. engl. ed., rev., reprint. with corr. Course of Theoretical Physics by L. D. Landau and E. M. Lifshitz ; Vol. 6. Amsterdam [u.a]: Elsevier/Butterworth Heinemann, 2011. 539 pp. ISBN: 978-0-7506-2767-2.

[LN10]   Victor S. L'vov and Sergey Nazarenko. "Weak Turbulence of Kelvin Waves in Superfluid He". In: *Low Temperature Physics* 36.8 (Aug. 2010), pp. 785–791. ISSN: 1063-777X, 1090-6517. DOI: 10.1063/1.3499242.

[LNR07]   Victor S. L'vov, Sergei V. Nazarenko, and Oleksii Rudenko. "Bottleneck Crossover between Classical and Quantum Superfluid Turbulence". In: *Physical Review B* 76.2 (July 26, 2007), p. 024520. ISSN: 1098-0121, 1550-235X. DOI: 10.1103/PhysRevB.76.024520.

[Lon38]   F. London. "The λ-Phenomenon of Liquid Helium and the Bose-Einstein Degeneracy". In: *Nature* 141 (Apr. 9, 1938), pp. 643–644. DOI: 10.1038/141643a0.

[LS14a]   M. La Mantia and L. Skrbek. "Quantum Turbulence Visualized by Particle Dynamics". In: *Physical Review B* 90.1 (July 29, 2014), p. 014519. ISSN: 1098-0121, 1550-235X. DOI: 10.1103/PhysRevB.90.014519.

[LS14b]   M. La Mantia and L. Skrbek. "Quantum, or Classical Turbulence?" In: *EPL (Europhysics Letters)* 105.4 (Feb. 1, 2014), p. 46002. ISSN: 0295-5075, 1286-4854. DOI: 10.1209/0295-5075/105/46002.

[Mar+15]   A. Marakov et al. "Visualization of the Normal-Fluid Turbulence in Counterflowing Superfluid He 4". In: *Physical Review B* 91.9 (Mar. 6, 2015), p. 094503. ISSN: 1098-0121, 1550-235X. DOI: 10.1103/PhysRevB.91.094503.

[Max83]   Martin R. Maxey. "Equation of Motion for a Small Rigid Sphere in a Nonuniform Flow". In: *Physics of Fluids* 26.4 (1983), p. 883. ISSN: 00319171. DOI: 10.1063/1.864230.

[MBG01]   J. S. Marshall, P. Brancher, and A. Giovannini. "Interaction of Unequal Anti-Parallel Vortex Tubes". In: *Journal of Fluid Mechanics* 446 (Nov. 10, 2001), pp. 229–252. ISSN: 0022-1120, 1469-7645. DOI: 10.1017/S0022112001005754.

[MK20]   Nicolás Pablo Müller and Giorgio Krstulovic. "Kolmogorov and Kelvin Wave Cascades in a Generalized Model for Quantum Turbulence". In: *Physical Review B (in press)* (July 1, 2020). arXiv: 2007.00540 [cond-mat, physics:physics].

[Mof00]   H. K. Moffatt. "The Interaction of Skewed Vortex Pairs: A Model for Blow-up of the Navier–Stokes Equations". In: *Journal of Fluid Mechanics* 409 (Apr. 25, 2000), pp. 51–68. ISSN: 0022-1120, 1469-7645. DOI: 10.1017/S002211209900782X.

[MPK20]   Nicolás P. Müller, Juan Ignacio Polanco, and Giorgio Krstulovic. "Intermittency of Velocity Circulation in Quantum Turbulence". In: (Oct. 15, 2020). arXiv: 2010.07875 [cond-mat, physics:physics].

[MT83]   K. P. Martin and J. T. Tough. "Evolution of Superfluid Turbulence in Thermal Counterflow". In: *Physical Review B* 27.5 (Mar. 1, 1983), pp. 2788–2799. ISSN: 0163-1829. DOI: 10.1103/PhysRevB.27.2788.

[MT98]   J Maurer and P Tabeling. "Local Investigation of Superfluid Turbulence". In: *Europhysics Letters (EPL)* 43.1 (July 1, 1998), pp. 29–34. ISSN: 0295-5075, 1286-4854. DOI: 10.1209/epl/i1998-00314-9.

[NAB97]   C. Nore, M. Abid, and M. E. Brachet. "Decaying Kolmogorov Turbulence in a Model of Superflow". In: *Physics of Fluids* 9.9 (Sept. 1997), pp. 2644–2669. ISSN: 1070-6631, 1089-7666. DOI: 10.1063/1.869473.

[Nav+16]   Nir Navon et al. "Emergence of a Turbulent Cascade in a Quantum Gas". In: *Nature* 539.7627 (Nov. 2016), pp. 72–75. ISSN: 0028-0836, 1476-4687. DOI: 10.1038/nature20114.

[Naz11]   Sergey Nazarenko. *Wave Turbulence*. Lecture Notes in Physics 825. Heidelberg: Springer, 2011. 279 pp. ISBN: 978-3-642-15941-1 978-3-642-15942-8.

[NO06]   Sergey Nazarenko and Miguel Onorato. "Wave Turbulence and Vortices in Bose–Einstein Condensation". In: *Physica D: Nonlinear Phenomena* 219.1 (July 2006), pp. 1–12. ISSN: 01672789. DOI: 10.1016/j.physd.2006.05.007.

[NR11]   Alan C. Newell and Benno Rumpf. "Wave Turbulence". In: *Annual Review of Fluid Mechanics* 43.1 (Jan. 21, 2011), pp. 59–78. ISSN: 0066-4189, 1545-4479. DOI: 10.1146/annurev-fluid-122109-160807.

[NW03]   Sergey Nazarenko and Robert West. "Analytical Solution for Nonlinear Schrödinger Vortex Reconnection". In: *Journal of Low Temperature Physics* 132.1/2 (2003), pp. 1–10. ISSN: 00222291. DOI: 10.1023/A:1023719007403.

[Ors69]   Steven A. Orszag. "Numerical Methods for the Simulation of Turbulence". In: *Physics of Fluids* 12.12 (1969), pp. II–250. ISSN: 00319171. DOI: 10.1063/1.1692445.

[Pag+11]   Dany Page et al. "Rapid Cooling of the Neutron Star in Cassiopeia A Triggered by Neutron Superfluidity in Dense Matter". In: *PHYSICAL REVIEW LETTERS* (2011), p. 4.

[Pao+08]   M. S. Paoletti et al. "Velocity Statistics Distinguish Quantum Turbulence from Classical Turbulence". In: *Physical Review Letters* 101.15 (Oct. 6, 2008), p. 154501. ISSN: 0031-9007, 1079-7114. DOI: 10.1103/PhysRevLett.101.154501.

[PBO13]   Davide Proment, Carlo F. Barenghi, and Miguel Onorato. "Interaction and Decay of Kelvin Waves in the Gross-Pitaevskii Model". In: (Aug. 4, 2013). arXiv: 1308.0852 [cond-mat, physics:nlin, physics:physics].

[Pis99]   Len M. Pismen. *Vortices in Nonlinear Fields: From Liquid Crystals to Superfluids, from Non-Equilibrium Patterns to Cosmic Strings*. Oxford Science Publications 100. Oxford : New York: Clarendon Press ; Oxford University Press, 1999. 290 pp. ISBN: 978-0-19-850167-1.

[Pit61]   L. P. Pitaevskii. "Vortex Lines in an Imperfect Bose Gas". In: *Journal of Experimental and Theoretical Physics* 40.2 (Jan. 8, 1961), p. 646.

[PJ08]   Nick P Proukakis and Brian Jackson. "Finite-Temperature Models of Bose–Einstein Condensation". In: *Journal of Physics B: Atomic, Molecular and Optical Physics* 41.20 (Oct. 28, 2008), p. 203002. ISSN: 0953-4075, 1361-6455. DOI: 10.1088/0953-4075/41/20/203002.

[PK20a]   Juan Ignacio Polanco and Giorgio Krstulovic. "Counterflow-Induced Inverse Energy Cascade in Three-Dimensional Superfluid Turbulence". In: (May 20, 2020). Comment: 5 pages, 4 figures. arXiv: 2005.10106 [cond-mat, physics:physics].

[PK20b]   Juan Ignacio Polanco and Giorgio Krstulovic. "Inhomogeneous Distribution of Particles in Coflow and Counterflow Quantum Turbulence". In: *Physical Review Fluids* 5.3 (Mar. 11, 2020), p. 032601. ISSN: 2469-990X. DOI: 10.1103/PhysRevFluids.5.032601.

[PK20c]   Davide Proment and Giorgio Krstulovic. "Matching theory to characterize sound emission during vortex reconnection in quantum fluids". In: *Phsyical Review Fluids* 5 (10 Oct. 2020), p. 104701. DOI: 10.1103/PhysRevFluids.5.104701.

[PK87]   Alain Pumir and Robert M. Kerr. "Numerical Simulation of Interacting Vortex Tubes". In: *Physical Review Letters* 58.16 (Apr. 20, 1987), pp. 1636–1639. ISSN: 0031-9007. DOI: 10.1103/PhysRevLett.58.1636.

[PNO09]   Davide Proment, Sergey Nazarenko, and Miguel Onorato. "Quantum Turbulence Cascades in the Gross-Pitaevskii Model". In: *Physical Review A* 80.5 (Nov. 12, 2009), p. 051603. ISSN: 1050-2947, 1094-1622. DOI: 10.1103/PhysRevA.80.051603.

[Poo+05]   D. R. Poole et al. "Motion of Tracer Particles in He II". In: *Physical Review B* 71.6 (Feb. 23, 2005), p. 064514. ISSN: 1098-0121, 1550-235X. DOI: 10.1103/PhysRevB.71.064514.

[PR93]   Yves Pomeau and Sergio Rica. "Model of Superflow with Rotons". In: *Physical Review Letters* 71.2 (July 12, 1993), pp. 247–250. ISSN: 0031-9007. DOI: 10.1103/PhysRevLett.71.247.

[PS87]   Alain Pumir and Eric D. Siggia. "Vortex Dynamics and the Existence of Solutions to the Navier–Stokes Equations". In: *Physics of Fluids* 30.6 (1987), p. 1606. ISSN: 00319171. DOI: 10.1063/1.866226.

[Raf07]   Markus Raffel. *Particle Image Velocimetry: A Practical Guide ; with ... 42 Tables*. Berlin: Springer, 2007. ISBN: 978-3-540-72307-3 978-3-540-72308-0 978-1-281-07030-2.

[Ram+01]   C. Raman et al. "Vortex Nucleation in a Stirred Bose-Einstein Condensate". In: *Physical Review Letters* 87.21 (Nov. 1, 2001), p. 210402. ISSN: 0031-9007, 1079-7114. DOI: 10.1103/PhysRevLett.87.210402.

[RBL09]   P.-E. Roche, C. F. Barenghi, and E. Leveque. "Quantum Turbulence at Finite Temperature: The Two-Fluids Cascade". In: *EPL (Europhysics Letters)* 87.5 (Sept. 1, 2009), p. 54006. ISSN: 0295-5075, 1286-4854. DOI: 10.1209/0295-5075/87/54006.

[Rob03a]   Paul H. Roberts. "On Vortex Waves in Compressible Fluids. I. The Hollow–Core Vortex". In: *Proceedings of the Royal Society of London. Series A: Mathematical, Physical and Engineering Sciences* 459.2030 (Feb. 8, 2003), pp. 331–352. ISSN: 1364-5021, 1471-2946. DOI: 10.1098/rspa.2002.1034.

[Rob03b]   Paul H. Roberts. "On Vortex Waves in Compressible Fluids. II. The Condensate Vortex". In: *Proceedings of the Royal Society of London. Series A: Mathematical, Physical and Engineering Sciences* 459.2031 (Mar. 8, 2003), pp. 597–607. ISSN: 1364-5021, 1471-2946. DOI: 10.1098/rspa.2002.1033.

[Roc+07]   P.-E Roche et al. "Vortex Density Spectrum of Quantum Turbulence". In: *Europhysics Letters (EPL)* 77.6 (Mar. 2007), p. 66002. ISSN: 0295-5075, 1286-4854. DOI: 10.1209/0295-5075/77/66002.

[Rou+14]   B. Rousset et al. "Superfluid High REynolds von Kármán Experiment". In: *Review of Scientific Instruments* 85.10 (Oct. 2014), p. 103908. ISSN: 0034-6748, 1089-7623. DOI: 10.1063/1.4897542.

[RR09a]   Sergio Rica and David C. Roberts. "Induced Interaction and Crystallization of Self-Localized Impurity Fields in a Bose-Einstein Condensate". In: *Physical Review A* 80.1 (July 16, 2009), p. 013609. ISSN: 1050-2947, 1094-1622. DOI: 10.1103/PhysRevA.80.013609.

[RR09b]   David C. Roberts and Sergio Rica. "Impurity Crystal in a Bose-Einstein Condensate". In: *Physical Review Letters* 102.2 (Jan. 15, 2009), p. 025301. ISSN: 0031-9007, 1079-7114. DOI: 10.1103/PhysRevLett.102.025301.

[RSC18]   Jason Reneuve, Julien Salort, and Laurent Chevillard. "Structure, Dynamics, and Reconnection of Vortices in a Nonlocal Model of Superfluids". In: *Physical Review Fluids* 3.11 (Nov. 8, 2018), p. 114602. ISSN: 2469-990X. DOI: 10.1103/PhysRevFluids.3.114602.

[Rus+17]   E. Rusaouen et al. "Intermittency of Quantum Turbulence with Superfluid Fractions from 0% to 96%". In: *Physics of Fluids* 29.10 (Oct. 2017), p. 105108. ISSN: 1070-6631, 1089-7666. DOI: 10.1063/1.4991558.

[Saf90]   P. G. Saffman. "A Model of Vortex Reconnection". In: *Journal of Fluid Mechanics* 212 (-1 Mar. 1990), p. 395. ISSN: 0022-1120, 1469-7645. DOI: 10.1017/S0022112090002026.

[Saf93]   P. G. Saffman. *Vortex Dynamics*. 1st ed. Cambridge University Press, Jan. 29, 1993. ISBN: 978-0-521-47739-0 978-0-521-42058-7 978-0-511-62406-3. DOI: 10.1017/CBO9780511624063.

[SB09a]   Y. A. Sergeev and C. F. Barenghi. "Normal Fluid Eddies in the Thermal Counterflow Past a Cylinder". In: *Journal of Low Temperature Physics* 156.3-6 (Sept. 2009), pp. 268–278. ISSN: 0022-2291, 1573-7357. DOI: 10.1007/s10909-009-9900-4.

[SB09b]   Y. A. Sergeev and C. F. Barenghi. "Particles-Vortex Interactions and Flow Visualization in 4He". In: *Journal of Low Temperature Physics* 157.5-6 (Dec. 2009), pp. 429–475. ISSN: 0022-2291, 1573-7357. DOI: 10.1007/s10909-009-9994-8.

[SBP16]   Vishwanath Shukla, Marc Brachet, and Rahul Pandit. "Sticking Transition in a Minimal Model for the Collisions of Active Particles in Quantum Fluids". In: *Physical Review A* 94.4 (Oct. 19, 2016), p. 041602. ISSN: 2469-9926, 2469-9934. DOI: 10.1103/PhysRevA.94.041602.

[Sch74]   K. W. Schwarz. "Spherical Probes and Quantized Vortices: Hydrodynamic Formalism and Simple Applications". In: *Physical Review A* 10.6 (Dec. 1, 1974), pp. 2306–2317. ISSN: 0556-2791. DOI: 10.1103/PhysRevA.10.2306.

[Sch85]   K. W. Schwarz. "Three-Dimensional Vortex Dynamics in Superfluid He 4 : Line-Line and Line-Boundary Interactions". In: *Physical Review B* 31.9 (May 1, 1985), pp. 5782–5804. ISSN: 0163-1829. DOI: 10.1103/PhysRevB.31.5782.

[Sch88]   K. W. Schwarz. "Three-Dimensional Vortex Dynamics in Superfluid He 4 : Homogeneous Superfluid Turbulence". In: *Physical Review B* 38.4 (Aug. 1, 1988), pp. 2398–2417. ISSN: 0163-1829. DOI: 10.1103/PhysRevB.38.2398.

[Ser+15]   S. Serafini et al. "Dynamics and Interaction of Vortex Lines in an Elongated Bose-Einstein Condensate". In: *Physical Review Letters* 115.17 (Oct. 21, 2015), p. 170402. ISSN: 0031-9007, 1079-7114. DOI: 10.1103/PhysRevLett.115.170402.

[Ser+17]   Simone Serafini et al. "Vortex Reconnections and Rebounds in Trapped Atomic Bose-Einstein Condensates". In: *Physical Review X* 7.2 (May 25, 2017), p. 021031. ISSN: 2160-3308. DOI: 10.1103/PhysRevX.7.021031.

[Shu+19]   Vishwanath Shukla et al. "Quantitative Estimation of Effective Viscosity in Quantum Turbulence". In: *Physical Review A* 99.4 (Apr. 4, 2019), p. 043605. ISSN: 2469-9926, 2469-9934. DOI: 10.1103/PhysRevA.99.043605.

[Sig85]   Eric D. Siggia. "Collapse and Amplification of a Vortex Filament". In: *Physics of Fluids* 28.3 (1985), p. 794. ISSN: 00319171. DOI: 10.1063/1.865047.

[vSL17]   P. **v**Svan**v**cara and M. La Mantia. "Flows of Liquid ^{4} He Due to Oscillating Grids". In: *Journal of Fluid Mechanics* 832 (Dec. 10, 2017), pp. 578–599. ISSN: 0022-1120, 1469-7645. DOI: 10.1017/jfm.2017.703.

[SL94]   Zhen-Su She and Emmanuel Leveque. "Universal Scaling Laws in Fully Developed Turbulence". In: *Physical Review Letters* 72.3 (Jan. 17, 1994), pp. 336–339. ISSN: 0031-9007. DOI: 10.1103/PhysRevLett.72.336.

[SMO93]   M. J. Shelley, D. I. Meiron, and S. A. Orszag. "Dynamical Aspects of Vortex Reconnection of Perturbed Anti-Parallel Vortex Tubes". In: *Journal of Fluid Mechanics* 246 (Jan. 1993), pp. 613–652. ISSN: 0022-1120, 1469-7645. DOI: 10.1017/S0022112093000291.

[Son12]   E. B. Sonin. "Symmetry of Kelvin-Wave Dynamics and the Kelvin-Wave Cascade in the T = 0 Superfluid Turbulence". In: *Physical Review B* 85.10 (Mar. 21, 2012), p. 104516. ISSN: 1098-0121, 1550-235X. DOI: 10.1103/PhysRevB.85.104516.

[Son87]   E. B. Sonin. "Vortex Oscillations and Hydrodynamics of Rotating Superfluids". In: *Reviews of Modern Physics* 59.1 (Jan. 1, 1987), pp. 87–155. ISSN: 0034-6861. DOI: 10.1103/RevModPhys.59.87.

[SP16]   Vishwanath Shukla and Rahul Pandit. "Multiscaling in Superfluid Turbulence: A Shell-Model Study". In: *Physical Review E* 94.4 (Oct. 3, 2016), p. 043101. ISSN: 2470-0045, 2470-0053. DOI: 10.1103/PhysRevE.94.043101.

[Sre84]   K. R. Sreenivasan. "On the Scaling of the Turbulence Energy Dissipation Rate". In: *Physics of Fluids* 27.5 (1984), p. 1048. ISSN: 00319171. DOI: 10.1063/1.864731.

[SS04]   Catherine Sulem and Pirre-Louis Sulem, eds. *The Nonlinear Schrödinger Equation: Self-Focusing and Wave Collapse*. Vol. 139. Applied Mathematical Sciences. New York, NY: Springer New York, 2004. ISBN: 978-0-387-98611-1. DOI: 10.1007/b98958.

[SSL03]   L. Santos, G. V. Shlyapnikov, and M. Lewenstein. "Roton-Maxon Spectrum and Stability of Trapped Dipolar Bose-Einstein Condensates". In: *Physical Review Letters* 90.25 (June 27, 2003), p. 250403. ISSN: 0031-9007, 1079-7114. DOI: 10.1103/PhysRevLett.90.250403.

[Sun+12]   Can Sun et al. "Observation of the Kinetic Condensation of Classical Waves". In: *Nature Physics* 8.6 (June 2012), pp. 470–474. ISSN: 1745-2473, 1745-2481. DOI: 10.1038/nphys2278.

[Svi95]   Boris V. Svistunov. "Superfluid Turbulence in the Low-Temperature Limit". In: *Physical Review B* 52.5 (Aug. 1, 1995), pp. 3647–3653. ISSN: 0163-1829, 1095-3795. DOI: 10.1103/PhysRevB.52.3647.

[TA11]   Makoto Tsubota and Hiroyuki Adachi. "Simulation of Counterflow Turbulence by Vortex
           Filaments: Statistics of Vortex Reconnections". In: *Journal of Low Temperature Physics*
           162.3-4 (Feb. 2011), pp. 367–374. ISSN: 0022-2291, 1573-7357. DOI: `10.1007/s10909-010-`
           `0290-4`.

[TB09]   Federico Toschi and Eberhard Bodenschatz. "Lagrangian Properties of Particles in Turbu-
           lence". In: *Annual Review of Fluid Mechanics* 41.1 (Jan. 2009), pp. 375–404. ISSN: 0066-4189,
           1545-4479. DOI: `10.1146/annurev.fluid.010908.165210`.

[TBM20]   Simon Thalabard, Jérémie Bec, and Alexei A. Mailybaev. "From the Butterfly Effect to
           Spontaneous Stochasticity in Singular Shear Flows". In: *Communications Physics* 3.1 (Dec.
           2020), p. 122. ISSN: 2399-3650. DOI: `10.1038/s42005-020-0391-6`.

[Tho68]   W. Thomson. "VI. On Vortex Motion". In: *Transactions of the Royal Society of Edinburgh*
           25.1 (1868), pp. 217–260. ISSN: 0080-4568, 2053-5945. DOI: `10.1017/S0080456800028179`.

[Tho80a]   William Thomson. "On Gravitational Oscillations of Rotating Water". In: *Proceedings of
           the Royal Society of Edinburgh* 10 (1880), pp. 92–100. ISSN: 0370-1646. DOI: `10.1017/`
           `S0370164600043467`.

[Tho80b]   William Thomson. "Vibrations of a Columnar Vortex". In: *The London, Edinburgh, and
           Dublin Philosophical Magazine and Journal of Science* 10.61 (Sept. 1880), pp. 155–168. ISSN:
           1941-5982, 1941-5990. DOI: `10.1080/14786448008626912`.

[Tis38]   L. Tisza. "Transport Phenomena in Helium II". In: *Nature* 141.3577 (May 1938), pp. 913–
           913. ISSN: 0028-0836, 1476-4687. DOI: `10.1038/141913a0`.

[Vas15]   J. Christos Vassilicos. "Dissipation in Turbulent Flows". In: *Annual Review of Fluid Me-
           chanics* 47.1 (Jan. 3, 2015), pp. 95–114. ISSN: 0066-4189, 1545-4479. DOI: `10.1146/annurev-`
           `fluid-010814-014637`.

[VCC12]   S. Villerot, B. Castaing, and L. Chevillard. "Static Spectroscopy of a Dense Superfluid".
           In: *Journal of Low Temperature Physics* 169.1-2 (Oct. 2012), pp. 1–14. ISSN: 0022-2291,
           1573-7357. DOI: `10.1007/s10909-012-0639-y`.

[VD07]   William F Vinen and Russell J Donnelly. "Quantum Turbulence". In: *Physics Today* 60.4
           (Jan. 4, 2007), p. 43. DOI: `10.1063/1.2731972`.

[Vil+16]   Alberto Villois et al. "A Vortex Filament Tracking Method for the Gross–Pitaevskii Model
           of a Superfluid". In: *Journal of Physics A: Mathematical and Theoretical* 49.41 (Oct. 14,
           2016), p. 415502. ISSN: 1751-8113, 1751-8121. DOI: `10.1088/1751-8113/49/41/415502`.

[Vin05]   W F Vinen. "How Is Turbulent Energy Dissipated in a Superfluid?" In: *Journal of Physics:
           Condensed Matter* 17.45 (Nov. 16, 2005), S3231–S3238. ISSN: 0953-8984, 1361-648X. DOI:
           `10.1088/0953-8984/17/45/006`.

[VN02]   W F Vinen and J J Niemela. "Quantum Turbulence". In: *Journal of Low Temperature Physics*
           128.516 (Jan. 9, 2002), p. 65.

[VPK16]   Alberto Villois, Davide Proment, and Giorgio Krstulovic. "Evolution of a Superfluid Vor-
           tex Filament Tangle Driven by the Gross-Pitaevskii Equation". In: *Physical Review E* 93.6
           (June 30, 2016), p. 061103. ISSN: 2470-0045, 2470-0053. DOI: `10.1103/PhysRevE.93.061103`.

[VPK17]   Alberto Villois, Davide Proment, and Giorgio Krstulovic. "Universal and Nonuniversal As-
           pects of Vortex Reconnections in Superfluids". In: *Physical Review Fluids* 2.4 (Apr. 4, 2017),
           p. 044701. ISSN: 2469-990X. DOI: `10.1103/PhysRevFluids.2.044701`.

[VPK20]   Alberto Villois, Davide Proment, and Giorgio Krstulovic. "Irreversible Dynamics of Vor-
           tex Reconnections in Quantum Fluids". In: *Physical Review Letters* 125 (16 Oct. 2020),
           p. 164501. DOI: `10.1103/PhysRevLett.125.164501`.

[VS18]   Alberto Villois and Hayder Salman. "Vortex Nucleation Limited Mobility of Free Electron Bubbles in the Gross-Pitaevskii Model of a Superfluid". In: *Physical Review B* 97.9 (Mar. 13, 2018), p. 094507. ISSN: 2469-9950, 2469-9969. DOI: 10.1103/PhysRevB.97.094507.

[VTM03]   W. F. Vinen, Makoto Tsubota, and Akira Mitani. "Kelvin-Wave Cascade on a Vortex in Superfluid H e 4 at a Very Low Temperature". In: *Physical Review Letters* 91.13 (Sept. 25, 2003), p. 135301. ISSN: 0031-9007, 1079-7114. DOI: 10.1103/PhysRevLett.91.135301.

[WA00]   T Winiecki and C. S Adams. "Motion of an Object through a Quantum Fluid". In: *Europhysics Letters (EPL)* 52.3 (Nov. 1, 2000), pp. 257–263. ISSN: 0295-5075, 1286-4854. DOI: 10.1209/epl/i2000-00432-x.

[Wal+14]   P. Walmsley et al. "Dynamics of Quantum Turbulence of Different Spectra". In: *Proceedings of the National Academy of Sciences* 111 (Supplement_1 Mar. 25, 2014), pp. 4691–4698. ISSN: 0027-8424, 1091-6490. DOI: 10.1073/pnas.1312544110.

[WP74]   Gary A. Williams and Richard E. Packard. "Photographs of Quantized Vortex Lines in Rotating He II". In: *Physical Review Letters* 33.5 (July 29, 1974), pp. 280–283. ISSN: 0031-9007. DOI: 10.1103/PhysRevLett.33.280.

[Xue+16]   Zhike Xue et al. "Observing the Release of Twist by Magnetic Reconnection in a Solar Filament Eruption". In: *Nature Communications* 7.1 (Sept. 2016), p. 11837. ISSN: 2041-1723. DOI: 10.1038/ncomms11837.

[YGP79]   E. J. Yarmchuk, M. J. V. Gordon, and R. E. Packard. "Observation of Stationary Vortex Arrays in Rotating Superfluid Helium". In: *Physical Review Letters* 43.3 (July 16, 1979), pp. 214–217. ISSN: 0031-9007. DOI: 10.1103/PhysRevLett.43.214.

[YH20a]   Jie Yao and Fazle Hussain. "A Physical Model of Turbulence Cascade via Vortex Reconnection Sequence and Avalanche". In: *Journal of Fluid Mechanics* 883 (Jan. 25, 2020), A51. ISSN: 0022-1120, 1469-7645. DOI: 10.1017/jfm.2019.905.

[YH20b]   Jie Yao and Fazle Hussain. "Separation Scaling for Viscous Vortex Reconnection". In: *Journal of Fluid Mechanics* 900 (Oct. 10, 2020), R4. ISSN: 0022-1120, 1469-7645. DOI: 10.1017/jfm.2020.558.

[ZCV04]   T. Zhang, D. Celik, and S. W. Van Sciver. "Tracer Particles for Application to PIV Studies of Liquid Helium". In: *Journal of Low Temperature Physics* 134.3/4 (Feb. 2004), pp. 985–1000. ISSN: 0022-2291. DOI: 10.1023/B:JOLT.0000013213.61721.51.

[ZLF12]   V. E Zakharov, V. S L'vov, and G Falkovich. *Kolmogorov Spectra of Turbulence. I, I,* 2012. ISBN: 978-3-642-50054-1.

[Zme+15]   D. E. Zmeev et al. "Dissipation of Quasiclassical Turbulence in Superfluid He 4". In: *Physical Review Letters* 115.15 (Oct. 8, 2015), p. 155303. ISSN: 0031-9007, 1079-7114. DOI: 10.1103/PhysRevLett.115.155303.

[ZV05]   Tao Zhang and Steven W. Van Sciver. "Large-Scale Turbulent Flow around a Cylinder in Counterflow superfluid4He (He (II))". In: *Nature Physics* 1.1 (Oct. 2005), pp. 36–38. ISSN: 1745-2473, 1745-2481. DOI: 10.1038/nphys114.